CORA Cork Open Research Archive
Cartlann Taighde Oscailte Chorcaí

Title	Understanding key geological processes and controls on cold-water coral habitat development in submarine canyons
Authors	O'Reilly, Luke
Publication date	2022
Original Citation	O'Reilly, L. G. R. 2022. Understanding key geological processes and controls on cold-water coral habitat development in submarine canyons. PhD Thesis, University College Cork.
Type of publication	Doctoral thesis
Rights	© 2022, Luke Gerald Ronnie O'Reilly. - https://creativecommons.org/licenses/by-nc-nd/4.0/
Download date	2026-11-05 18:42:46
Item downloaded from	https://hdl.handle.net/10468/14054

UCC
University College Cork, Ireland
Coláiste na hOllscoile Corcaigh

Ollscoil na hÉireann, Corcaigh

National University of Ireland, Cork



Understanding Key Geological Processes and Controls on Cold-water Coral Habitat Development in Submarine Canyons

Thesis presented by

Luke Gerald Ronnie O'Reilly, BSc (Hons)

[ORCiD: 0000-0001-9340-7376]

for the degree of

Doctor of Philosophy

University College Cork

School of Biological Earth and Environmental Sciences

Head of School/Department: Prof. Astrid Wingler

Supervisor(s): Prof. Andy Wheeler & Dr Aaron Lim

2022

Table of Contents

List of Figures vii

List of Tables ix

List of Abbreviations xiii

Declaration xv

Acknowledgements xvi

Abstract 1

Chapter 1: Cold-water Corals and Submarine Canyons 3

1.1 Cold-water Corals 4

1.2 Coral Mound Development 8

1.3 An Overview of Coral Mounds in the NE Atlantic 12

1.4 Submarine Canyons 15

1.4.1 The Porcupine Bank Canyon 16

1.4.2 Watermasses 18

1.5 The (de)glaciation of the British and Irish Ice Sheet 20

1.6 Aims and objectives of this research 23

1.7 Author contributions 26

Chapter 2: Using Novel Methods to Track British and Irish Ice Sheet Dynamics since the Late Pleistocene, along the west Porcupine Bank, NE Atlantic 29

Abstract 29

2.1 Introduction 31

2.2 Geographical Setting 34

2.3 Methods 36

2.3.1 ROV-Vibrocorer 36

2.3.2 Core analysis 36

2.3.2.1 Computed Tomography 36

2.3.2.2 Grain Size Analysis 37
2.3.2.2.1 Grain Size End-Member Modelling 38
2.3.2.2.1.1 Ground Truthing 38
2.3.2.3 AMS radiocarbon measurements 39
2.3.3 Age Model 39
2.4 Results 40
2.4.1 Description of CE18011_VC2 40
Unit A (48–73 cmbsf) 40
Unit B (42–48 cmbsf) 41
Unit C (18–42 cmbsf) 41
Unit D (0–18 cmbsf) 43
2.4.1.1 End-member modelling analysis 43
2.4.1.1.1 Ground Truthing 43
2.4.2 Chronostratigraphic framework 44
2.4.2.1 Age Model Development 45
2.4.3 Sedimentation rates and ice rafted debris events 46
2.5 Discussion 48
2.5.1 Sedimentology 50
2.5.1.1 What are the causes of the IRD pulses? 50
2.5.1.1.1 Pre-Last Glacial Maximum 51
2.5.1.1.2 Post-Last Glacial Maximum 52
2.5.1.2 The Impacts of Glaciation on Background Sedimentation 53
2.5.2 The impacts of (de)glaciation on hydrodynamics 54
2.5.3 Explanation of the Hiatus 55
2.6 Conclusions 56
2.7 Acknowledgements 57

Chapter 3: Environmental Forcing by Submarine Canyons: Evidence Between Two Closely Situated Cold-Water Coral Mounds (West Porcupine Bank and Porcupine Bank Canyon, NE Atlantic). 59

Abstract 59

3.1 Introduction 61

3.2 Regional Setting 65

3.2.1 Hydrography 66

3.2.2 CWC Distribution 67

3.3. Methods 67

3.3.1 Vibrocoring 67

3.3.2 Core analysis 68

3.3.2.1 Computer Tomography 68

3.3.2.2 Grain Size Analysis 69

3.3.3 AMS radiocarbon measurements 70

3.3.4 Stable-isotope analysis 71

3.3.5 Benthic foraminiferal assemblages 72

3.4. Results 73

3.4.1. Core CE_VC1 73

3.4.2 Core RH_VC7 73

3.4.3 Chronology and coral mound aggradation rates 75

3.4.3 Benthic foraminifera 78

3.4.3.1 Multivariate analysis and Species Diversity 82

3.4.3.2 Distance-based Redundancy Analysis (dbRDA) 84

3.5 Discussion 87

3.5.1 The Controls of Mound Development in the wPB 87

3.5.1.1. Early Holocene 87

3.5.1.2 Early – Middle Holocene Transition 88

3.5.1.3 Mid-Holocene 89

3.5.2 Proximity to the canyon – an essential driver for coral growth 91

3.5.3 Summary of environmental factors controlling wPB and PBC mounds during the Holocene 94

3.6. Conclusion 95

3.7 Acknowledgements 97

Chapter 4: Are Submarine Canyons Refugia for Scleractinian Cold-water Corals in Glacial Periods?: Evidence from the Porcupine Bank Canyon, NE Atlantic 98

Abstract 98

4.1 Introduction 100

4.2 Regional Setting 104

4.2.1 Cold-water Coral Reef and Mound Distributions 106

4.3 Materials and Methods 107

4.3.1 Novel ROV-Vibrocoring 107

4.3.2 Core analysis 108

4.3.2.1 Computer Tomography 108

4.3.2.2 Radiocarbon and Uranium-series dating 109

4.3.2.2.1 AMS radiocarbon measurements 109

4.4. Results 111

4.4.1. Description and CT-based classification of Cold-Water Coral-Bearing Cores 111

4.4.1.1 Coral Mound Summit Cores 111

4.4.1.2 Coral Rubble Cores from the Flat wBP Top Sediments 111

4.4.1.3 Canyon Slope/Foot of the Slope Cores 112

4.5. Interpretation & Discussion 119

4.5.1 Geomorphological Control of and Cold-Water Coral Distribution 119

4.5.1.1 Coral Mound Summit Cores 119

4.5.1.2 Coral Rubble Cores from the Flat wBP Top Sediments 121

4.5.1.3 Canyon Slope/Foot of the Slope Cores 123

4.5.1.4 Coral Development Model 123

4.5.2 Glacial Occurrence of Cold-water Corals: Unprecedented Evidence on the High Latitude European NE Atlantic margin 125

4.5.2.1 Mechanism: Submarine Canyons Serve as *Desmophyllum pertusum* Refugia 128

4.6. Conclusion 131

4.7 Acknowledgements 132

Chapter 5. Conclusions 133

5.1 Recommendations for Future Studies 135

Appendices 137

Additional Material 210

Thesis References 238

List of Figures

Figure 1: Global distribution of the scleractinian cold-water corals 5

Figure 2: Mound formation model by Roberts and Cairns (2014). 10

Figure 3: Effects of accommodation space and sediment input on mound formation model proposed by Wang et al. (2021) 11

Figure 4: Cold-water coral mound provinces off Ireland..... 13

Figure 5: Oceanography and topography of the Porcupine Bank Canyon ... 17

Figure 6: The maximum extent of the British-Irish Ice Sheet off Ireland..... 22

Figure 7: Map of the study site..... 34

Figure 8: Log of core CE18011_VC2 42

Figure 9: Surface microtextures identified on ice-rafted debris 44

Figure 10: Age model and subsequent classification of core CE18011_VC2 46

Figure 11: Multiproxy data of core CE18011_VC2 plotted versus time..... 49

Figure 12: Map of the study site..... 65

Figure 13: Logs of cores CE18011_VC1 and RH17002_VC7. 75

Figure 14: SEM images of dominant benthic foraminifera (plate 1 & 2) 79

Figure 15: Multiproxy data of cores CE18011_VC1 & RH17002_VC7 versus time..... 81

Figure 16: Agglomerative dendrogram of benthic foraminifera assemblages 83

Figure 17: Distance-based redundancy analysis of benthic foraminifera assemblages..... 85

Figure 18: Conceptual development of mound developmentderived from cores CE18011_VC1 and RH17002_VC7 95

Figure 19: Map of the study site..... 105

Figure 20: Compilation of core logs from cores CE18011_VC1, CE18011_VC4, CE18011_VC5, CE18011_VC6, CE18011_VC8, RH17002_VC1 and RH17002_VC1..... 115

Figure 21: Sketch of CWC reef patterns affected by geomorphological settings 124

Figure 22: Fossil chronology of D. pertusum in high latitudes as proposed by Henry et al. (2014) 127

List of Tables

Table 1: Environmental parameters controlling CWCs 7

Table 2: Radiocarbon results of core CE18011_VC2 45

Table 3: Summary of acquisition of core CE18011_VC1 and RH17002_VC7 68

Table 4: Radiocarbon results of core CE18011_VC1 and RH17002_VC7 .. 77

Table 5: Percentage relative abundance of dominant benthic foraminifera from each benthic foraminifera assemblage in core CE18011_VC1 and RH17002_VC7..... 82

Table 6: Results of db-RDA test on benthic foraminifera assemblages in core CE18011_VC1 and RH17002_VC7 86

Table 7: Summary of acquisition of cores CE18011_VC1, CE18011_VC4, CE18011_VC5, CE18011_VC6, CE18011_VC8, RH17002_VC1 and RH17002_VC7..... 108

Table 8: Radiocarbon results of core CE18011_VC1, CE18011_VC4, CE18011_VC5, CE18011_VC6 and RH17002_VC7 116

Appendices

Appendix I: Computed tomography processing procedures 137

Appendix II: Organic matter and carbonate dissolution procedures 139

Appendix III: Grain size analysis and operating procedures 140

Appendix IV: End-member modelling for core CE18011_VC2 142

Appendix V: Correlation of sortable silt (%) versus mean sortable silt (μm) for core CE18011_VC2 143

Appendix VI: Age model parameters for core CE18011_VC2 144

Appendix VII: Additional sedimentological data plot for core CE18011_VC2 145

Appendix VIII: Compilation of down core sedimentological data from each core analysed during this PhD 147

Appendix IX: Species list and raw quantitative data of benthic foraminifera for core CE18011_VC1 and RH17002_VC7 158

Appendix X: Species list and relative abundance data of benthic foraminifera for core CE18011_VC1 and RH17002_VC7 166

Appendix XI: Paleoenvironmental information derived from cores CE18011_VC1, CE18011_VC2, CE18011_VC5 and RH17002_VC7 174

Appendix XII: Relative abundance of all benthic foraminifera species in BFAs for core CE18011_VC1 and RH17002_VC7 177

Appendix XIII: Ecological preferences of dominant benthic foraminifera 179

Appendix XIV: ROV-vibrocorer 181

Appendix XV: Coral preservation patterns in core CE18011_VC1, CE18011_VC4, CE18011_VC5 and RH17002_VC7 182

Appendix XVI: Corals used for U/Th dating 183

Appendix XVII: Courses completed during PhD 201

Appendix XIII: Research cruises undertook as part of, and during, the PhD 202

Appendix XIX: Awards and grants received during PhD 203

Appendix XX: Conferences attended during PhD..... 205

Appendix XXI: Conferences organized during PhD..... 207

Appendix XXII: Outreach during PhD..... 208

Additional Material

A: Additional cores and corresponding logs 210

B: Additional discussion on stable isotopes from core CE18011_VC2 212

C: Additional benthic foraminifera picked from CE18011_VC5 217

List of Abbreviations

μm – micrometres

AMOC – Atlantic Meridional Overturning Circulation

AMS – accelerator mass spectrometry

AR – aggregation rate

BFA – Benthic foraminifera assemblages

cm – centimetres

cmbsf – centimetres below the sea floor

CoCoHaCa – Controls of cold-water coral habitats in submarine canyons

CPP – coral preservation potential

CT – computed tomography

CWC – Cold-water corals

db-RDA – distance-based redundancy analysis

EM – end-member

EMMA – end-member modelling algorithm

ENAW – Eastern North Atlantic Water

ENAW-MOW-TZ – Eastern North Atlantic-Mediterranean Outflow Water-Transition Zone

GI – Greenland Interstadial

GISP – Greenland Ice Sheet Project

GS – Greenland Stadial

GSD – Grain Size Distribution

IRD – ice-rafted debris

ka – thousand year

ka BP – kilo annum before present

Kyr – thousand year

LGM – Last Glacial Maximum

mg – milligrams

MGS – Mean Grain Size

MIS – marine isotope stage

MOW – Mediterranean Outflow Water

MSD – matrix sediment density

MSS – Mean Sortable Silt Size

NASP – North Atlantic Subpolar Gyre

PBC – Porcupine Bank Canyon

PCA – principal component analysis

POM – particulate organic matter

PS – Porcupine Seabight

ROV – remotely operated vehicle

RSL – relative sea level

RT – Rockall Trough

RV – research vessel

SR – sedimentation rate

U/Th – uranium/thorium

VC – vibrocore

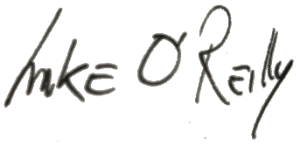
wPB – western Porcupine Bank

YD – Younger Dryas

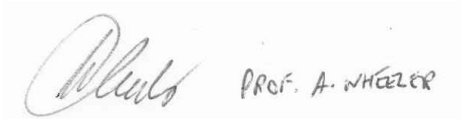
Declaration

The research presented here is the author's work and has not been submitted

for another degree at University College Cork or elsewhere.

Signed 

Luke O’Reilly, author

Signed 

Prof. Andrew Wheeler, co-supervisor of research

Signed 

Dr Aaron Lim, co-supervisor of research

Acknowledgements

After this long journey, it's clear that I would not have gotten through it without the love and support of my family, friends and colleagues.

To my mom and dad, Carol and Ronnie, thank you for bringing me into this world, and I love you both. Thank you for my education at home and at school. Thank you for giving me room to develop and thank you for protecting me when times were tough. Mom, thanks for the copious offers of food, tea, coffee and thank you for always being merry – it helped when my stack was low. Dad, thanks for being an ear and being a cool dude – you gave good advice to me through the years gone by. To Naomi, I would not have pursued this career were it not for you. You are single handily the biggest inspiration in my life. I am at ease now that you have found Lasse (and he to you), and I wish ye the very best of luck with yere future together. As the eldest of the siblings, you have walked the path first, making it easier for Sophia and me. Thank you forever. To Sophia, I am grateful for your boldness and confidence. You unknowingly thought me these skills throughout the years, and I relied heavily on this branch of my shadow personality throughout the PhD. You are never afraid of doing what you want and it's something I try to live up to. Although you immigrated at the beginning of the pandemic, you always kept in touch. Your virtual ears were much appreciated. I hope I can make it up to you now that I have finished this project. I missed you very much.

To my nana and grandad, Mary and Gerald, and my grandad Ronnie and my departed granny Elma. Thank you all for your stories of times gone by. Thank you all for giving me perspective. Thank you to my aunts, uncles and cousins. You all walk to your own beat, that's for sure.

To my loving partner, Vicky. I think the world of you. I am sorry for the times I was absent-minded and the times that I faded away. My best interest was always at heart so that we could make a life for ourselves. Your never-give-up attitude helped me incredibly. Thank you for fighting for us. Thank you for feeding me and being my haven. Thank you, Sandra, for welcoming me

into your home. Thank you to the rest of Vicky's family: Raymond, Sonia, Yvonne, Paddy and Timmy, as well as my nephew Dylan and niece Chloe. You all helped me take my mind out of chaos into a place of love. I wish Yvonne and Timmy best of luck with their new child Ava and I am proud to call myself her uncle.

To Evan O'Mahony. Life brought us together eight years ago. Since then, we've been waltzing back and forth with our careers and I'm looking forward to working together side-by-side. Thanks for everything, dude. To Kevin Baker, thank you for being my friend over the past twelve years. We've grown a lot in the years gone by, but I like to think that Luke and Baker of then are just happy we're still buds. I am very proud of you and your endeavours. To Gerard Summers, you spiced up things on our first research cruise and have been spicing it up ever since. From the bottom of my heart, thank you for your support, kindness, and banter. To John Mensah Appah, thank you for your knowledge of life and faith. I would pick no other person to do a PhD alongside. You are about to embark on a new journey, and I wish you the best of luck, my bro.

To the rest of the research group: Larissa Macedo, Felix Butschek, Alicia Cardenas, Riccardo Arosio, Audrey Recouvreur, Guillaume Michel and those gone by (Rasher Strachan, Jared Peters and Kimberley Harris), thank you all for your support and valuable input. Thank you Siobhán Burke for helping me in the initial stages of the PhD, it will not be forgotten. Thank you to the fellow cave dwellers of present and those gone by in particular Daniel Falk, Odhran McCarthy, Juergen Lang, Darren Daly, Austin Hynes, Eileen McCarthy, Obaid Alharbi, Valentina Rossi and Tiffany Slater. Thank you to the team in UCC Geology, in particular, John Reavy, Ed Jarvis and Pat Meere, cheers for everything, chaps. Thank you for granting me a valuable education and everlasting friendship. Thank you to Andre Banning for our shortlived friendship. To the UCC geology class of 2017, thank you all for your support. I wish you all the best of luck with your future careers. Big shout out to the geodudes Vinny Lillis, Michael O'Sullivan and Oscar Daly, who kept in touch throughout all the madness. Thanks to the technician Luke Harman for being

there for the heavy lifting and positive vibes. Thanks to Mary Lehane, Ronan Hennesy and Allen Whitaker for helping me with lab-based objectives. Thank you to all of the administrative team, Christine Dennehy, Elaine Kelly, Phil Fogarty, Mary McSweeney and Gillian Aughney, for logistical assistance. Thank you to the Head(s) of School Astrid Wingler and Andy Wheeler for making BEES a great place to conduct a PhD. I would also like to thank all of the safety officers for keeping the school safe to work in, particularly during the pandemic. Thank you to John Boyd, would helped me with the “big picture” stuff.

Without the support of Jürgen Titschack, it's fair to say the last 4 years would have been much more difficult. Thank you, Jürgen, for developing me as a scientist and your continued warmth and kindness. Throughout the pandemic, you took time away from your family to review my work drafts. I'm not sure I could ever repay you but know that if ever the chance I get to supervise an up-and-coming scientist, I will give them the same time you gave me. Another key influence on my journey was Robin Fentimen. I would like to thank Robin for his patience. The world of benthic foraminifera is a crazy one. Thank you for giving me your insights. I would certainly not have finished in time were it not for you stepping in. Felix Butschek also deserves enormous praise. Thank you, Felix, for teaching me some of your expansive knowledge and thanks for asking me how I am from time to time. Best of luck with your own PhD, brother.

To Andy Wheeler. You took a massive leap of faith 4 years ago. You expressed caution and rightly so. I was unproven in the world of science. Thank you for giving me this opportunity. Thank you for stepping in when I was straying off the path. Most of all, thank you for backing me. I know sometimes I lack focus and understanding, so I thank you for helping me overcome these barriers. You were a fantastic supervisor to me.

To Aaron. You are the man. You are incredibly generous with your time; thank you for this. Your focus is something to behold. Thank you for granting me some of it. Thanks for always asking how I am. Thank you also for asking

others how they are. Sometimes I think poorly of myself and my abilities, but you always bring me back up. Thank you for giving me time throughout the last four years. Zoe and Lucy are fortunate to have you. As are you with them.

Finally, I would like to thank the crew and scientific team of the RH17011 and CE18011 research cruises. Without each of their participations, this PhD would not have been possible.

Thank you all,

Luke

Overwhelmed as one would be, placed in my position.
Such a heavy burden now to be the one.
Born to bear and bring to all the details of our ending.
To write it down for all the world to see.
But I forgot my pen…Typical

MJ Keenan & Tool

In March 2020, our lives were changed unimaginably. I would like to thank the essential workers and health care professionals who facilitated our wellbeing during the global pandemic. This research is dedicated to those we lost.

Abstract

Cold-water corals are sessile, filter-feeding organisms that baffle water flow inducing sedimentation around their framework. Through geological time, should environmental conditions permit, they can produce positive topographic features on the seafloor called mounds through successive and persistent reef development. These reef ecosystems are considered biodiversity “hotspots” between 200 and 1000 m in the Atlantic Ocean. They are regarded as vulnerable marine ecosystems, providing essential ecosystem services. Over the past two decades, a considerable body of information has been accumulated on understanding the temporal development of CWC reef and mound formation. However, this research is limited in resolution, the range of study sites and datasets analysed. Here, an assessment of the temporal variation of CWC reefs and mounds situated in the west Porcupine Bank (wPB) and Porcupine Bank Canyon (PBC) is presented as well as background palaeoenvironmental information from an off-mound core.

Previous studies of the spatial distribution of reefs and mounds reveal that they are dispersed across a variety of geomorphological settings in the region, including the canyon head, along the canyon lip and on the bank. This research broadly aims to understand the temporal distribution of the coral habitats within these contrasting settings. In 2015 and 2016, the QuERCi I and QuERCi II research cruises attempted coring the substrates of the canyon using traditional methods (i.e. gravity and box-corers). However, the acquired cores were insufficient in size and lacked an understanding of what habitat they were taken from. As such, 2 more research cruises (CoCoHaCa I and CoCoHaCa II) were carried out in 2017 and 2018 using sophisticated novel coring systems (ROV-vibrocoring). These methods proved successful, and cores were acquired through various CWC habitats in the canyon (mound summits, flanks, bank, slope and foot of the slope) and presented herein. This data includes novel 3-dimensional computed tomography (CT) derived imagery alongside traditional sedimentological approaches.

The CT imagery was used to classify reef and mound formation/cessation. The cores were then split, sampled and investigated using a series of analytical techniques. The phases of formation/cessation were first constrained using radiocarbon dating and the cores were subsequently examined using grain size analysis to interpret the hydrodynamic regime. Stable isotope analysis on planktic and benthic foraminifera was then used to investigate paleoenvironmental conditions, which were contextualized by benthic foraminifera assemblages.

An off-mound core was examined to elucidate the impact of the (de)glaciation of the British-Irish Ice Sheet (BIIS) on the wPB. Analysis of the core revealed that several fluxes of ice-rafted debris were deposited to the site. It was found that bottom currents became sluggish during stadial phases. Evidence for iceberg scouring in the core was also identified. Two coral bearing cores acquired from mound summits of variable distance to the canyon were then analysed. It was found that mound growth was twice as fast on the canyon lip than mounds 1 km away on the wPB. Multiproxy data revealed that a high food signal occurs closer to the canyon. This suggests that submarine canyons play a key role in enhancing particle supply and therefore influences coral growth and mound developmenton the margin. The radiocarbon dates acquired from coral bearing cores on the wPB suggest that corals occupied the bank since at least 45.1 ka BP. This finding subsequently resulted in revising our understanding of CWC re-expansion into the NE Atlantic during favourable climatic conditions, highlighting the crucial role played by submarine canyons.

Findings outlined in this thesis provides the scientific community with new insights into the tolerances of cold-water corals during ecological tipping points. Furthermore, it highlights the need to investigate other submarine canyons occupied by CWCs in the NE Atlantic using ROV-vibrocoring.

Chapter 1: Cold-water Corals and Submarine Canyons

The work presented here provides a detailed multidisciplinary investigation of the temporal variation of cold-water coral (CWC) mounds in the Porcupine Bank Canyon (PBC) and western Porcupine Bank (wPB) in the north-eastern Atlantic Ocean. These mounds were examined using novel scientific methods (remotely operated vehicle mounded vibrocoring; 3-dimensional segmented computed tomography) combined with traditional sedimentological approaches (grain size analysis; radiocarbon dating; stable isotope analysis; benthic foraminifera assemblages). This work provides a geological understanding of the environmental controls on mound development in the NE Atlantic in a broader context. Furthermore, it uses the mound record alongside an off-mound record to provide insights into British-Irish Ice Sheet (BIIS) dynamics, water mass variations and paleoenvironmental signals throughout the Late Pleistocene to Mid–Holocene.

1.1 Cold-water Corals

Cold-water corals (CWCs) are cnidarians which include stony corals (Scleractinia), soft corals (Octocorallia, including ‘‘precious’’ corals, gorgonian sea fans, and bamboo corals), black corals (Antipatharia), and hydrocorals (Stylasteridae; Cairns, 2001, Roberts et al., 2009). They are azooxanthellate (i.e. coral species lacking photosynthesizing dinoflagellates) and regularly arrange as colonies supported by a common skeleton (Roberts et al., 2009). CWCs act as a crucial catalyst for the biodiversity of continental margins, thus forming a unique ecosystem (Duineveld et al., 2004). In general, they thrive in water depths beyond the photic zone (Freiwald et al., 2004). *Desmophyllum pertusum* (synonymous with *Lophelia pertusa*; see Addamo et al., 2016) is the most widespread reef-forming CWCs and are described as ‘ecological engineers’ (Freiwald et al., 2004, Roberts et al., 2009). *D. pertusum d*epths vary globally – some occur ~40–1000 m in high to mid- latitude waters and others can occur at depths up to 3273 m in low latitude waters (Freiwald et al., 2004, Roberts et al., 2006; see Fig. 1). *D. pertusum* is believed to be sensitive to environmental variablity compared to other reef-forming species (Weinberg *et al*., 2009). Other framework species such as *Madrepora oculata* form anastomosing colonies, which have a continuously outward growth of branches from consistent budding of polyps (Freiwald, 2002). *Madrepora*-dominated corals are characterised by thickets rather than frameworks and are thus much more fragile (Stetson et al., 1962, Freiwald, 1998). However, their weak structure limits growth, and heights over 50 cm are rare (Stetson et al., 1962, Freiwald, 1998, De Mol et al., 2002). In comparison, *D. pertusum* form larger dendroidal structures, with neighbouring branches merging, thus increasing the framework's robustness (De Mol et al., 2002).

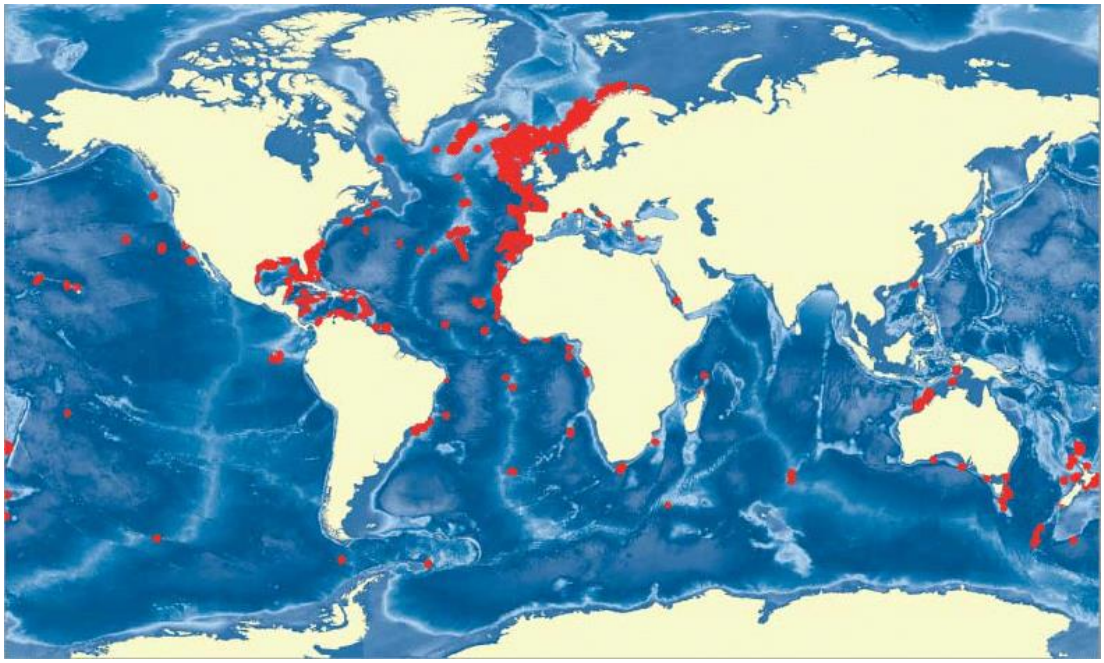


Figure 1: Global distribution of the scleractinian cold-water corals (CWCs; red filled dots). Their high density in the NE Atlantic is since most of the investigations of the CWCs have been carried out in the NE Atlantic. Data from Freiwald A, Rogers A, Hall-Spencer J, Guinotte JM, AJ Davies, Yesson C, Martin CS, Weatherdon LV (2017).

The biotic and abiotic controls of CWC reefs and mounds are frequently under revision (e.g. Freiwald et al., 2004, Wheeler et al., 2007, Roberts et al., 2009, Wienberg and Titschack, 2017, Hebbeln et al., 2019). Literature does, however, agree on several common essential parameters. Early larval settlement and successive growth are dependent on nutrient availability and seawater parameters (alkalinity, pH, dissolved inorganic carbon and carbonated ion concentration; Maier et al. (2011), McCulloch et al. (2012), Flögel et al. (2014)). Furthermore, water mass characteristics (temperature, salinity, seawater density and dissolved oxygen) and their circulation (Freiwald, 2002, Dorschel et al., 2005b, Roberts et al., 2006, Rüggeberg et al., 2007, Wienberg et al., 2010, Fink et al., 2012; see Table 1) controlling reef and mound succession have also been defined. $\delta^{13}C$ and $\delta^{15}N$ from CWC tissues showed that that can feed on a variety of foods varying from microzooplankton, faecal pellets, degraded phytodetritus, dissolved organic matter and bacteria (Mortensen et al., 2001, Duineveld et al., 2004, Carlier et al., 2010, Wienberg et al., 2013, Mueller et al., 2014, Orejas et al., 2016). Catching organisms of this size allows these corals to remain seasonally active

for prolonged periods. CWCs, in particular, *D. pertusum,* is shown to be tolerant to extensive periods of minimal food supply (Larsson et al., 2013).

CWCs grow favourably in turbulent hydrodynamic settings (Freiwald, 2002, Kenyon et al., 2003, Masson et al., 2003). As CWCs are sessile suspension feeders, they rely on a highly energetic hydrodynamic regime (i.e. bottom currents or internal tides) to transport nutrients from the ocean's surface to the coral's tentacles (Frederiksen et al., 1992, Duineveld et al., 2004). High-frequency sampling with short-term instrumentation has revealed that tidal variability can significantly impact mixing across buoyancy layers or force near-surface/intermediate waters to depths (Davies et al., 2009). CTD scans show the importance of advection as a turbidity source on the reef (Davies et al., 2009). Moreover, current acceleration due to topography has a marked effect on stimulating the advection of food for CWC (Thiem et al., 2006) These high-speed currents are also believed to keep the living reef structures unobstructed with respect to fine-grained sediment deposition (White et al., 2005).

Table 1. Summary of the general environmental parameters controlling CWC (*D. pertusum* and *M. oculata*) reef and mound growth in the Atlantic Ocean.

Parameter	Atlantic range	NE Atlantic range	References
Temperature (°C)	4–14	5.9–10.6	(Freiwald, 2002, Roberts et al., 2003, Freiwald et al., 2004, Davies et al., 2008, Davies and Guinotte, 2011, Wienberg and Titschack, 2017)
Salinity (PSU)	35–38.8	35–36	(Freiwald, 2002, Roberts et al., 2003, Freiwald et al., 2004, Davies et al., 2008, Davies and Guinotte, 2011, Wienberg and Titschack, 2017)
Seawater density (kg m^{-3})	27.2–27.7	27.35–27.65	(Freiwald, 2002, Dullo et al., 2008, Flögel et al., 2014)
Dissolved oxygen (ml/L)	2.6–7.2	3–6.7	(Freiwald, 2002, Dodds et al., 2007, Davies et al., 2008, Flögel et al., 2014, Wienberg and Titschack, 2017, Hanz et al., 2019)
pH	7.86–8.3	7.92–8.3	(Davies and Guinotte, 2011, McCulloch et al., 2012)
$\Omega_{aragonite}$ (mmol/kg)	1.35–4.06	1.35–3.03	(Findlay et al., 2014)
Total Alkalinity (µmol/kg)	2259–2742	2287–2377	(Davies et al., 2008, Davies and Guinotte, 2011)
DIC (µmol/kg)	2088–2349	2088–2186	(Davies et al., 2008, Davies and Guinotte, 2011)

1.2 Coral Mound Development

Of the 1335 species of scleractinians, only 10 are considered to construct deep water coral frameworks, 6 of which are coral mound-forming (Cairns, 2001). Mound developmentis controlled by the sustained growth of framework forming corals with contemporaneous supply and deposition of sediments with energetic bottom currents (Roberts et al., 2006). The interplay between bottom current strength and presence of coral framework, influences the amount of sediments baffled, whereby coral pieces reduce current speeds and allows bypassing sediments to settle between their branches (Dorschel et al., 2007b, Guihen et al., 2013). Over time, when coral growth outpaces sediment accumulation, mounds can form during prevailing optimal conditions (Roberts et al., 2006). Changes in climatic processes can cause unfavourable environmental conditions for coral mound development, which results in the stagnation of mound accumulation and/or erosion (Dorschel et al., 2005a, Roberts et al., 2006). Thus, the developmental pattern of coral mounds over millennial time scales is controlled by a complex interplay of environmental factors. These range from distinct physical chemical properties of the ambient water masses (e.g. temperature, pH, water density and dissolved oxygen concentrations; e.g. Freiwald, 2002, Davies et al., 2008, Davies and Guinotte, 2011, Flögel et al., 2014; see also Table 1) and the supply of food by surface ocean productivity and strong bottom-water hydrodynamics (e.g. (Thiem et al., 2006, Mienis et al., 2007, Davies et al., 2009, Mienis et al., 2012, Hebbeln et al., 2016).

Mound development models are constantly updated (Squires, 1964, Wilson, 1979, Dorschel et al., 2005b, Roberts et al., 2006, De Mol et al., 2007, Rüggeberg et al., 2007, de Haas et al., 2009, Douarin et al., 2013, Roberts and Cairns, 2014), all of which consider several critical stages of development (Fig. 2). The colonization of coral larvae, followed by colony growth under favourable conditions for coral growth, progresses to the formation of a coral thicket, which grows to prominent topographical features such as CWC reefs and eventually mounds (Fig. 2). The coral mound material is primarily composed of coral fragments (coral content of 0–50 % weight content; see

Dorschel et al., 2007b, Titschack et al., 2009). Coral mounds are found in depths of 200–1000 m in the Atlantic Ocean (Roberts et al., 2006, Wheeler et al., 2007, Hebbeln and Samankassou, 2015, Wienberg and Titschack, 2017) and are several tens to hundreds of metres in height (Mienis et al., 2006). Mound provinces are found where several to hundreds of individual mounds cluster within geographically bound areas (e.g. Huvenne et al., 2002, Huvenne et al., 2003, van Rooij et al., 2003, Foubert et al., 2005, Wheeler et al., 2005b, Huvenne et al., 2007, Wheeler et al., 2007, Wienberg et al., 2018, Tamborrino et al., 2019).

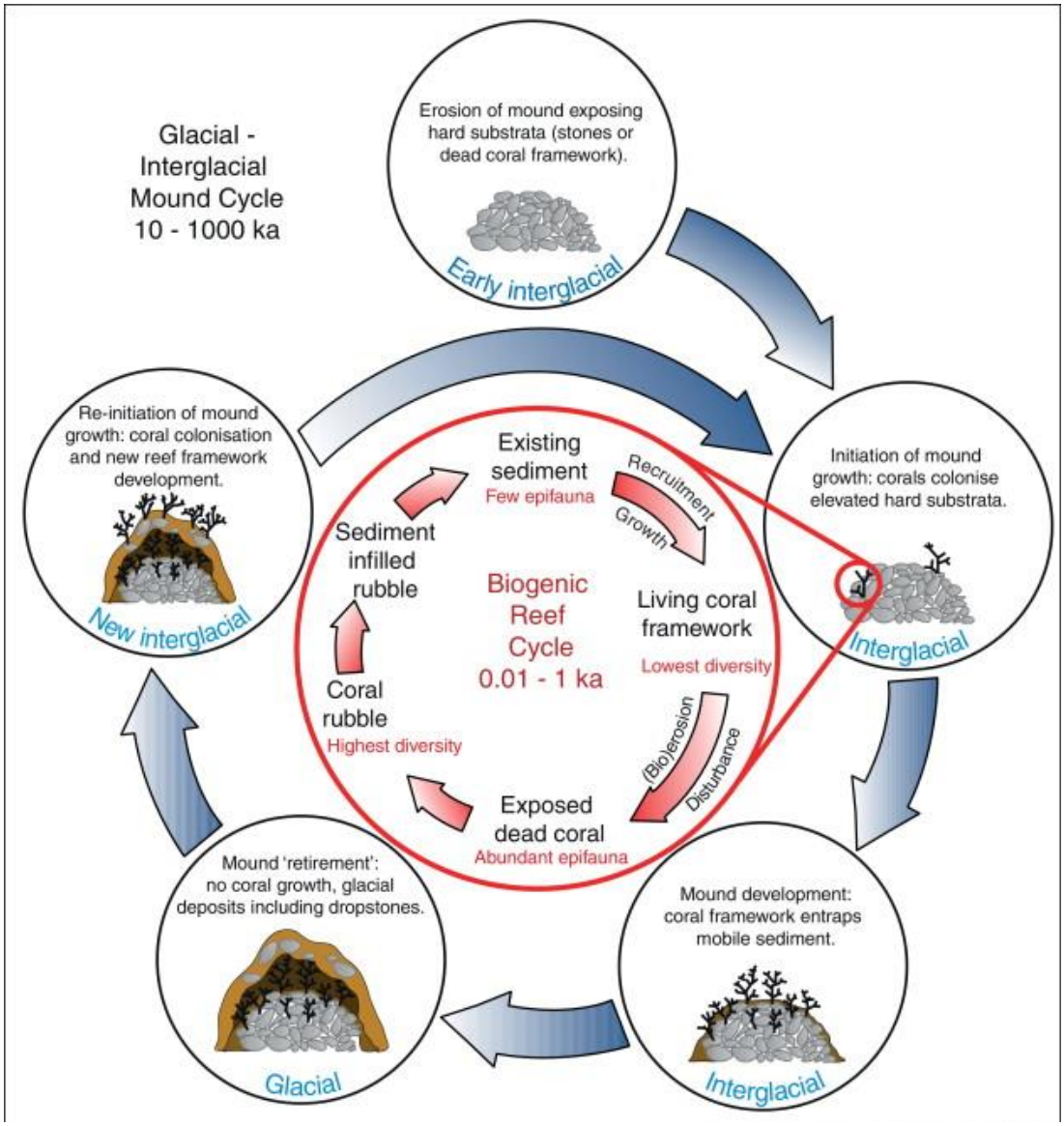


Figure 2: Diagram from (Roberts and Cairns, 2014) redrawn from (Roberts et al., 2006) showing: (1) outer circle; cyclic stages of carbonate mound growth from initiation, development, 'retirement' and re-colonisation; (2) inner circle; more minor scale cycle of reef microhabitats, succession and faunal diversity.

An often-overlooked contributor to the stability of the mound is induced sedimentation through current flow baffling, which can contribute up to >60% of infill (Dorschel et al., 2007a, Mienis et al., 2009b, Van der Land et al., 2010, Titschack et al., 2015). Ecological accommodation space generated by the coral framework plays a vital role in baffling sediments by creating local low energy environments (Pomar, 2001, Flügel, 2004, Titschack et al., 2009, Wang et al., 2021). Baffling by coral frameworks is considered an essential component in the formation of CWC mounds in the deep sea (Mullins et al.,

1981, Foubert et al., 2008, Paull et al., 2008, Mienis et al., 2009a, Wheeler et al., 2011, Victorero et al., 2016, Wang et al., 2021). A conceptual model of mound formation using this interplay between baffling and coral-derived ecological accommodation space was recently developed by Wang et al. (2021; see Fig. 3).

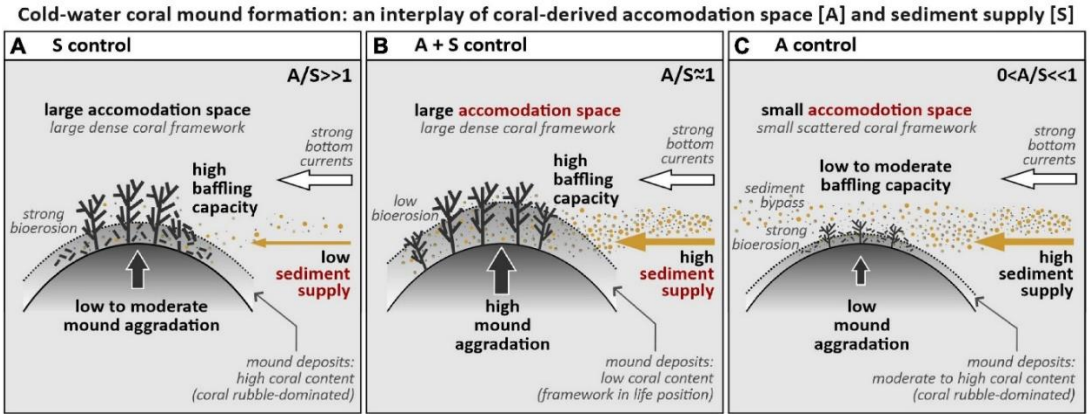


Figure 3: From Wang et al. (2021). The diagram shows three model development scenarios based on accommodation space (A) provided by the coral framework and sediment input (S). A – where large A and low S occurs, the coral framework endures higher rates of biodegradation and fragmentation, leading to low to moderate mound aggradation. B - where A and S are equal, corals are sufficiently buried before biodegradation and fragmentation processing, leading to high mound aggradation. C – where both A and S are low, environmental conditions inhibit the growth of large coral pieces. Therefore, lower A is generated and consequently, S is low also. This results in high biodegradation and fragmentation, causing predominance of coral rubble, leading to low mound aggradation rates.

1.3 An Overview of Coral Mounds in the NE Atlantic

Along the NE Atlantic margin, CWCs inhabit a belt that extends from northern Norway (70°N; Lindberg et al., 2007, López Correa et al., 2012) down to western Africa (4°; Buhl-Mortensen et al., 2016). Carbonate mound provinces have been found from offshore Ireland, including the Porcupine Bank (Wheeler et al., 2005a, Wheeler et al., 2005b, Wheeler et al., 2007, Dorschel et al., 2009), in the Porcupine Seabight (Hovland et al., 1994, Henriet et al., 1998b, De Mol et al., 2002, Huvenne et al., 2003, De Mol et al., 2005, Frank et al., 2005, Huvenne et al., 2005, De Mol et al., 2007, Huvenne et al., 2007, White, 2007, Wheeler et al., 2011), and on the Rockall Trough (Kenyon et al., 2003, van Weering et al., 2003, Frank et al., 2005, Schröder-Ritzrau et al., 2005, White et al., 2005, Noë et al., 2006, Duineveld et al., 2007, Roberts et al., 2008, Wienberg et al., 2008, Frank et al., 2009, Mienis et al., 2009a, van Oevelen et al., 2009). Within each of the well-delineated Irish mound provinces (Fig. 4), growth initiation occurs after an erosional event.

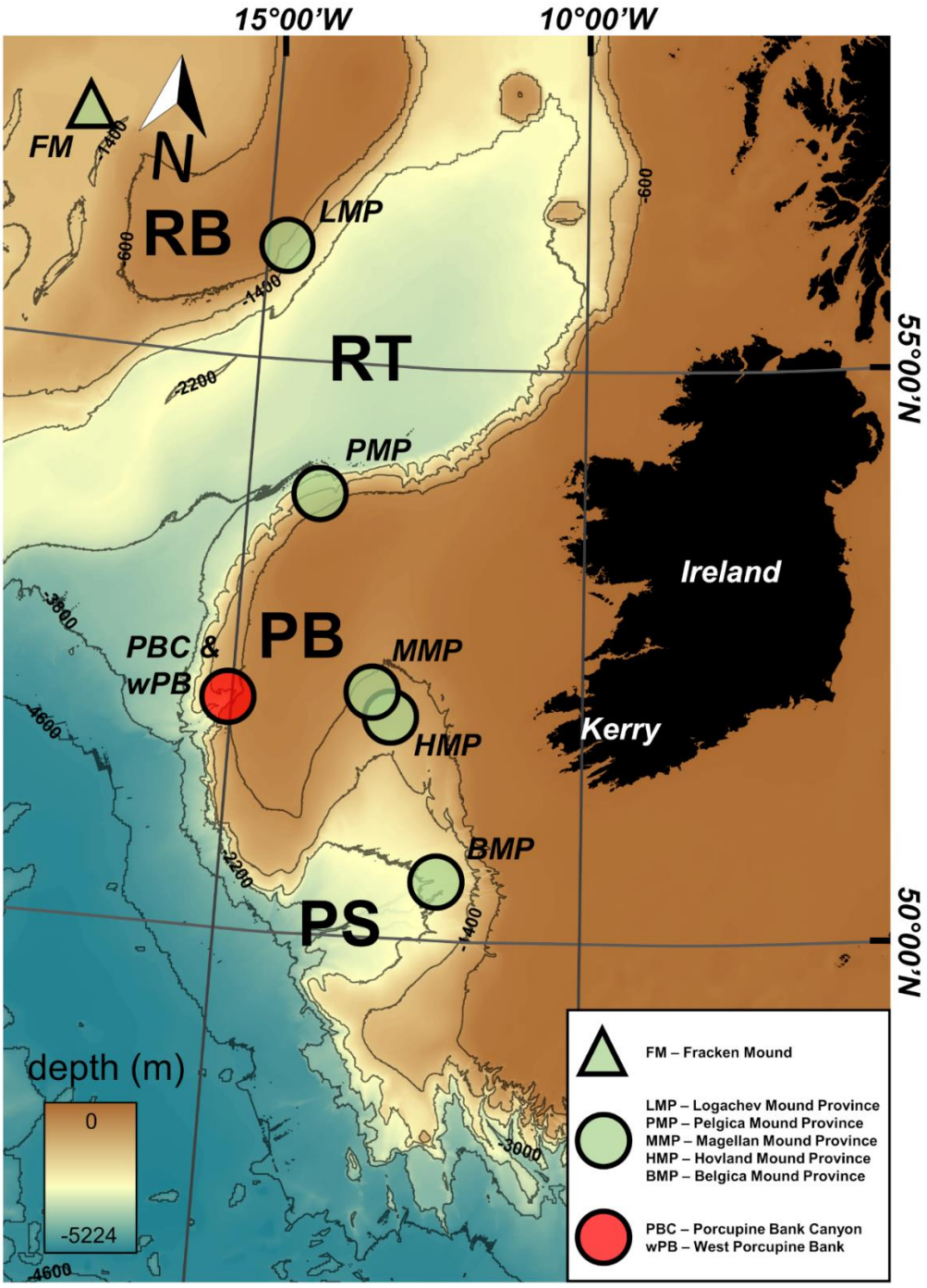


Figure 4: Mound provinces from other studies (green) and this study (red). PS – Porcupine Seabight, PB – Porcupine Bank, RT – Rockall Trough and RB – Rockall Bank. Map created using ArcGIS Desktop v10.6 (www.arcgis.com). Data sources – (a) - General Bathymetric Charts of the Oceans (gebco.net).

Research shows that these mounds develop during interglacial periods, whereas mound cessation typically dominated glacial periods (Roberts et al., 2006, Rüggeberg et al., 2007, Mienis et al., 2009b, Wienberg et al., 2010,

Douarin et al., 2013), with minor exceptions (e.g. Dorschel et al., 2005b, Eisele et al., 2008). No *D. pertusum* species has been found to date between these latitudes during the last glacial period, suggesting the destructive nature of these climates to coral colonies and carbonate mounds (Kenyon et al., 2003, Frank et al., 2009). Frank et al. (2011) outline the limiting biogeographical factors of reef-forming CWC ecosystems between ~50°N and ~70°N. They postulate that ice age oscillations and the associated temporal variations caused by these events directly affect primary productivity, temperature and ocean dynamics. As a result, the transgression/regression of the polar front in the eastern Atlantic can be seen throughout the fossil coral records. McCulloch et al. (2010) note that throughout similar environmental conditions in the temperate East Atlantic, coral growth remains relatively unaffected, that is, that coral growth is constantly occurring. De Mol et al. (2005) suggest this development continuum is due to the northward advection of coral larvae through currents such as the Mediterranean Outflow Water. Since then, Henry et al. (2014) have provided the most up-to-date hypothesis for CWC re-expansion in the NE Atlantic from the Mediterranean Sea, which acted as the central refuge for corals through the last glacial period. They postulate that coral larvae were transported to the higher latitudes due to re-invigorated Atlantic Meridional Overturning Circulation (AMOC). Over 400 years, larvae were dispersed from the Gulf of Cádiz over 7,500 km northward along the continental margin. During the early Holocene, it has been suggested that the northern migration of the polar front had a major impact on restoring previous optimal environmental conditions for *D. pertusum* growth (Frank et al., 2011). The developmentof extensive CWC ecosystems initiated by the establishment of enhanced bottom currents that transport potentially more nutrients to the growth site has been described along the Irish margin, particularly during the Early Holocene (Dorschel et al., 2005b, Rüggeberg et al., 2007). Moreover, sedimentation rates completely overwhelm and outpace coral growth in glacial periods, hence rendering mound progression infeasible (Roberts et al., 2006, Dorschel et al., 2007a).

1.4 Submarine Canyons

Environmental variability is markedly higher in continental margin settings compared to shelf or abyssal plain settings (Levin et al., 2001, Snelgrove and Smith, 2002, Levin and Dayton, 2009, Levin et al., 2010). This variability causes habitat heterogeneity across a range of spatial scales (Levin et al., 2001). Submarine canyons are a principle cause of habitat heterogeneity on continental margins (e.g. Vetter, 1994, Tyler, 1995, Vetter and Dayton, 1998, Vetter and Dayton, 1999, Levin et al., 2001, Genin, 2004, Schlacher et al., 2007, Levin et al., 2010, Schlacher et al., 2010) and globally there are over 2,000 active submarine canyons (Harris and Whiteway, 2011). Submarine canyons are regular features along continental margins that connect continental shelves to deep ocean basins (Shepard and Dill, 1966). They are characteristically rich in high organic-matter and trap coastally-derived and surface-derived organic detritus by channelling (e.g. Vetter, 1994, Vetter and Dayton, 1998, Vetter and Dayton, 1999, Company et al., 2008, De Leo et al., 2010). Furthermore, they enhance local primary productivity by inducing upwelling (e.g. Klinck, 1996, Hickey, 1997, Allen and Hickey, 2010). As such, they act as a conduit between the shelf and the deep sea, transporting sediments in episodic turbidity currents or mass wasting events (e.g. Nittrouer and Wright, 1994, de Stigter et al., 2007, Oliveira et al., 2007, Arzola et al., 2008, Allen and de Madron, 2009, Harris and Whiteway, 2011). Their enhanced habitat heterogeneity and organic matter cause biomass hotspots (Vetter and Dayton, 1998, Vetter and Dayton, 1999, Yoklavich et al., 2000, Brodeur, 2001, Schlacher et al., 2007, Buhl-Mortensen et al., 2010, De Leo et al., 2010, Schlacher et al., 2010, Vetter et al., 2010, De Leo et al., 2012), and thus areas adjacent to canyons are prone to higher rates of commercial fishery production (e.g. Vetter and Dayton, 1999, Yoklavich et al., 2000).

The variable topography of submarine canyons is characterised by complex patterns of hydrography, flow and sediment transport and deposition (Shepard et al., 1974, Oliveira et al., 2007, García et al., 2008). The incising nature of submarine canyons on the shelf intercept organic-matter-rich-sediments (Shepard, 1963, Mullenbach et al., 2004, Piper and Normark, 2009, Walsh and

Nittrouer, 2009) and can transport the material downslope to inhabiting macro fauna (e.g. Vetter and Dayton, 1998, Vetter and Dayton, 1999, Liu et al., 2016). Focusing of internal waves, bathymetric steering of outer-shelf and upper-slope currents and coastally-trapped waves can cause the mixing of canyon waters and upwelling of cold, nutrient-rich waters to the sea surface (Sobarzo et al., 2001, Aslam et al., 2018), causing enhanced local primary productivity (Ryan et al., 2005, De Leo et al., 2010). Due to their morphological heterogeneity, submarine canyons offer a variety of habitats to biologically diverse benthic communities, particularly along steep bedrock exposures where enhanced particulate organic matter concentrations occur (Yoklavich et al., 2000, Brodeur, 2001, De Mol et al., 2010). Submarine canyons are considered a refuge to CWCs during unfavourable climatic periods (Huvenne et al., 2011, Fernandez-Arcaya et al., 2017, van den Beld et al., 2017), and thus may offer reefs protection during glacial periods. In the Bay of Biscay, NE Atlantic, CWCs have been identified in over 24 canyons (van den Beld et al., 2017), suggesting that other canyons along the margin may play a similar role.

1.4.1 The Porcupine Bank Canyon

The Porcupine Bank (PB) slopes into the Rockall Trough (RT) to the west and to the Porcupine Seabight (PS) to the south-east (Fig. 5a). The Bank is a horst block separating rift basins formed during Middle to Late proto-North Atlantic extension (Shannon, 1991). At its maximum, the ~48 km long and ~29 km wide Porcupine Bank Canyon (PBC) represents the largest submarine canyon on the PB at ~52˚N (Dorschel et al., 2010), approximately 490 km west of Co. Kerry (Fig. 5a). The canyon incises into the South Bróna Basin (Shannon, 1991; Shannon et al., 2007) trending NE-SW (Fig. 5a and 5c). It is believed to be tectonically-controlled from the westward extension of the Iapetus Suture (Chenin et al., 2015; Schiffer et al., 2020). Mesozoic and Cenozoic deposits thin northwards and towards the margins of the basin (Shannon, 2007). The canyon was then shaped by British-Irish Ice Sheet glaciations during the Quaternary (Elliott et al., 2006, O'Reilly et al., 2007, Ó Cofaigh et al., 2012, Sacchetti et al., 2012a). Within the thalweg of the upper canyon, water can reach up to 4250 m in depth (Fig. 5c) where it exits into the Rockall Trough.

Channels branching into the continental slope can reach between 1400 and 800 m water depths in the upper canyon study area (Fig. 5c).

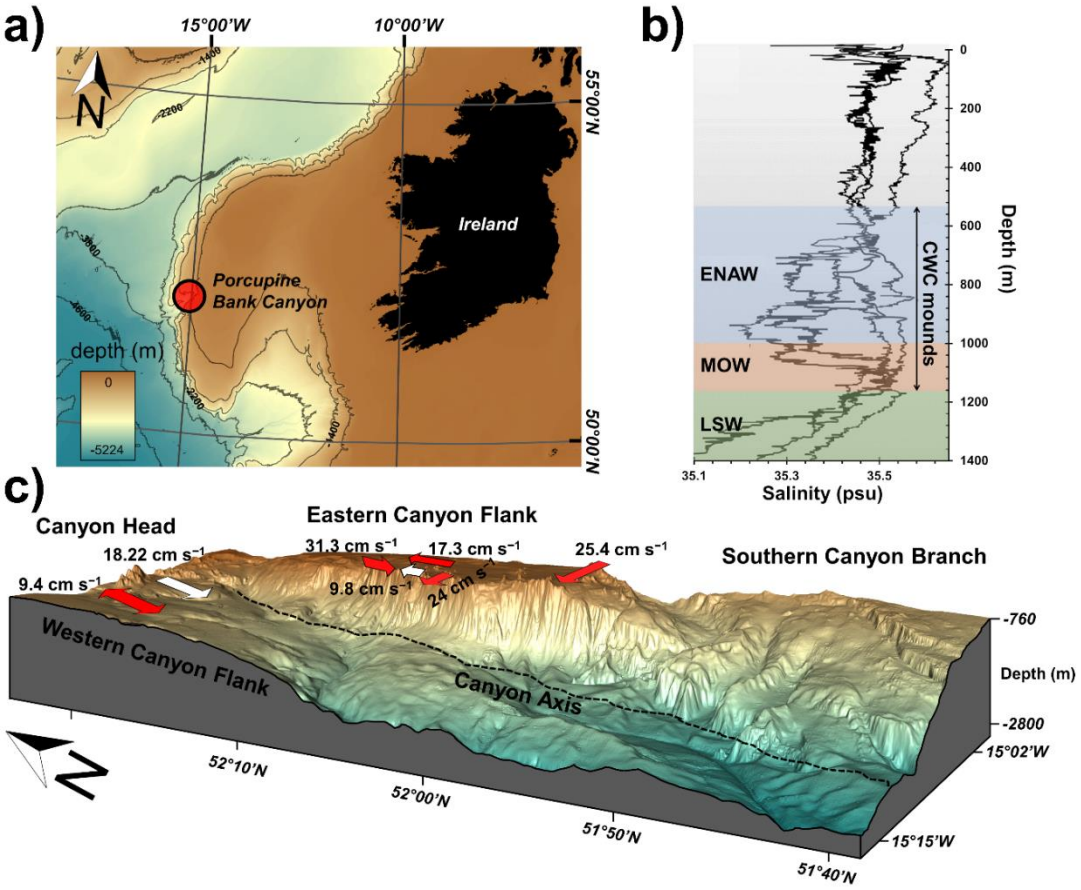


Figure 5: Oceanography and topography of the PBC. a) Geographical location of the PBC (red). Map created using ArcGIS Desktop v10.6 (www.arcgis.com) using bathymetry from General Bathymetric Charts of the Oceans (gebco.net); b) schematic adapted from Mazzini et al. (2011) showing salinity profiles and water masses within the Porcupine Bank Canyon. The depth distribution of coral mounds in the region is indicated by a double-sided arrow within the Eastern North Atlantic Water and Mediterranean Outflow water masses; and c) bathymetry of the Porcupine Bank Canyon (PBC), showing the overall canyon geography. ADCP data from Lim et al. (2020) represented by arrows orientated with prevailing current direction. Mean current speeds also shown (see Lim et al. 2020). Red arrows represent ADCP data from summits of topographic highs (i.e. CWC mound), whereas white are from topographic lows (i.e. off-mound). Map created using AMIRA version 2018.36 (see Stalling et al., 2005; http://amira.zib.de); data sources bathymetry (10 m resolution) collected during CE18011 research cruise (Lim et al., 2018).

1.4.2 Water masses

The PBC is influenced by many currents and water masses at different water depths. The northerly flowing Eastern North Atlantic Watermass (~200–700 m; see Fig. 5b; see White and Bowyer, 1997, Mazzini et al., 2011, Mohn et al., 2014) originates from the Bay of Biscay and travels towards northern latitudes, moved along by the Shelf Edge Current (Ellett and Martin, 1973, Dickson and McCave, 1986, Pollard et al., 1996, White, 2007, Mazzini et al., 2011).This water mass is underlain by the more saline Mediterranean Outflow Water (MOW) at 800–1000 m water depth (see Fig. 5b). The denser Labrador Sea Water occurs at 1100 m water depth (Appah et al., 2020). The region is also known to be influenced by minor water masses derived from the western North Atlantic, which is carried northward by the eastern boundary slope current (van Aken and Becker, 1996, van Aken, 2000, White, 2007). Current speeds in the canyon are highly variable and are influenced by topographic steering (Lim et al., 2020b; see Fig. 5). Brief episodic high current speeds events occur, that exceed 110 cm s^{-1} (Lim et al., 2020b). The highest mean current speeds are recorded on the eastern canyon flank (31.3 cm s^{-1}; see Fig. 5c) which flows predominantly to the south, whereas the lowest mean current speed is captured at the head of the canyon (9.4 cm s^{-1}), that flows to the north and south (Fig. 5c). Benthic water temperatures vary minimally between the settings (±0.4 °C; see Lim et al., 2020b), with the wPB recording slightly warmer waters (summer mean = 9.6 °C) than along the lip of the PBC (summer mean = 9.2 °C). From the nearby Porcupine Bank, Dickson and McCave (1986) first recorded the presence of near bed cooling events, and attributed it to upwelling caused by Ekman-transport, triggered by strong northerly gales. It was recently shown that the PBC is also subjected to frequent upwelling events, with temperature drops of up to 1.17°C (Wheeler et al., 2021). Consequently, it is likely that these findings corroborate the findings of Dickson and McCave (1986), whereby the canyon may function as a conduit for Ekman transport-induced upwelling, up onto the shelf. Internal waves associated with the transition zone between intermediate waters (i.e. the ENAW and MOW), can contribute to high amounts of turbulent energy and particles (Vic et al., 2019). Additionally, the vertical movement of waters up and down the slope,

enables internal waves to enhance the lateral transport of POM and therefore substantially supporting food and sediment supply to sessile benthos (e.g. Rice et al., 1990, Duineveld et al., 2007, Hebbeln et al., 2016, Lim et al., 2018a). A case study from the Belgica Mound Province shows that the deglacial invigoration of the MOW combined with a development of a boundary between the ENAW and MOW, was the key event in the Holocene re-initiation of CWC mound formation (Wienberg et al., 2020). Upwelling from the PBC may thus provide a similar circumstance for CWCs living on the bank, whereby enriched particles (and food supply) from the enriched boundary between the ENAW-MOW (see Fig. 5b) are redeposited to shallower depths.

Dickson and McCave (1986) also share pioneering insights into bottom and intermediate nepheloid layers on the Porcupine Bank that formed through bottom erosion under internal tides and waves. The interfaces within the water column (between the saline MOW, the oxygen minimum zone and the ENAW; see Fig. 5b) supports the widespread distribution of the nepheloid layers between 300–1000 m (Dickson and McCave, 1986, Rice et al., 1991). Local hydrodynamics (including internal tides) can cause resuspension of material and generate nepheloid layers at specific density boundaries/isopycnals (Puig et al., 2014, Wilson et al., 2015) that are rich in concentrations of suspended material (including POM). Other mechanisms for development include downwelling following slack periods of tides (Davies et al., 2009) and Ekman drainage (see White et al., 2005). In the case of the Porcupine Bank and Porcupine Bank Canyon, nepheloid development is most likely due to tidal influence, similar to the findings in other NE Atlantic CWC sites (i.e. Dorschel et al., 2007a, Mienis et al., 2007). Indeed, semi-diurnal cycles are present in the PBC today (Wheeler et al., 2021), that could generate internal tides. However, further numerical modelling is necessary to capture the full extent of this tidal influence on the system. It has been proposed that nepheloid layers can expedite labile organic matter to the deep, and thus, represent an important food resource for deep-sea fauna (Frederiksen et al., 1992, Demopoulos et al., 2017) including CWCs (e.g Mienis et al., 2007). Falling surface particles can accrue in nepheloid layers (Ransom et al., 1998) and subsequently initiate reproductive processes in flora and fauna (Tyler and

Gage, 1984). This in turn can affect species abundance, biomass, and richness of associated ecosystems. Although the topic of nepheloid layers lies beyond the scope of this thesis, it likely represents an important factor when considering food supply to CWCs.

1.5 The (de)glaciation of the British and Irish Ice Sheet

During glacial periods in the Late Pleistocene, large amounts of freshwater were released into the NE Atlantic from melting marine termination ice sheets. This played a significant role in the decelerating Atlantic currents (i.e. Stanford et al., 2011, Bigg et al., 2012, Toucanne et al., 2015). The AMOC reduced and retreated to shallower depths during cold periods (Austin and Kroon, 2001). Nutrient availability and primary productivity in surface waters can be affected by polar water, mass migration, meltwater pulses, a proximal ice margin's systematic development and increased stratification (Thierens et al., 2013). Thus, surface water productivity in the PBC could relate closely to the evolution of active ice sheets. One of these ice sheets, the British-Irish Ice Sheet (BIIS), plays an integral part in the temporal development of CWCs along the greater NE Atlantic continental margin.

The maximum extent of the BIIS has been studied for well over a century (Geikie, 1864, Bowen et al., 1986, Clark et al., 2012, Roberts et al., 2020; see Fig. 6). The earliest studies that measured the timing of the BIIS along its marine margin off Ireland, were based on ice-rafted debris (IRD) from deep-sea sediments (Knutz et al., 2001, Peck et al., 2006, Peck et al., 2007, Scourse et al., 2009). IRD is a terrigenous material transported within the matrix of an iceberg and deposited in marine sediments when the ice melts (Kuijpers et al., 2014). As such, a broad correlation can be detected between this material and former glacial episodes (Ó Cofaigh, 2007). Phases of IRD delivery have been identified on the limits of the Porcupine Bank (Heindel et al., 2010, Smeulders et al., 2014, O'Reilly et al., 2022), from deep-water sites in the Rockall Trough and Porcupine Seabight (Knutz et al., 2001, Peck et al., 2006, Peck et al., 2007, Scourse et al., 2009), to the Bay of Biscay (Toucanne et al., 2015), all identifying periods of BIIS instability. Scourse et al. (2009) showed that the

majority of IRD in these cores are BIIS derived, with the exception of Heinrich events fluxes, which were deposited via the Laurentide Ice Sheet. The material was delivered to the respective sites by several fast-flowing ice streams, that were dynamically variable through space and time (Eyles and Mccabe, 1989, Ó Cofaigh and Evans, 2001, Bradwell et al., 2007, Evans et al., 2009, Hubbard et al., 2009, Clark et al., 2012, Chiverrell et al., 2013). Glaciers which deposited this material to the wPB (i.e. O'Reilly et al., 2022) likely followed the Malin Sea Ice Stream with minor input from the Irish Sea and Donegal Bay Ice Streams (Benetti et al., 2021; Purcell, 2018). These records, alongside other palaeoceanographical proxies, describe that the BIIS was highly dynamic and unstable while maintaining a marine termini (Peck et al., 2006, Peck et al., 2007).

Models based on landform mapping, support these findings of a dynamic BIIS deglacial history, that experienced large oscillations during the Late Pleistocene (Clark et al., 2012). Specifically, since 48 ka BP, it underwent a series of sub-millennial scale retreat/expansion phases (Knutz et al., 2001, Wilson and Austin, 2002, Peck et al., 2007, Hibbert et al., 2010, Hall et al., 2011). During the Late Pleistocene, it is known that the BIIS covered the majority of Britain and Ireland, reaching it maximum extent by 27 ka BP (Fig. 6). (Scourse et al., 2009, Clark et al., 2012, Peters et al., 2015, Roberts et al., 2020, Ó Cofaigh et al., 2021; see also Fig. 6). At 26 ka BP, the ice sheet shows asymmetric behaviour and a back-step retreat from the shelf edge (Dowdeswell et al., 1999). Rising sea levels (Dunlop et al., 2010, Ó Cofaigh et al., 2010, Clark et al., 2012) and climate (J. Clark et al., 2012) and ocean warming have been proposed as the key processes initiating BIIS retreat on the continental shelf to the west and north of Ireland. Until 17 ka BP, the marine boundary of the ice sheet underwent periodic calving, delivering ice-rafted debris (IRD) across the margin (Knutz et al., 2001).

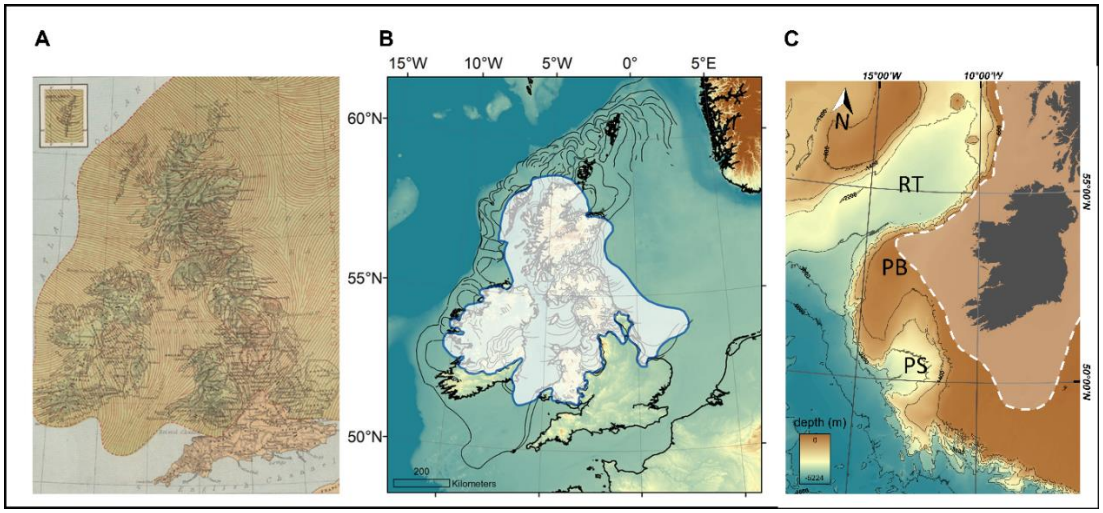


Figure 6: Comparison of the development of the extent of the BIIS. A) Geikie (1864); B) Bowen et al. (1986) accumulated evidence from glaciogenic sediments and landforms to (blue line), which was later expanded during the 21st Century using shipborne geophysical data (black lines show ice extent and retreat, modified from Clark et al. (2012) and; C) Adapted from O'Reilly et al., 2022. The configuration of the BIIS at the Last Glacial Maximum (white dashed line) is based on BRITICE-CHRONO reformulation (after Roberts et al., 2020; Ó Cofaigh et al., 2021). Maximum ice extent offshore from western Ireland is likely reached at ~26–24 cal. ka BP. PS – Porcupine Seabight, PB – Porcupine Bank, RT – Rockall Trough. (Maps created using ArcGIS Desktop v10.6 (www.arcgis.com); data sources – General Bathymetric Charts of the Oceans (gebco.net).

1.6 Aims and objectives of this research

This thesis contains a body of work whose overall aim is to analyse the temporal variation of CWCs in the wPB and PBC across 45.1 – 5.6 ka. Specifically, it aims to determine how CWC habitats in/near canyons respond to environmental change and to use the CWC records to determine regional and local environmental change. This research is divided into a series of focused research investigations explained below. Each individual research investigation has been written as a paper and is either "published", "submitted", or "in preparation to be submitted" to an international, peer-reviewed scientific journal and is presented in this thesis as a chapter (chapters 2, 3 and 4). The research programme aims to build on each chapter progressively.

Chapter 2 (**Using Novel Methods to Track British and Irish Ice Sheet Dynamics since the Late Pleistocene, along the west Porcupine Bank, NE Atlantic**) develops an understanding of background environmental and sedimentological conditions of the western Porcupine Bank. Mazzini et al. (2011) describe iceberg ploughmarks across the region. These seabed forms were caused by grounded icebergs originating from the deglaciation of the British Irish Ice Sheet. As such, understanding the impacts of this ice sheet on the study site is imperative to interpreting coral growth and mound formation. On account of this, Chapter 2 aims to answer the following research questions:

1. **What ice-ocean interactions occurred on the wPB?**
2. **Are similar signals seen in other regional records?**

To address these research questions, sampling of the site was carried out to acquire a core from an off-mound setting. To track presence of glaciers, the core was scanned using three-dimensional computed tomography, to measure quantities of ice-rafted debris. This record was then compared to other regional ice-rafted debris records. To ascertain the environmental change imposed on the site during glaciated events, grain size analysis and stable isotope analysis were used to track changes in hydrodynamics and water mass properties. After gaining an insight into the background

environmental processes, Chapter 3 **(Environmental Forcing by Submarine Canyons: Evidence Between Two Closely Situated Cold-Water Coral Mounds (West Porcupine Bank and Porcupine Bank Canyon, NE Atlantic)** focuses on cold-water corals and their dependence on canyon processes. Today, mounds are mostly focused on the canyon lip, with some sporadic mounds found nearby on the adjacent bank (Mazzini et al., 2011; Appah et al., 2020; Lim et al., 2020b). This, at the very least, suggests correlation is at play between proximity to the canyon with mound formation. Despite numerous prior research into the present-day distribution of the mounds (i.e. Dorschel et al., 2009; Mazzini et al., 2011; Lim et al., 2020b), questions still remain pertaining to the why mounds are concentrated on the canyon lip. As such chapter 3 aims, in brief, to answer the following research questions:

1. **Why are coral mounds mostly distributed along the canyon lip?**
2. **How do environmental influences differ with distance from the canyon lip and how does this impact mound development?**

To address this problem, two cores from the summits of coral mounds of variable distance from the PBC were collected using an ROV-vibrocorer. The cores were then subjected to multiproxy analysis (three-dimensional computed tomography, grain size analysis, stable isotope analysis, radiometric dating and benthic foraminifera assemblaging) to identify local environmental controls on each of the mounds. These findings were then compared to regional mound studies, to understand how the mounds in the vicinity of the PBC responded to climatic shifts.

Chapter 4 (**Are Submarine Canyons Refugia for Scleractinian Cold-water Corals in Glacial Periods?: Evidence from the Porcupine Bank Canyon, NE Atlantic**) explores the current hypothesis of NE Atlantic coral mound renewal during the Holocene. For the past two decades, the cold-water coral scientific community used models based on biogeographical and gene-flow data, to account for the synchronous timing of NE Atlantic mound re-initiation following the Younger Dryas (e.g. De Mol et al., 2005; Henry et al., 2014). These models assume the CWCs cannot and do not inhabit other

geomorphological areas which may function as a haven for corals. Areas which may offer refuge for these animals (and thus disprove this model) are submarine canyons (e.g. Huvenne et al., 2011, van den Beld et al., 2017; Wienberg et al., 2018). However, their complex topography and sedimentological heterogeneity are difficult to sampling using conventional coring methods (i.e. piston and gravity cores). On this basis, Chapter 4 aims to answer the following research questions:

1. Are submarine canyons refuges for CWCs during regionally unfavourable environmental conditions? 2. If so, does this realisation undermine established models of NE Atlantic Holocene CWC re-establishment during the early Holocene phase?

To address these questions, ROV-vibrocoring acquired cores along a cross-section of the region, including the continental bank, canyon lip, canyon slope and foot of the slope. This study is the first to successfully acquire cold-water coral bearing cores from each setting. 3D-segmented CT is used to further assess reef development from each location across the canyon. Radiocarbon and U/Th dating was used to understand the timing of canyon and cold-water coral reef development.

1.7 Author contributions

Chapter 1 – Luke O'Reilly was responsible for the reviewing of the literature with constructive discussions from Andy Wheeler.

Chapter 2 – Luke O'Reilly was responsible for the concept of this study. Aaron Lim, Luke O'Reilly, Siobhán Burke and Gerard Summers were responsible for the acquisition of the MBES. Gerard Summers and Aaron Lim processed the MBES. Luke O'Reilly, Aaron Lim and Andy Wheeler collected core CE18011_VC2. Luke O'Reilly was responsible for the transportation and storage of core CE18011_VC2. OJ O'Connor, Niamh Moore and Luke O'Reilly collected the computer tomography data. Luke O'Reilly and Jurgen Titschack processed the computed tomography data. Luke O'Reilly split the cores under the guidance of Luke Harmen. Luke O'Reilly photographed the cores. Luke O'Reilly sampled and measured the grain size of the siliciclastic sediments. Luke O'Reilly calculated the settling velocity and end member populations. Luke O'Reilly prepared and measured the samples for the measurement of total carbonate and total organic content. Luke O'Reilly prepared the samples for stable isotope analysis. Torsten Vennemann measured the stable isotopes of the samples. Luke O'Reilly prepared the samples for AMS ^{14}C dating. Luke O'Reilly built the age model under the guidance of Felix Butschek. Luke O'Reilly interpreted the data and wrote the manuscript with constructive discussions from Andy Wheeler, Jurgen Titschack, Aaron Lim, Felix Butschek, Robin Fentimen, Evan O'Mahony and John Boyd. Luke O'Reilly designed the figures. Luke O'Reilly revised the manuscript twice after receiving feedback from James Scourse and an anonymous reviewer. Andy Wheeler, Felix Butschek and Jurgen Titschack gave further feedback on both revised drafts of the manuscript.

Chapter 3 – Luke O'Reilly was responsible for the concept of this study. Aaron Lim, Luke O'Reilly, Siobhán Burke and Gerard Summers were responsible for the acquisition of the MBES. Gerard Summers and Aaron Lim processed the MBES. Luke O'Reilly, Aaron Lim and Andy Wheeler collected cores CE18011_VC1 and RH17002_VC7. Luke O'Reilly was responsible for the transportation and storage of cores CE18011_VC1 and RH17002_VC7. OJ

O'Connor, Niamh Moore and Luke O'Reilly collected the computer tomography data. Luke O'Reilly and Jurgen Titschack processed the computed tomography data. Luke O'Reilly split the cores under the guidance of Luke Harmen. Luke O'Reilly photographed the cores. Luke O'Reilly designed the study. Luke O'Reilly designed the figures. Luke O'Reilly sampled and measured the grain size of the siliciclastic sediments. Luke O'Reilly prepared the samples for stable isotope analysis. Torsten Vennemann measured the stable isotopes of the samples. Luke O'Reilly prepared the samples for AMS ^{14}C dating. Luke O'Reilly built the age models. Luke O'Reilly prepared the samples for benthic foraminifera analysis (core sampling, wet sieving, dry sieving, weighing and splitting). Initial benthic foraminifera picking and identification was done by Luke O'Reilly. Robin Fentimen reassessed the samples to determine the finalized benthic foraminifera assemblages used in this thesis. Luke O'Reilly re-checked each of the assemblages under the guidance of Robin Fentimen. Robin Fentimen acquired the SEM images of dominant benthic foraminifera selected from the assemblages. Luke O'Reilly interpreted the data. Luke O'Reilly used statistical analysis under the guidance of Felix Butschek. Luke O'Reilly wrote the manuscript with constructive discussions from Robin Fentimen, Felix Butschek and Andy Wheeler.

Chapter 4 – Luke O'Reilly was responsible for the concept of this study. Aaron Lim, Luke O'Reilly, Siobhán Burke and Gerard Summers were responsible for the acquisition of the MBES. Gerard Summers and Aaron Lim processed the MBES. Luke O'Reilly, Aaron Lim and Andy Wheeler collected cores CE18011_VC1, CE18011_VC2, CE18011_VC4, CE18011_VC5, CE18011_VC6, CE18011_VC8, RH17002_VC1 and RH17002_VC7. OJ O'Connor, Niamh Moore and Luke O'Reilly collected the computer tomography data. Luke O'Reilly and Jurgen Titschack processed the computed tomography data. Luke O'Reilly split the cores under the guidance of Luke Harmen. Luke O'Reilly photographed the cores. Luke O'Reilly prepared the samples for AMS ^{14}C and U/TH dating. Jurgen Titschack further prepared the samples for U/Th dating. Luke O'Reilly designed the figures. Luke O'Reilly built the age models. Luke O'Reilly interpreted the data and

wrote the manuscript with constructive discussions from Jurgen Titschack and Andy Wheeler.

Chapter 2: Using Novel Methods to Track British and Irish Ice Sheet Dynamics since the Late Pleistocene, along the west Porcupine Bank, NE Atlantic

(Current status: Published, *Quaternary Science Reviews*,

https://doi.org/10.1016/j.quascirev.2022.107463)

*O'Reilly, Luke[1], Lim, Aaron[1,2], Titschack, Jürgen[3,4], Moore, Niamh[5,6], O'Connor, O.J.[5,6], Appah, John[1], Robin Fentimen[7], Felix Butschek[1,8], Harris, Kimberley[9], Vennemann, Torsten[10] and Wheeler, Andrew J.[1,8]

*Corresponding author

[1]*School of Biological, Earth & Environmental Sciences / Environmental Research Institute, Distillery Fields, North Mall Campus, University College Cork (UCC), Ireland*

[2]*Green Rebel, Crosshaven Boatyard, Crosshaven, Co. Cork, Ireland*

[3]*MARUM – Center for Marine Environmental Sciences, University of Bremen, Bremen, Germany*

[4]*Senckenberg am Meer, Marine Research Department, Wilhelmshaven, Germany*

[5]*Department of Radiology, Cork University Hospital (CUH), Wilton, Cork, Ireland*

[6]*Department of Radiology, University College Cork*

[7]*ENS Lyon (Dept of Earth Sciences, Ecole Normale Superieure de Lyon, 46 allée d'Italie, 69364 Lyon cedex 07)*

[8]*iCRAG (Irish Centre for Research in Applied Geosciences)*

[9]*DP Energy Ireland Ltd, Mill House, Buttevant, P51 TN35, Co. Cork, Ireland*

[10]*IDYST – Institute of Earth Surface Dynamics, University of Lausanne, Switzerland*

Abstract

Extensive research has been undertaken to elucidate the glacial history of the British Irish Ice Sheet (BIIS) in the NE Atlantic. BRITICE-CHRONO has compiled terrestrial and marine based evidence, to provide an empirical reconstruction of ice sheet expansion and retreat during the Late Pleistocene. Across the Irish margin, particular focus has been given to seafloor sediments which contain ice-rafted debris (IRD). However, there are few publications on IRD from areas proximal to the maximum extent of the BIIS, which would offer further insights on the behaviour of the ice sheet during (de)glacial events. Previous exploratory surveys of the west Porcupine Bank (wPB) visually identified IRD on the seafloor and these present a new study site to investigate the extent of

the BIIS and the course of its icebergs. Moreover, there are uncertainties about the effects of icebergs on the marine life and cold-water corals occupying the nearby Porcupine Bank Canyon. Assessing a sediment core containing an IRD analogue for the wPB would thus, have a dual purpose. In the past however, coring missions of the wPB using traditional coring methods (i.e. piston and gravity cores) were unsuccessful. Here, we utilized a novel ROV-mounted vibrocoring procedure to capture a 0.75 m IRD-bearing sediment core from the wPB. Then further novel analytical methods (computed tomography-based IRD-detection) were used to quantify IRD every 0.02 cm to provide the highest resolution record of BIIS related IRD to date. From this, several fluxes of IRD deposition onto the wPB between 31.6 – 9 ka BP were revealed and corroborated by other published records from across the NE Atlantic. It was shown that the wPB IRD fluxes occur simultaneously with other parts of the margin. The IRD signal also shows that iceberg calving occurred on the wPB during the Younger Dryas. Grain-size analysis of the core allowed for a reconstruction and interpretation of the palaeoenvironmental conditions during these IRD flux events and shows that BIIS-derived glaciers had a major impact on hydrodynamic conditions in the wPB. Subsequently, intensive scouring led to a major hiatus in the core during 27.3–17.2 ka BP. These results are a useful addition to BIIS literature on this part of the shelf. Furthermore, it shows that bottom currents were influenced by (de)glacial events, an important finding when considering the presence of nearby current-dependant benthos.

2.1 Introduction

Marine sediments can contain depositional sequences from melting glaciers that provide crucial information for the modelling of former marine-terminated ice-sheets (Boulton, 1996, Greenwood and Clark, 2009, Ó Cofaigh et al., 2012, Rea et al., 2018, Wadham et al., 2019). Understanding the response of these marine-influenced ice-sheets to changes in ocean processes (Andresen et al., 2011, Lloyd et al., 2011) and atmospheric warming (Carr et al., 2013), can provide insights into the responses of larger scale ice masses to changing ocean and atmosphere conditions (Bond et al., 1993). Geomorphological and sedimentological features from the British-Irish Ice-Sheet (BIIS) show an intricate deglaciation history (Clark et al., 2012a), which provides an understanding into the response of contemporaneous analogues such as changes to the Greenland Ice-sheet. In recent years, much attention has been given to the sedimentological and geochronological parameters controlling the timing of BIIS retreat during the last glacial-interglacial cycle, e.g. through the BRITICE-CHRONO project (http://www.britice-chrono.org/; see Peters et al., (2015), (2016), Praeg et al., (2015), Sejrup et al., (2016), Arosio et al., (2017), Bateman et al., (2017), Evans et al., (2017), Small et al., (2017), Smedley et al., (2017), Callard et al., (2018), Chiverrell et al., (2018), Evans et al., (2018), Lockhart et al., (2018), Roberts et al., (2018), Small et al., (2018), Wilson et al., (2018), Bradwell et al., (2019), Ó Cofaigh et al., (2019), Evans et al., (2019), Roberts et al., (2019), Scourse et al., (2019), Callard et al., (2020), Tarlati et al., (2020)). Along the western Irish Shelf, the BIIS reached its local maximum extent between 29 and 23 ka BP (Ó Cofaigh et al., 2012, Peters et al., 2015) during the Last Glacial Maximum (LGM; Clark et al. 2009). Thereafter, the marine-terminating portion of the BIIS retreated to the northeast until final deglaciation after 15 ka (Clark et al., 2012a). However, evidence for episodic readvances in the final stages of BIIS deglaciation in its northerly sectors of the ice mass (Ó Cofaigh et al., 2012, Purcell, 2014) and along the NE Irish Coastlines (McCabe and Clark, 1998, Ballantyne and Ó Cofaigh, 2017), indicated a complex end stage history and it seems numerous re-advancements events remain to be discovered (Peters et al., 2016). Cores taken from areas proximal to BIIS ice stream terminations provide an

opportunity for insights into the late history of the BIIS deglacial events in offer such insights in the Rockall Trough (Georgiopoulou et al., 2012, Callard et al., 2018, Roy et al., 2020, Tarlati et al., 2020), the Porcupine Seabight (PS) (Peck et al., 2007, van Rooij et al., 2007, Scourse et al., 2009a) and the Goban Spur (Hall and McCave, 1998a, Hall and McCave, 1998b, Scourse et al., 2000, Haapaniemi et al., 2010).

Within these studies, particular emphasis has been given to the role of ice-rafted debris (IRD) plays in charting the retreat of ice-sheets. IRD is terrigenous material transported within an iceberg from a marine (or lake) terminating glacier and deposited in marine (or lacustrine) sediments as the iceberg melts (Kuijpers et al., 2013) and quantifying IRD in marine sedimentary sequences can provide critical information about the evolution of ice sheets (Andrews, 2000, Kuijpers et al., 2013). Rapidly deposited layers of IRD correspond to periods of abrupt climate change and increased iceberg calving during past glacial cycles, including enigmatic phases of instability such as Heinrich events, Dansgaard-Oeschger cycles or Bond events (Heinrich, 1988, Andrews, 2000, Kuijpers et al., 2013). IRD records from the west coast of Ireland are an established method for reconstructing Pleistocene glacial development (e.g. (Knutz et al., 2001, Peck et al., 2006, Peck et al., 2007, Scourse et al., 2009a, Owen, 2010, Tarlati et al., 2020). Sedimentary records from the Porcupine Bank (Owen, 2010, Smeulders et al., 2014b) and PS (Knutz et al., 2001, Rüggeberg et al., 2005, Peck et al., 2006, Peck et al., 2007, Rüggeberg et al., 2007, van Rooij et al., 2007, Scourse et al., 2009a, Thierens et al., 2012) all show episodic delivery of IRD to the seafloor. However, despite extensive research undertaken by BRITICE-CHRONO, there are continuing uncertainties associated with timing and extent of BIIS glacial history on the Porcupine Bank, in particular within areas proximal to the ice sheet.

Explorative surveys of the west Porcupine Bank (wPB) have identified an abundance of IRD and ploughmarks (Mazzini et al., 2011, Wheeler et al., 2017, Lim et al., 2018b) caused by grounded icebergs during glacial sea level low stands (Dorschel et al., 2010). Nearby, the Porcupine Bank Canyon (PBC) incises the shelf, and likely acts as a conduit for glacial and glaciofluvial

sediment (Sacchetti et al., 2012b). As such, it represents a unique study site to fill current gaps in the understanding of the seafloor proximal to the BIIS. Assessing IRD records from the wPB would in turn enrich the literature on this part of the continental shelf and in particular the PBC which is a documented biological hotspot on the Irish Margin (Appah et al., 2020b, Lim et al., 2020b). The role of BIIS glaciation on sedimentation and hydrodynamics adjacent to this important habitat remains unclear. Therefore understanding BIIS deglaciation has a twofold purpose. Until now however, conventional coring missions (i.e. piston and gravity cores) have been unsuccessful in the challenging conditions and substrates presented by the wPB (Wheeler et al., 2014).

Thus, the aim of this study is to investigate the ice-ocean interactions on the wPB by utilizing novel coring methods (ROV-vibrocorer). The acquired sediment core was subjected to further novel technologies (computed tomography-based IRD evaluation) to provide a high resolution (0.02 cm) assessment of ice rafted material. From this it was found that IRD was deposited across several flux events since at least 31.6 ka BP. Regional studies are used to interpret climatic signals inferred from the IRD fluxes and their origins. Insights into past bottom and surface water oceanography are constrained from grain-size data and isotopic composition of benthic and planktonic foraminifera. Essentially, this research investigates the glacial history of the BIIS in an area proximal to its maximum extent, building upon current research by BRITICE-CHRONO. In doing so, this study also highlights new techniques in acquiring cores from difficult terrains and shares innovative methods in assessing IRD with the scientific community.

2.2 Geographical Setting

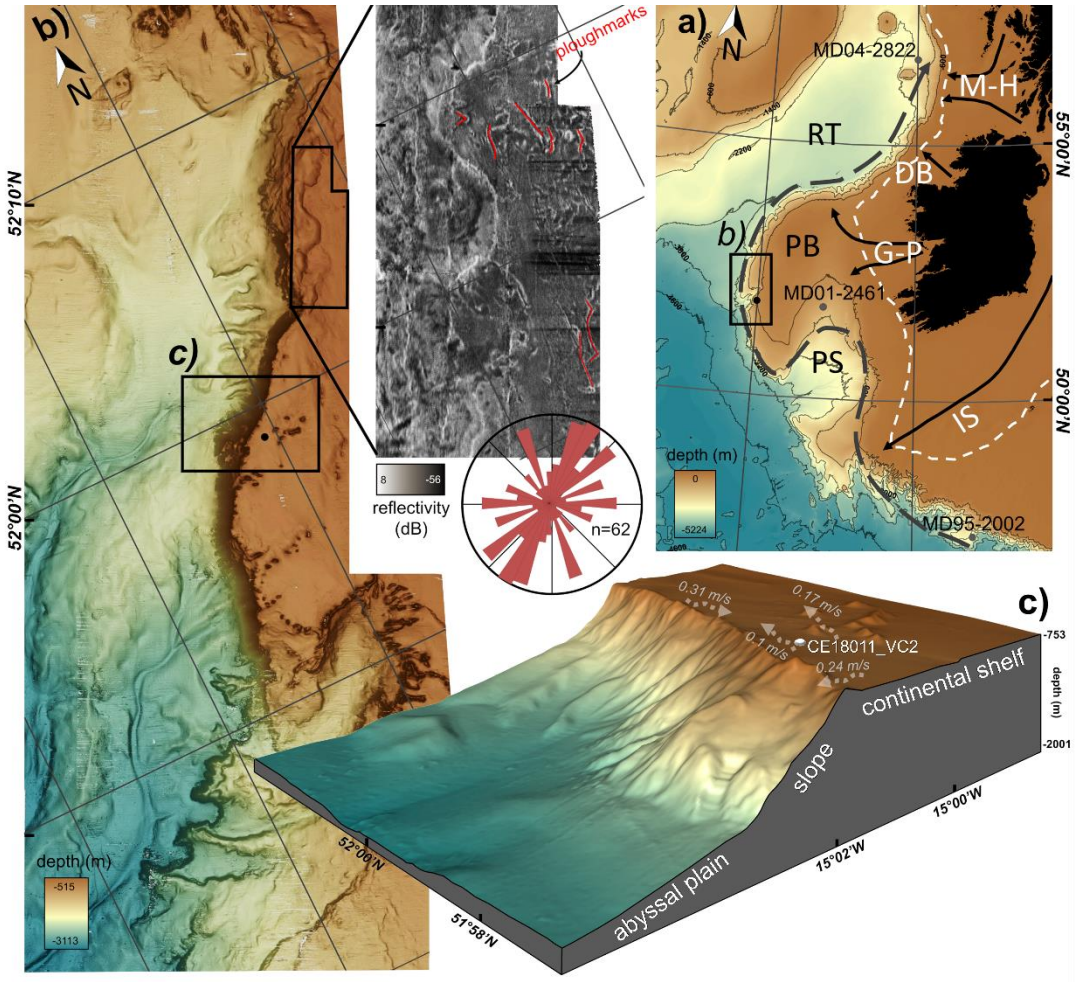


Figure 7: (a) Location of the study site within the western Porcupine Bank (black rectangle) on the Irish continental margin (PB - Porcupine Bank, PS - Porcupine Seabight, RT - Rockall Trough). White dashed line indicates BIIS maximal extent, based on BRITICE-CHRONO reformulation (after Roberts et al., 2020; Ó Cofaigh et al., 2021. Grey dotted line showing flow direction of Eastern North Atlantic Water for the LGM which also enters the PS (Wienberg et al., 2020). Black arrows indicate the main ice streams derived from the BRITICE-CHRONO reconstruction described by (Wilton et al., 2021); M-H - Malin-Hebrides, DB - Donegal Bay, G-P - Galway-Porcupine, IS - Irish Sea). Cores mentioned in this study annotated by black dot: MD04-2822 from Knutz et al. (2001), MD01-2461 from (Peck et al., 2006), and MD95-2002 from Toucanne et al. 2015. (b) Bathymetry map of the upper Porcupine Bank Canyon modified after (Lim et al., 2020b). *Note insert: red lines summarizing several plough marks identified from multibeam echosounder backscatter data. Rose diagram showing ploughmarks orientation (n = 62).* (c) Overview of coring site used in this study. Grey arrows show modern day current direction and associated mean current speeds (Lim et al., 2020b). (Maps created using ArcGIS Desktop v10.6 (www.arcgis.com); data sources – (a) - General Bathymetric Charts of the Oceans (gebco.net); (b and c) – additional bathymetry (10 m resolution) collected during CE18011 research cruise (Lim et al., 2018b).

The wPB forms the outermost part of the continental shelf west of Ireland (Fig. 7a) and is part of a N-S trending plateau forming the north-western margin of the PS Basin (Naylor and Shannon, 1975). Part of the wPB is incised by the NE–SW striking Porcupine Bank Canyon (PBC), located roughly 300 km west of Cork, Ireland (Dorschel et al., 2010) (Fig. 7a). It is tectonically controlled (Shannon, 1991, Shannon et al., 2007) and the largest submarine canyon on Ireland's margin. It has three confluent axial channels, each with an axial length of about 60 km (Elliott et al., 2006), which meander along the continental rise and feed into the canyon head (Fig. 7a). High reflectivity in multibeam backscatter data from the north eastern sector of the canyon head shows compacted sands exposed as a result of iceberg ploughmarks (Dorschel et al., 2010, Mazzini et al., 2011) (Fig. 7b insert), which trend mostly NE-SW. Along the interface between the wPB and the PBC, a series of escarpments extend from south to north and are up to 10 km in length and 60 m in height (Mazzini et al., 2011). The coring site is located adjacent to this interface at the eastern canyon flank. The area was recently declared of ecological significance and was designated as a *Special Area of Conservation* under the European Union Habitats Directive (2016). It is home to significant cold-water coral (CWC) habitats (Dorschel et al., 2010, Mazzini et al., 2011, Lim, 2019b, Lim, 2019a, Appah et al., 2020b, Lim et al., 2020b), deemed "ecosystem engineers" (Jones et al., 1994).

Eastern North Atlantic Water (ENAW; ~200–700 m water depth) is carried from south to north over the seafloor by a poleward Shelf-Edge Current (Dickson and McCave, 1986, Pollard et al., 1996, White et al., 2007, Mazzini et al., 2011) (Fig. 7a), where the flow becomes locally focussed by positive topographic expressions (Lim et al., 2020b). Mediterranean Outflow Water (MOW) exists between 800 and 1000 m water depth. It is characterised by a high salinity (White et al., 2007, Lim et al., 2020b) and overlies the denser Labrador Sea Water that occurs at 1100 m water depth (Appah et al., 2020b).

2.3 Methods

2.3.1 ROV-Vibrocorer

Core CE18011_VC2 was acquired from the study site onboard the *RV Celtic Explorer* during the Cold-Water Coral Habitats in Submarine Canyons (CoCoHaCa) II cruise (cruise number CE18011; (Lim et al., 2018b) using the *Holland I* Remotely Operated Vehicle (ROV) equipped with a vibrocore rig (developed by P&O Maritime and the Marine Institute Ireland). It was retrieved from the seabed adjacent to cold-water coral mounds along the eastern canyon flank on the wPB (depth – 731 m; Fig. 7c). The positioning of the ROV was acquired through the integration of a Kongsberg HAINS inertial navigation system, ultra-short baseline (USBL) system (Sonardyne Ranger 2) and doppler velocity log (DVL). The core was stored vertically at 4°C to minimise sediment deformation.

2.3.2 Core analysis

Non-destructive and destructive multiproxy analytical methods were performed on core CE18011_VC2 to assess relevant paleoenvironmental conditions.

2.3.2.1 Computed Tomography

All computed tomography images were acquired using a 64 section Multi-slice scanner (GE Healthcare, Discovery CT 750 HD) at Cork University Hospital, Cork, Ireland. Images were acquired at a slice thickness of 0.625 mm, using 120 kV, 600 mA and a rotation time of 0.8sec, a pitch of 0.984 and a bony convolution algorithm. Images were reconstructed using Model based Iterative Reconstruction (MBIR) Veo (GE Healthcare, GE Medical Systems, Waukesha, WI, USA) with pure iterative reconstruction using a resolution preference of 20% (RP20) increasing the spatial resolution by 20%. An overlapping reconstruction was performed with a final voxel size of 0.195 x 0.195 x 0.625 mm. The original data was recalculated to obtain an isotropic voxel size of 0.2 mm.

Computed Tomography (CT) processing was completed following procedures outlined by (Bartels et al., 2017, Bartels et al., 2018) (see also Appendix I).

Overlapping IRD volumes were determined for every CT-slice (every 0.2 mm) considering a 51-CT slice window that corresponded to a 1.02 cm interval within the core. Also, the IRD count and the IRD grain-size analyses considered 51 CT-slices. This method was shown to be more effective way of assessing IRD than traditional methods (i.e. hand picking; see (Bartels et al., 2017). Reworking by bottom-current can bias IRD concentrations through the selective removal of fines. To counter this potential bias IRD fluxes were calculated (Scourse et al., 2009)

2.3.2.2 Grain Size Analysis

Core CE18011_VC2 was frozen at -20 °C and split using an electric circular handsaw, photographed and lithologically described. The matrix sediment composition was determined from 15 samples (every 5 cm) by weight loss after chemical dissolution of the organic matter and carbonate material by following the procedures outlined by Pirlet et al. (2011) (see Appendix II). The siliciclastic matrix fraction was then investigated for grain-size variations. Grains >2 mm were sieved from the samples with a 2 mm sieve. Grains <2 mm were measured using a Malvern Instruments Mastersizer 3000 (MS3000) at University College Cork with a refined standard operating procedure (see Appendix III). The calculated grain-size distribution (GSD) is an average of five total measurements of a sample. This result was used for further statistical analyses in GRADISTAT (see Blott and Pye, (2001) where median grain size (Dx_{50}), mean grain sizes (MGS), kurtosis and sorting were automatically calculated (the latter two using the Folk and Ward method (Folk and Ward, 1957). The mean sortable silt (MSS) was calculated from the differential volume or weight distribution of grains within the 10–63 μm terrigenous silt fraction, following the approach of McCave and Andrews (2019a). In this study, the MGS and MSS size is used as a proxy to trace changes in near-bottom current strength (McCave et al., 1995b). Stronger bottom-currents yield a coarser mean size of a non-cohesive silt fraction, due to selective deposition and winnowing (McCave et al., 1995b). A calculation of settling velocities further helped to reconstruct bottom-water hydrodynamics (see Soulsby, 1997; Huvenne et al., 2009b).

2.3.2.2.1 Grain Size End-Member Modelling

Meaningful sub-populations of GSDs were acquired through end-member modelling algorithms (EMMA) (Weltje, 1997, Prins and Weltje, 1999, Weltje and Prins, 2003). This analysis uses linear mixed modelling to ascertain dominant GSDs which explain the total variation in all GSD, and is a standard approach applied across a range of marine environments (Prins and Weltje, 1999, Prins et al., 2002, Stuut et al., 2007, Tjallingii et al., 2008, Thierens et al., 2010, Jonkers et al., 2015). End-members were determined using the AnalySize MATLAB package version 1.2.0 (available at https://github.com/greigpaterson/AnalySize/releases; (Paterson and Heslop, 2015, Hateren et al., 2017). This approach offers the simplest explanation for the identified variations in GSDs that originated from statistically indistinguishable provenance and/or transport process in each sample (Prins and Weltje, 1999, Weltje and Prins, 2003). The minimum number of EMs were constrained by assessing the coefficients of determination (r^2), which represent the degree of variance present in each grain-size population (Weltje and Prins, 2003). The total % of each EM for a given interval was then plotted versus depth.

2.3.2.2.1.1 Ground Truthing

Ground-truthing the end-members can strengthen the interpretation of the transport mechanisms associated with the grains. In this study, grain surface microtextural analysis were analysed from intervals dominated by EMb to provide provenance and transport information (see Thierens et al., 2010). New methods by McCave and Andrews (2019b) were followed to determine if a) the lithic fine fraction possesses characteristics of sorting by current, or b) it is an artifact of glacially eroded sediment deposited from melting icebergs that may have fallen through a sluggish water column and deposited on the seafloor relatively undisturbed. As a result, a downcore correlation coefficient was used to separate core intervals dominated by sediments of glacial origin from sediments transported by near bottom currents. Accordingly, a sortable silt percentage (SS%) was calculated by taking the sum weight of the 10–63 μm fraction of the sample divided by the total fine fraction (% <63 μm). A

downcore correlation (r_{run}) was then examined between MSS and SS%, whereby r_{run} of <0.5 should be rejected as a proxy for current strength.

2.3.2.3 AMS radiocarbon measurements

The chronostratigraphy of core CE18011_VC2 is based on 7 accelerator mass spectrometry (AMS) radiocarbon measurements from monospecific samples of the planktonic foraminifera *Globigerina bulloides* taken from the >150 µm aliquot size. Samples were taken from above and below boundaries between sedimentological units (Table 2). The samples were cleaned in an ultrasonic bath prior to submission. At least 15 mg of calcium carbonate was used to acquire each date respectively. The measurements were carried out at DirectAMS Laboratories, Washington, USA. All obtained ages were corrected for ^{13}C and a mean ocean reservoir (ΔR) age of -191 years (±94; Stephen Hopper and Paula Reimer, Queens University Ulster, personal communication, 2021). This ΔR value was calculated using the MARINE20 calibration curve (Heaton et al., 2020) for the west coasts of Ireland, Scotland, Orkney and Outer Hebrides (Reimer et al., 2002), although ΔR could vary through time (Austin et al. 2011). AMS ^{14}C ages were converted to calendar years using the MARINE20 curve (Heaton et al., 2020) of the web-based CALIB7.10 software (Stuiver and Reimer, 1993); http://calib.org/calib/calib.html) and reported as kiloyears before present (ka BP, Present= 1950CE).

2.3.3 Age Model

The age model is based on the radiometric dates (Table 2) and was calculated using the R package “rbacon” (Blaauw et al., 2020), which uses Bayesian statistics to reconstruct accumulation history of deposits (Blaauw and Christen, 2011). Sedimentation rates were then determined every 1 cm from the calculated age model. Further information on the parameters used to construct the age model can be found in Appendix VI.

2.4 Results

Analysis performed on core CE18011_VC2, including the core logs, sedimentary and micropaleontological data, CT-scan and geochronology (see section 4.1), are presented against depth to identify weakly bioturbated intervals to help build a chronostratigraphic framework (see section 2.4.2) and determine major IRD pulses (see section 2.4.3).

2.4.1 Description of CE18011_VC2

Core CE18011_VC2 can be divided into 4 lithological units (Fig. 8), based on the different pulse of IRD identified during CT (Fig, 2g). Clear shifts in IRD across unit boundaries can be easily seen in Fig. 8e for Units A, B and C whereas the change is less abrupt between Units C and D. Changes in other variables (Fig. 8g–k) confirm this visual core subdivision. For detailed sedimentological data, see Appendix VIII.

Unit A (48–73 cmbsf)

Unit A (Fig. 8o) is composed of dark brown (Fig. 8c) very poorly sorted (Fig. 8m; average 4.6 µm; see also Appendix VIII) sandy silts and silty sands (Fig. 8l) with a relatively small MGS (Fig. 8i; average 26 µm) and MSS (average 24 µm), with low kurtosis (Fig. 8k; average 0.83). Unit A also showed a low σMSD (Fig. 8h). Settling velocities calculated for this interval are relatively fast (Fig. 8j; average 0.37 ms^{-1}).

CT scanning revealed two high x-ray density intervals within Unit A, visible at 57–60 and 52–54 cmbsf (Fig. 8b), that show sharp contacts to the underlying lower density sediments. The lower sections of this unit (i.e. 60–73 cmbsf) also had a high-density signature with minor pockets of lower density sediments throughout (see also Fig. 8b and 8c). Minor peaks in standard deviation in matrix sediment density (σMSD; Fig. 8h) are visible at 62 and 51 cmbsf. Bioclastic material is observed in trace amounts (Fig. 8d). Between 66–73 cmbsf, IRD clasts are abundant (up to 31 clasts/cm^3; Fig. 8g). Moderate amounts (up to 11 clasts/cm^3) of IRD are visible in the remainder of the unit. Vol. % of IRD in Unit A (Fig. 8g) occurs continuously throughout the unit, but several pulses are seen peaking at 71 (7.8 vol.%), 63 (5 vol.%) and 50 (4 vol.%) cmbsf. A large sub-cm clast is present at 63 cmbsf.

Unit B (42–48 cmbsf)

Unit B (Fig. 8o) is composed of dark brown (Fig. 8c) poorly sorted (Fig. 8m; 3.3 µm; see also Appendix VIII) silty sands (Fig. 8l) with relatively small MGS (Fig. 8i; 12 µm) and small MSS (Fig. 8i; 21 µm), with a high kurtosis (Fig. 8k; 1.1). Unit B also showed a low σMSD (Fig. 8h). Settling velocities calculated for this interval are slow (Fig. 8j; 0.23 ms^{-1}).

Unit B recorded a low X-ray density unit with a dewatering fracture from core recovery visible at its top (Fig. 8b). Bioclastic material is abundant within Unit B (Fig. 8d). IRD clasts are present in trace amounts (Fig. 8g; <3 clasts/cm^3; <0.2 vol.%). At the top of Unit B, an erosive boundary is visible (Fig. 8b and 2c).

Unit C (18–42 cmbsf)

Unit C (Fig. 8o) is composed of very poorly sorted (Fig. 8m; average 4.7 µm; see also Appendix VIII) sandy silts and silty sands (Fig. 8l). The sediment colour composition progresses from dark brown to very dark greyish brown at 33 cmbsf (Fig. 8c). It has a relatively large MGS (Fig. 8i; average 36 µm) and moderate MSS (Fig. 8i; average 26 µm), with a low kurtosis (Fig. 8 k; average 0.85). Settling velocities calculated for this interval are relatively fast (Fig. 8j; average 0.38 ms^{-1}).

Unit C recorded variable X-ray density, whereby in the lower sections (Fig. 8b; between 30–42 cmbsf), the sediment appears to become more heterogenous, with the less dense sediments (dark grey) becoming mixed with the denser sediments (light grey). This interval also showed a high σMSD (Fig. 8h). Contrastingly, the upper section of the unit becomes more homogenous with low σMSD. A dewatering structure is visible at 32 cmbsf. The base of the unit is an erosive boundary (Fig. 8b and 8c). Bioclastic material is abundant between 28–42 cmbsf, and is mostly composed of angular shells, but a scaphopod and gastropod are also present (Fig. 8d). IRD in Unit C occurs continuously throughout the unit (average 7 clasts/cm^3; Fig. 8g). Large sub-cm clasts influence several pulses in IRD vol.% seen at 40 (3.5 vol.%), 32 (3.9 vol.%), 24 (6.6 vol.%) and 21 (2.5 vol.%) cmbsf.

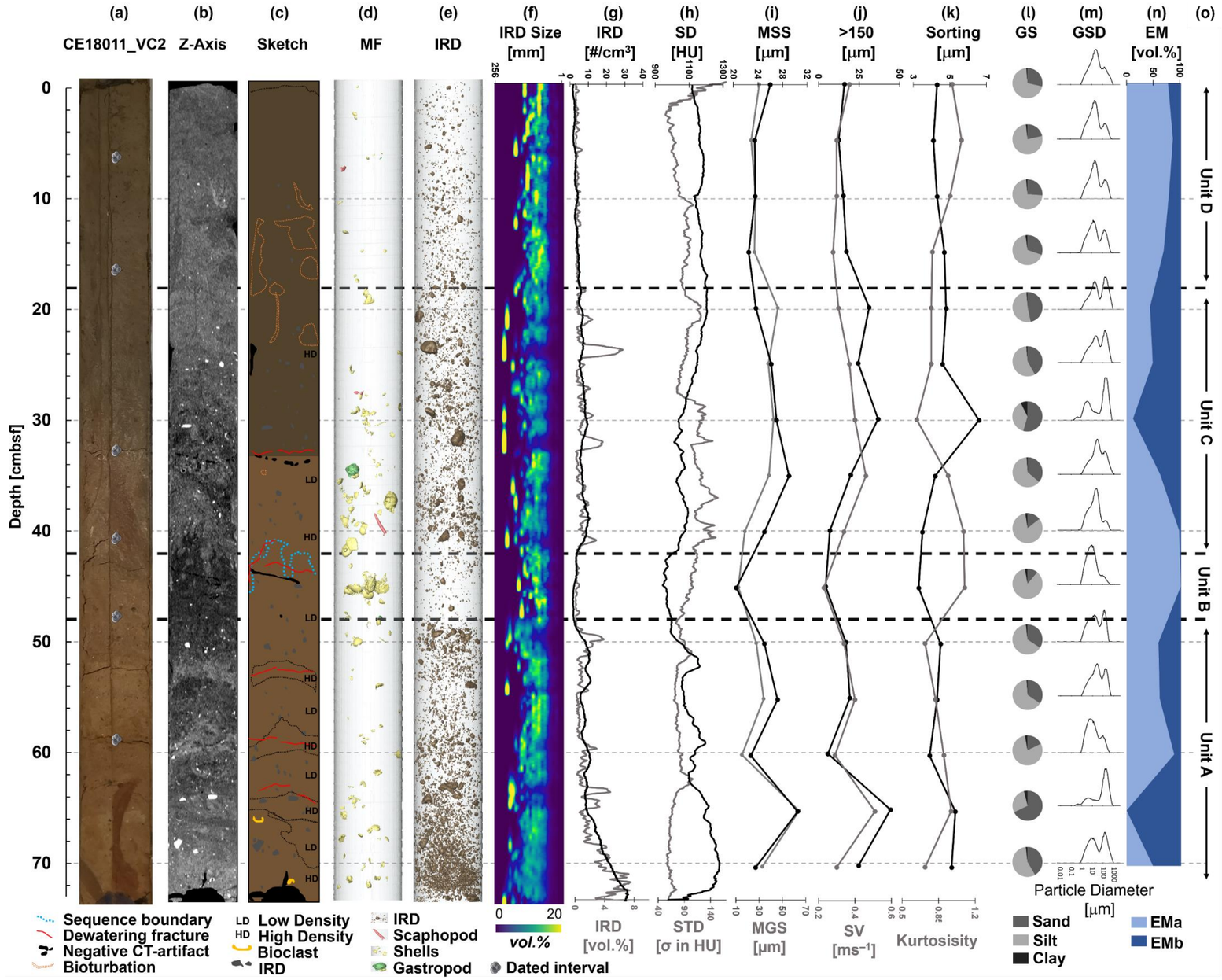


Figure 8: a-r Compiled computed tomography (CT), sedimentology and microfossil data of core VC18011_VC2 plotted versus depth in centimetres below seafloor (cmbsf). Units A–D identified following multiproxy assessment of core. (a) true-colour image of core; (b) orthogonal CT-image of core, with darkness a function of density. Note: IRD throughout (high density; white); (c) sketch log interpreted from x-ray; (d) 3D image of bioclasts identified in core (see legend for bioclast types); (e) 3D image of ice-rafted debris (IRD) content; (f) IRD clast size distribution (0–20 vol.% of clasts: blue to red, respectively); (g) Number of IRD clasts per cm^3 (black) and vol.% of IRD (grey) derived from CT data; (h) Sediment density (black; see Appendix I) and standard deviation sediment density (grey); (i) Mean sortable silt size (black) and mean grain size (grey); (j) Vol.% of sediment >150µm (black) and settling velocities (ms^{-1}; grey); (k) sorting (black) and kurtosity (grey) of sediments (l) sand, silt and clay percentages shown as pie charts, centred at appropriate depth intervals; (m) grain-size distributions of siliciclastic sediments; (n) End Member dominance calculated for each grain size distribution; (o) inferred boundaries between units.

Unit D (0–18 cmbsf)

Unit D (Fig. 8o) is composed of very dark greyish brown (Fig. 8c) very poorly sorted (Fig. 8m; average 4.3 µm; see also Appendix VIII) sandy silts. The unit has a relatively moderate MGS (Fig. 8i; average 26 µm) and moderate MSS (average 24 µm), with a low kurtosis (Fig. 8k; average 0.95). Settling velocities calculated for this interval are relatively moderate (Fig. 8j; average 0.31 ms^{-1}).

Unit D recorded high X-ray densities with pockets of lower density sediment (dark grey circles) and vertical stratification visible between 12–18 cmbsf (Fig. 8c and 8d). A minor amount of bioclast material is present (Fig. 8d). IRD clasts are present in trace amounts (Fig. 8g; <3 clasts/cm^3; <0.5 vol.%).

2.4.1.1 End-member modelling analysis

End-member modelling identified two meaningful sub-populations of GSDs (Fig. 8n, Appendix IV). The relative strength of these end-members, EMa and EMb, describe the changes in down-core grain-size variation with a high R^2 value accounting for 92 % of the variance seen in CE18011_VC2 (Appendix IV; section b). Adding a third end member increases the variance captured to 98%, although it increases the risk of modelling noise rather than signal (Thierens et al., 2010). Therefore, two end members were considered as reliable. The principal GSDs of EMa are centred around a mean of 14 µm and a mode of 19 µm, whereas EMb is centred around a mean of 59 and a mode of 163 µm (Appendix IV; section d). Core VC18011_VC2 is dominated by EMa (Fig. 8n). Two minor layers are EMb dominated, seen in the lower part of Unit A at 65 cmbsf and the upper part of Unit C at 30 cmbsf.

2.4.1.1.1 Ground Truthing

A downcore correlation of MSS and SS% of the fine fraction obtained a value of 0.1. However, upon the removal of two outliers (from 30 and 65 cmbsf, both which showed more of a preference to EMb) a value of 0.6 was recorded (see Appendix V).

20 sand-sized quartz grains were selected at random from intervals dominated by EMb and subsequently investigated using a digital light microscope. In general, evidence of mechanical abrasion was identifiable across each of the grains from these intervals (Fig. 9a-e), including conchoidal fractures, block

breakage, glacial grinding and crushing. Moreover, solution pits were also identifiable in places (Fig. 9a). Grains were typically angular to sub-angular in size and had high relief.

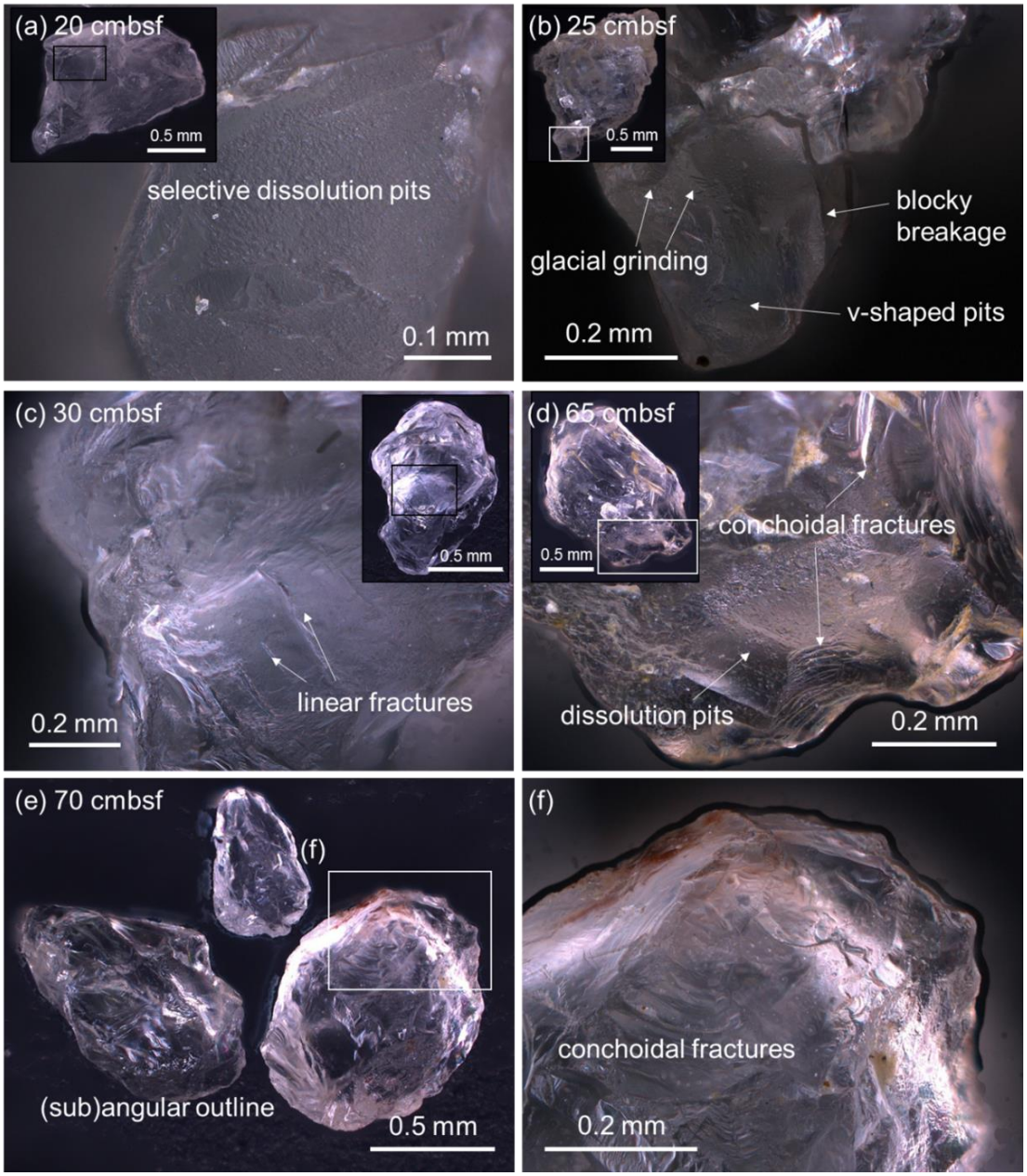


Figure 9: Surface microtextures identified in EMb dominated intervals. Note: subfigues a-f each show characteristics of glacial provenance (i.e. subangular outlines, blocky fractures etc.)

2.4.2 Chronostratigraphic framework

The chronostratigraphic framework of the core VC18011_VC2 is constrained by seven AMS ^{14}C ages, which range between 33.4 ka BP (at 59 cmbsf) and 9.8 ka BP (core top at 7 cmbsf; see Table 2).

Table 2: Radiocarbon results acquired from monospecific planktic foraminifera samples for core CE18011_VC2 discussed in this study. Calculated sedimentation rates (SR) also shown. Note: age acquired at 41 cm taken immediately above determined hiatus.

Lab ID	Depth	Frac. of mod.	^{14}C age		Calibrated age (cal. ka BP)			Bayesian modelled age (ka BP)			SR
	(cm)	pMC	[a]	±	μ-2σ	μ+2σ	Median	μ-2σ	μ+2σ	Median	[cm/ka]
D-AMS 038053	7	32.55	9016	37	9.5	10.1	9.8	8.7	9.3	9	5.7
D-AMS 038051	17	31.86	9188	45	9.7	10.3	10	9.7	10.1	9.9	12.1
D-AMS 039751	26	27.13	10479	41	11.4	12.2	11.8	11.2	11.9	11.6	6.2
D-AMS 038052	33	17.32	14084	51	16	16.8	16.4	15.3	16	15.7	1.9
D-AMS 039276	41	15.26	15102	63	17.3	18.1	17.7	16.7	17.5	17.1	6
D-AMS 034705	48	3.802	26265	114	29.4	30.2	29.8	28.7	29.8	29.3	4.1
D-AMS 034765	59	2.517	29578	252	32.8	34.1	33.4	31.9	33.6	32.8	4.3

2.4.2.1 Age Model Development

The age model was clipped at the oldest and youngest dated boundaries. However, estimates determined by the model past the limits of these ages are visible in Fig. 10a and Fig. 11. The age model (Fig. 10a) shows that the constrained section of the core spans an interval of about 9–32.8 ka BP, with an unconformity present from 27.3 to 17.2 ka BP (at 42 cmbsf). Outside the limits of the age model, the core spans from 37.6–7.6 ka BP. Consequently, Unit A spans from older than 32.8 ka BP to 29.3 ka BP, Unit B spans from 29.3–27.3 ka BP, Unit C spans from 17.2–10.1 ka BP and Unit D spans from 10.1 ka BP to younger than 9 ka BP.

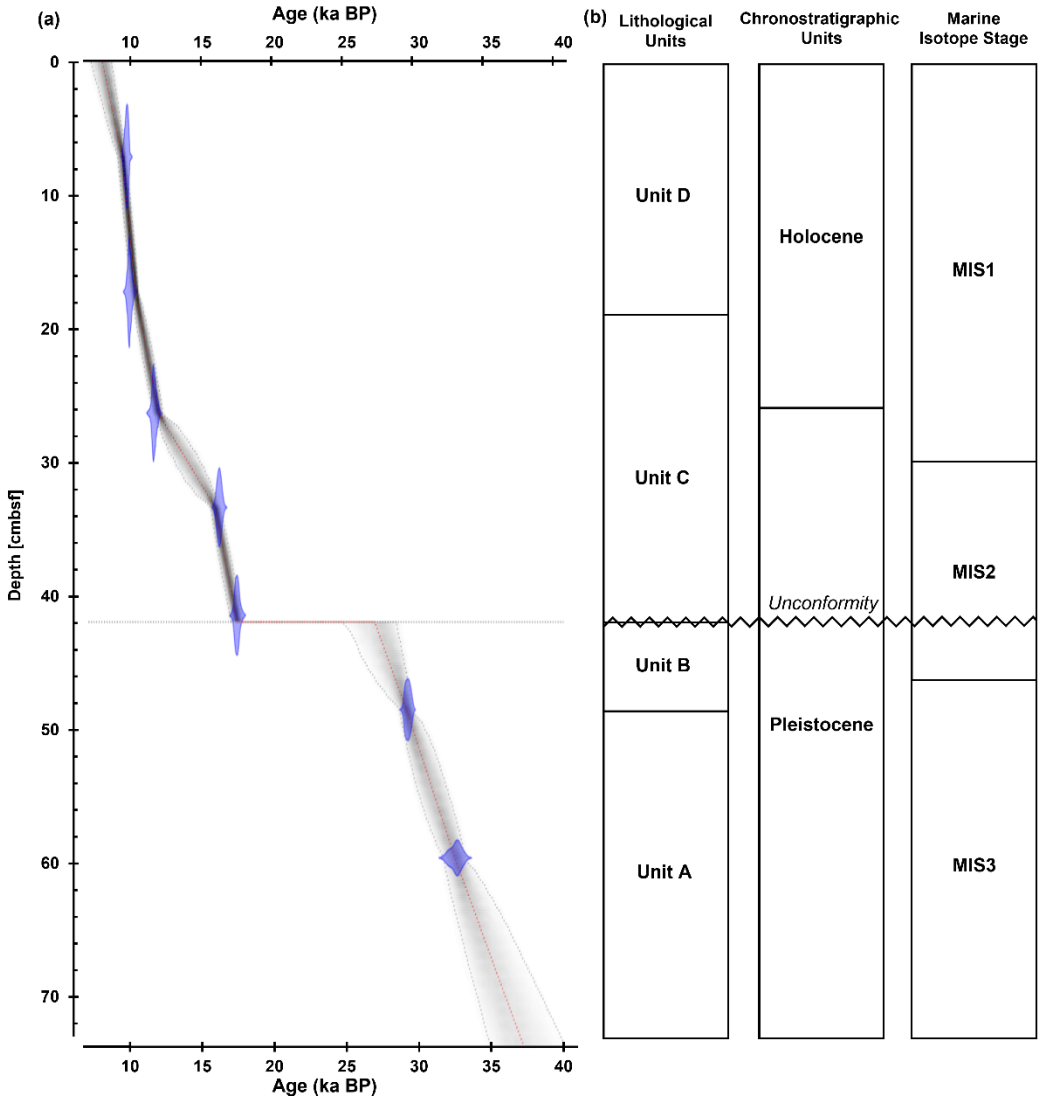


Figure 10: (a) Age model established with RBacon using 7 AMS ^{14}C dates. (b) Subsequent classification of core CE18011_VC2 versus depth.

2.4.3 Sedimentation rates and ice rafted debris events

Maximum sedimentation rates reach 6 cm/ka during the Late Pleistocene, which increases to 12.1 cm/ka during the Holocene (Table 2). The CT imagery of core CE18011_VC2 shows the prevalence of large and varying concentrations of IRD clasts (Fig. 8f). During the Late Pleistocene, IRD flux shows that IRD is deposited in events (Fig. 11c). Below the oldest dated interval at 32.8 ka BP, IRD decreases steadily from 37.6–34.1 ka BP from 113–48 cm^{-2} yr^{-1}. Following this, a brief peak IRD flux occurs at 33.7 ka BP (50 cm^{-2} yr^{-1}). IRD flux decreases to 25 cm^{-2} yr^{-1} until 32.9 ka BP. Within the constrained section of the core, the oldest flux peak event occurs at 32.5 ka

BP (40 cm^{-2} yr^{-1}). Two peaks additional are centred 31.4 ka BP (50 cm^{-2} yr^{-1}) and 30.7 (48 cm^{-2} yr^{-1}). IRD flux decreases rapidly to 6 cm^{-2} yr^{-1} until 29 ka BP. Following this low occurrence of IRD flux, it then increases rapidly to 34 cm^{-2} yr^{-1} until the base of the unconformity at 27.3 ka BP (Fig. 11). At the top of the unconformity, a peak in IRD flux is visible at 16.9 ka BP (65 cm^{-2} yr^{-1}). IRD flux decreases steadily to 30 cm^{-2} yr^{-1} until 15.7 ka BP. The period of low IRD flux (maximum flux rates - 17 cm^{-2} yr^{-1}; minimum flux rates 9 cm^{-2} yr^{-1}) correlates with low sedimentation between 15.7–11.6 ka BP (1.9 cm/ka; see Table 1 and Fig. 11). During the Holocene, several minor IRD flux peaks are visible centred at 11.2 ka BP (46 cm^{-2} yr^{-1}), 10.7 ka BP (43 cm^{-2} yr^{-1}) and 10.3 ka BP (38 cm^{-2} yr^{-1}). Between 9.9 and 9 ka BP, sedimentation rates peak (12.1 cm/ka). Contemporaneous with this, three IRD flux peaks are visible at 9.9 ka BP (60 cm^{-2} yr^{-1}), 9.6 ka BP (56 cm^{-2} yr^{-1}) and at 9.0 ka BP (42 cm^{-2} yr^{-1}). IRD flux then remains low until the top of the core (maximum flux rates - 17 cm^{-2} yr^{-1}; minimum flux rates 8 cm^{-2} yr^{-1}). Visual inspection of sediment grains >150 μm from these pulses show diagnostic features of glacial crushing (Fig. 9).

2.5 Discussion

This study is the first to utilize the *Holland 1 ROV* vibrocoring rig, allowing users to precisely target coring sites, through the use of front facing cameras and sonar on the ROV. For this study, it was essential to core through surface sediments which had not undergone scouring, and to uncover the cause of the ploughmarks identified in the backscatter data. Core records elsewhere on the PB (<50 km north of the site), show an enhancement of currents correlating with interstadial warming during MIS2 (Øvrebø et al., 2006), that resulted in the winnowing of older stadial deposits. Novel ROV-assisted vibrocoring techniques used in this allowed sampling of CE180011_VC2 from one of the least hydrologically inactive areas of the wPB and adjacent canyon setting (average speeds of 0.1 m s^{-1}; Lim et al. 2020). This area is considered too far from local control of bathymetric features (i.e. carbonate mounds and the submarine canyon) that intensify currents in the region, and instead is influenced by regional processes such as the northerly flowing ENAW (Lim et al., 2020b). Moreover, coring in sandy substrate with traditional coring units (i.e. gravity and piston coring) can prove difficult, a testament of which is outlined through previous coring missions in this part of the NE Atlantic (e.g. Wheeler et al., 2014).

The collected core was subjected a non-destructive CT-based IRD analysis that allows the assessment of IRD >1 mm every 0.02 cm with their number/volume, their relative volume and their size distribution (Fig. 8d–f). The traditional method of IRD quantification (“picking”) may miss crucial boundaries between IRD pulses. The implementation of CT based IRD detection and quantification can further constrain these time periods and synchronise NE Atlantic IRD reconstructions. Additionally, grain-size analysis and end-member modelling analysis reveal how hydrodynamics on the wPB were influenced by BIIS (de)glaciation.

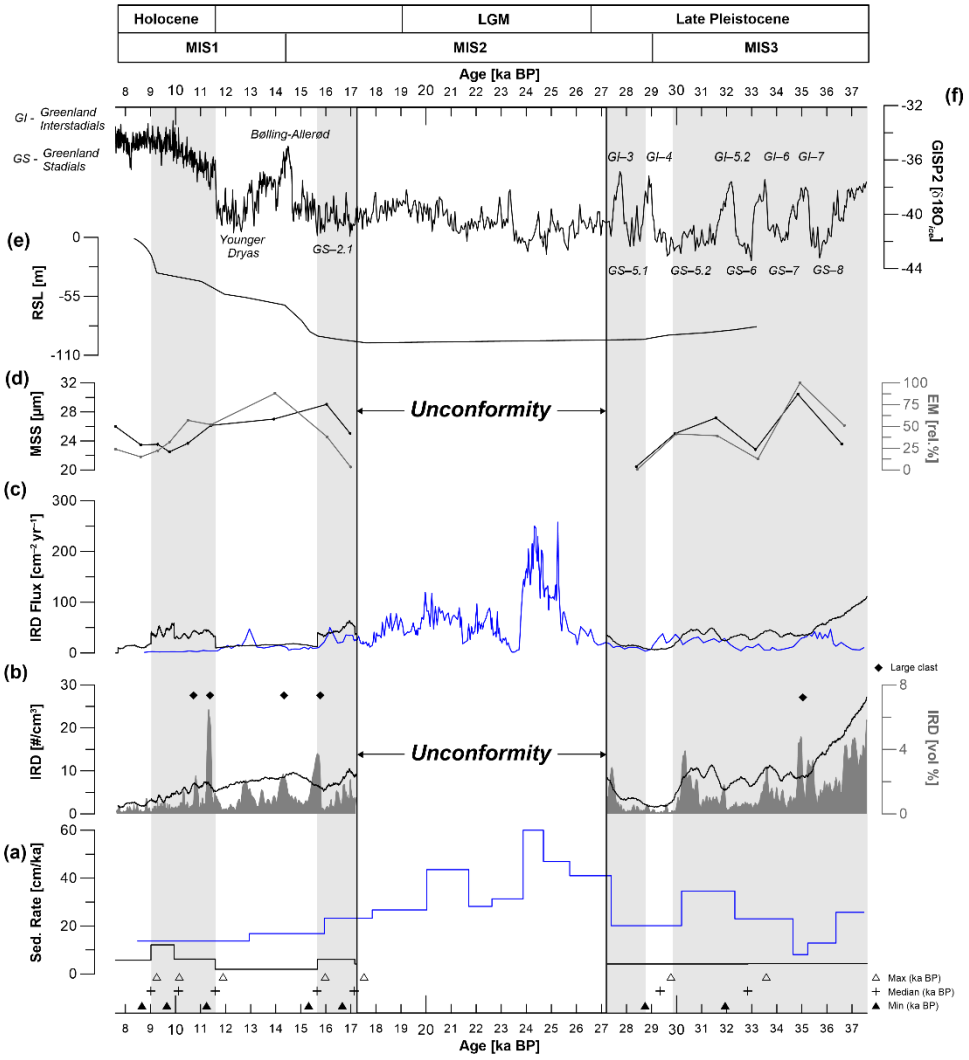


Figure 11: Compilation of multi-proxy data obtained from core VC18011_VC2 (in black and grey) plotted against time. Includes an unconformity from 27.3–17.2 ka BP. Periods containing high IRD fluxes are shown as shaded grey areas. Modelled ages (in kiloyears BP) at bottom are annotated by black cross (median), white triangles (maximum) and black triangles (minimum). The data of Peck et al. 2006 from the Porcupine Seabight is also shown (in blue). To exclude any potential offsets, the data set was recalibrated using the MARINE20 calibration curve (Heaton et al., 2020). (a) sedimentation rates; (b) IRD volume percentage (solid black line), IRD clasts per cubic centimetre (light grey filled in); (c) IRD flux; (d) Mean sortable silt (SS - black) and relative percentage of end members (grey), whereby 0% represents an end member composed entirely of EMa and 100% represents an end member composed of EMb; (e) Relative sea-level estimates in metres were calculated from models composed by (Brooks et al., 2008) and was simulated by the glacial rebound model of Bradley et al. (2011) and applied to the area (personal communication Robin Edwards, Trinity College Dublin, 2021); (f) GISP Greenland Ice Core $\delta^{18}O$ values.

2.5.1 Sedimentology

CT scanning reveals that core CE18011_VC2 is composed of four broad lithostratigraphic units based on the presence of IRD (Fig. 8). Grain-size analysis of the core shows that it is composed of either poorly sorted sandy silts or silty sands (Fig. 8l). Mean sortable silt values and calculated settling velocities show that the wPB maintained high current speeds throughout the Late Pleistocene and Early Holocene (minimal calculated velocity is 0.23 m s^{-1}; Fig. 8i and 8j). The presented age model suggests that sedimentation rates were higher in the Early Holocene than in the Late Pleistocene (Fig. 11), with the top and bottom sections of the core estimated to be younger than 9 ka BP and older than 32.8 ka BP in age, respectively. The diagnostic feature of this core is its IRD record, which occurs in pulses (Fig. 8e; Fig. 8f). Throughout the core, IRD clast sizes typically range between 5 to 7 mm (Fig. 8f; see data availability). Several sub-cm clasts were also identified during this investigation (Fig. 8e). Finally, an erosive boundary was identified between Units B and C (Fig. 10).

2.5.1.1 What are the causes of the IRD pulses?

Icebergs present an important source of glacial sediment in marine records, which can be transported hundreds of km from the ice margin (Syvitski et al., 1996, deGelleke et al., 2013). An abundance of IRD pulses have been captured throughout core CE18011_VC2 (Fig. 8f) and show depositional similarities with records from other glaciated margins across the NE Atlantic (Peck et al., 2006, Peck et al., 2007, Scourse et al., 2019, Tarlati et al., 2020). Grains identified within these events are overall angular to sub-angular in shape, suggesting this material was abraded by reworking or current transport. Surface microtextures identified on quartz grains (Fig. 9), including conchoidal fracturing, provides evidence for glacially-induced mechanical abrasion, caused by ice transport (e.g. Helland and Holmes, 1997, Mahaney and Kalm, 2000, Mahaney, 2002, Damiani et al., 2006, Eldrett et al., 2007, Cowan et al., 2008, Woronko, 2016, Wu et al., 2020), confirming glacial origins. However, the IRD pulses captured and what they represent, can be difficult to decipher due to a number of regional controls (for instance the rate and trajectory of calving icebergs; ocean and ice temperature; see Scourse *et al*., 2009). Local

controls, including bioturbation and winnowing can also overestimate the amount of IRD in certain sections of a geological core. Additionally, an absence of IRD deposition does not necessarily translate to a period where icebergs were not along the wPB (i.e. within Units C and A; Figure 8e). Furthermore, where IRD *is* present, this does not mean a complete deglaciation occurred (i.e. within units D and B). All these factors play a part in concealing true ice rafting events within the IRD pulses identified within this study. However, integrating our records with IRD records from nearby localities can be used to interpret these signals correctly.

2.5.1.1.1 Pre-Last Glacial Maximum

At least five peaks in IRD clasts/cm^3 and volume% occur prior to the LGM (Fig. 11b). One non-constrained by the age model and are centred at 33.7 ka BP. The remaining four events are constrained and are centred at 32.5, 31.4, 30.7 and 27.3 ka BP (Fig. 11b) are marginally greater to the PS (Fig. 11c). Other IRD depositional records also show this millennial-scale IRD cyclicity starting from 45 ka BP (Knutz et al., 2001, Peck et al., 2007, Scourse et al., 2009a). Several authors attributed these cycles to Dansgaard-Oeschger cycles (Knutz et al., 2001, Wilson and Austin, 2002a, Wilson et al., 2002, Peck et al., 2006, Scourse et al., 2009a, Haapaniemi et al., 2010) that occur on a periodicity of roughly 1.5 ka (Schulz, 2002). This atmospheric warming could be a key function in the calving of icebergs during this time, and result in IRD deposition along the Irish margin, including the wPB. Observational data suggests that these icebergs originated largely from the Malin Sea Ice Stream but may also have a minor contribution from the Irish Sea and Donegal Bay Ice Streams (Benetti et al., 2021; see also Purcell, 2018), controlled by the bifurcation between the sub-polar and subtropical gyres (Purcell, 2018) coupled with the millennial meridional migration of the North Atlantic Polar Front (Scourse *et al*., 2009). In contrast, recent studies show that the Galway-Porcupine Lobe (see Fig. 7a) was a major drainage pathway for icebergs (Callard et al., 2020, Ó Cofaigh et al., 2021) and thus, may be dominant source of IRD to the wPB. However, no evidence has been found that icebergs from this sector followed a dominant steam (i.e. the Galway-Porcupine Ice Steam; see Wilton et al.,

2021). As such, our records would be well suited to a future provenance study to identify the source(s) of IRD through time.

2.5.1.1.2 Post-Last Glacial Maximum

Sedimentation resumes above the unconformity occurs following a 10.1 kyr long hiatus (27.3–17.2 ka BP). Fluxes in IRD are observed between 17 and 15.7 ka BP (peaking at 16.9 ka BP) and are again marginally higher when compared to the PS during this time. Simultaneous IRD peaks have also been observed in the Rockall Trough (16.9 ka BP; see Tarlati et al. (2020) and as far afield as the Bay of Biscay (16.7 ka BP; see Toucanne et al., (2015). Offsets of a few hundred years between the sites could be due to differences in proximity to the BIIS combined with uncertainties in the age models and calibration curves used (i.e. MARINE20 curve; see Heaton et al., 2020).

Following this event, IRD flux remains low between 15.7–11.6 ka BP during the Bølling–Allerød interval, despite IRD abundances remaining relatively high (Fig. 11b and 5c). During this time, sedimentation rates are low (1.9 cm/ka) perhaps suggesting there may have been a period of non-deposition or strong bottom currents. During intervals between pulses of icebergs, winnowing is likely to have taken place where currents become intensified, concurrent with other parts of the margin (Øvrebø et al., 2006). A large error is attributed to these sediments within the age model (Fig. 10a), supporting this further. Thus, IRD abundances for this period will be greatly overestimated (i.e. Fig. 11b). Icebergs which deposited this material likely sourced from the Celtic Sea Ice Stream (Purcell, 2018).

Holocene IRD fluxes are suspect (Fig. 11c). With the exception of Bond et al. (1997), no other regional records show such events through this period. Thus, ages which constrain this period are erroneously young and are possibly better represented by their maximum calibrated ages that tie the event down to 12.7–9.3 ka BP (Fig. 11; see also Table 1). Considering environmental modifications to these sediments supports this forced readjustment. Lower density pockets of sediment and vertical stratifications were noted throughout Unit D (Fig. 8b and 2c), as well as a minor increase in the standard deviation in matrix sediment density (Fig. 8c and 2h; see also Appendix VII section i) suggests

partial mixing by burrowing organisms (i.e. bioturbation) causing an age reversal. This, alongside low confidence in the topmost dates, lead us to postulated that this IRD event is part of the Younger Dryas (YD) flux event recorded in the PS (Fig. 11c) and the Porcupine Trough (12.9 ka BP; Tarlati et al., 2020), marking the conclusion of large-scale iceberg melting and the ultimate retreat of the BIIS. Crucially, this demonstrates that active calving margins were present on the wPB during the YD.

In summary, NE Atlantic IRD capture the release of icebergs during BIIS deglaciation along with the landward retreat of the ice sheet margin (Clark et al., 2012a), including proximal areas (i.e. the wPB). IRD supply to the wPB occurred more or less synchronously to other NE Atlantic localities throughout this period. High fluxes of IRD punctuating this deposition are interpreted as a function of mixed calving events and the presence of icebergs originated from the Donegal-Malin Ice Stream (see Purcell, 2018) or from the Galway-Porcupine Ice Stream (see Wilton *et al*., 2021). Nearby ploughmarks strike mostly NE-SW (Fig. 7b insert), suggesting longshore transport of icebergs occurred, which would favour the observational based of southerly Donegal-Malin Ice Stream origin (e.g. Purcell, 2018). Equivalently, these ploughmarks could still be caused from Galway-Porcupine icebergs, which may have undergone a sharp change in drift direction towards the wPB (James Scourse, personal communication, 2021).

2.5.1.2 The Impacts of Glaciation on Background Sedimentation

Sediments on the wPB are likely to be from cross slope and upwelling currents related to the PBC (Lim et al., 2020b). The correlation between MSS and SS% (Fig. 10) confirms that the fine fraction of this sediment reflects predominantly hydrodynamics and changes in current strength. Two outliers removed from the correlation were extracted from peak IRD intervals and each showed evidence of extensive glacial crushing. The dominance of EMa (Fig. 11d) and low modes reported in the GSD (Appendix VII) during glacial periods, provide evidence that sediments are locally sourced (and sorted) by relatively weaker bottom currents. Recent paleotidal simulations show that the glaciated NE

Atlantic was megatidal (Scourse et al., 2018). As such, tidal pumping may have a control on bed stresses at >700 water depth, further driving sorting processes (e.g. Woodworth et al., (2019) and references therein) on the wPB.

By comparison, during interglacial and glacial interstadial phases, EMb dominates (Fig. 11d). Surface microtextures on quartz grains (Fig. 9) confirm that each occurrence of this EM has glacial provenance. These sediments also have considerable amounts of fine IRD (i.e. >150μm; Appendix VII section d), highlighting the dominance of iceberg sediment supply to the area during warming phases. The wPB is considerable distance to the end-moraines captured on the PB (e.g. Peters et al., 2015; Peters et al., 2016; Ó Cofaigh et al., 2021), thus plumites are an unlikely source of this material.

Generally, the sections of the core that align with periods of minimised IRD deposition show a preference to EMa and an increase in sedimentation rate. In contrast, IRD pulses are synchronous with the dominance of EMb and low sedimentation rates. These observations are consistent with interpretations from the nearby PB with interglacial sediments consisting of hemipelagic sediments with little to no IRD, whereas glacial sediments are characteristically IRD-rich fine-grained muds and clays. (Øvrebø and Shannon, 2005, Øvrebø et al., 2006).

2.5.2 The impacts of (de)glaciation on hydrodynamics

Mean grain size data of the non-carbonate sortable silt is an established proxy for paleocurrent strength (McCave et al., 1995b). The validity check introduced by McCave & Andrews (2019b) showed that sortable silt on the wPB provides reliable current vigour estimates (although note that Weiser et al. (2021) pointed out that the validity check should be used with caution). As such, changes observed in current velocity are reflected temporally by grain size data.

Assuming peaks in MSS at 35 and 30.5 ka BP correspond to GI–7 and GI–5.2 (Fig. 11d), it is inferred that subsequent calculated current velocities are higher during interstadial/warming periods. These peak current velocities (0.51 and 0.40 ms^{-1}) are high enough to cause erosion and winnowing of clay and silt sizes (e.g. Black et al., 2003; van Ledden et al., 2004; Jacobs et al., 2011),

ultimately overestimating the coarser fraction of the GSD. Present day current speeds measured from this site are generally slow (mean = 0.09 ms^{-1}), however short pulses of strong currents (0.34 ms^{-1}) are also observed (Lim et al., 2020b). Such pulses would also be adequate in removing finer material. GSD from the GI–7 high velocity event shows a positively skewed tri-modal distribution (Fig. 8m), evidence that the removal of finer material has occurred (see McLaren 1981). This GSD was also identified as an outlier when ground truthing the end-members (Appendix V). On the basis of its GSD, the GI–5.2 high velocity event remains valid and should be considered representative of current speeds (0.40 ms^{-1}) during Late Pleistocene interstadial phases. Lower current speeds recorded between these higher velocity events may thus be likely to correspond to stadial phases such as at 36.4 ka BP with GS–8 (0.30 ms^{-1}), 33.1 ka BP with GS–6 (0.29 ms^{-1}) and at 28 ka BP with GS–5.1 (0.23 ms^{-1}). This sluggish nature of glaciated currents can be linked to the deceleration of North Atlantic currents, resulting from the freshwater release from melting ice-sheets (Øvrebø et al., 2006, Stanford et al., 2011, Bigg et al., 2012, Toucanne et al., 2015) and a reduction in current speeds and internal waves and tides between the ENAW and MOW (Manighetti and McCave, 1995b, Manighetti and McCave, 1995a, McCave et al., 1995a, McCave et al., 1995b, Dorschel et al., 2005b).

2.5.3 Explanation of the Hiatus

An erosive boundary was identified in core CE18011_VC2 (Fig. 8c) between lithological Units B and C at 41cmbsf. The age model presented in this study suggests that 10.1 kyr worth of depositional record was missing between 27.3 to 17.2 ka BP (Fig. 11), during which the BIIS underwent several stages of advances and retreat (Peck et al., 2006, Peck et al., 2007, Peters et al., 2015, Peters et al., 2016). The BIIS reached its local maximum extent between 29 and 23 ka (Ó Cofaigh et al., 2012, Peters et al., 2015, Ó Cofaigh et al., 2021). At 27 ka BP, the BIIS advanced in all directions and was as far-reaching as the continental edge (Wilton et al., 2021). Consequently, it must be assumed that following the LGM, areas proximal to the BIIS, such as the wPB, experienced an amplified release of icebergs, ultimately increasing IRD deposition across the margin. Paleotidal modelling show that megatides

influenced the Galway-Porcupine sector during early deglaciation (Scourse *et al*., 2018). This, in combination with a high rate of RSL rise and shallow water depth, may have been sufficient to further transport these icebergs from the north towards the wPB (Ward *et al*., 2020). The wPB would have acted as an obstacle for such southward flowing BIIS glaciers (Sacchetti et al., 2012b), extensively scouring the area. Iceberg ploughmarks identified in the north of the wPB core site (see Fig. 7 insert) are remnants of such icebergs, which ploughed the seabed during glacial sea level low stands (Dorschel et al., 2010). It is postulated that the erosive boundary identified in core CE118011_VC2 was caused by this intensive scouring. Sedimentation resumed following the retreat of the grounded ice on the seafloor, thought to be caused by glacio-isostatically induced high RSL (Ó Cofaigh et al., 2021). Indeed, the nearest modelled RSL for the wPB increases soon after the hiatus (Fig. 11e), supporting this hypothesis. However, as the wPB resides outside the maximum extent of the BIIS (Ó Cofaigh et al., 2012, Peters et al., 2015), the modelled RSL is greatly thus exaggerated, as this area of the margin did not experience isostatic rebound. Elsewhere, RSL from the Slyne Trough during the last glaciation show that sea levels decrease until 15 ka BP and deepen rapidly thereafter (Ó Cofaigh et al., 2021). As such, RSL estimations provided for the wPB should be interpreted with caution. Alternatively, the resumption of sedimentation could relate to the retreat of ice to land and/or could correlate with a thinner ice thickness. Either scenario would prevent further scouring of the wPB after 17.2 ka BP.

2.6 Conclusions

Using novel methods, this study documents the impact of BIIS glaciation on the wPB. ROV vibrocoring increased the accuracy of coring procedures and provided access to a once problematic study site. This method provides a forward for further paleoenvironmental coring missions, as it gives visual confirmation of sample acquisition and provides a brief survey of the sample site. Additionally, the analysis of non-destructive CT-scanning provided detailed sedimentological data every 0.02 cm. As such, this study is the highest resolution BIIS IRD record to date, which clearly describes each phase of IRD deposition in core CE18011_VC2 throughout the Late Pleistocene.

IRD fluxes are in part, concurrent with other NE Atlantic glacial reconstructions from 32.8 ka BP to 9 ka BP, which ultimately captures BIIS (de)glaciation. Using regional studies, this IRD material originated from glaciers that either a) followed the Malin Sea Ice Stream with minor input from the Irish Sea and Donegal Bay Ice Streams (Benetii et al., 2021; Purcell, 2018) or b) from an alternative route originating from the Galway-Porcupine Lobe. A detailed study on the composition of the IRD, would further clarify the provenance of this material. The wPB IRD record also suggests that an active calving margin were present in the region during the YD. Grain size distributions and mean sortable silt size illustrate that during glaciated events, bottom currents decelerate, which agrees with other studies from across the margin. A hiatus was identified from 27.3–17.2 ka BP and is the result of extensive iceberg scouring on the wPB.

Core CE18011_VC2 provides a useful analogue of IRD for areas proximal to the maximum extent of the BIIS. Additionally, results that demonstrate a reduced hydrodynamic regime during glacial events, would be well suited to a temporal assessment of nearby contemporaneous cold-water coral mounds, which likely experienced inhabitable conditions through the Late Pleistocene.

Author Contributions: Luke O'Reilly: Investigation, Conceptualization, Formal analysis, Writing – original draft, Visualization, Data Curation. Aaron Lim: Funding acquisition, Supervision, Investigation, writing – review & editing. Jürgen Titschack: Methodology, writing – review & editing. OJ O'Connor: Methodology. Niamh Moore: Methodology. John Appah: Investigation. Robin Fentimen: Writing – review & editing. Felix Butschek: Investigation, Writing – review & editing. Kimberley Harris: Project administration. Torsten Vennemann: Investigation, Writing – review & editing. Andrew Wheeler: Supervision, Funding acquisition, Writing – review & editing.

2.7 Acknowledgements

The authors would like to thank Mr Paddy O' Driscoll (P & O) for his assistance in developing the vibrocoring unit used in this study. We thank the JQS Editor Colm Ó Cofaigh for his patience and generosity with this extended contribution. The authors would like to express sincere thanks to James

Scourse and an anonymous reviewer for their extremely helpful and thorough comments/suggestions on two earlier versions of the manuscript. All shiptime is funded under the National Development Plan (2019), National Grant-aided Shiptime Programme. Luke O'Reilly is funded by Science Foundation Ireland project "MMMonKey_Pro" ([grant number: 16/IA/4528]) which is co-funded by the Geological Survey Ireland and Marine Institute Ireland. Jürgen Titschack received funding from the Cluster of Excellence "The Ocean Floor—Earth's Uncharted Interface" (Germany's Excellence Strategy—EXC-2077-390741603 of the DFG). Felix Butschek is funded from the European Union's Horizon 2020 research and innovation program under grant agreement No 818123 (iAtlantic). The authors would like to thank the MMMonKey_Pro team members and members of the Marine Geosciences Research Group at UCC, as well as scientific parties, officers, and crew of cruise CE18011. All authors have read and approved the manuscript.

Chapter 3: Environmental Forcing by Submarine Canyons: Evidence Between Two Closely Situated Cold-Water Coral Mounds (West Porcupine Bank and Porcupine Bank Canyon, NE Atlantic).

(Current Status: submitted, *Marine Geology*)

*O'Reilly, Luke[1], Fentimen, Robin[2], Butschek, Felix[1], Titschack, Jürgen[3,4], Lim, Aaron [1,5], Moore, Niamh[6,7], O'Connor, O.J.[6,7], Appah, John[1], Harris, Kimberley[8], Vennemann, Torsten[9] and Wheeler, Andrew J.[1,10]

**Corresponding author*

[1]School of Biological, Earth & Environmental Sciences / Environmental Research Institute, Distillery Fields, North Mall Campus, University College Cork (UCC), Ireland

[2]ENS Lyon (Dept of Earth Sciences, Ecole Normale Superieure de Lyon, 46 allée d'Italie, 69364 Lyon cedex 07)

[3]MARUM – Center for Marine Environmental Sciences, University of Bremen, Bremen, Germany

[4]Senckenberg am Meer, Marine Research Department, Wilhelmshaven, Germany

[5]Green Rebel, Crosshaven Boatyard, Crosshaven, Co. Cork, Ireland

[6]Department of Radiology, Cork University Hospital (CUH), Wilton, Cork, Ireland

[7]Department of Radiology, University College Cork

[8]DP Energy Ireland Ltd, Mill House, Buttevant, P51 TN35, Co. Cork, Ireland

[9]IDYST – Institute of Earth Surface Dynamics, University of Lausanne, Switzerland

[10]Irish Centre for Research in Applied Geosciences - iCRAG / SFI Research Centre for Energy, Climate and Marine - MaREI, University College Cork, Ireland

Abstract

Cold-water corals are regarded as "ecosystem engineers" and build reefs and mounds that are biodiversity hotspot in the deep oceans. These ecosystems are well developed along the Irish continental margin. Within the Porcupine Bank Canyon, NE Atlantic, mounds are found mostly clustered along the canyon lip, with individual disconnected mounds occurring nearby on the

western Porcupine Bank. Benthic foraminifera coupled with 3D segmented computer tomography is used to characterise oceanographic conditions affecting ecosystems in each of these settings. Novel remotely operated vehicle-mounted vibrocoring was utilized to acquire a core from two closely situated coral mound summits with varying proximity to the Porcupine Bank Canyon. Lithological, computed tomography and particle size core logs along with age models from 9 radiocarbon dates reveal the local cold-water coral development pattern. Benthic foraminiferal assemblages were examined to reconstruct past environmental conditions, extending the current understanding of these communities in the NE Atlantic. Regional climatic shifts caused changes to coral mound development. Additionally, ratios of epifaunal and infaunal benthic foraminifera species show similar adaptations. AMS dating reveals that coral mound growth is higher adjacent to the Porcupine Bank Canyon than more generally on the western Porcupine Bank. Additionally, quantitative data on benthic foraminifera and geochemical data ($\delta^{13}C$) shows that higher organic matter is available closer to the canyon. These data confirm that submarine canyons play a crucial role in influencing macro and micro benthic fauna distributions. Their complex geomorphology creates an enhanced food supply to the directly adjacent areas of the seafloor, creating ecological hotspots in the deep sea. A better understanding of the controls of coral habitats adjacent to submarine canyons is developed, improving future management of these important ecosystems.

3.1 Introduction

Cold-water corals (CWCs) are widespread across the NE Atlantic and occupy a range of geomorphological settings, including open slope continental margins (Roberts et al., 2009, Hebbeln and Samankassou, 2015, Davies et al., 2017, van den Beld et al., 2017), seamounts (Roberts et al., 2008, Sakai et al., 2009, Wienberg et al., 2013, Davies et al., 2015), fjords (Roberts et al., 2009, Titschack et al., 2015) and submarine canyons (Huvenne et al., 2011, Davies et al., 2014, Stewart et al., 2014, van den Beld et al., 2017, Lim et al., 2018b). Through geological time, they can grow to form mounds several kilometres across and exceeding 300 m in height (De Mol et al., 2002, Kenyon et al., 2003, Huvenne et al., 2005, Mienis et al., 2006, Wheeler et al., 2007). These mounds are composed mainly of the framework-building scleractinian corals *Desmophyllum pertusum* (formerly named *Lophelia pertusa*; see Addamo et al., 2016) and *Madrepora oculata*. Coral mound development relies on the interplay between CWC growth and sediment input. The capacity of coral framework to baffle suspended sediment is an essential component of successful mound aggradation, whereby current-suspended sediments become entrapped, stabilizing the biogenic construction (Huvenne et al., 2009a, Thierens et al., 2013, Titschack et al., 2015, Titschack et al., 2016). The accumulation and preservation of CWC framework and associated hemipelagic sediments can provide useful paleo-archives to monitor environmental change, especially in areas where stratigraphic records are lacking due to periods of non-deposition or prolonged erosion (Titschack et al., 2009, Frank et al., 2011, Thierens et al., 2013, Hebbeln et al., 2016). CWC mounds offer a high temporal resolution of intermediate water mass activity (Fink et al., 2012, López Correa et al., 2012, Thierens et al., 2013, Stalder et al., 2014, Hebbeln et al., 2016, Fentimen et al., 2020b). However, CWCs mound aggradation is impacted by climatically driven hiatuses and are thus discontinuous (Dorschel et al., 2005b, Kano et al., 2007, Frank et al., 2009, Thierens et al., 2013, Stalder et al., 2018). As such, CWC mounds provide detailed records across restricted periods.

Submarine canyons are steep-sided valleys that incise continental margins (Shepard, 1981, Pratson et al., 2009, Amblas et al., 2018). Topography and

physical environment control the flow of water through these settings (Hall et al., 2014, Kämpf, 2018), which differs from the continental slope (Genin et al., 1986, Davies et al., 2008). High structural complexity and steep topographies elevate current velocities (Genin et al., 1986), creating stronger internal waves than along the surrounding slopes (Quaresma et al., 2007). These characteristics drive turbulent mixing (Hall et al., 2014, Wilson et al., 2015, Aslam et al., 2018) and sediment resuspension that trigger turbidity flows within the canyon (de Stigter et al., 2007, Arzola et al., 2008, Hall et al., 2017, Amblas et al., 2018, Aslam et al., 2018). Subsequently, this provides the mechanism for shelf-slope particulate exchange (Quaresma et al., 2007, Arzola et al., 2008, García et al., 2008, Allen and de Madron, 2009, Huvenne and Davies, 2014, Puig et al., 2014, Amaro et al., 2016, Fernandez-Arcaya et al., 2017, Saldías and Allen, 2020). Increased particulate organic matter (POM) and the formation of nepheloid layers are associated with this internal wave-driven turbulent mixing (Wilson et al., 2015, Hall et al., 2017, Aslam et al., 2018). These phenomena generate environmental heterogeneity within canyons, providing an ideal setting for enhanced biological diversity (Levin et al., 2001, De Leo et al., 2010, Levin et al., 2010, Schlacher et al., 2010), leading to deep-sea biodiversity hotspots (De Leo et al., 2010).

CWCs are found within numerous submarine canyons along the NE Atlantic margin, forming isolated colonies, small patch reefs several metres across, large reef systems and living as dense aggradations on vertical walls (Roberts et al., 2006, Buhl-Mortensen et al., 2010, Morris et al., 2013, Wheeler et al., 2017, Lim et al., 2018b, Corbera et al., 2019, Price et al., 2019). CWCs occupying the west Porcupine Bank (wPB) and Porcupine Bank Canyon (PBC) have recently received attention. Their present-day distribution is strongly influenced by POM supply, oceanographic and hydrographic processes, seabed terrain (depth and slope) and canyon morphological features (Appah et al., 2020). Strong currents within the PBC are further intensified locally by CWC mounds, suggesting they are critical in delivering food and nutrients to the reefs (Lim et al., 2020b). Despite the considerable body of research into the spatial distribution and controls on CWC habitats within the PBC, their temporal distribution is still poorly resolved. Furthermore, recent evidence

suggests that submarine canyons provide a refuge for CWCs during periods of stress (Wienberg et al., 2018), emphasizing the need to assess this deep-sea setting.

Benthic foraminifera can provide crucial insights into the lifecycle of CWCs (Margreth et al., 2009, Stalder et al., 2014, Spezzaferri et al., 2015, Stalder et al., 2015, Fentimen et al., 2018, Mojtahid et al., 2021). They link lower and higher levels of deep-sea food webs (Lipps and Valentine, 1970, Gooday, 1994, Gooday, 2019). Furthermore, they account for the connection between the biotic and abiotic factors that control CWC habitat distribution (i.e. nature of substrates, ecological demands, an abundance of CWCs, microhabitat availability) and local physio-chemical processes (water mass properties, current speed variability, organic carbon fluxes) that influence foraminifera distributions (Margreth et al., 2009, Smeulders et al., 2014a, Spezzaferri et al., 2015, Mojtahid et al., 2021). The flux of organic matter primarily controls the composition and diversity of benthic foraminiferal communities to the sea floor (see Fentimen et al., 2021 and references therein). Regionally, assessments of recent (0–33 ka) benthic foraminiferal assemblages from CWCs in the Porcupine Seabight (Margreth et al., 2009, Schönfeld et al., 2011, Morigi et al., 2012, Smeulders et al., 2014a, Fentimen et al., 2018, Fentimen et al., 2020b), the Rockall Bank (Morigi et al., 2012), northwest of Scotland (Mojtahid et al., 2021), offshore Norway (Mackensen et al., 1985, Cedhagen, 1994, Freiwald and Schönfeld, 1996, Spezzaferri et al., 2013, Stalder et al., 2014) and the Alboran Sea (Margreth et al., 2011, Stalder et al., 2015, Stalder et al., 2018, Fentimen et al., 2020a) have been carried out. These studies, however, fail to encompass the variability of mound aggradation at a local scale. Often, analysed cores are located relatively far apart across the study site. This may result in local-scale findings interpreted as regional-scale processes. Moreover, it may lead to relatively oversimplified interpretations of mound development processes through time. Furthermore, they are typically acquired using vessel-deployed coring instruments with little ground control on seabed conditions at great water depths.

Therefore, the main aims of this study are to identify the environmental controls on CWC mound development in the wPB and PBC using reliable

sampling techniques. BFAs have not been used alongside novel proxies such as 3D-segmented CT and associated coral preservation patterns (CPP) (see Titschack et al., 2015, Wang et al., 2019) in any study of CWC mounds so far. Doing so can identify the environmental conditions that determine CPP type and thus mound development (Rüggeberg et al., 2007, Margreth et al., 2009, Margreth et al., 2011, Schönfeld et al., 2011, Fink et al., 2012, Stalder et al., 2014, Stalder et al., 2015, Fentimen et al., 2018, Fentimen et al., 2020a). Consequently, this enables a precise examination of local mound development variability. For this purpose, novel Remotely Operated Vehicle (ROV) vibrocores were collected from the mound summits of two sites of different proximity to the canyon to assess their development and environmental controls throughout the Early Holocene/Middle Holocene transition.

3.2 Regional Setting

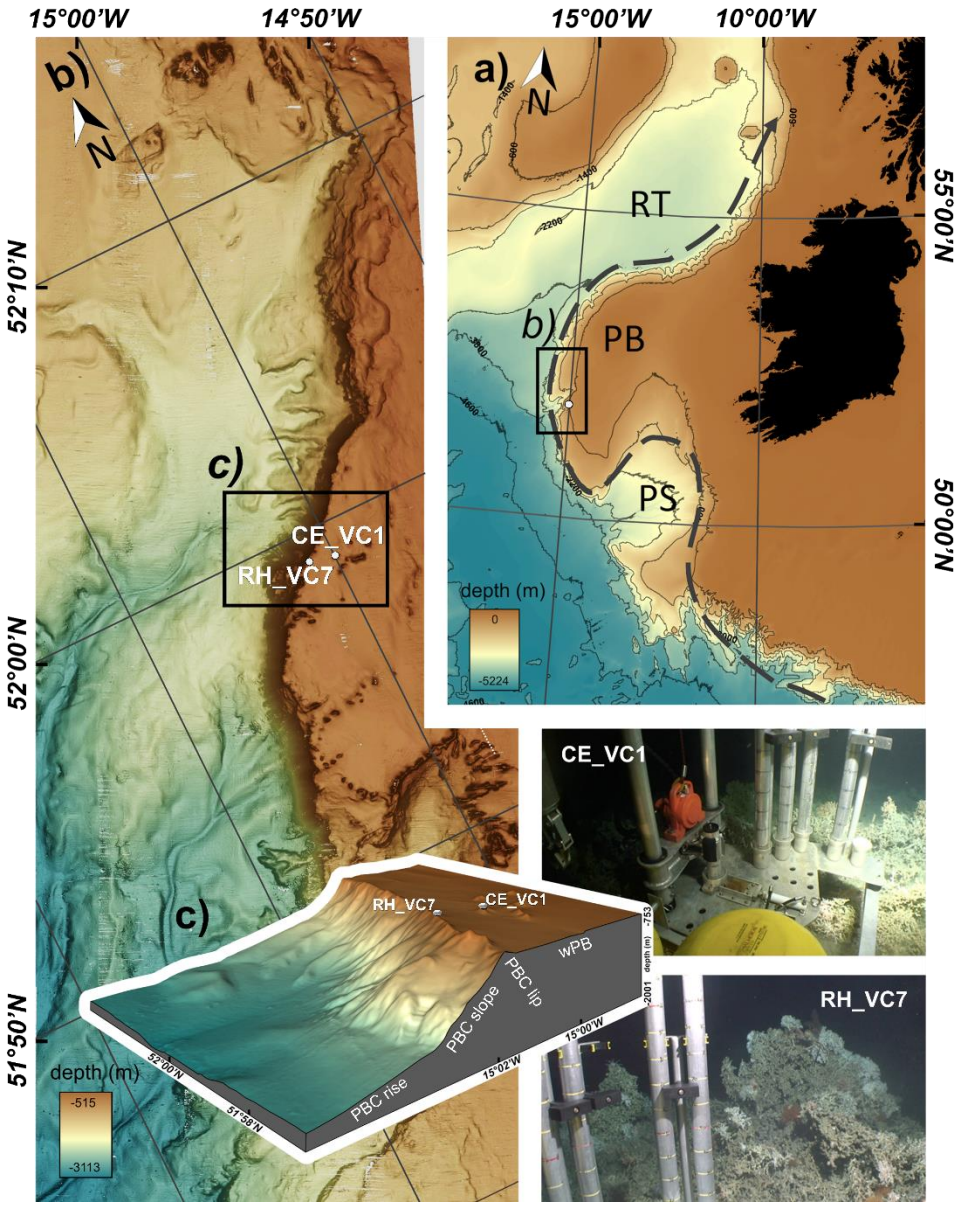


Figure 12: (a) Location of the study site within the western Porcupine Bank (black rectangle) on the Irish continental margin (PB - Porcupine Bank, PS - Porcupine Seabight, RT - Rockall Trough) adapted from O'Reilly et al., 2022 . Grey dashed line showing the flow direction of Eastern North Atlantic Water. (b) Bathymetry map of the upper Porcupine Bank Canyon modified after Lim et al. (2020). (c) Overview of coring sites used in this study. Insets on the bottom right from core site CE_VC1 (top) and RH_VC7 (bottom). Maps created using ArcGIS Desktop v10.6 (www.arcgis.com) and AMIRA version 2018.36 (see Stalling et al., 2005; http://amira.zib.de); data sources – (a) - General Bathymetric Charts of the Oceans (gebco.net); (b and c) – additional bathymetry (10 m resolution) collected during CE18011 research cruise (Lim et al., 2018).

The wPB occupies the westernmost limits of the Porcupine Bank (Fig. 12a; see also 1c). Ice-rafted debris was deposited on the bank since at least 33 ka BP (O'Reilly et al., 2022), potentially providing suitable elevated substrates for CWC larvae to settle (Roberts et al., 2006). Since 9.7 ka, the study site has endured a period of non-deposition and/or erosion (O'Reilly et al., 2022; see also Øvrebø et al., 2005). The incision of the bank by the PBC is tectonically steered through faulting (Shannon, 1991) and trends north-east to south-west (Shannon et al., 2007, Lim et al., 2020ba) with the addition of a smaller southern branch off the main canyon. The eastern canyon wall of the asymmetric canyon is dipping steeply (60 to 70 degrees) and is 800 m in height. At the base of this wall (>2,800 m) exists the widest and deepest sinuous channels in the PBC system (Lim et al., 2020ba). Iceberg plough marks are visible along the upper canyon (Mazzini et al., 2011, O'Reilly et al., 2022).

3.2.1 Hydrography

Eastern North Atlantic Water (ENAW) flows northerly at ~200–700 m water depth (White and Bowyer, 1997, Mazzini et al., 2011). This water mass forms at the Bay of Biscay and is advected northwards along the Porcupine Bank by the poleward Shelf-Edge Current (Ellett and Martin, 1973, Dickson and McCave, 1986, Pollard et al., 1996, White, 2007, Mazzini et al., 2011). The presence of the Porcupine Bank accelerates these contour flowing currents, which flow along the margin (Wheeler et al., 2005b). The high salinity Mediterranean Outflow Water (MOW) occurs at 800–1000 m water depth and underlays the ENAW (White, 2007, Mohn et al., 2014). The denser Labrador Sea Water occurs at 1100 m water depth (Appah et al., 2020).

Bedforms such as current-aligned scours in the lee of coral mounds reflect the long-term net effect of enhanced bottom currents shaping the seafloor (Lim et al., 2020b). *In situ* acoustic doppler current profile measurements show that the wPB is less hydrographically active than along the lip of the PBC (mean current velocity values of 17.3 cm s^{-1} and 24 cm s^{-1}, respectively; (Lim et al., 2020b). Benthic water temperatures vary minimally between the settings (±0.4 °C), with the wPB recording slightly warmer waters (summer mean – 9.6 °C) than along the lip of the PBC (summer mean – 9.2 °C). Furthermore, the

dominant current direction flowing over the wPB is orientated north-east (Lim et al., 2020b). In contrast, the lip of the PBC is characterised by a westerly current direction (Lim et al., 2020b), likely as a result of exchange between open slope and canyon waters.

3.2.2 CWC Distribution

Initial reports of the distribution of CWCs in the PBC are described by Mazzini et al. (2011). They observed that parallel to the lip (or the ridge between the wPB and PBC slope), steep-sided CWC mound features exist. On the eastern part of this canyon, mounds on the lip range from 30 – 50 m in height and extend for approximately 30 km (Lim et al., 2020ba). On the wPB, slightly larger (70 m in height) corals mounds are visible, are not connected, and follow a north-east to south-west distribution. More recently, Lim et al. (2020a) identified the environmental window of CWC growth in the region. They found that current speeds determine living and dead (i.e. rubble) distributions, whereby slower current speeds favour living corals and higher dead coral ratios are concurrent with elevated current speeds (Lim et al., 2020b). High concentrations of resuspended particulate organic matter (POM; 1,330–3,965 μg l^{-1}) are recorded in the study area (Appah et al., 2020), representing an abundance of food availability for benthic communities. Phosphatic rich authigenic deposits also indicate high biological productivity (Mazzini et al., 2011).

3.3. Methods

3.3.1 Vibrocoring

Cores (Table 3) were acquired using the Holland I ROV equipped with a vibrocore rig from the PBC onboard the ILV Granuaile during the CoCoHaCa research cruise (cruise number RH17002; see Wheeler et al., 2017) for core RH17002_VC7 (hereby shortened to RH_VC7) and onboard the RV Celtic Explorer during the CoCoHaCa II research cruise (cruise number CE18011; see Lim et al., 2018b) for core CE18011_VC1 (hereby shortened to CE_VC1). The novel use of the ROV granted the acquisition of precise samples from summits of coral mounds in the wPB and PBC with direct ground-truthing by live video footage following ROV video surveys (Wheeler et al., 2014, Wheeler

et al., 2015, Wheeler et al., 2016, Wheeler et al., 2017, Lim et al., 2018b) (see Fig. 12 inset). Cores acquired were 75 mm in diameter and were stored vertically at 4°C to minimise sediment deformation. Cores RH17002_VC7 and CE18011_VC1 were recovered with lengths of 81 and 130 cm, respectively (Table 3).

Table 3: Summary of vibrocores collected from the west Porcupine Bank (wPB) and Porcupine Bank Canyon (PBC) during the CoCoHaCa I (RH17002) and CoCoHaCa II (CE18011) research cruises.

Core ID	Acquisition Date	Geographical Setting	Lat. [DD]	Long. [DD]	Water Depth [m]	Length [cm]
CE_VC1	05.05.2018	wPB CWC mound summit	51.9829	–14.9995	660	130
RH_VC7	21.06.2017	PBC CWC mound summit	51.9892	–15.0129	651	81

3.3.2 Core analysis

Non-destructive and destructive multiproxy analytical methods were performed on the CWC-bearing cores to assess relevant paleoenvironmental conditions.

3.3.2.1 Computer Tomography

All computed tomography images were acquired using a 64 section multi-slice scanner (GE Healthcare, Discovery CT 750 HD) at Cork University Hospital, Cork, Ireland. Images were acquired at a slice thickness of 0.625mm, using 120 kV, 600 mA and a rotation time of 0.8sec, a pitch of 0.984 and a bony convolution algorithm. Images were reconstructed using Model-based Iterative Reconstruction Veo (GE Healthcare, GE Medical Systems, Waukesha, WI, USA) with pure iterative reconstruction using a resolution preference of 20% (RP20), increasing the spatial resolution by 20%. An overlapping reconstruction was performed with a final voxel size of 0.195 x 0.195 x 0.625 mm. The original data was recalculated to obtain an isotropic voxel size of 0.2 mm.

Core descriptions of coral-bearing cores are based on analysis of computer tomography (CT) scan data (see Appendix I for detailed processing

procedures). CWC preservation patterns (CPP) were defined by quantifying macrofossil clast size and orientation following classification standards introduced by Titschack et al. (2015) and further defined by Wang et al. (2019). Three CPPs (A to C) were identified. CPP A represents coral framework in a living position, characterised by large >-4.7Φ (>2.6 cm) average coral clast and variable orientations of up to 90°. CCP B represents a slightly collapsed coral framework, characterised by moderate clast sizes of -4.7 to -4.4Φ (~2.6–2.1 cm) and orientations <60°. CCP C represents coral rubble, characterised by small average clast sizes smaller than -4.4Φ (~2.1 cm) and orientations of <45° or no obvious orientation. Facies classification and coral content cores CE_VC1 and RH_VC7 can be found in Fig. 13.

Variations to the accumulation rate (AR) and preservation state of CWC clasts can reflect variations in environmental conditions (Titschack et al., 2015, Titschack et al., 2016, Wang et al., 2019). High AR is a function of rapid CWC growth and enhanced sediment supply that becomes entrapped in the framework. Coral framework produces low energy micro-environments in areas of relatively higher hydrodynamics. This rapid burial prevents CWC clasts from biodegradation and physical fragmentation, thus capturing corals in the living position (Titschack et al., 2015). In comparison, in periods of reduced CWC growth, or where dead coral framework remains exposed for a prolonged time, degradation and fragmentation of the coral skeleton may occur, leading to the formation of coral rubble. Using assigned CPP in combination with mound AR can give valuable insights into the environment affecting the temporal development of coral mounds (Titschack et al., 2015, Titschack et al., 2016, Wang et al., 2019).

3.3.2.2 Grain Size Analysis

The cores were frozen at -20 °C and split using an electric circular handsaw, photographed and lithologically described. The matrix sediment composition was determined every 5 cm by weight loss after the chemical dissolution of the organic matter and carbonate material by following the procedures outlined by Pirlet et al. (2011) (see Appendix II). The siliciclastic matrix fraction was then investigated for grain-size variations, using a Malvern Instruments Mastersizer 3000 (MS3000) at University College Cork with a refined standard operating

procedure (see Appendix III). The calculated grain-size distribution (GSD) is an average of five total measurements of a sample. This result was used for further statistical analyses in GRADISTAT (see Blott and Pye, 2001), where median grain size (Dx50), mean grain sizes (MGS), kurtosis and sorting were automatically calculated (the latter two using the Folk and Ward method (Folk and Ward, 1957). The mean sortable silt (MSS) was calculated from the differential volume or weight distribution of grains within the 10–63 µm silt fraction, following McCave and Andrews' (2019) approach. In this study, the MGS and MSS sizes are used to trace changes in near-bottom current strength (McCave et al., 1995). Stronger bottom-currents yield a coarser mean grain size of a non-cohesive silt fraction due to selective deposition and winnowing (McCave et al., 1995b).

3.3.3 AMS radiocarbon measurements

A mixed sampling strategy was applied to CE_VC1 and RH_VC7 due to the narrowness of the vibrocores (75 mm) and varying abundances of dateable material. Where possible, monospecific planktic foraminifera (*Globigerina bulloides*) were sampled. If the sum weight of the material collected was inadequate (i.e. <15 mg), the epibenthic foraminiferal species *Cibicides lobatulus*, *Cibicides refulgens* and *Discanomalina coronata* were picked. Finally, pristine-looking coral pieces (*M. oculata*) were dated if the sum weight of benthic foraminifera was still inadequate. The base of pristine-looking coral pieces was chosen from CCP A (coral in the living position; see Titschack et al., 2015, Wang et al., 2019).

As such, two monospecific planktic foraminifera and four mixed benthic foraminifera samples were taken from the cores by extracting 1 cm^3 of sediment at various depths and used for dating (see Table 2). Foraminifera samples were picked from a >150 µm aliquot size and cleaned in an ultrasonic bath for 180 seconds prior to submission. Three coral pieces were sampled from the cores (see Table 2). Each fragment was cleaned following the methods described by Adkins et al. (2002). Nine measurements were carried out at DirectAMS Laboratories, Washington, USA.

Water column stratification significantly impacts offsets between contemporary planktic and benthic foraminifera radiocarbon ages. The reliability of the acquired dates should thus be taken with caution when interpreting the developed chronology for the cores. To this end, age models were constructed using Paleo Data View (Langner and Mulitza, 2019) to allow applicability and consistency across synthesis. AMS ^{14}C ages were converted to calendar years with the IntCal20 curve (Reimer et al., 2020) and reported as kiloyears before present (ka BP, Present= 1950CE). The age model was developed in a Bayesian framework using BACON (Blaauw and Christen, 2011). The model was tuned to regional benthic foraminifera $\delta^{18}O$ stacks (Lisiecki and Stern, 2016).

3.3.4 Stable-isotope analysis

The planktic species *G. bulloides* was picked from the >150 µm size fraction. It was chosen due to its abundance in the cores, sizeable geographic distribution in the North Atlantic, and its high abundance during different climatic periods (Chapman, 2010). The epibenthic foraminifera *Cibicidoides pachyderma* was picked from the 212-250 µm size fraction to avoid discrepancies in measurements due to ontogenic processes within this species (i.e. Schiebel and Hemleben, 2007). A minimum weight of 0.05 mg of sample was collected for each aliquot. Measurements were made in the Institute of Earth Surface Dynamics at the University of Lausanne on a ThermoFisher Scientific Delta V gas source mass spectrometer using a GasBench (Spötl and Vennemann, 2003). The normalized carbon and oxygen isotope values are expressed as per mil deviation (‰) with respect to the international Vienna Pee Dee Belemnite standard (VPDB). The analytical standard deviation (1σ) for $\delta^{18}O$ and $\delta^{13}C$ was ±0.07 ‰, and ±0.05 ‰ for eight repeated measurements of the in-house standard carbonate (Carrara Marble) analysed in the same sequence as the planktic samples and ±0.05 ‰ and ±0.02 ‰ for the benthic samples, respectively. A correction of -0.3 ‰ was included for *C. pachyderma* (Voelker et al., 2015) and –1 ‰ for *G. bulloides* (Howard Spero, personal communication, 2021) to account for a potential species-specific fractionation effect (vital effects) on the measured ^{13}C isotopic compositions.

3.3.5 Benthic foraminiferal assemblages

Benthic foraminiferal assemblages (BFA) were investigated from 31 samples selected at 5 to 10 cm intervals from the >125 µm fraction. Foraminifera were picked under a light stereomicroscope at the Laboratory of Geology, University of Lyon (France). Taxonomic identification follows Margreth (2010) and Spezzaferri (2015). The subsamples where foraminifera were very abundant were split with an Otto microsplitter, and the whole splits were counted (see Appendix IV). To help with the taxonomical identification Scanning Electron Microscope (SEM) photographs were acquired at the Department of Geosciences, University of Fribourg (Switzerland), using a Thermo Fischer SEM FEIXL30SFEG. A detailed description of the ecological preference of the dominant morphospecies is given in Appendix XIII.

To calculate expected species richness, samples were rarefied to n=200 in R, compensating for sample count differences between each assemblage. In addition, evenness was calculated using Hill's ratio $E_{1,0}$ based on Shannon diversity, whereby high values (approaching 1) indicate more evenness between species (Hill, 1973, Alatalo, 1981). Abundance data were standardized to dry-weight (n g^{-1}) to compensate for variable sub-samples sizes and used to compute a Hellinger distance matrix. Average agglomerative clustering was performed using the unweighted pair-group method using arithmetic averages. Tests of multivariate group dispersions were conducted to prevent the confusion of location and dispersion effects (Anderson 2006) and returned insignificant differences in variance between sites and between species clusters but significant differences in group dispersion between facies. Therefore, only sites and species clusters were considered as group factors along with continuous environmental data and the age model. To test for significance of the selected environmental factors on species assemblages, distance-based redundancy analysis (db-RDA) was implemented using 10,000 permutations as a non-parametric method for multivariate analysis of variance (Legendre and Anderson, 1999, McArdle and Anderson, 2001). These methods were implemented using the packages *vegan* (Oksanen, 2020) and *adespatial* (Dray et al., 2021) in the statistical programming environment R (R Core Team, 2021).

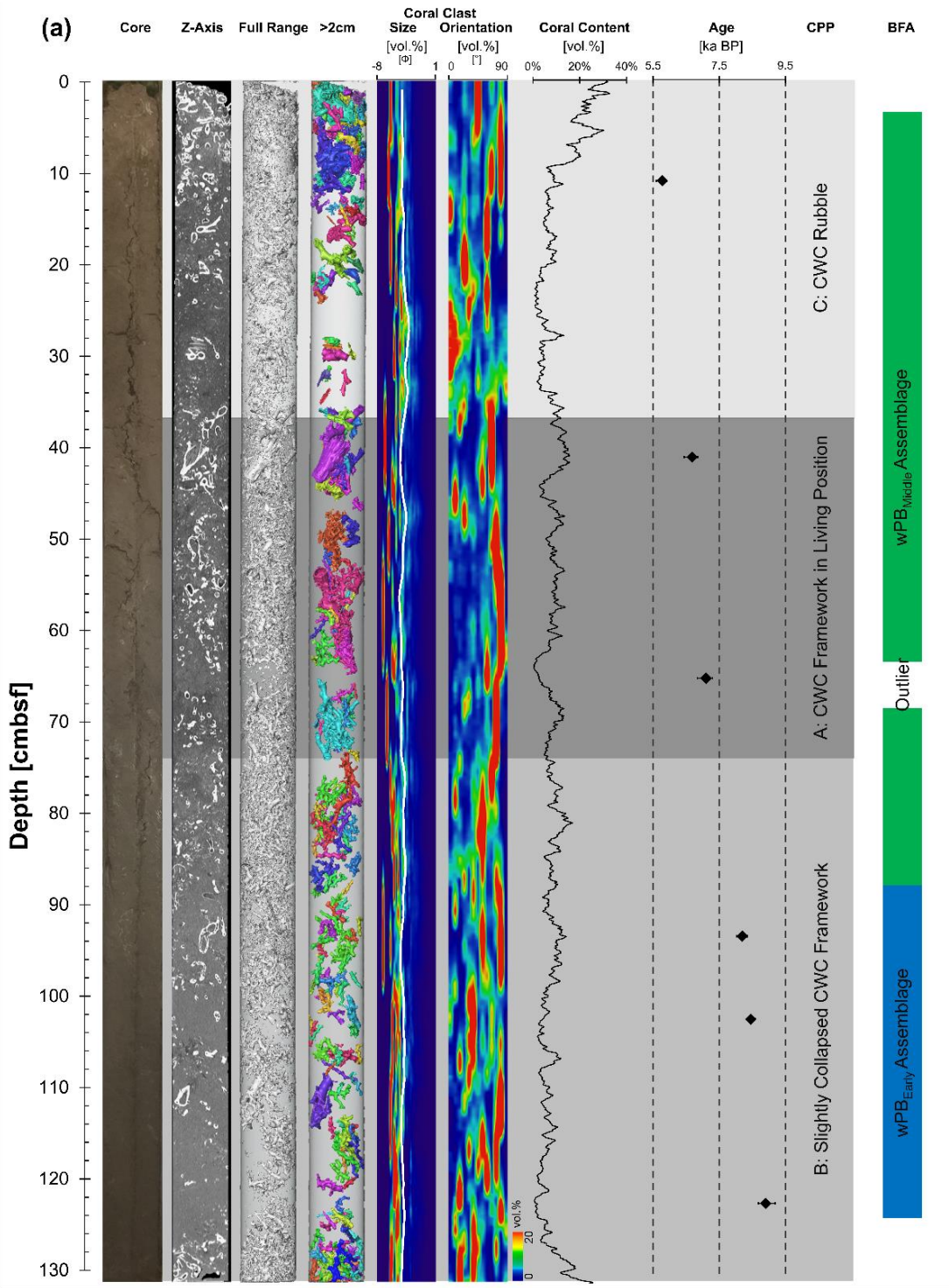
3.4. Results

3.4.1. Core CE_VC1

Core CE_VC1 contains well-preserved CWC fragments (mainly *D. pertusum* and *M. oculata*) embedded in a homogenous matrix of predominately brown sediments (Fig. 13). CPP A (representing coral framework in a living position) occurs between 36–73 cm (Fig. 13). CCP B (representing a slightly collapsed coral framework) occurs between 73–130 cm. Coral rubble (CCP C) occurs between 0–36 cm. MGS recorded in core CE_VC1 are between 7.1 and 15.5 µm (see Appendix VIII). MSS fluctuates between 17.1 and 25.3 µm. Core CE18011_VC1 has relatively low planktic $\delta^{13}C$ (range: -0.48 to 0.03 ‰; see Appendix XI).

3.4.2 Core RH_VC7

Core RH_VC7 contains well-preserved CWC fragments (mainly *D. pertusum* and *M. oculata*) embedded in a homogenous matrix of predominately brown sediments (Fig. 13). CPP A occurs between 0–56 cm (Fig. 13). CCP B occurs between core depths of 56–80cm. MGS recorded in core RH_VC7 are between 8.2 and 12.4 µm (see Appendix VIII). MSS fluctuates between 17.9 and 21.4 µm. Core RH_VC7 has a relatively low planktic $\delta^{13}C$ (range: -0.84 to -0.33 ‰; see Appendix XI).


(a)
Core
Z-Axis
Full Range
>2cm
Coral Clast Size [vol.%] [Φ]
Orientation [vol.%] [°]
Coral Content [vol.%]
Age [ka BP]
CPP
BFA
Depth [cmbsf]
C: CWC Rubble
A: CWC Framework in Living Position
B: Slightly Collapsed CWC Framework
wPB Middle Assemblage
Outlier
wPB Early Assemblage

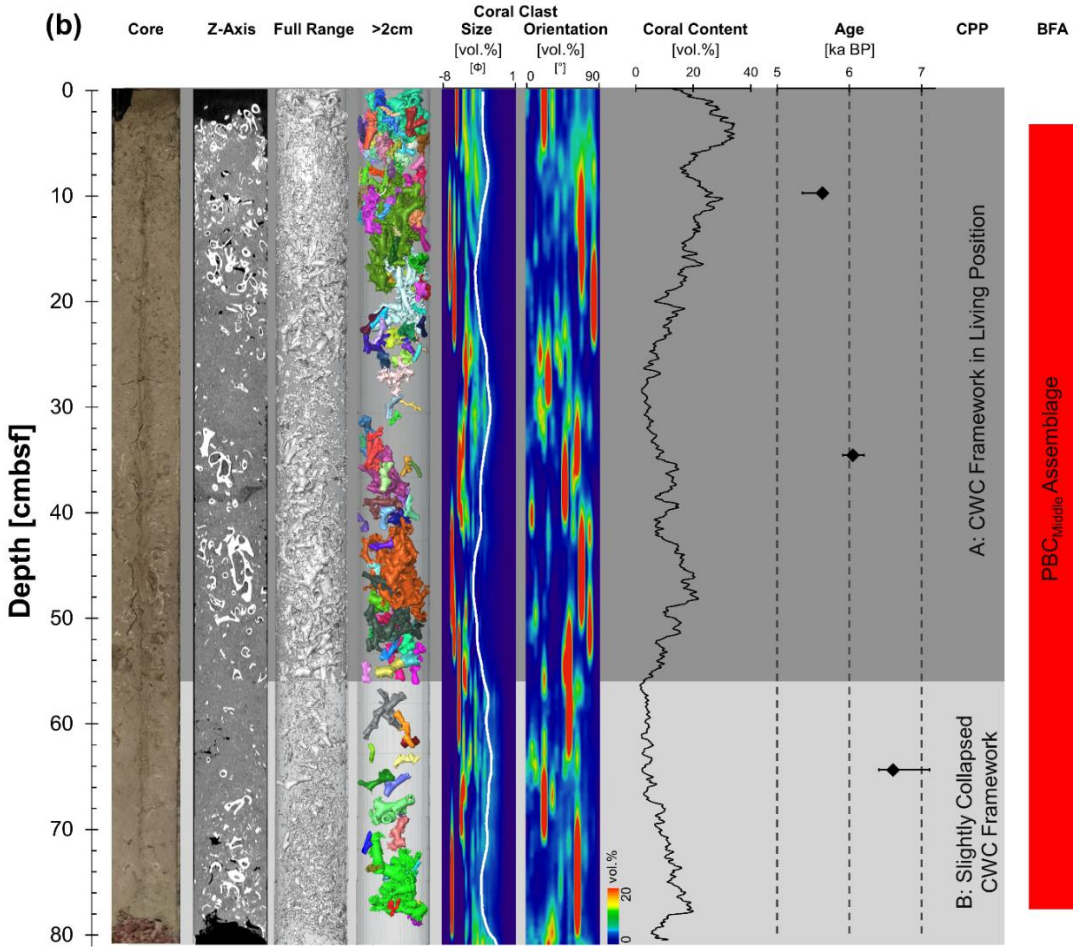


Figure 13: Logs of cores CE_VC1 from the wPB (a) and RH_VC7 from the PBC (b). From left to right: True colour image of the core; orthogonal CT-image of core, with darkness a function of density; core CT 3D image of coral clasts in full-size range; coral clasts larger than >2cm; coral clast size distribution where the white line indicates mean clast size (blue to red colour map denotes % volume of clasts on a scale of 0–20); coral clast orientation quantified coral content based on the CT data; coral content (black); ^{14}C ages were calibrated using IntCal20 (Reimer et al., 2020) with PaleoDataView (Langner and Mulitza, 2019) and determined with Bayesian statistics using the R-package BACON (Blaauw and Christen, 2011). Ages plotted as kilo-annum before present (ka BP) with 2σ calibrated age range (see Table 2); cold-water coral preservation patterns CPPs; A-C; and benthic foraminifera assemblages (BFA).

3.4.3 Chronology and coral mound aggradation rates

Six AMS ^{14}C ages were obtained from core CE_VC1, using planktic foraminifera (at 122 cmbsf), benthic foraminifera (at 102, 93, 41 and 11 cmbsf) and coral pieces (at 65 cmbsf) which range from 8.9 ka BP to 5.8 ka BP (see Table 4). Three ages (8.9 ka BP, 8.5 ka BP and 8.2 ka BP) date back to the early Holocene and three ages (7.1, 6.7 ka BP and 5.8 ka BP) are from the

mid-Holocene (see Table 4). During the early Holocene, the coral mound AR fluctuates between 58.7 and 32.7 cm ka^{-1} (see Table 4). During the mid-Holocene, the AR decreases to 20.4 cm ka^{-1} and increases rapidly to 394.4 cm ka^{1} (see Table 4) and then decreases to 30.4 cm ka^{-1}. The mean AR for CE_VC1 is 47.0 cm ka^{-1}. Three AMS ^{14}C ages were obtained from core RH_VC7 (Table 2) using benthic foraminifera (at 65 cmbsf) and coral pieces (at 35 and 10 cmbsf), which range from 6.6 ka BP to 5.6 ka BP. All dates (6.6 ka BP, 6.1 ka BP and 5.6 ka BP) occur in the mid-Holocene. During this period, the coral mound aggradation rates (AR) fluctuate between 74.4 and 64.6 cm ka^{-1}. The mean AR for RH_VC7 is 32.9 cm ka^{-1}.

Table 4: AMS 14C dates obtained from benthic and planktic foraminifera and CWC fragments collected from cores RH17002_VC7, CE18011_VC1 and CE18011_VC5. Reservoir (res.) ages and error, calibrated (cal.) age determined from Paleo Data View (Langner and Mulitza, 2019). Ages were tuned to regional benthic foraminifera $\delta^{18}O$ stacks (Lisiecki and Stern, 2016). Age model (AM) age was determined using BACON (Blaauw and Christen, 2011). Aggradation rates (AR) are calculated through linear interpolation of acquired ages. Top most and bottom most ARs were calculated using best estimates of the top and bottom cores age using BACON, whereby Bayesian statistics was utilized to interpolate beyond constrained age limits.

Core	Depth [cmbsf]	Lab ID	Dated Material	Conventional Age [ka]		Cal. age [ka BP]					AR
				^{14}C Age	Error	Res. Age	Res. Age Error	μ-2σ	μ+2σ	Median	[cm ka^{-1}]
CE_VC1	11	D-AMS 039278	Mixed benthic foraminifera	5.579	0.03	0.53	0.051	5.602	5.923	5.779	30.4
	41	D-AMS 039277	Mixed benthic foraminifera	6.461	0.03	0.523	0.05	6.437	6.851	6.684	394.4
	65	D-AMS 045772	*M. oculata*	6.529	0.03	0.534	0.05	6.838	7.295	7.101	20.4
	93	D-AMS 037306	Mixed benthic foraminifera	7.9	0.03	0.512	0.051	8.025	8.35	8.198	32.7
	102	D-AMS 037307	Mixed benthic foraminifera	8.16	0.03	0.475	0.05	8.33	8.586	8.455	58.7
	122	D-AMS 034764	*G. bulloides*	8.486	0.04	0.526	0.053	8.689	9.184	8.907	-
RH_VC7	10	D-AMS 043458	*M. oculata*	5.429	0.03	0.505	0.052	5.35	5.687	5.627	64.6
	35	D-AMS 043459	*M. oculata*	5.786	0.03	0.518	0.051	5.911	6.203	6.05	74.4
	65	D-AMS 034770	*G. bulloides*	6.194	0.04	0.52	0.055	6.407	7.113	6.608	-

3.4.3 Benthic foraminifera

A total of 109 benthic foraminiferal taxa were observed across the cores in this study (see Appendix IX). 16 taxa were noted as dominant (i.e. showing relative abundances ≥5% in at least one sample; see Mojtahid et al., 2021; see also Fig. 14 and Appendix X). The ecological preferences of these species can be found in Appendix XIII. 101 taxa were represented in CE_VC1 and 83 in RH_VC1. Twelve dominant species were observed in each core, of which eight were identical in both cores.

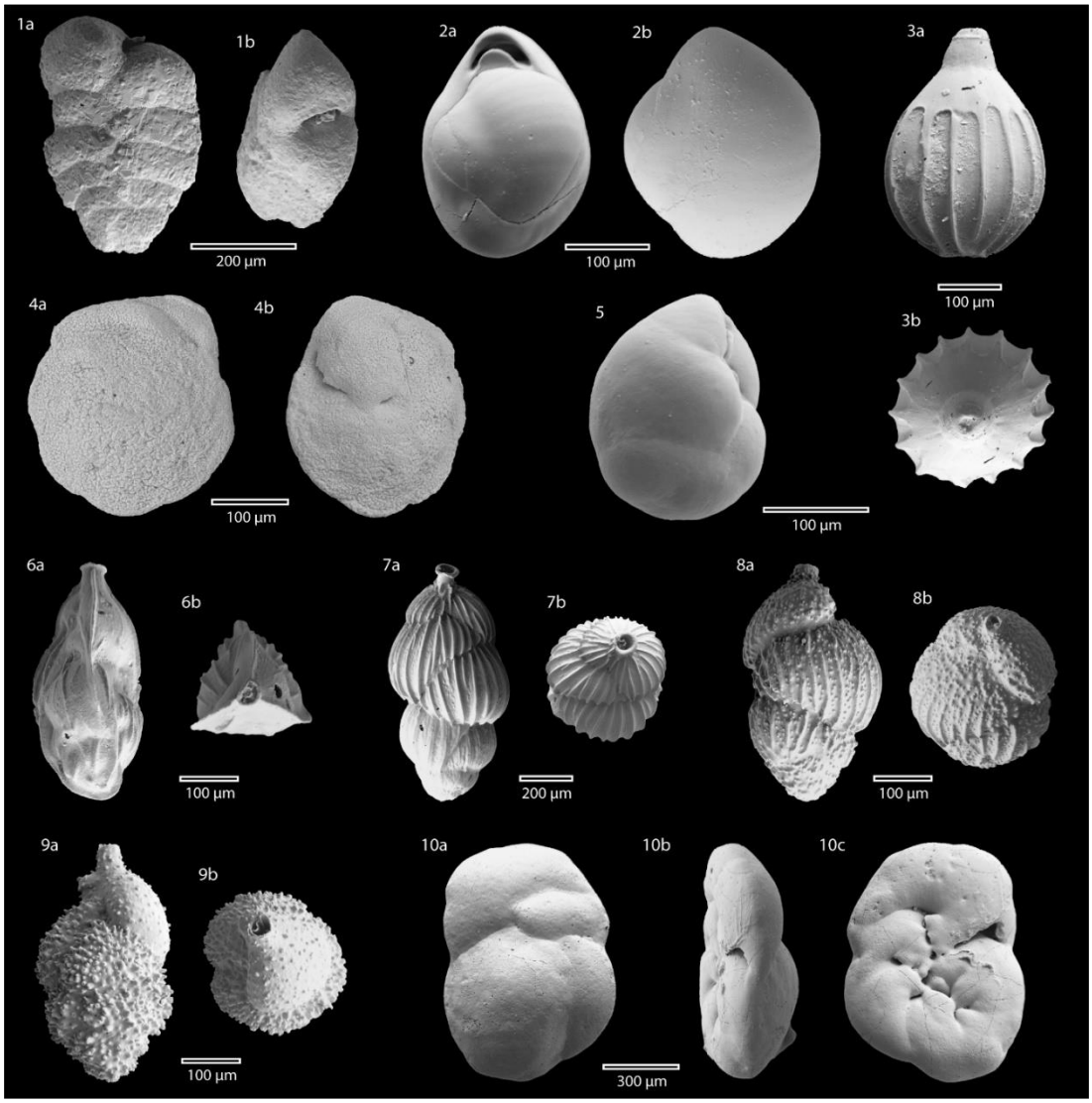


Figure 14: Dominant benthic foraminifera species across this study. Plate 1.1 - *Spiroplectammina sagitulla* (Defrance, 1824) a. side view, b. apertural view; **2**. *Biloculinella globula* (Bomemann, 1855) a. apertural view, b. side view; **3**. *Homalohedra borealis* (Loeblich and Tappan, 1954) a. side view, b. apertural view; **4**. *Nuttallides umbonifera* (Cushman, 1933) a. spiral side; b. umbilical side; **5**. *Globocassidulina subglobosa* (Brady, 1881) side view; **6**. *Trifarina angulosa* (Williamson, 1858) a. lateral view, b. apertural view ; **7**. *Uvigerina mediterranea* (Hofker, 1932) a. lateral view, b. apertural view; **8**. *Uvigerina pygmae* (d'Orbigny, 1826) a. lateral view, b. apertural view; **9**. *Uvigerina auberiana* (d'Orbigny, 1839) a. lateral view, b. apertural view; **10**. *Hyrrokkin sarcophaga* (Cedhagen, 1994) a. spiral side, b. peripheral view, c. umbilical side.

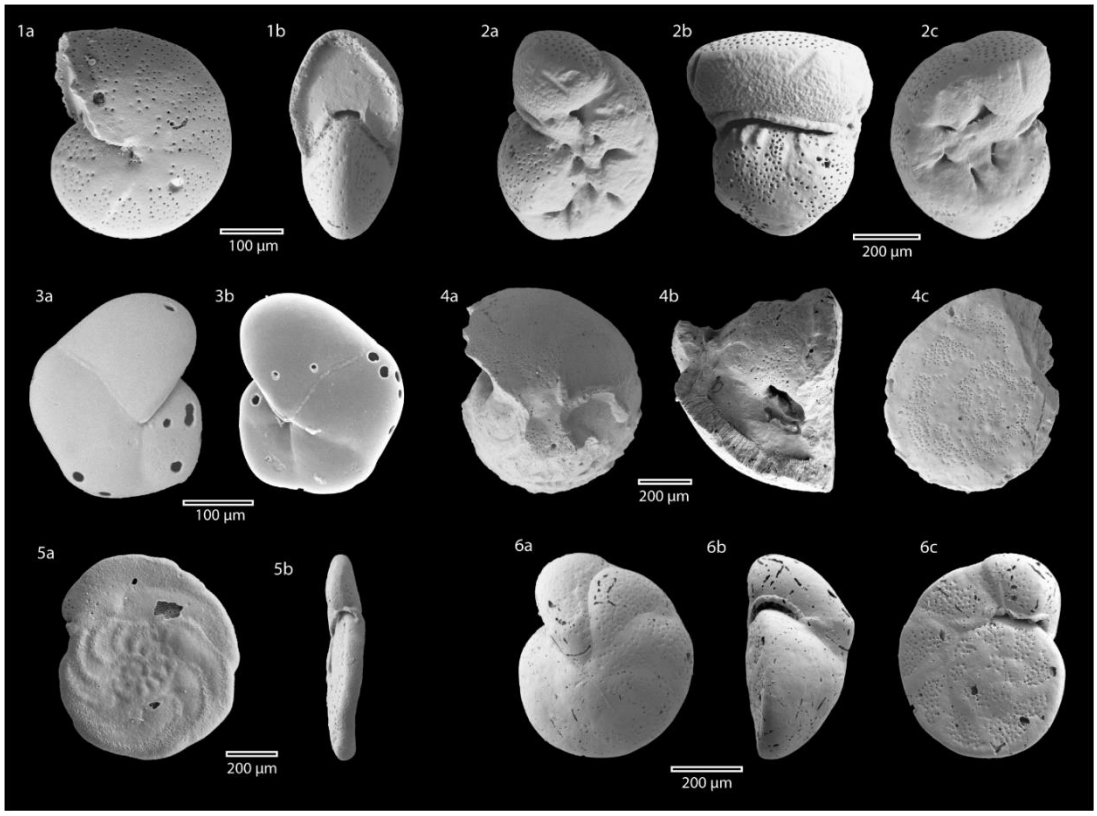


Figure 14 continued: Plate 2. 1. *Melonis barleeanum* (Williamson, 1858) a. side view, b. apertural view; **2**. *Discanomalina coronata* (Parker and Jones, 1865) a. spiral side, b. peripheral view, c. umbilical side; **3**. *Pullenia subcarinata* (d'Orbigny, 1839) a. side view 1, b. side view 2; **4**. *Cibicides refulgens* (Montfort, 1808) a. spiral side, b. peripheral view, c. umbilical side; **5**. *Planulina ariminensis* (d'Orbigny, 1826) a. spiral side, b. peripheral view; **6**. *Cibicides pachyderma* (Rzehak, 1886) a. spiral side, b. peripheral view, c. umbilical side

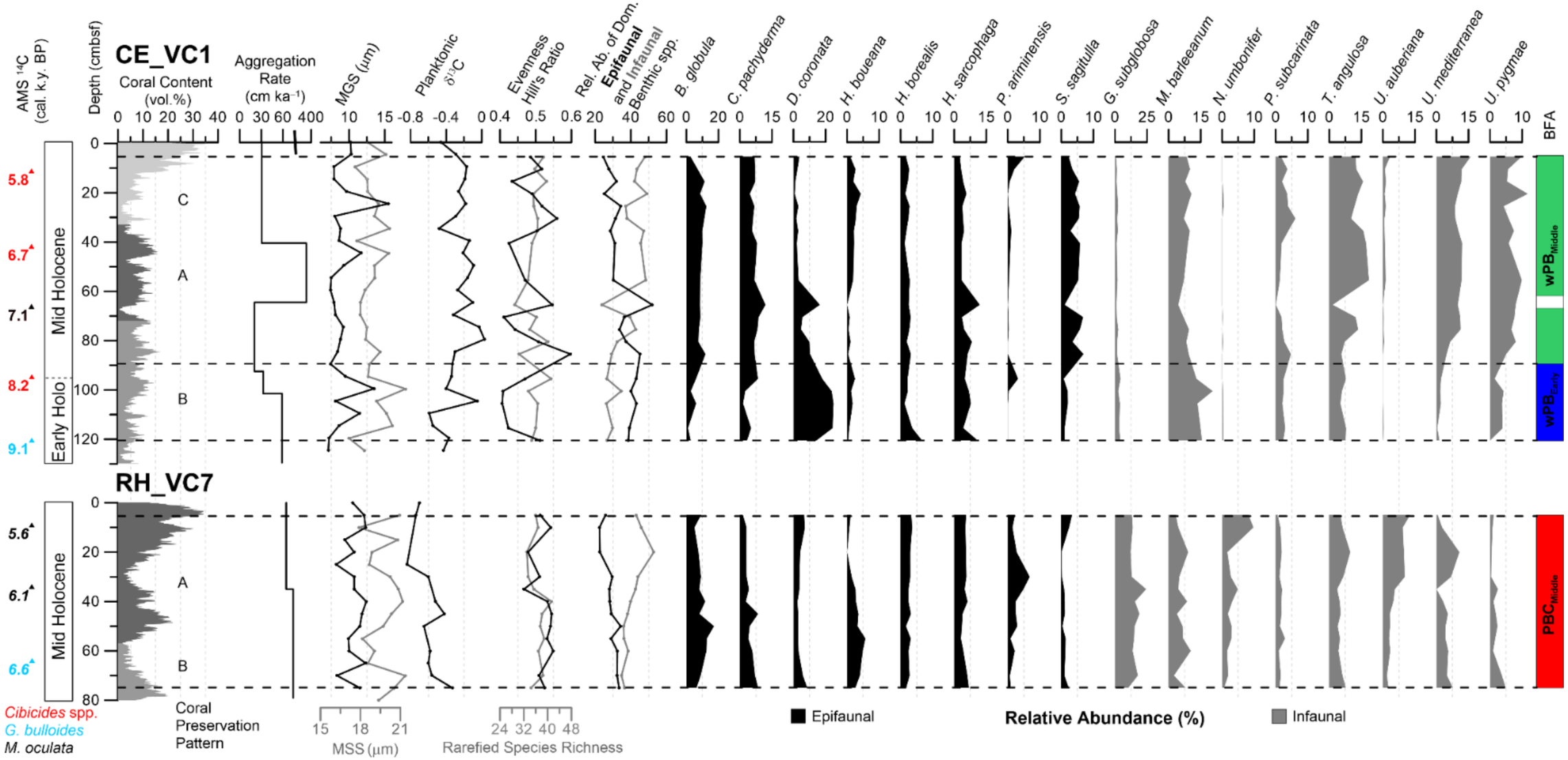


Figure 15: Multiproxy data used in this study for cores CE_VC1 (top) and RH_VC7 (bottom). From left to right: The chronology of the core is based on AMS ^{14}C ages of the planktic foraminifera species *G. bulloides*, the benthic foraminifera genus Cibicides and the cold-water coral species M. oculata (Note: that the boundary between the Early Holocene and Middle Holocene may be tied by the near absence of coral at 68 cmbsf); Distribution of cold-water coral content with associated CPP (see Fig. 13); aggradation rates interpolated from AMS ^{14}C dates; mean grain size (MGS – black) and mean sortable silt size (MSS – grey), planktic $\delta^{13}C$; evenness Hill's Ratio (black) and rarefied species richness (grey) of the entire benthic foraminifera population; relative abundance of dominant benthic foraminifera species (epifaunal – black, infaunal – grey); relative abundance of individual dominant benthic foraminifera species (epifaunal – black, infaunal – grey); and associated benthic foraminifera assemblages (BFA)

Table 5: Percentage relative abundance of dominant benthic foraminifera from each BFAs. Also shown is the mean relative abundance across the whole study.

Species	PBC_{Middle} (%)	wPB_{Middle} (%)	wPB_{Early} (%)	Mean (%)
D. coronata	5.5	5.5	20.7	10.5
M. barleeanum	6.5	8.9	15.4	10.3
T. angulosa	6.1	12.1	6.9	8.4
B. globula	8.8	8.4	4.1	7.1
G. subglobosa	14	1.9	3.6	6.5
C.pachyderma	5.5	7.3	4.9	5.9
H. sarcophaga	5.5	4.7	6.5	5.6
U. mediterranea	5.2	9.9	1.6	5.6
U. pygmae	2.6	6.9	2.5	4
H. borealis	2.4	2.3	2.8	2.5
S. sagitulla	1.5	4.7	1.3	2.5
P. subcarinata	1.4	2.6	2.4	2.2
H. boueana	2.8	1.5	1.5	1.9
U. auberiana	4.8	0.7	0	1.8
P. ariminensis	2	0.9	1.2	1.3
N. umbonifer	2.8	0.1	0.2	1

3.4.3.1 Multivariate analysis and Species Diversity

Multivariate analysis performed on the complete and standardized dataset reveals variations in the relative number of individuals (n g^{-1}) from one sample to another. Listed in Appendix X are species contributing to average dissimilarity/similarity and abundance. According to their associated BFA, information on diversity (rarefied species richness and evenness Hill's ratio) will also be discussed.

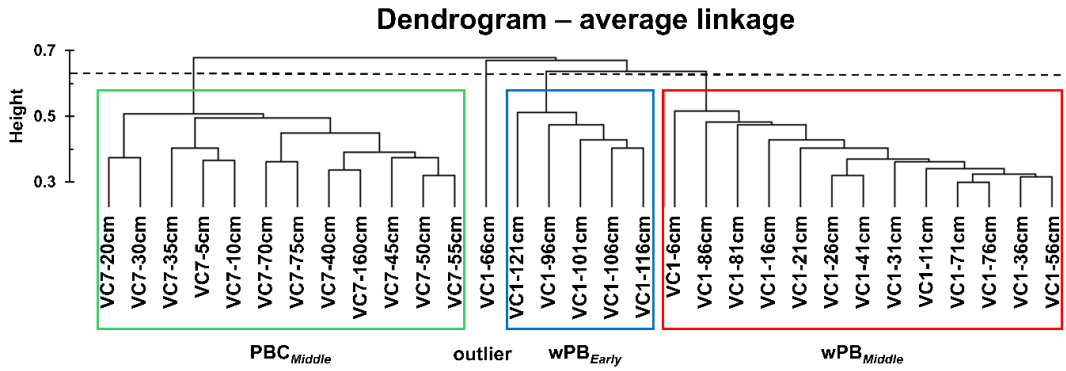


Figure 16: Agglomerative dendrogram based on the Hellinger dissimilarity matrix of the benthic foraminiferal community dataset from cores CE_VC1 and RH_VC1. Cut at a dissimilarity of 0.6, three clusters (PBC_{Middle}, wPB_{Middle} and wPB_{Early}) and an outlier can be recognized.

The agglomerative cluster analysis distinguished 3 clusters (blue, green and red, composed of 5, 12 and 13 samples, respectively; see Fig. 16; see also Fig. 13a and 13b) and an outlier sample at 64% similarity. Each cluster relates to a specific benthic foraminiferal assemblage (BFA). The blue cluster groups all samples in CE_VC1 from 96–121 cmbsf and will be hereafter referred to as the "Early Holocene wPB Assemblage" (abbreviated to wPB_{Early}; see Fig. 16). The green cluster groups samples in CE_VC1 from 6–86 cmbsf, except for 66 cmbsf, representing the outlier. The green cluster will be hereafter referred to as the "Middle Holocene wPB Assemblage" (abbreviated to wPB_{Middle}). The red cluster groups all samples in RH_VC7 and will be hereafter referred to as the "Middle Holocene PBC Assemblage" (abbreviated to PBC_{Middle}). The assemblages are plotted versus depth in Fig. 13a and 13b.

The wPB_{Early} Assemblage is characterised by *Discanomalina coronata* (20.7 relative %; hereby abbreviated to %; Table 3; see also Appendix XI) and *Melonis barleeanum* (15.4 %) Less abundant species are *Trifarina angulosa* (6.9 %), *Hyrrokkin sarcophagi* (6.5 %), *Cibicides pachyderma* (4.9 %), *Biloculinella globula* (4.1 %) and *Globocassidulina subglobosa (*3.6 %). An average of 37 expected species (max – 41, min – 34) is present throughout this assemblage according to rarefied species richness, with an average evenness Hill's ratio $E_{1,0}$=0.45 (max – 0.51, min – 0.41).

The wPB_{Middle} assemblage is characterised by *T. angulosa* (12.1 %; Table 3; see Appendix XI) and *Uvigerina mediterranea* (9.9 %). Less abundant species *are M. barleeanum* (8.9 %), *B. globula* (8.4 %), *C. pachyderma* (7.3 %), *Uvigerina pygmae* (6.9 %), *D. coronata* (5.5 %) and *H. sarcophaga* (4.7 %). An average of 35 expected species (max – 40, min – 30) is present throughout this assemblage according to rarefied species richness, with an average evenness of $E_{1,0}$=0.49 (max – 0.60, min – 0.41).

The PBC_{Mid} assemblage is characterised by *G. subglobosa* (14.0 %; Table 3; see Appendix XI) and *B. globula* (8.8 %). Less abundant species are *M. barleeanum* (6.5 %), *T. angulosa* (6.1 %), *C. pachyderma* (5.5 %), *H. sarcophaga* (5.5 %), *D. coronata* (5.5 %), and *U. mediterranea* (5.2 %). An average of 37 expected species (max – 41, min – 33) is present throughout this assemblage according to rarefied species richness, with an average evenness of $E_{1,0}$=0.52 (max – 0.55, min – 0.47).

3.4.3.2 Distance-based Redundancy Analysis (dbRDA)

Testing environmental variables' significance in shaping foraminiferal community composition through dbRDA showed that site was a highly significant parameter ($p<0.001$, pseudo-$F_{1,25}$=14.29; see Table 4). In addition, site explained the greatest variation in the species composition data (R^2=0.29; see Table 4). The age model was the second-most-important variable, explaining 14% of the variation ($p<0.001$, pseudo-$F_{1,25}$=6.77; see Table 4). Other factors such as mean sediment grain size, mean sortable silt (a proxy for current velocity) and organic content were insignificant. A significant ($p<0.01$) interaction effect between the site and age model was detected. This accounted for 5.7% of the variance (Table 4) and indicated that periodic differences in community change between the two sites occurred. Space-time interaction confounds ecological interpretation (Legendre et al., 2010) and thus, the two sites were tested for temporal effects independently. The age model remained highly significant ($p<0.001$) at both sites with $F_{1,7}$=3.09 and R^2=0.24 for VC7 at the PBC and $F_{1,14}$=7.35 and R^2=0.31 for VC1 at the wPB.

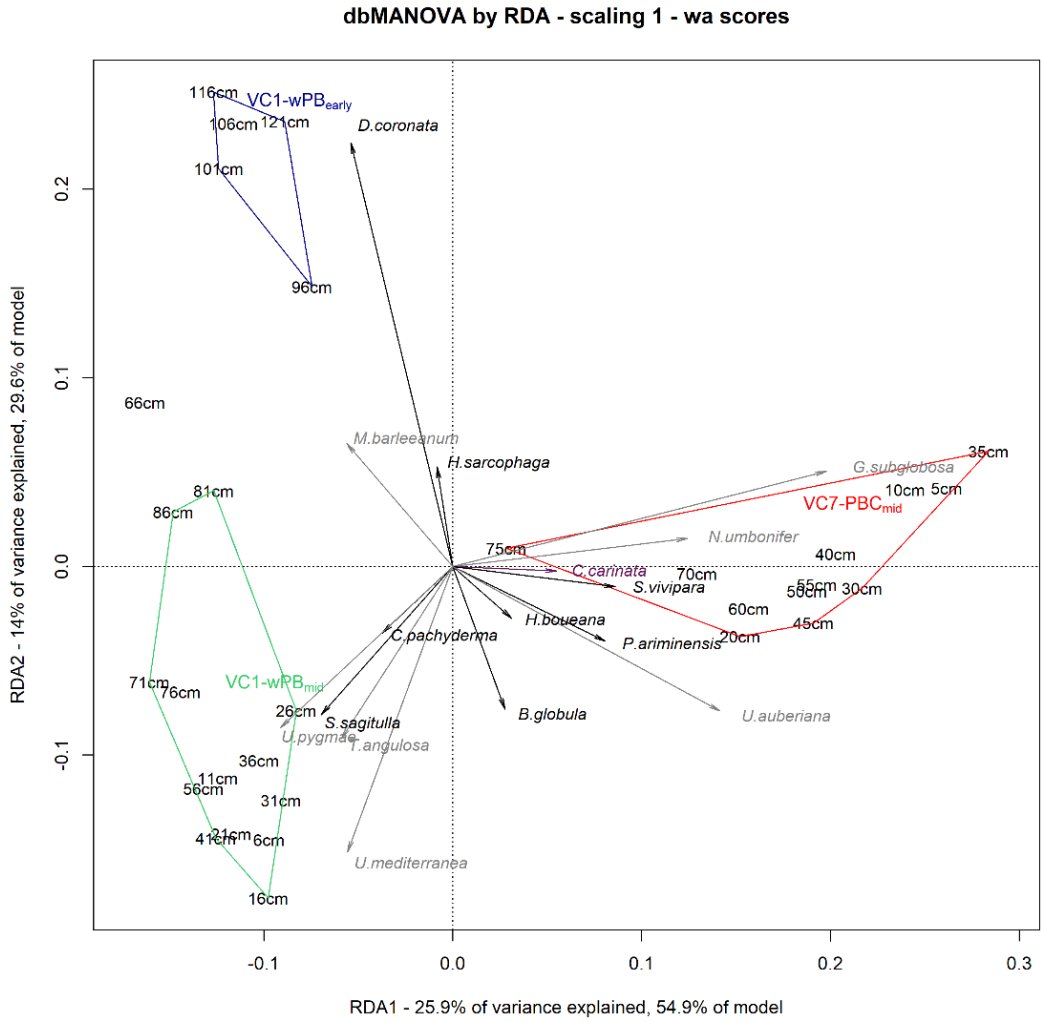


Figure 17: Scaling one triplot representation of the redundancy analysis (RDA) ordination on Hellinger-transformed data constrained by the three groups identified through average agglomerative clustering in the same colour-coding as Figure 16. RDA1-3 are highly significant, RDA 1 separating the wPB assemblages from the PBC, and RDA 2 differentiating between the early and mid-Holocene assemblage at wPB. With an adjusted R^2 value of 0.434, the model explains a large proportion of variation in the data. Grey arrows represent species scores for infaunal foraminifera, and black arrows are for epibenthic species. The purple species has a shallow infaunal to epifaunal lifestyle. Only the species that contribute most to reduced space are shown to avoid over-plotting.

Table 6: Results of the db-RDA test. R^2 represents the proportion of variance in the dependent variable explained by the respective explanatory variables. Pseudo F represents the ratio of total dissimilarities among groups to within group dissimilarity, each divided by their respective degrees of freedom. The p-value reports the proportion of random permutations exceeding the observed pseudo-F statistic, determining the significance codes (*** for highly significant p-values < 0.001 and ** for significance at an α of 0.01).

Explanatory variable	**R^2**	**pseudo-F**	**p-value (>F)**
Site	0.29135	14.1325	0.0001***
Age	0.13812	6.6996	0.0001***
Sortable Silts	0.02515	1.2199	0.2409
Grain size	0.01526	0.7405	0.6603
Organic content	0.01473	0.7144	0.6921
Site-Age Interaction	0. 05682	2.9735	0.0057**

3.5 Discussion

3.5.1 The Controls of Mound Development in the wPB

3.5.1.1. Early Holocene

Mean ARs determined from core CE_VC1 suggest that mound development occurs on the wPB during the early Holocene (mean 40.9 cm ka^{-1}; see Table 2) where rates are comparable to mound development on the Rockall Bank (60 cm kyr-1; see Frank et al., 2009). In comparison, higher ARs are captured in the Norwegian fjords (1500 cm ka^{-1}, see Titschack et al., 2015), suggesting that the wPB provides limited environmental conditions for positive mound development during the Early Holocene. The BFA wPB_{Early} characterises the period and is consistent with other BFAs from CWC mound observations of Morigi et al. (2012) and Smeulders et al. (2014a), noticeably with the abundance of epifaunal species including *B. globula*, *H. sarcophaga* and, in particular, *C. pachyderma* and *D. coronata* (Fig. 15). These species live on elevated substrates (e.g. coral frameworks, coral rubble and dropstones), feeding on food particles transported by strong bottom currents (Hald and Vorren, 1987, Linke and Lutze, 1993, Schönfeld, 1997, Schönfeld, 2002a, Schönfeld, 2002b, Hawkes and Scott, 2005). During the early Holocene, it has been suggested that the northern migration of the polar front impacted the restoration of previous optimal environmental conditions for CWC growth (Frank et al., 2011), despite triggering enhanced surface ocean productivity (Rüggeberg et al., 2007). Furthermore, the return of the MOW to the region resulted in enhanced bottom currents (Dorschel et al., 2005b, Øvrebø et al., 2006, Rüggeberg et al., 2007). These processes are evident along the shelf edge (see Howe et al., 1994, Howe, 1996, Armishaw et al., 2000, Knutz et al., 2001, Knutz et al., 2002a, Knutz et al., 2002b, Øvrebø et al., 2006). High MGS and MSS values were also recorded (13.5 µm and 21.4 µm, respectively; see Fig. 15), further supporting the idea that elevated bottom currents were present in the region. High current speeds likely resulted in the removal of sediment infill, exposing the dead coral framework, ultimately reducing mound formation (see also Dorschel et al., 2009, Titschack et al., 2015). The resulting low AR, combined with high MSS and relative abundance of epifaunal species,

particularly *D. coronata*, are testament to persistently elevated bottom currents during the Early Holocene.

Food from surface waters is in high supply throughout this phase, as indicated by the mean trend in the $\delta^{13}C$ signals (Fig. 15). Furthermore, a synchronous increase in the relative abundance of *M. barleeanum* occurs (Fig. 15). This opportunistic infaunal species is typical of productive waters high in POM (Corliss, 1985, Gooday, 1986, Caralp, 1989, Loubere, 1998, Murray, 2006a, Koho et al., 2008; see Fig. 4) and has been observed in Early Holocene CWC mounds in the Porcupine Seabight (Schönfeld et al., 2011, Morigi et al., 2012, Smeulders et al., 2014a). The re-organization of the regional water column structure, combined with this enrichment in water productivity, likely increased the food supply to the corals during the Holocene (Frank et al., 2011).

3.5.1.2 Early – Middle Holocene Transition

ARs decrease during the early – mid-Holocene transition (20.4 cm ka^{-1}; see Table 2 and Fig. 15), suggesting a slowing of mound development. A steady decrease in MGS and MSS (7.4 and 18.7 μm, respectively) and relative abundances of *D. coronata* is observed (see Fig. 15). Climate simulations show that large parts of the Northern Hemisphere, including the NE Atlantic, were affected by periods of abrupt cooling of 1–3 °C at 8.2 ka (Barber et al., 1999, Thomas et al., 2007, Morrill et al., 2013), caused by the centennial meltwater pulse from the collapse of the Hudson Bay ice saddle (Carlson et al., 2008, Carlson et al., 2009, Gregoire et al., 2012, Wagner et al., 2013, Matero et al., 2017, Appah et al., 2020). Regionally, this short climactic shift has been observed in CWC mound studies from the Porcupine Seabight and Rockall Trough, where mound development slows due to decelerated bottom current speeds (O'Reilly et al., 2004, Frank et al., 2009).

A freshwater discharge of this magnitude during the 8.2 ka climate reversal may have also slowed the northern flowing ENAW along the wPB. This would temporarily slow mound development, consequently promoting the degradation of coral bioclasts. Concurrently, an increase in Hills Ratio and a simultaneous decrease in rarefied species richness (see Fig. 15) suggest that conditions favour fewer benthic foraminifera species. The benthic and

planktonic $\delta^{18}O$ remain relatively constant throughout this phase (Appendix XI), potentially suggesting that water mass temperature and/or salinity on this part of the continental margin remained somewhat unaffected. Therefore, changes to current speed and concurrent reduced food availability are likely the primary driver for slowing mound development. Subsequently, this alteration to the available ecological niche for benthic foraminifera markedly impacted community structure.

3.5.1.3 Mid-Holocene

Between 8.2 and 7.1 ka BP, mound AR on the wPB remains low (20.4 cm ka^{-1}). Mounds from the Rockall Bank and Porcupine Seabight record similar estimations (15 cm kyr-1; see Frank et al., 2009), suggesting a regional reduction in mound AR in the NE Atlantic. The coral clasts throughout this phase become progressively more aligned parallel to the seafloor (i.e. 90°; see Fig. 13a between 93 – 63 cmbsf). Furthermore, low MGS and MSS (average 8.3 and 18.5 µm, respectively; see Appendix VIII) indicate that current speeds on the wPB were sluggish throughout this phase. This conjecture is further supported by a steady reduction in the abundance of *D. coronata* across this time interval. Collectively, these pieces of evidence capture the hydrodynamic forcing on mound development by providing food and suspended sediment. In this case, the coral skeleton is exposed to degradation processes for a longer duration resulting from decelerated currents and thus lower framework supporting sediment infill (Titschack et al., 2015, Titschack et al., 2016, Wang et al., 2019). More exposed to bioerosion, the framework eventually breaks and become deposited on the seafloor. This change in macrohabitat appears to have a knock-on effect on microhabitat. A distinct difference is visible between the early and mid-Holocene foraminiferal assemblage at wPB. The shift from the wPB_{Early} to the wPB_{Middle} Assemblage may constitute a re-structuring of the benthic community after environmental conditions had become unfavourable for numerous rarer species occupying ecosystem niches dependent on more upright coral clasts.

Between 7.1 and 6.7 ka BP, mound development on the wPB becomes more favourable, as indicated by the shift to CPP A (defined as “coral in living position”). Furthermore, MGS and MSS increase slightly to average values of

8.9 and 18.9 µm, respectively (see Appendix VIII). In this instance, the framework generates coral-derived accommodation space (Pomar, 2001, see also Wang et al., 2021), creating a local low energy environment for current-transported sediments to settle (Flügel, 2004, Titschack et al., 2009). When combined with a high sediment supply, this entrapment mechanism results in high mound aggradation (394.4 cm ka^{-1}). This window of favourable mound development is captured by the wPB_{Middle} Assemblage (Fig. 15). This assemblage is abundant with infaunal benthic foraminifera, mostly *M. barleeanum*, *T. angulosa* and *Uvigerina spp.* (Fig. 15). *Uvigerina* spp. represent high fluxes of organic C and labile organic matter (Altenbach et al., 1999, Fontanier et al., 2002, Murray, 2006a). *T. angulosa* is commonly associated with shelf-edge–upper-slope areas under strong bottom currents (Hald and Vorren, 1984, Mackensen et al., 1985, Qvale and Weering, 1985, Austin and Evans, 2000, Schönfeld, 2002a, Mojtahid et al., 2021). The development of this infaunal community infers high food availability, delivered by strong bottom currents. Typically, strong bottom currents result in the removal of framework strengthening hemipelagic material. This ultimately leads to the fragmentation of coral pieces and degradation of the mound. In this case, the coral framework granted sufficient accommodation space (Wang et al., 2021), ensuring that mound development outpaces the rate of erosion. This results in a faster burial of CWC pieces, reducing the likelihood of biodegradation processes. This interplay is widely documented in CWC mound literature (De Mol et al., 2002, de Haas et al., 2009, Dorschel et al., 2009, Mienis et al., 2013). Off northwest Scotland, Mojtahid et al. (2021) determine *T. angulosa* species indicate the influence of the ENAW during the Holocene. However, within their study, high abundances of *T. angulosa* were present when CWC became less frequent. The authors postulate that a retracted Subpolar Gyre affected food delivery to the seafloor. Similar observations have been made by Smeulders et al. (2014a) for the Porcupine Bank and Rockall Bank, whereby *T. angulosa* abundance correlates with coral debris facies. The opposite is observed in the wPB, whereby higher abundances of *T. angulosa* correlate with higher mound AR (Fig. 15). In the likelihood that similar conditions occurred along the Irish continental margin, the nearby PBC system causes a bathymetric discontinuity and thus causes

variations to local water masses by upwelling (Allen et al., 2001). As such, it likely provides the local reefs with rich food supply, promoting mound development.

3.5.2 Proximity to the canyon – an essential driver for coral growth

The topmost 0.4 m of CE_VC1 is contemporaneous with the entirety of RH_VC7 and is constrained between 6.7–5.6 ka BP (Fig. 15). As such, site-specific mound development across this period can be compared. In core CE_VC1, CPP is represented entirely by coral rubble (CPP C; see Fig. 15). In contrast, the bottommost 0.24 m of core RH_VC7 is represented by slightly collapsed coral framework (defined as CPP B) and the topmost 0.56 m is represented by the coral framework in living position (defined as CPP A). Mean mound AR in core RH_VC7 is greater by a factor of two when compared to core CE_VC1 (see Table 2 and Fig. 15). Isotopic data show that higher planktic $\delta^{13}C$ occurs in core RH_VC7 (range: -0.84 to -0.33 ‰) than in core CE_VC1 (range: -0.46 to -0.19‰; Fig. 15; see Fig. 15 and Appendix XI), This supports the idea that proximity of mounds to the canyon is a crucial factor for food supply.

The incising geomorphology of submarine canyons result in complex patterns of hydrography, sediment transport and accumulation (Shepard et al., 1974, Oliveira et al., 2007, García et al., 2008), that can increase suspended particulate matter concentrations and transport of organic matter (Genin, 2004, Canals et al., 2006, Company et al., 2008). They intercept the path of slope currents flowing along isobaths (Font et al., 1988) and can entrain particles (including POM) travelling along the margin (Huthnance, 1995). Downwelling above canyons commonly occur, further intensifying the ability of canyons to trap particles transported via a long-shore current (Granata et al., 1999, Palanques et al., 2005, Allen and Madron, 2009). In the instance of the PBC, Ekman downwelling may be induced by northerly gales combined with the northward flow of the slope current (e.g. Ratmeyer et al., 2006). Furthermore, the interaction between canyon geomorphology and local hydrodynamics produces vortex stretching and vertical motions (Klinck, 1996,

Hickey, 1997), leading to local upwelling of nutrients that stimulate primary production (Ryan et al., 2005). These processes can enrich benthic productivity within canyons resulting in increased biodiversity (Rowe et al., 1982, Schlacher et al., 2007, Vetter et al., 2010). Thus, adjacent to the margins of a submarine canyon resides a diverse interplay of downwelling and upwelling currents, rich in particles including organic matter. For benthic sessile filter feeders, such as CWCs, this enrichment mechanism on the continental margin provides them with essential food and sediment supply. Upwelling has been observed on the continental slope of the Porcupine Bank at 51°41'N and 14°39'W in 464 m water depth (Dickson and McCave, 1986) and has since been corroborated in the PBC by Wheeler et al. (2021)

The re-initiation of Holocene CWCs at the Porcupine Seabight is likely linked to the strengthening of the Eastern North Atlantic Water-Mediterranean Outflow Water-Transition Zone (ENAW-MOW-TZ; Friewald, 2002, Dullo et al., 2008; Wienberg et al., 2020). Along the slopes of the PBC, the boundary between the ENAW-MOW resides at ~800 m depth (Mazzini et al., 2011, Appah et al., 2020) and, as such, represents an enriched source of particles (including organic matter). Dense and diverse populations of CWC have been recorded growing within this boundary, and are orientated upright on slopes of the PBC (Appah et al., 2020). A limiting factor of mound development on the slopes however, is the steep topography, which in parts exceeds 70°. Instead, mounds favour the shallower adjacent banks of the continental margin (Fig. 5), a few hundred metres above the ENAW-MOW boundary. This suggests that the PBC plays a pivotal role in upwelling and acting as a conduit for enhanced particulate organic matter resuspension and supply.

Coral framework functions as a sediment trap for lateral and vertical advected sediment flux and as such higher ARs coincide with favourable growth conditions (Genin et al., 1986, Mienis et al., 2007, Davies et al., 2009, Frank et al., 2009, Mienis et al., 2009b, Douarin et al., 2013). A comparison of AR between these two sites across a comparable timescale (in this instance between 6.7 and 5.6 ka BP; see Fig. 15) show advantageous conditions are present adjacent to the canyon (68 cm ka^{-1} in the PBC versus 31.5 cm ka^{-1} in the wPB). Corals from core RH_VC7 (i.e. from the PBC) consist mainly of

corals in the living position, whereas corals from core CE_VC1 (i.e. from the wPB) consist of coral rubble. This suggests that proximity to the canyon results in faster mound development due to higher food availability. BFAs from both cores are discussed below to test this hypothesis further.

Food availability is a key driver for benthic foraminiferal distribution (Lutze and Coulbourn, 1984, Jorissen et al., 2007, Fontanier et al., 2008). Cores CE_VC1 and RH_VC7 have a comparable mean species diversity of 35.7 and 36.7 species per sample, respectively. However, on a comparable species-to-species level, the PBC_{Middle} Assemblage of RH_VC7 is characteristic of higher organic matter flux than both wPB_{Early} and wPB_{Middle} assemblages in core CE_VC1. The infaunal *G. subglobosa* and *N. umbonifera* were identified as suitable discriminating species between the assemblages (see Appendix XII). These infaunal phytodetritovores are regarded as an indicator species for positive fluxes in organic matter in response to bloom events in the NE Atlantic (Corliss, 1979, Gooday, 1994, Mackensen et al., 1995, Fariduddin and Loubere, 1997, Altenbach et al., 1999, Fontanier et al., 2002, Suhr et al., 2003, Fontanier et al., 2005, Murray, 2006a, Alve, 2010). The PBC_{Middle} Assemblage also reveals higher proportions of the shallow infaunal *U. auberiana* (Fig. 15), a species associated with steady to episodic labile organic content (higher protein and phytopigment content; see Gooday and Hughes, 2002, Suhr et al., 2003, Gooday, 2019). The high abundance of this species is strong evidence that organic matter is more available within closer proximity to the canyon. Thus, increased food supply seems to be the most important ecological parameter controlling the BFAs on the mound summits.

Multivariate analysis confirms that site and age account for 43% of the variance within the BFAs across both sites. These two factors are highly significant, with a p-value of <0.0001 (Table 4), demonstrating that the chance of the explanatory variables' influence on the foraminiferal community occurring at random is 1 in 10,000. Site is the single most significant contributor to the model, indicating that the distance from the canyon plays an important role, perhaps along with other site-specific abiotic factors. Interestingly, the site contribution to variance over a short distance of 1 km between the two coral mound summits outweighs the temporal contribution to

variance for 2–4 thousand years. Respectively, the environmental differences between the canyon lip and 1 km away as expressed through the foraminifera present is much greater that the environmental change experienced at both sites over the last few thousand years. However, the age model still explains 14% of the variation in the community data of the global model and is highly significant (Table 4). The error introduced through the Bayesian age model and shorter core record captured in core VC7 may affect this. Nevertheless, its significance among multiple abiotic factors highlights the observable shift in BFAs across time, specifically at the 8.2 ka boundary. The higher temporal contribution at the longer wPB core site when temporal effects are tested for each core independently ($R^2_{VC1} = 0.31$ compared to $R^2_{VC7} = 0.24$ at the PBC) stresses the importance of the 8.2 ka event as a tipping point. Planktic $\delta^{13}C$ could only be tested on a smaller subset of the data because there were insufficient foraminifera to obtain stable isotope ratios in all core subsamples (see Appendix VIII). However, the variable was selected for at a 0.1 α-level and corresponds with the BFA in core RH_VC7 (Fig. 15), suggesting a more enriched organic signal is seen along the PBC canyon lip compared to the wPB. These findings, alongside higher AR, show that the canyon's lip is a highly favourable location for CWC development in the wPB and PBC region. Elsewhere on the NE Margin, CWCs decline due to a deficient food source, corals in the PBC region thrive. This indicates that areas adjacent to submarine canyons, such as the PBC, may act as refuges for CWCs, providing habitable conditions throughout periods of stress. Section 4.5.2.1 of this thesis explores other examples of potential canyon lip coral reefs/mounds

3.5.3. Summary of environmental factors controlling wPB and PBC mounds during the Holocene.

In summary, strong bottom currents resulted in slow mound development in the wPB during the Early Holocene (Fig. 18a). Regional climate driven processes (see Barber et al., 1999, Thomas et al., 2007, Morrill et al., 2013) reduced sediment supply to the wPB during the Early Holocene–mid-Holocene transition, which further slowed mound development (Fig. 18b). Between 7.1–6.7 ka BP, a rapid growth phase in the wPB mound was observed (Fig. 18c) and is likely linked with the major hydrological reorganisation in the NE Atlantic

(Thornalley et al., 2009, Colin et al., 2010). Finally, between 6.7 – 5.6, the wPB mound growth reduces rapidly (Fig. 18d). During this time, the contemporaneous PBC mound thrived and grew at least twice as fast as the wPB mound. An enriched $\delta^{13}C$ signal is captured in RH_VC7, suggesting proximity to canyon is a crucial factor behind enhanced CWC growth.

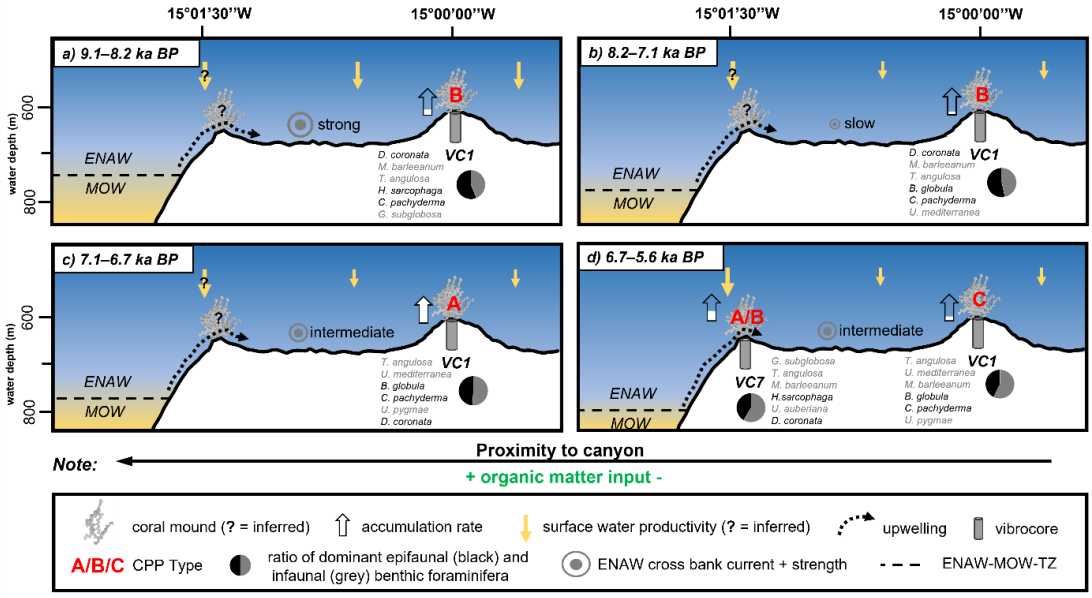


Figure 18: Summary of environmental factors controlling wPB and PBC mounds during the Holocene. Accumulation rates (white arrow) and coral preservation pattern (CPP; red) describe environmental variability. Benthic foraminifera at each core locality is listed by decreasing dominance alongside the ratio of dominant epifaunal (black) and infaunal (grey) species. Bottom currents strength (grey circle) inferred from mean grain size, mean sortable silt size and benthic foraminiferal distribution. Surface water productivity (orange arrow) reflected by variations in $\delta^{13}C$ from planktic foraminifera (Note: it likely remains more enriched over the lip of canyon from Ekman driven downwelling of surface waters (see Granata et al., 1999, Palanques et al., 2005, Ratmeyer et al., 2006, Allen and Madron, 2009), and is annotated with black question marks). Upwelling (black arrow) remains prominent throughout each period. (a) 9.1–8.2 ka BP; (b) 8.2–7.1 ka BP (c) 7.1 – 6.7 ka BP; and (d) 6.7–5.6 ka BP

3.6. Conclusion

This study uses a novel method (ROV-vibrocoring, 3D-segmented computed tomography) combined with more commonly applied paleoenvironmental practices (benthic foraminifera assemblages, grain size analysis, stable isotope analysis and AMS ^{14}C dating) to assess the Holocene build-up of two nearby cold-water coral mound summits. Previously, paleoenvironmental assessments using benthic foraminifera from coral-bearing cores were

acquired using traditional gravity coring procedures and were acquired from areas generally far apart. Our methods introduced here provide a more representative temporal development model and should be considered the benchmark in future endeavours. Paleoenvironmental reconstructions of the wPB are currently confined to 9.7 ka (O'Reilly et al., 2022). This study utilizes CWC-bearing records to extend our knowledge by 3 ka to the mid-Holocene (6 ka).

Strong bottom currents resulted in slow mound development in the wPB during the Early Holocene (Fig. 18a). Regional climate-driven processes (see Barber et al., 1999, Thomas et al., 2007, Morrill et al., 2013) reduced sediment supply to the wPB during the Early Holocene–mid-Holocene transition, which further slowed mound development (Fig. 18b). Between 7.1–6.7 ka BP, a rapid growth phase in the wPB mound was observed (Fig. 18c) and is likely linked with the major oceanographic reorganisation in the NE Atlantic (Thornalley et al., 2009, Colin et al., 2010). Finally, between 6.7 – 5.6 ka BP, the wPB mound growth reduces rapidly (Fig. 18d), although the contemporaneous PBC mound grew at least twice as fast as the wPB mound. The succession of CWCs in the region can be linked with enhanced shelf currents, the existence of the ENAW-MOW-TZ (Friewald, 2002, Dullo et al., 2008; Wienberg et al., 2020) and crucially, upwelling caused by canyon topography. These mechanisms collectively create an ideal setting for CWC habitats, such as along the lip of the PBC (Fig. 12b). Furthermore, proximity to the canyon results in higher aggradation rates and food availability.

Open questions remain regarding a) the initial colonization of CWCs in the region and b) their ability to survive during glaciated events. No CWCs have been found from glacial periods along the margin. This study would be significantly enhanced if a coral bearing core taken from the area could be found extending further back through time. Gravity cores taken from larger carbonate mounds identified by Mazzini et al. (2011) may fill this gap in the record. The hypothesis that submarine canyons act as a refuge for CWCs could thus be tested and substantiated.

3.7 Acknowledgements

The authors would like to thank Mr Paddy O'Driscoll (Marine Institute) for his assistance in developing the vibrocoring unit used in this study. All shiptime is funded under the National Development Plan (2019), National Grant-aided Shiptime Programme. Luke O'Reilly is funded by Science Foundation Ireland project "MMMonKey_Pro" ([grant number: 16/IA/4528]), which is co-funded by the Geological Survey, Ireland and Marine Institute. Felix Butschek is funded from the European Union's Horizon 2020 research and innovation program under grant agreement No 818123 (iAtlantic). Jürgen Titschack received funding from the Cluster of Excellence "The Ocean Floor—Earth's Uncharted Interface" (Germany's Excellence Strategy—EXC-2077-390741603 of the DFG). The authors would like to thank the University of Lyon and the University of Fribourg for access to the optical microscope and SEM. Luke O'Reilly would like to thank the MMMonKey_Pro team members and members of the Marine Geosciences Research Group at UCC and scientific parties, officers, and crew of cruise RH17002 and CE18011.

Chapter 4: Are Submarine Canyons Refugia for Scleractinian Cold-water Corals in Glacial Periods?: Evidence from the Porcupine Bank Canyon, NE Atlantic

(Current Status: in preparation to be submitted)

*O'Reilly, Luke[1], Titschack, Jürgen[2,3], Lim, Aaron [1,4], Moore, Niamh[5,6], O'Connor, O.J.[5,6], Appah, John[1], and Wheeler, Andrew J.[1,7]

**Corresponding author*

[1]School of Biological, Earth & Environmental Sciences / Environmental Research Institute, Distillery Fields, North Mall Campus, University College Cork (UCC), Ireland

[2]MARUM – Center for Marine Environmental Sciences, University of Bremen, Bremen, Germany

[3]Senckenberg am Meer, Marine Research Department, Wilhelmshaven, Germany

[4]Green Rebel, Crosshaven Boatyard, Crosshaven, Co. Cork, Ireland

[5]Department of Radiology, Cork University Hospital (CUH), Wilton, Cork, Ireland

[6]Department of Radiology, University College Cork

[7]SFI Research Centre for Applied Geosciences - iCRAG / SFI Research Centre for Energy, Climate and Marine - MaREI, University College Cork, Ireland

Abstract

The current understanding of how Holocene cold-water corals re-colonised the NE Atlantic is based on a compilation of biogeographic modelling and genetic studies. These studies suggest that coral larvae were dispersed from the Mediterranean, following current pathways facilitated by a strengthened Atlantic Meridional Overturning Circulation. However, there is no evidence of CWCs growing during glacial periods from the greater European continental Atlantic margin, that can disprove the concept of larval dispersion. Submarine canyons are regarded as refuges for CWC during unfavourable periods. Acquiring temporal samples from CWC inhabited canyons may therefore give a true representation of their tolerances during the last glacial period. This study aims to provide an alternate hypothesis for Holocene re-colonisation of CWCs in the NE Atlantic. Here, remotely operated vehicle-mounted vibrocores

reveal temporal records of cold-water corals occupying the Porcupine Bank Canyon, 300 kilometres west of Ireland. These cores were collected from various geomorphological settings in the canyon, specifically coral mound summits, coral rubble cores from the flat continental bank and along the slope and foot of the canyon Three-dimensional segmented computed tomography classified these records, revealing distinct patterns of reef development in different parts of the canyon. AMS ^{14}C dating the records provided unprecedented evidence for corals colonising the Irish margin since during the last glacial period. Results show that the Porcupine Bank Canyon provided the corals with refuge during the British-Irish Ice Sheet's intense (de)glaciation. This study provides a revision of the hypothesis for the Holocene re-colonisation of CWCs in the NE Atlantic from the lower latitudes (40°N) to the higher latitudes (70°N). On a broader scale, it highlights the need for stricter conservation measures of these essential ecosystem.

4.1 Introduction

Over the last two decades, significant focus has been given to scleractinian framework cold-water corals (CWCs), as they generate essential habitat diversity for benthic life in the deep sea (Freiwald et al., 2004, Roberts et al., 2006, Buhl-Mortensen et al., 2010, Lim et al., 2020a). Of particular interest are the framework-forming cold-water corals (CWCs) *Desmophyllum pertusum* (synonymous with *Lophelia pertusa* - see Addamo et al., 2016) and *Madrepora oculata* in the NE Atlantic that form small patch reefs and mounds in canyons (De Mol et al., 2011b, Reveillaud et al., 2008, Tyler et al., 2009) and on seamounts (Duineveld et al., 2004), to extensive living reefs and giant carbonate mounds on continental slopes (Wheeler et al., 2007, Dorschel et al., 2010, Wienberg and Titschack, 2017) and on the Norwegian shelf (Fosså et al., 2005, Freiwald et al., 2002). Today, CWCs appear to thrive along some parts of NE Atlantic continental slopes, colonising the tops of coral mounds, on dropstones, as extensive areas of coral ridges and as smaller reefs. Mounds in Irish waters have been categorised into mound provinces, many of which are located on the Porcupine Bank (e.g. Wheeler et al., 2007, Dorschel et al., 2010), in the Porcupine Seabight (Hovland et al., 1994, Henriet et al., 1998, De Mol et al., 2002, Huvenne et al., 2003, Wheeler et al., 2005b, White and Dorschel, 2010) and on both sides of the Rockall Bank (Kenyon et al., 2003, van Weering et al., 2003, Wheeler et al., 2005a, Mienis et al., 2006, Wienberg et al., 2008). Particular attention has been given to understanding the temporal variation of CWC presence and coral mound development/cessation, to determine their ecological tipping points, provide better prognoses for their future fate to climate change, and optimise conservation measures for these important deep-sea ecosystems (Hebbeln et al., 2019 and references therein). The primary biogenic component of these CWC reefs and coral mounds are the framework building species *D. pertusum* and *M. oculata* (Cairns, 2001). The framework of these species, in particular *D. pertusum*, enhances local biodiversity on continental margins by: a) facilitating the colonisation of sessile fauna on their skeletons; b) providing microhabitats; c) proving nursery grounds; and d) enhancing available organic material within the structure through increased sediment accumulation (e.g.

Mortensen et al., 1995, Fosså et al., 2002, Duineveld et al., 2004, Reed et al., 2006, Dorschel et al., 2007a, Henry and Roberts, 2007, Roberts et al., 2009, Buhl-Mortensen et al., 2010). Multiple studies reviewed and summarised the environmental constraints for CWC occurrence (e.g. Freiwald et al., 2004, Roberts et al., 2006, De Mol et al., 2009, Davies and Guinotte, 2011, Roberts and Cairns, 2014, Hebbeln et al., 2019) which are continuously updated (see Raddatz and Rüggeberg, 2021 and references therein).

The earliest recorded evidence of framework-forming scleractinian CWCs living in the Porcupine Seabight 2.6 million years ago (Kano et al., 2007, Huvenne et al., 2009). High primary productivity (Raddatz et al., 2014) and vigorous hydrodynamic conditions (Thierens et al., 2010) resulted in ideal environmental conditions for the growth of giant mounds in the region (Kano et al., 2007). Following a major hiatus (between 1.2 to 0.7 million years) during the mid-Pleistocene transition, the carbonate mounds show episodic development throughout the Late Quaternary during warm interglacial phases (Dorschel et al., 2005, Roberts et al., 2006, De Mol et al., 2007, Eisele et al., 2008, Wienberg et al., 2020). Glacial coral mound development and CWC occurrence in the NE Atlantic are restricted to low latitudes, e.g.from the Gulf of Cádiz (Wienberg et al., 2010, Eisele et al., 2011, Wienberg and Titschack, 2017, Wienberg et al., 2018). De Mol et al. (2005)'s hypothesis that the inferred simultaneous start-up phase of mound development observed across the NE Atlantic during the Holocene was initiated through the migration of CWCs from the Mediterranean. Henry et al. (2014) substantiated this hypothesis by compiling biogeographical and genetic records revealing an impressive 7,500 expansion across 400 years. Furthermore, they propose the primary mechanism behind this re-dispersal of coral larvae from the Mediterranean, was driven by a re-invigorated Atlantic Meridional Overturning Circulation. Consequently, this hypothesis would account for the synchronous timing of renewed NE Atlantic CWC growth and mound development occurring at the onset of the Holocene (e.g. Frank et al., 2009, López Correa et al., 2012, Douarin et al., 2014, Elliot et al., 2019). However, recent studies have found that submarine canyons functions as havens for CWCs through major climatic

shifts (i.e. deglacial periods; e.g. Huvenne et al., 2011, Puig and Gili, 2019, Wienberg et al., 2020).

Submarine canyons are geomorphic features incised into continental shelves and slopes (Shepard, 1972, Harris and Whiteway, 2011, Puig et al., 2014). Their varied topography and morphology give rise to complex oceanographical, hydrographical and biological processes (Allen et al., 2001, Bosley et al., 2004, Trotter et al., 2019) that enhance primary productivity and increase particulate matter concentrations (Bosley et al., 2004, Ryan et al., 2005). They are the main transport pathways between the shelf and the deep sea, funnelling sediments, nutrients and organic matter (de Stigter et al., 2007, Allen and de Madron, 2009, Mazzini et al., 2011, Puig et al., 2013, Puig et al., 2014). These characteristics cause heterogeneity on the continental margin, significantly increasing biomass availability and, in turn, biodiversity (Vetter and Dayton, 1999, Schlacher et al., 2007, Danovaro et al., 2009, De Leo et al., 2010). Canyons may also serve as refugia for fish and wildlife during periods of poor ocean productivity (Benson et al., 1997, Benson et al., 2002, Croll et al., 2005). Consequently, canyons might provide critical “stepping stones" along the continental slopes for coral larval dispersal and coral gene-flow during intervals of unfavourable conditions on the adjacent continental slopes. They might function as local CWC larval spreading centres for coral recolonisation when favourable habitable conditions re-emerge on the adjacent continental slopes.

The Porcupine Bank Canyon (PBC) is the largest submarine canyon on the Porcupine Bank and western Irish margin. It has been designated a Special Area of Conservation (SAC) under the EU Habitat Directive (92/43/EEC) as a submarine canyon hosting many CWCs. Exploratory surveys of the canyon (see Wheeler et al., 2017, Lim et al., 2018) revealed rich biodiversity (Appah et al., 2020), with high abundances of *D. pertusum* (Appah et al., 2020). Since exploration of the area began, understanding the temporal variance of CWCs within the region was limited, mainly due to failed coring attempts using conventional methods (i.e. piston and gravity coring; see Wheeler et al., 2015). However, recent advancements and availability of underwater submersibles such as remotely operated vehicles (ROVs) with attached vibrocoring systems

grant successful sample acquisition from these challenging areas (Wheeler et al., 2017, Lim et al., 2018). Recently, O'Reilly et al. (submitted; see Chapter 3) used these techniques to determine mound development during the early to middle Holocene. Their study revealed that conditions along the canyon lip had higher food supply than on the surrounding continental bank, linking this to upwelling generated by the canyon. Furthermore, across a contemporaneous period, it was shown that mound aggradation rates were twice as high along the canyon lip than on the continental bank (see chapter 3). While this study provides insights into the most recent western Porcupine Bank (wPB) and PBC coral mound development in the Holocene, the timing and environmental controls of mound development before 9.1 ka BP remain unknown. Of particular interest would be the development of an understanding of how corals responded to glacial conditions and if the deglaciation of the British-Irish Ice Sheet (BIIS) also had any impact. For instance, it has been shown that the wPB was subjected to multiple stages of ice-rafting and was also scoured by grounded glaciers (O'Reilly, et al., 2022; see chapter 2).

This research aims to test the hypothesis that submarine canyons act as refuges for CWCs during regionally unfavourable environmental conditions on the adjacent continental slope on the example of the PBC. Furthermore, it will discuss the potential consequences for re-colonisation events on CWC larval transport and gene-flow and identify the temporal change of CWCs throughout the LGM. To achieve our goals, (i) novel ROV-vibrocoring (Wheeler et al., 2017, Lim et al., 2018) was applied for the first time to retrieve coral-bearing cores from various canyon settings (bank, lip, slope and pro-slope), (ii) computed tomography was used to analyse coral deposits and to reconstruct their process of deposition, and (iii) radiogenic dating of matrix sediment and coral pieces were applied to constrain the temporal development of the CWCs in the PBC.

4.2 Regional Setting

The wPB occupies the westernmost limits of NE Atlantic continental margin within the Porcupine Bank (Fig. 19a). The study site has endured a period of non-deposition and/or erosion since 9.7 ka (O'Reilly et al., 2022). Furthermore, ice-rafted debris was deposited on the bank since at least 33 ka BP (O'Reilly et al., 2022). The incision of the bank by the PBC is tectonically controlled (Shannon, 1991) and trends north-east to south-west (Shannon et al., 2007, Lim et al., 2020b). The canyon is asymmetric in shape with a steep (60 to 70 degrees) high (800 m) eastern canyon wall. For the most part, the steepness of the walls prevents sediment deposition, except for pockets of tallus deposits that accumulate between the step-wise protrusion of hard bedrock (Wheeler et al., 2017). At the base of this steep wall (>2,800 m) exists the most comprehensive channels in the PBC system (Lim et al., 2020b). Iceberg plough marks are visible on the adjacent lip of the wPB (Mazzini et al., 2011, O'Reilly et al., 2022).

Contemporary oceanography reveals the Eastern North Atlantic Water (ENAW) that flows northerly at ~200–700 m water depth (White and Bowyer, 1997, Mazzini et al., 2011). This water mass forms at the Bay of Biscay and is advected northwards along the Porcupine Bank by the poleward Shelf-Edge Current (Ellett and Martin, 1973, Dickson and McCave, 1986, Pollard et al., 1996, White, 2007, Mazzini et al., 2011). The shape of the Porcupine Bank accelerates contour currents along its margin (Wheeler et al., 2005b). The more saline Mediterranean Outflow Water (MOW) occurs at 800–1000 m water depth and underlays the ENAW (White, 2007, Mohn et al., 2014). The denser Labrador Sea Water occurs at 1100 m water depth (Appah et al., 2020). Bedforms, such as current-aligned scours in the lee of coral mounds reflect the long-term net effect of enhanced bottom currents shaping the seafloor (Dorschel et al., 2009)..

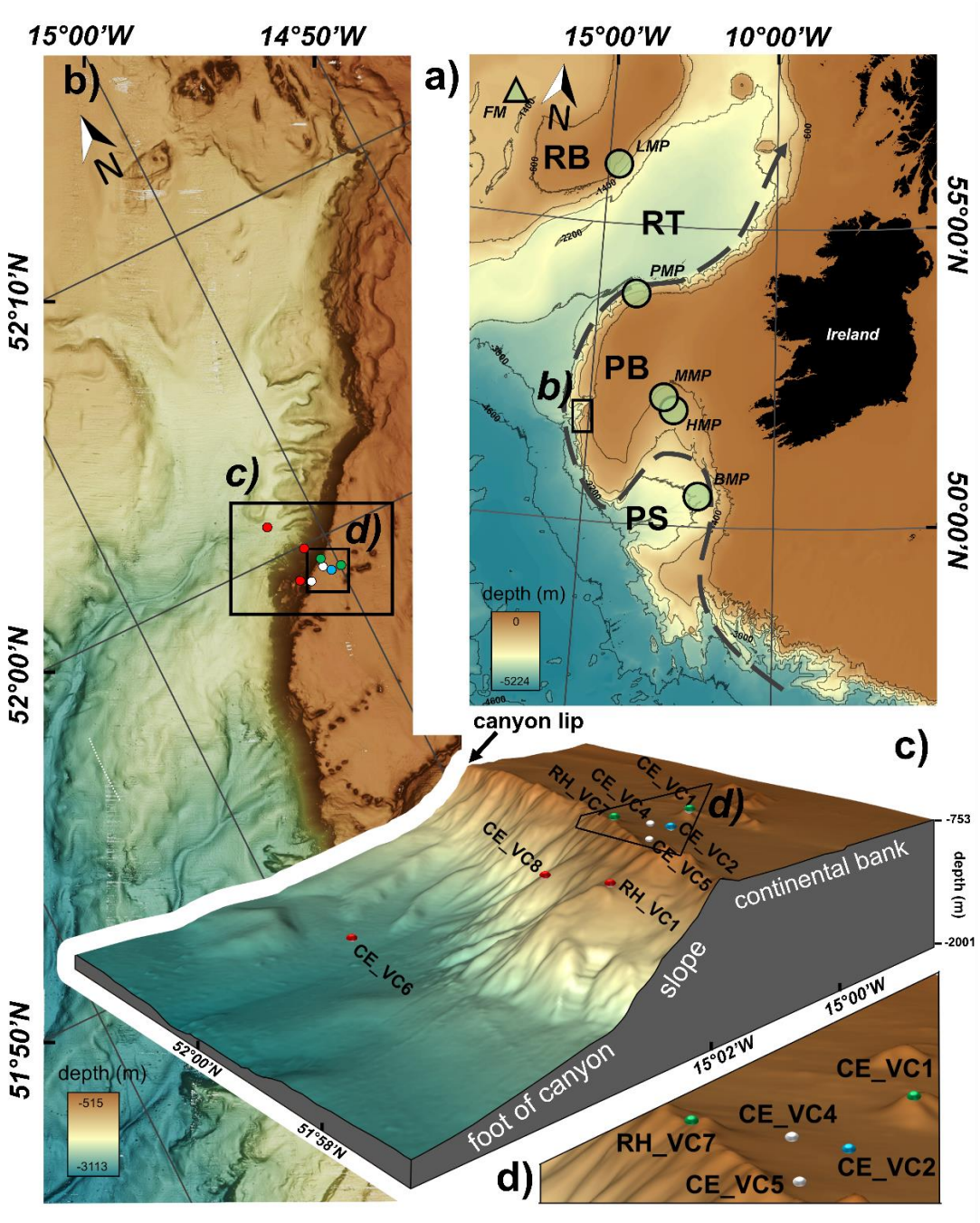


Figure 19: (a) Location of the study site at the western Porcupine Bank and Porcupine Bank Canyon (black rectangle) on the Irish continental margin (PB - Porcupine Bank, PS - Porcupine Seabight, RB - Rockall Bank, RT - Rockall Trough; white circles are representing regional mounds and provinces, whereby FR – Fracken Mounds, BMP – Belgica Mound Province, HMP – Hovland Mound Province, MMP – Magellan Mound Province, PMP – Pelgica Mound Province and LMP – Logachev Mound Province) adapted from O'Reilly et al. (2022). Grey dashed line showing flow direction of Eastern North Atlantic Water. (b) Bathymetry map of the upper Porcupine Bank Canyon modified after Lim et al. (2020). Note cores taken from the region with designated colour according to geomorphological setting (green – coral mound summit; white – coral rubble core and red – canyon slope/foot of slope cores. Also shown is core CE_VC2 (white) for comparison with O'Reilly et al. (2022) (c) Overview of coring sites

used in this study. Maps created using ArcGIS Desktop v10.6 (www.arcgis.com) and AMIRA version 2018.36 (see Stalling et al., 2005; http://amira.zib.de); data sources – (a) - General Bathymetric Charts of the Oceans (gebco.net); (b and c) – additional bathymetry (10 m resolution) collected during CE18011 research cruise (Lim et al., 2018).

4.2.1 Cold-water Coral Reef and Mound Distributions

Adjacent substrates occupied by coral reefs are mainly composed of sediment (47.6%), coral rubble (36.5%), bedrock (7.7%), dropstones (4.6%) and dead/live coral (3.6%; see Appah et al., 2020). The main reef-forming species is *D. pertusum,* which is most abundant in the southern section of the canyon due to high POM concentrations (Appah et al., 2020). Coral mounds form 50 – 250 m high dense clusters between 550 – 900 m depth along the lip of the canyon following an N-S trend (Fig. 19b and c; Lim et al., 2020b). The mounds are elongated with near-symmetrical steeply dipping slopes (20-30°). A series of unconnected mounds expand onto the wPB, following an E-W trend (Fig. 19b and c). The wPB mounds have relatively more live coral framework than the mounds along the canyon lip (Lim et al., 2020b). In addition, *in situ* acoustic doppler current profile measurements showed that the wPB mounds are subjected to lower current speeds than mounds along the canyon lip (mean values of 17.3 cm s^{-1} and 24 cm s^{-1}, respectively (Lim et al., 2020b). The mean current speeds in the region range from 18.2 – 31.3 cm s^{-1}, whereby the highest occur along the canyon flank (Lim et al., 2020b). Furthermore, the dominant current direction flowing over the wPB is orientated north-east (Lim et al., 2020b). In contrast, the lip of the PBC is characterised by a westerly current direction (Lim et al., 2020b), suggesting an exchange between open slope and canyon waters. Depth, slope and habitat type are critical environmental drivers that affect benthic taxa distribution along this part of the canyon (Appah et al., 2020). It was determined that the highest Shannon's diversity index occurs along with this geomorphological setting, suggesting that current regimens influence benthic fauna distributions (Appah et al., 2020).

4.3 Materials and Methods

4.3.1 Novel ROV-Vibrocoring

Fourteen cores were acquired using the Holland I Remotely Operated Vehicle equipped with a vibrocore rig (see Appendix XIV) from the wPB and PBC onboard the ILV Granuaile during the CoCoHaCa research cruise (cruise number RH17002 abbreviated as RH; see Wheeler et al., 2017) and RV Celtic Explorer during the CoCoHaCa II research cruise (cruise number CE18011 abbreviated as CE; see Lim et al., 2018). The novel use of the ROV granted the acquisition of precise samples from various geomorphological settings with direct ground-truthing by live video footage following ROV-dedicated video surveys (Wheeler et al., 2014, Wheeler et al., 2015, Wheeler et al., 2016, Wheeler et al., 2017, Lim et al., 2018). The acquired cores were 75 mm in diameter and were stored vertically at 4°C to minimise sediment deformation. Drilling for each core was terminated when in contact with an obstruction. Seven coral-bearing cores from each of these settings were selected based on their recovery size, ranging from 31 to 180 cm (Table 7). Cores CE_VC1 and RH_VC7 were taken from the summits of coral mounds occupied by living corals on the wPB and the lip of the PBC, respectively. Cores CE_VC4 and CE_VC5 were taken from areas adjacent to coral mounds. Cores CE_VC8 and RH_VC1 were taken from the slope of the PBC, where sediments accumulated between protruding bedrock. Finally, core CE_VC8 was taken from the foot of the slope of the PBC.

Table 7: Summary of vibrocores collected from the west Porcupine Bank (wPB) and Porcupine Bank Canyon (PBC) during the CoCoHaCa I (RH17002) and CoCoHaCa II (CE18011) research cruises.

Core ID	Geomorph. Setting	Lat [DD]	Long [DD]	Water Depth [m]	Length [cm]	CT	Dates
RH_VC1	PBC slope	51.9835	-15.0337	840	31	✓	U/Th*
RH_VC7	PBC CWC mound	51.9892	-15.0129	651	81	✓	AMS
CE_VC1	wPB CWC mound	51.9829	-14.9995	660	130	✓	AMS
CE_VC4	PBC rubble	51.98467	-15.0109	671	180	✓	U/Th*
CE_VC5	PBC rubble	51.9847	-15.0109	699	115	✓	U/Th*
CE_VC6	Foot of the PBC slope	51.9841	-15.0248	1857	40		AMS & U/Th*
CE_VC8	PBC slope	51.9957	-15.0262	1202	34	✓	U/Th*

**Pending*

4.3.2 Core analysis

Non-destructive and destructive multiproxy analytical methods were performed on the CWC-bearing cores to assess their sedimentary history and paleoenvironment setting.

4.3.2.1 Computer Tomography

All computed tomography images were acquired using a 64 section multi-slice scanner (GE Healthcare, Discovery CT 750 HD) at Cork University Hospital, Cork, Ireland. Images were acquired at a slice thickness of 0.625 mm, using 120 kV, 600 mA and a rotation time of 0.8 s, a pitch of 0.984 and a bony convolution algorithm. Images were reconstructed using Model-based Iterative Reconstruction (MBIR) Veo (GE Healthcare, GE Medical Systems, Waukesha, WI, USA) with pure iterative reconstruction using a resolution preference of 20% (RP20), increasing the spatial resolution by 20%. An overlapping reconstruction was performed with a final voxel size of 0.195 x 0.195 x 0.625 mm. The original data was recalculated to obtain an isotropic voxel size of 0.2 mm.

Core descriptions of coral-bearing cores are based on computer tomography (CT) scan data analysis. CWC preservation patterns (CPP) were defined by

quantifying macrofossil clast size and orientation following classification standards introduced by Titschack et al. (2015) and further defined by Wang et al. (2019). These range from CPP A to D (see Appendix I). CPP A represents coral framework in a living position, characterised by large average coral clast size of >-4.7 Φ (>2.6 cm) and variable orientations of up to 90°. CCP B represents a slightly collapsed coral framework, characterised by moderate clast sizes of -4.7 to -4.4 Φ (~2.6–2.1 cm) and orientations <60°. CCP C represents coral rubble, characterised by small average clast sizes of <-4.5 Φ (~2.1 cm) and orientations of <45° or no obvious orientation. A fourth classification was added to this study, CCP D, representing sediments that are sparse/or barren of CWC fragments.

4.3.2.2 Radiocarbon and Uranium-series dating

4.3.2.2.1 AMS radiocarbon measurements

A mixed sampling strategy was applied due to the thickness of the vibrocores (75 mm) and varying abundances of dateable material. The dates were then further corroborated using Paleo Data View (Langner and Mulitza, 2019; see successive paragraphs below) to offset differences in fractionation effects caused by alternative reservoir ages. Where possible, monospecific planktic foraminifera (*Globigerina bulloides*) were sampled. If the sum weight of the material collected was inadequate (i.e. <15 mg), the epibenthic foraminiferal species *Cibicides lobatulus*, *Cibicides refulgens* and *Discanomalina coronata* were picked. Finally, pristine-looking coral pieces (*M. oculata*) were dated where an insufficient amount of benthic foraminifera were present. The base of pristine-looking coral pieces was chosen from CCP A (coral in the living position; see Titschack et al., 2015, Wang et al., 2019).

As such, a total of 3 monospecific planktic foraminifera (*Globigerina bulloides)*, eight mixed benthic foraminifera (*Discanomanalia coronata* and *Cibicides spp.)* and three coral fragments (*Madrepora oculata*) were sampled from the cores at various depths and used for dating. Foraminifera samples were taken from a >150 µm aliquot size and cleaned in an ultrasonic bath prior to submission. At least 15 mg of calcium carbonate was used to acquire each date. For coral pieces, each fragment was cleaned following methods

described by (Adkins et al., 2002). Eleven measurements were carried out at DirectAMS Laboratories, Washington, USA and three measurements were carried out at 14Chrono, Queens University Belfast, UK.

Eleven coral samples from various depths were collected from cores CE_VC4 and CE_VC5 for Uranium-series dating. Eleven coral samples from various depths were collected from cores CE_VC6, CE_VC8 and RH_VC7 for Uranium-series dating. The samples were acquired by sieving the entirety of the cores. Samples were washed and then hand-picked based on their thickness, bioerosion and dissolution (see Appendix XVI). Before the analyses, all coral fragments were cleaned mechanically and chemically according to a procedure described by Frank et al. (2004). The U-series isotope measurements was performed on a ThermoFisher iCAP-Qs inductively coupled plasma mass spectrometer (ICP-MS) at the Institute of Environmental Physics, at the Heidelberg University (IUP), Germany. The reproducibility was assessed using the international uranium standard material HU1 (Cheng et al., 2000; Frank et al., 2004; Wefing et al., 2017). U-series coral ages are reported as ka BP.

Water column stratification significantly impacts offsets between contemporary planktic and benthic foraminifera radiocarbon ages. The reliability of the acquired dates should thus be taken with caution when interpreting the developed chronology for the cores. AMS ^{14}C ages were converted to calendar years with Paleo Data View (Langner and Mulitza, 2019) using the IntCal20 curve (Reimer et al., 2020) and the closest modelled reservoir ages of Butzin et al. (2017). The dates are reported as kiloyears before present (ka BP, Present = 1950CE). The age model was developed in a Bayesian framework using BACON (Blaauw and Christen, 2011) implemented within Paleo Data View (Langner and Mulitza, 2019). Coral mound aggradation rates (ARs) were calculated for cores CE_VC1 and RH_VC7 between dated intervals. In addition, the oldest and youngest coral ages in relation to the maximum and minimum core depths of the respective core intervals were used to calculate the mean AR for each core. Sedimentation rates (SRs) were calculated for core CE_VC5, based on the linear interpolation between the dated depths of the core.

4.4. Results

4.4.1. Description and CT-based classification of Cold-Water Coral-Bearing Cores

4.4.1.1 Coral Mound Summit Cores

The sedimentological and CT-based classification of cold-water coral bearing coral mound summit cores (CE_VC1 and RH_VC7) is available in section 3.4 of this thesis.

4.4.1.2 Coral Rubble Cores from the Flat wBP Top Sediments

Core CE_VC4 contains mostly poorly-preserved CWC rubble (Fig. 20; see Appendix XV). CPP B occurs at core depths of 144–125 cmbsf (Fig. 20) embedded in light brown sediments. CCP C occurs twice at core depths of 165–144 cmbsf (defined as CPP C_2) and 83–0 cmbsf (defined as CPP C_1). CPP C_2 is embedded in light brown sediments, whereas CCP C_1 is embedded in light greyish-brown sediments between 83–45 cmbsf and dark brown sediments between 45–0 cmbsf. Trace amounts of CWCs occur at 180–165 cmbsf (defined as CPP D_2) and 125–83 cmbsf (defined as CPP D_1), embedded in yellowish-grey sediments. One AMS ^{14}C date of late Pleistocene age (38 ka BP) was obtained from core CE_VC4 (83 cmbsf).

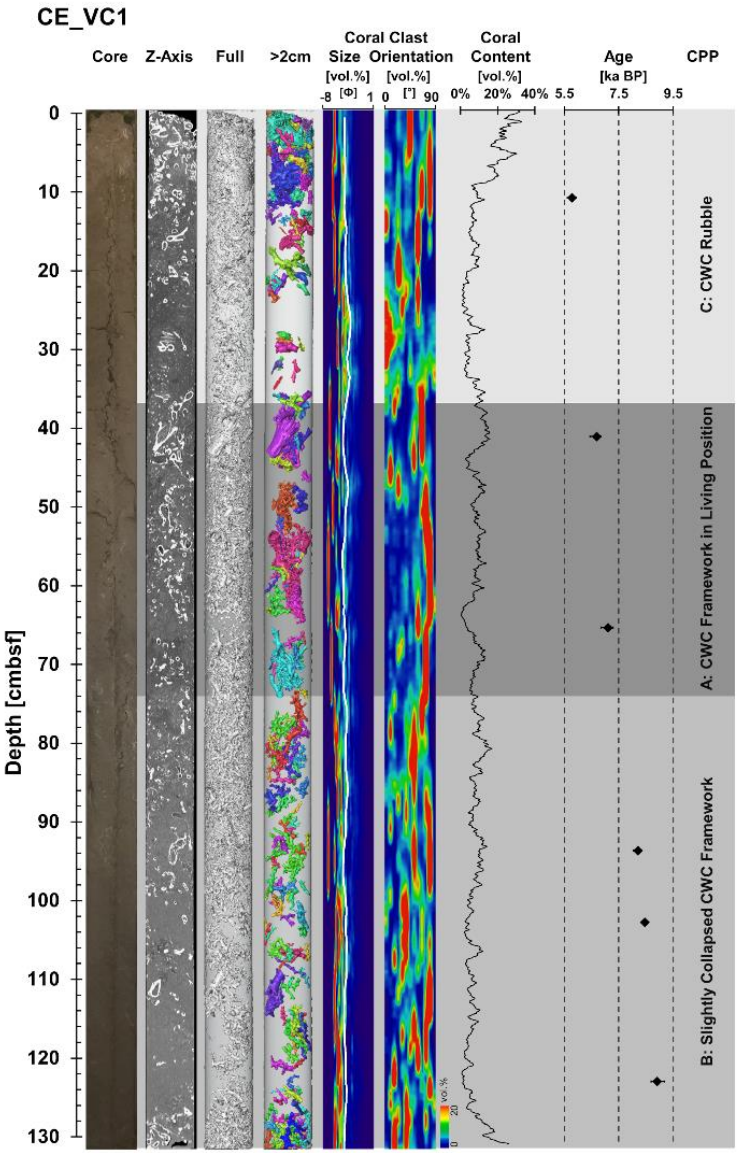
Core CE_VC5 contains mostly broken coral rubble embedded in brown sediments. CPP C occurs at 115 – 79 cmbsf (defined as CPP C_2) and 33–0 cmbsf (defined as CPP C_1). Trace amounts of corals occur from 79–33 cmbsf (defined as CPP D). The basal core (115–79 cmbsf) exhibits light brown sediments. Between 79–45 cmbsf, the sediments become progressively lighter. The top of the core (45–0 cmbsf) is brown sediments. Five AMS ^{14}C ages were obtained from core CE_VC5, ranging from 45.1 ka BP to 10.6 ka BP. Three dates (45.1, 40.8 and 37 ka BP) occur in the late Pleistocene, and two dates (11.1 and 10.6 ka BP) occur in the early Holocene. Maximum SR of 22.8 cm ka^{-1} occurs between 11.1 and10.6 ka BP. AR for the entire constrained core is 2.9 cm ka^{-1}.

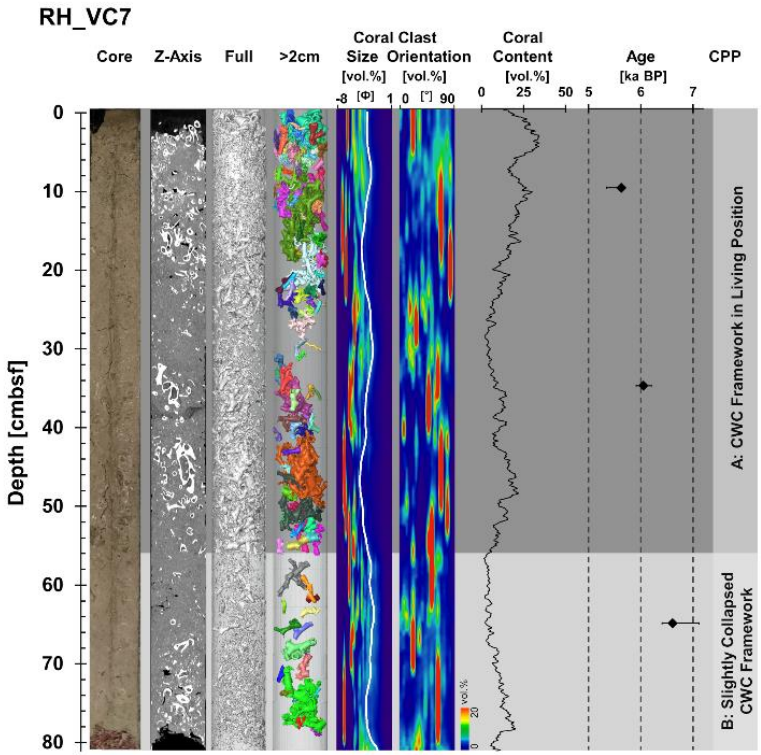
4.4.1.3 Canyon Slope/Foot of the Slope Cores

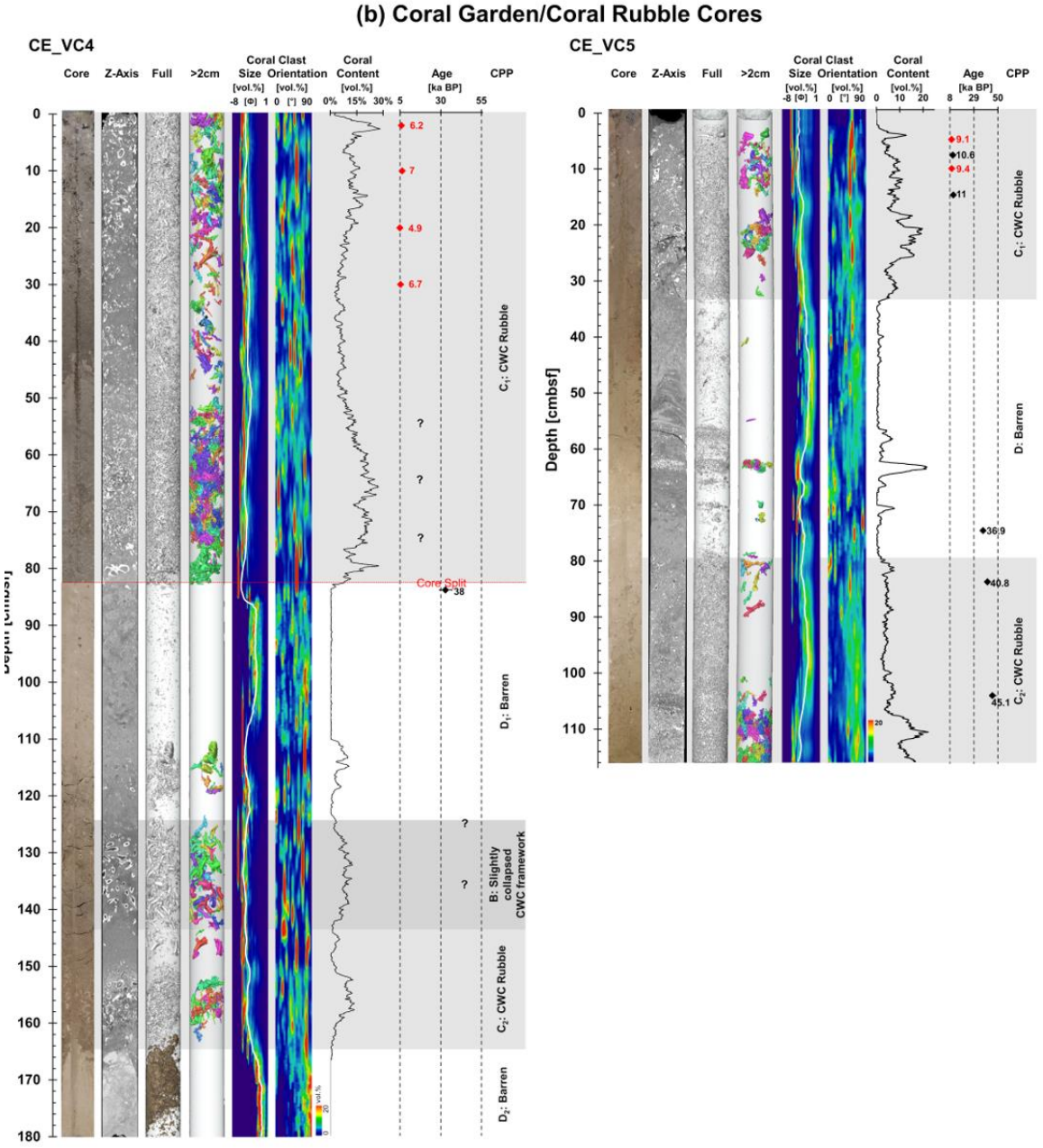
In core CE_VC6, bioclastic material (including coral pieces) and small black lithic clasts are abundant in the basal core (37–40 cmbsf; see Fig. 20c), embedded in dark brown sediments. The deposition of this material fines upwards until 29 cmbsf. One AMS ^{14}C age was obtained above visible bioclastic material from core CE_VC6, provided a late Pleistocene age of 15.0 ka BP. One U/Th date was obtained from the bioclastic material, whereby a *D. pertusum* clast provided a MIS 5b age of 87.5 ka BP.

In cores CE_VC8 and RH_VC7, bioclastic material (including coral pieces) is abundant at the base (34–18 and 30–11 cmbsf, respectively) and progressively fines upwards. The coral pieces are embedded in olive grey sediments. One U/Th date was obtained from the bioclastic material in core CE_VC8, whereby a *M. oculata* clast provided a MIS 4 age of 75.5 ka BP.

(a) Coral Summit Cores






(b) Coral Garden/Coral Rubble Cores
CE_VC4
CE_VC5
Core
Z-Axis
Full
>2cm
Coral Clast Size [vol.%] -8 [Φ] 1
Coral Clast Orientation [vol.%] 0 [°] 90
Coral Content [vol.%]
Age [ka BP]
CPP
Depth [cmbsf]
Core Split
C1: CWC Rubble
D1: Barren
B: Slightly collapsed CWC framework
C2: CWC Rubble
D2: Barren
D: Barren

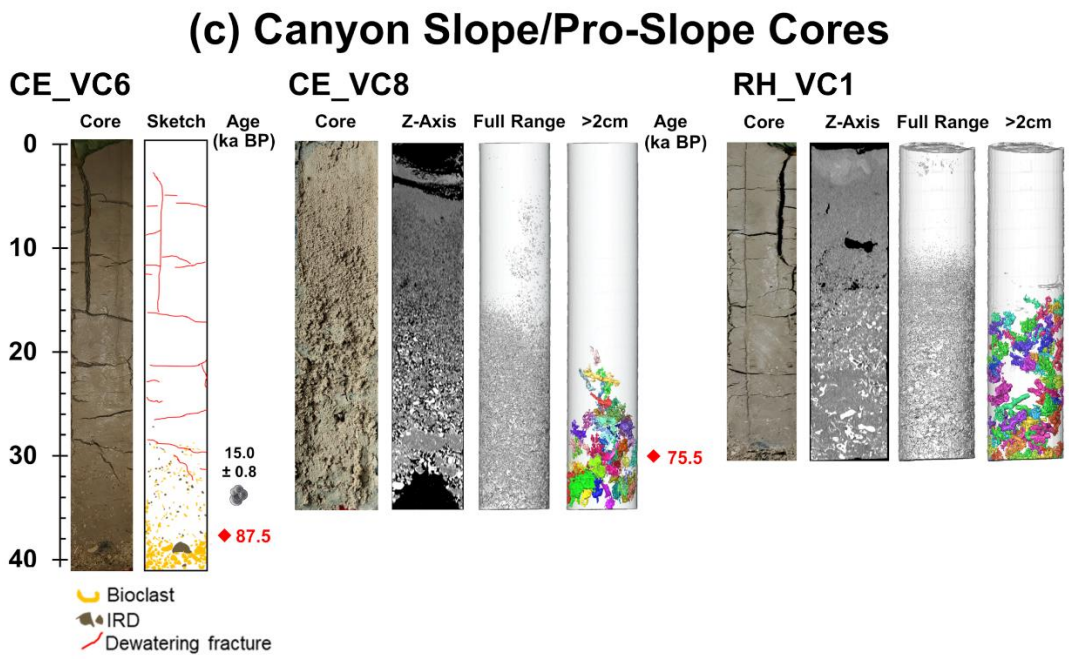


Figure 20: Logs of cores from coral mound summits (a), coral rubble areas adjacent to mound flanks (b) and canyon slope/foot of the slopes of the Porcupine Bank Canyon. For (a) and (b) left to right: Photograph of core; z-axis CT-image of core, with darkness a function of density; core CT 3D image of coral clasts in full-size range; coral clasts larger than >2cm; coral clast size distribution where white line indicating mean clast size (0–20 vol.% of clasts: blue to red, respectively); coral clast orientation quantified coral content based on the CT data; vol.% of coral content determined from CT; calibrated ^{14}C dates as kilo annum before present (black) and reliable U/Th dates as kilo annum before present (red); Cold-water coral (CWC) preservation patterns (CPPs; A - CWC framework in living position; B - slightly collapsed CWC framework; C - CWC rubble; D – barren of CWC). Note in (b) core split in core CE_VC4 at 83 cmbsf and pending U/TH dates. For (c) from left to right: the true colour image of Core CE_VC6, sketch of core inferred from true-colour image and calibrated ^{14}C date at 34 cmbsf; true colour image of cores CE_VC8, orthogonal CT-image of core, core CT 3D image of coral clasts in full-size range and coral clasts larger than >2cm; and true colour image of cores RH_VC1, orthogonal CT-image of core, core CT 3D image of coral clasts in full-size range and coral clasts larger than >2cm.

Table 8: AMS ^{14}C dates obtained from benthic and planktic foraminifera and CWC fragments collected from cores in this study. Ages from cores CE_VC1 and RH_VC7 (red) taken from chapter 3 of theisis. Reservoir (res.) ages and error, calibrated (cal.) age determined from Paleo Data View (Langner and Mulitza, 2019) using the modelled reservoir ages of Butzin et al. (2017). The age model (AM) was determined using BACON (Blaauw and Christen, 2011). Aggradation rates (AR) and sedimentation rates (SR) are calculated using BACON. Top most and bottom most ARs were calculated using best estimates of the top and bottom cores age using BACON, whereby Bayesian statistics was utilized to interpolate beyond constrained age limits.

Core	Depth [cm]	Lab ID	Dated Material	Conventional Age [ka]		Cal. age [ka BP]					AR/SR
				^{14}C Age ka BP	Error ka or %	Res. Age ka	Res. Age Error	μ-2σ ka BP	μ+2σ ka BP	Median ka BP	[cm ka^{-1}]
CE_VC1	11	D-AMS 039278	Mixed benthic	5.579	0.03	0.53	0.051	5.602	5.923	5.779	30.4
	41	D-AMS 039277	Mixed benthic	6.461	0.03	0.523	0.05	6.437	6.851	6.684	394.4
	65	D-AMS 045772	*M. oculata*	6.529	0.03	0.534	0.05	6.838	7.295	7.101	20.4
	93	D-AMS 037306	Mixed benthic	7.9	0.03	0.512	0.051	8.025	8.35	8.198	32.7
	102	D-AMS 037307	Mixed benthic	8.16	0.03	0.475	0.05	8.33	8.586	8.455	58.7
	122	D-AMS 034764	*G. bulloides*	8.486	0.04	0.526	0.053	8.689	9.184	8.907	-
VC4	83	D-AMS 038049	*G. bulloides*	34.5	0.2	1.285	0.455	36.682	39.319	38.015	-
CE_VC5	8	UBA 42672	Mixed benthic	9.816	0.03	0.414	0.053	10.287	10.769	10.582	22.8
	15	UBA 42902	Mixed benthic	10.761	0.05	1.172	0.056	10.77	11.354	11.048	2.2
	74	D-AMS 038050	Mixed benthic	33.839	0.19	1.395	0.455	35.572	38.965	36.969	2.1
	83	D-AMS 034766	Mixed benthic	38.084	0.31	1.875	0.493	38.911	41.939	40.82	6.3
	103	UBA 42673	*G. bulloides*	43.203	1.16	1.792	0.566	43.061	48.847	45.132	-
VC6	34	D-AMS 034767	*G. bulloides*	13.473	0.1	1.197	0.474	13.312	15.834	14.499	-
RH_VC7	10	D-AMS 043458	*M. oculata*	5.429	0.03	0.505	0.052	5.35	5.687	5.627	64.6
	35	D-AMS 043459	*M. oculata*	5.786	0.03	0.518	0.051	5.911	6.203	6.05	74.4
	65	D-AMS 034770	*G. bulloides*	6.194	0.04	0.52	0.055	6.407	7.113	6.608	-

Table 8 continued: U/Th dates acquired from from cold-water coral fragments in in this study. Provided are 232Th concentrations and decay corrected $^{234}U/^{238}U$ activity ratios [$\delta^{234}U(i)$] calculated from the given. High ^{232}Th concentration values (red).are most likely affected by diagenetic alternation and as such provide unreliable ages. Where ages have attributed high $\delta^{234}U_{ini}$ values (black italics), are also deemed unusable as these ratios exceed quality control thresholds (Andrea Schröder-Ritzrau. personal correspondence, 2022). Note: for cores CE_VC6, CE_VC8 and RH_VC7, coral pieces were extracted from the entire sieved sample and such have no depth value.

Core	Depth [cmbsf]	Lab ID	Dated Material	^{238}U (µg/g)	± (abs.)	^{232}Th (ng/g)	± (abs.)	$\delta^{234}U$ ($^{o}/_{oo}$)	± (abs.)	Age (uncor.) (ka)	± (abs.)	Age (cor.) (ka)	± (abs.)	$\delta^{234}U_{ini.}$ ($^{o}/_{oo}$)	± (abs.)
CE_VC4	2	IUP- 11506	*M. oculata*	4.5034	0.0014	0.4952	0.0018	151.41	0.65	6.221	0.023	6.194	0.027	154.08	0.66
	10	IUP- 11507	*M. oculata*	3.6671	0.0011	0.1170	0.0005	152.58	0.64	7.023	0.032	7.015	0.032	155.63	0.66
	20	IUP- 11524	*Coral fragment undetermined*	4.4599	0.0015	**6.489**	**0.013**	147.00	0.76	4.899	0.029	4.54	0.18	148.89	0.77
	30	IUP- 11525	*D. pertusum*	4.89120	0.00029	**14.959**	**0.027**	146.66	0.76	7.440	0.026	6.68	0.38	149.45	0.79
	55	IUP- 11526	*M. oculata*	4.06738	0.00026	2.2563	0.0056	117.20	0.83	118.36	0.51	118.22	0.51	***163.6***	***1.2***
	65	IUP- 11508	*M. oculata?*	4.1985	0.0012	0.7652	0.0019	117.19	0.67	111.50	0.46	111.45	0.46	***160.51***	***0.94***
	75	IUP- 11527	*Coral fragment (M. oculata ?)*	4.42550	0.00024	0.5816	0.0029	115.98	0.80	191.4	1.5	191.3	1.5	***199.0***	***1.6***
	125	IUP- 11528	*D. pertusum*	3.53745	0.00020	**14.867**	**0.031**	131.60	0.86	148.13	0.76	147.13	0.90	***199.3***	***1.4***
	135	IUP- 11529	*D. pertusum*	2.97885	0.00020	**4.197**	**0.011**	143.7	1.4	132.28	0.72	131.95	0.73	***208.5***	***2.1***
CE_VC5	5	IUP- 11520	*M. oculata*	4.4499	0.0020	**5.3409**	**0.0091**	148.07	0.61	9.438	0.032	9.14	0.15	151.94	0.63
	10	IUP- 11521	*M. oculata*	5.12265	0.00042	1.285	0.013	151.12	0.72	9.41	0.11	9.35	0.12	155.16	0.74
CE_VC6	N/A	IUP- 11509	*D. pertusum*	3.5527	0.0013	0.5431	0.0012	121.48	0.81	87.50	0.31	87.46	0.31	155.5	1.0
CE_VC8	N/A	IUP- 11510	*M. oculata*	4.3663	0.0017	1.0556	0.0021	116.23	0.67	75.52	0.31	75.45	0.31	143.81	0.83
RH_VC7	N/A	IUP- 11511	*M. oculata*	4.7215	0.0015	0.4992	0.0017	168.22	0.52	10.123	0.050	10.098	0.051	***173.08***	***0.54***
	N/A	IUP- 11522	*D. pertusum*	4.1096	0.0012	0.8275	0.0035	158.1	1.1	0.158	0.016	0.108	0.030	***158.2***	***1.1***
	N/A	IUP- 11523	*D. pertusum*	4.24588	0.00027	1.8178	0.0041	161.6	1.9	11.565	0.079	11.460	0.094	***166.9***	***2.0***

Age correction according to ^{232}Th concentration and a seawater $^{230}Th/^{232}Th$ ratio of 8±4.
Ag+A1:W20e correction is negligible within the uncertainties for all data.

4.5. Interpretation & Discussion

The *Holland 1 ROV* vibrocoring rig allowed for the precise recovery of cores(presented in this thesis) from various geomorphological settings of the wPB and PBC, including the continental bank, lip, slope and foot of the slope (Fig. 19). Previous gravity coring missions of the area proved unsuccessful due to the challenging seafloor morphology of the canyon and hard substrate (i.e. vertical walls; see Wheeler et al., 2014). 3D-segmented CT and radiocarbon dating show that certain reef and mound development facies types are found within specific geomorphological settings and restricted to limited time intervals.

4.5.1 Geomorphological Control of and Cold-Water Coral Distribution

4.5.1.1 Coral Mound Summit Cores

Cores acquired from the summits of coral mounds on the wPB (CE_VC1) and close to the canyon lip (RH_VC7) each span from the early to middle Holocene, between 9.1 to 5.7 ka BP (see Chapter 3). In contrast, cores acquired from geomorphological settings adjacent to these mounds occupied by coral rubble rich sediments deposited from the late Pleistocene to early Holocene, between 45.1 to 10.6 ka BP.

The temporal variability of mound AR in core from the coral mound summits is the product of coral framework construction, bioerosion, sediment trapping and compaction. Maximum AR captured in core CE_VC1 between 65–41 cmbsf are typical rates for fast mound development, allowing corals to be e in a living position (394 cm ka^{-1}; Fig. 20a). The radiocarbon ages suggest this rapid development rate occurred in the mid-Holocene between 7.1–6.7 ka BP. This 400-year environmental window showing optimal mound development is likely facilitated by a large and densely distributed coral framework that permits a high baffling capacity likely facilitated by optimal environmental conditions as well as sufficient sediment supply (Mullins et al., 1981, Dorschel et al., 2007b, Foubert et al., 2008, Huvenne et al., 2009, Mienis et al., 2009, Victorero et al., 2016, Wang et al., 2021). The high accommodation space provided by

the framework, when in conjunction with a high sediment supply, rapidly fills the framework, preventing bioerosion, thus preserving the framework in its living position (Wang et al., 2021). Except for this brief event, mound AR in the wPB and PBC (mean of 47.0 and 32.9 cm ka^{-1} for cores CE_VC1 and RH_VC7, respectively) are comparable to other Holocene NE Atlantic mounds (Frank et al., 2009, López Correa et al., 2012, Douarin et al., 2013, Elliot et al., 2019) These deposits are mainly characterised by CPP facies type B (defined as “slightly collapsed coral framework”; see Titschack et al., 2015, Titschack et al., 2016, Wang et al., 2019). In this instance, the coral framework provides sufficient accommodation space but a low sediment supply, thus leading to higher rates of bioerosion and fragmentation (Wang et al., 2021). Holocene coral mounds across the NE Atlantic Margin show similar fast and slow phases in mound development (Frank et al., 2009, López Correa et al., 2012, Douarin et al., 2013, Titschack et al., 2015) that deviate by a few hundred years across the region. These settings (the Porcupine Seabight, Norwegian fjords and SW Rockall Bank) endure unique changes to hydrodynamics and water-mass properties that account for changes to mound development. These are primarily controlled by the influence of the Sub Polar Gyre, that modified the North Atlantic climatic conditions on a centennial timescale (see Thornalley et al., 2009, Colin et al., 2010, Copard et al., 2012, Douarin et al., 2013). In addition, further climatic driven modifications were driven by atmospheric reorganisation throughout the early Holocene (e.g. Douarin et al., 2016). These adjustments possibly led to nutrient depletion for ecosystems on many spatial scales (Van Nieuwenhove et al., 2018).

The topmost attained dates from cores CE_VC1 and RH_VC7 (see Table 8; see also Fig. 20a) imply that mound development across the region has slowed and halted since at least 5.6 ka BP. This suggests that present-day coral mound development is less effective today than during the mid-Holocene in the PBC. Other regional records (see Eisele et al., 2011, Frank et al., 2011, López Correa et al., 2012, Douarin et al., 2013) show similar patterns, although they become less effective much later into the Holocene. Although the decline of mound development from other parts of the NE Atlantic appear to show a scattered pattern (Frank et al., 2009, López Correa et al., 2012, Douarin et al.,

2013, Elliot et al., 2019), it does suggest that in general, the wider European region was affected by the same external controls. Most likely, this was caused by large-scale environmental modifications associated with changes in the North Atlantic Sub Polar Gyre (Douarin et al., 2014).The low coverage of living coral frameworks seen today (Appah et al., 2020, Lim et al., 2020b) suggests that the external controls that impaired mound development is still at play.

4.5.1.2 Coral Rubble Cores from the Flat wBP Top Sediments

Core CE_VC5 was acquired approximately 100 m from the canyon lip at the boundary between coral mounds and surrounding continental margin; an area of relatively flat topography (Lim et al., 2018; see Fig. 19b, 1c, 1d; see also Fig. 21). Before coring, visual observations of the seafloor identified the sediments as containing coral rubble pieces and minor abundances of living coral. CT scanning and radiocarbon dating show that corals were growing since at least 45.1 ka BP and briefly after 37 ka BP (see Table 8; see Fig. 20b between 115–93 cmbsf). A similar coral rubble deposit is observed higher in the core between 33–0 cmbsf (Fig. 20b). Corals in this unit are constrained by AMS dating to 11–10.5 ka BP (Table 8). Considering the geomorphological setting, this unit has a relatively high sedimentation rate (SR) (22.8 cm ka^{-1}) instead of the average SR for the entire core (2.9 cm ka^{-1}).

Core CE_VC4, was acquired approximately 710 m to the west of the wPB mound (CE_VC1) and approximately 460 m to the south-east of the PBC summit, characterised by core RH_VC7 (see Fig. 19b and 1c). During the ROV-mounted acquisition of core CE_VC4, a minor abundance of coral rubble and living coral was observed on the seafloor, similar to core CE_VC5. A brief CPP B unit (defined as a “slightly collapsed coral framework”) is visible from 144–125 cmbsf (Fig. 20b; see also Fig. 21). The average mean coral clast size of this unit (-4.8 Φ; see Appendix XV) is comparable to CPP B in both CE_VC1 (-5 Φ) and RH_VC7 (-4.8 Φ), providing evidence for a brief phase of dense coral growth at this location which has become subsequently buried with no surface expression. Given the distance of both these cores from coral mounds and the generally flat topography of the wPB, an allochthonous origin, for

example, by debris flows, is unlikely. Debris flows originating from mounds are expected to immobilise close to the foot of the mounds where the maximal change in slope range from about 20–30° to ~0° (Lowe, 1982). Consequently, these coral rubble units are interpreted parautochthonous deposits originating from a broader coral colonisation on the open margin. The sparsely distributed abundances of coral framework would provide a small accommodation space compared to densely packed coral framework living on a mound summit (Wang et al., 2021). As such, a reduced baffling capacity restricts the deposition of current-transported sediments, exposing the reef to bioerosion and fragmentation, ultimately causing their collapse and the deposition as coral rubble (Titschack et al., 2015, Titschack et al., 2016, Wang et al., 2019, Wang et al., 2021). Despite the high sediment input, the associated AR is low. A similar process was observed in the Alborán Sea, during less favourable environmental conditions for CWC proliferation (Wang et al., 2021), eventually leading to hiatuses in mound development. This occurs in other CWC mound records from the Atlantic Ocean (Dorschel et al., 2005, Rüggeberg et al., 2007, Frank et al., 2009, Mienis et al., 2009b, Wienberg et al., 2018).

CT analysis of cores CE_VC4 and CE_VC5 show that between 40.8–11 ka BP, CWC content remained consistently low (Fig. 20b), suggesting that the development of coral mounds in this setting were inhibited resulting from the environmental conditions present on the margin. During the Late Pleistocene, an off-mound core taken from the wPB captured decelerated currents occurring during stadial events at 36.4, 33.1 and 28 ka BP. Several fluxes of ice-rafted debris were also captured in the core, describing the deglaciation history of the British-Irish Ice Sheet (O'Reilly et al., 2022). Low current speeds, combined with an enhanced input of terrigenous material during BIIS deglaciation, may have overburdened the coral frameworks with sediment (Wang et al., 2021). The negative impact of BIIS related processes, including changes to water masses and deposition of ice-rafted debris, on CWC mound development has been captured elsewhere on the margin (Freiwald et al., 2004, Frank et al., 2011, Pirlet et al., 2011, Bonneau et al., 2018). During these deglaciation events, alterations to the hydrographic regime reduced food supply to the corals (Pirlet et al., 2011). Furthermore, the wPB was subjected

to iceberg scouring since at least 17.2 ka BP. Grounded icebergs could be responsible for preventing the broader colonisation of the PB, as shown along the Norwegian-Svalbard margin (Ottesen et al., 2005). However, more severe limitations include shallowing sea levels and reducing primary production from expanded ice sheets.

4.5.1.3 Canyon Slope/Foot of the Slope Cores

Cores CE_VC8 and RH_VC1 represent the first cores retrieved from a coral tallus on steep canyon slopes. Today, the steep slopes of the PBC prevent mound development and are instead occupied by overhanging individual CWCs (Wheeler et al., 2017, Lim et al., 2018). Observations of ROV data show that this setting contains small tallus deposits that accumulate between steps of protruding bedrock (Wheeler et al., 2017, Lim et al., 2018). The cores acquired from these settings are short in length (each <40 cm; Table 7; Fig. 20c), likely due to the thickness of the respective tallus deposit. Analysis of the cores shows that they are composed of bioclastic material (including CWC pieces) and background sediment (Fig. 20c). CT imagery shows that the bioclastic material shows a fining upward sequence, indicative for a deposition by mass-wasting. Considering the steep topography of the slope and distance from source, the deposition by a debris fall process is likely (Titschack et al., 2005). In core CE_VC6 taken from the foot of the slope (Fig. 19b and 1c; see Table 7), a bioclastic-rich unit is visible at its base (Fig. 20c and Fig. 21), likely capturing the lateral continuity of the debris flow. A large black clast is also visible and is likely deposited from ice-rafting (i.e. O'Reilly et al., 2022) AMS ^{14}C dating directly above this unit potentially constrains this event to shortly after 15 ka BP (Table 8; see also Fig. 20c).

4.5.1.4 Coral Development Model

Figure 21 schematically summaries the coral development model for coral growing in close proximity of a submarine canyon as revealed by the analysis of cores from the wPB and PBC. Evidence from core CE18011_VC5 suggests that corals occupied the bank from 45.1 ka BP to at least 36.9 ka BP. CT-derived CPP from core CE18011_VC4 suggests that a brief period of mound development occurred on the bank during this phase. The mechanism behind

the sustained growth of the reefs is canyon-related upwelling, that provides the corals with an enriched food supply. The LGM enforced an environmental tipping point, whereby corals were unable to inhabit the bank. It is probable that corals survived along the slope of the PBC throughout this phase, where food supply remained frugal along watermass boundaries (i.e. ENAW-MOW boundary). Following the Younger Dryas, favourable environmental conditions returned to the region and corals recolonised the bank. During the early Holocene, mounds development on the canyon lip and wPB re-initiated.

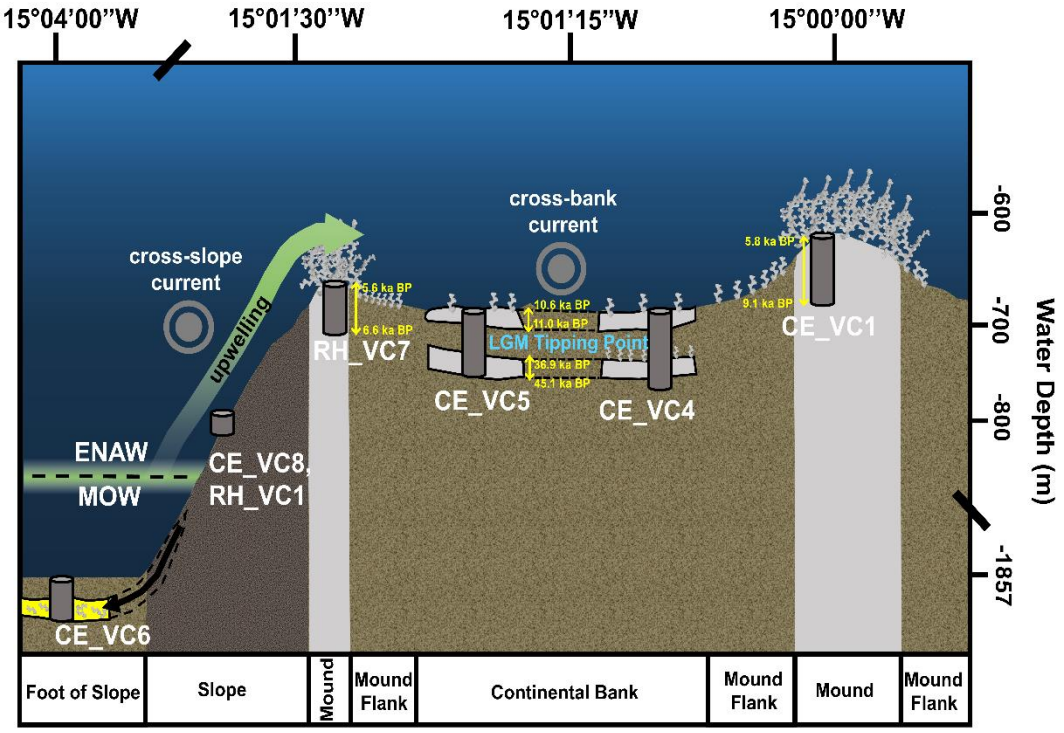


Figure 21: Sketch of CWC reef patterns affected by geomorphological settings. Cores CE_VC1 and RH_VC7 were taken from the summits of coral mounds from the wPB and along the canyon lip, respectively. Cores CE_VC4 and CE_VC5 were acquired along topographically flat sections of the wPB, where the colonisation of individual corals occur (defined as CPP C – grey). Upwelling (green) remains the most likely causation of canyon lip mound development, redepositing enriched particles found along the boundary between the ENAW and MOW. The mounds on the wPB also benefit from this, although not to the same degree (O'Reilly et al., 2022). In core CE_VC4, an initial phase of mound development is preserved on the surface of the lower CPP C facies. Cores CE_VC8 and RH_VC1 were captured along the slope of the PBC and are composed of coral debris (Fig. 20c). Core CE_VC6 was taken from the foot of the slope and is characterised by a bioclastic rich unit at its base (yellow), deposited during a debris flow. Note the detached scale on the x and y axes.

4.5.2 Glacial Occurrence of Cold-water Corals: Unprecedented Evidence on the High Latitude European NE Atlantic margin

Previously, it was thought that the export of Mediterranean waters triggered CWC larvae dispersal into the NE Atlantic after the completion of the Younger Dryas (De Mol et al., 2005, Henry et al., 2014). This research suggests that corals occupying the Gulf of Cádiz and/or the Mediterranean Sea during the last glacial followed the pathways of the MOW created by a re-invigorated AMOC during the deglacial led to the rapid CWC expansion in the NE Atlantic (~7500 km under 400 years; e.g. Douarin et al., 2013, Henry et al., 2014, Elliot et al., 2019). In contrast, Wienberg et al. (2018) suggested that canyons might serve as refugia for CWCs during unfavourable conditions on the slope and might act as local spreading sites for re-colonisation of the adjacent slopes. A confirmation of this hypothesis was so far hampered due to the challenging topography, which limited the operation of coring (Henry et al., 2014; see also Wheeler et al., 2014). Our novel ROV-vibrocoring method provides the first empirical evidence of canyon-related glacial coral occurrences off Ireland, extending the current estimates of CWCs occupying the Irish margin by over 30 ka BP (see Henry et al., 2014 and references therein).

Cores CE_VC4 and CE_VC5 provide glacial AMS ^{14}C dates from the matrix sediment surrounding coral pieces. This coral bearing facies type is interpreted as a coral garden, an area containing coral growth on the margin, that do not form large three-dimensional carbonate structures (Davies et al., 2017). Today, similar spatial distributions are observed in the area (Appah et al., 2020). The small coral frameworks baffled currents enducing sediment deposition supporting coral growth (e.g. Mullins et al., 1981, Dorschel et al., 2007b, Eisele et al., 2014, Victorero et al., 2016), by protecting the fossil part of the coral framework from degradational processes as is indicated by the low degree of bioerosion observed on the surface of the majority of coral pieces (see Appendix XVI). Consequently, a low deviation between the matrix sediment AMS ^{14}C dates and the age of the coral fragments are expected with the corals being older. A temporal offset between planktic foraminifera ages

from the matrix sediments and coral ages is described from the Mauritanian margin. Still, it is generally expected to be less than several thousand years (Eisele et al., 2014). Accordingly, the CWC occurrence and growth are assigned to the last glacial time interval. More conclusive evidence of glacial CWCs are provided by the U/Th dating of coral pieces from the canyon slope cores (Table 8). In core CE_VC6, a *L. pertusa* clast recorded an age of 87.5 ka BP, constraining it to MIS 5b. Additionally, in core CE_VC8 a *M. oculata* clast recorded an age of 75.7 ka BP, constraining it within MIS 4. Both of these U/Th ages suggest that either a) corals were surviving along the slopes of the canyon during glacial periods or b) that corals emerged remarkably fast in a canyon slope setting post glacial conditions.

The herein presented data provides just a glimpse into the complex coral history in the PBC. Further sampling is urgently needed to obtain a more complete impression of the glacial history of CWC occurrence in PBC and other submarine canyons in the NE Atlantic. In the event of similar findings, the hypothesis of submarine canyons as spreading points for CWCs presents a more reasonable rationale than the model invoked by Henry et al. (2014).

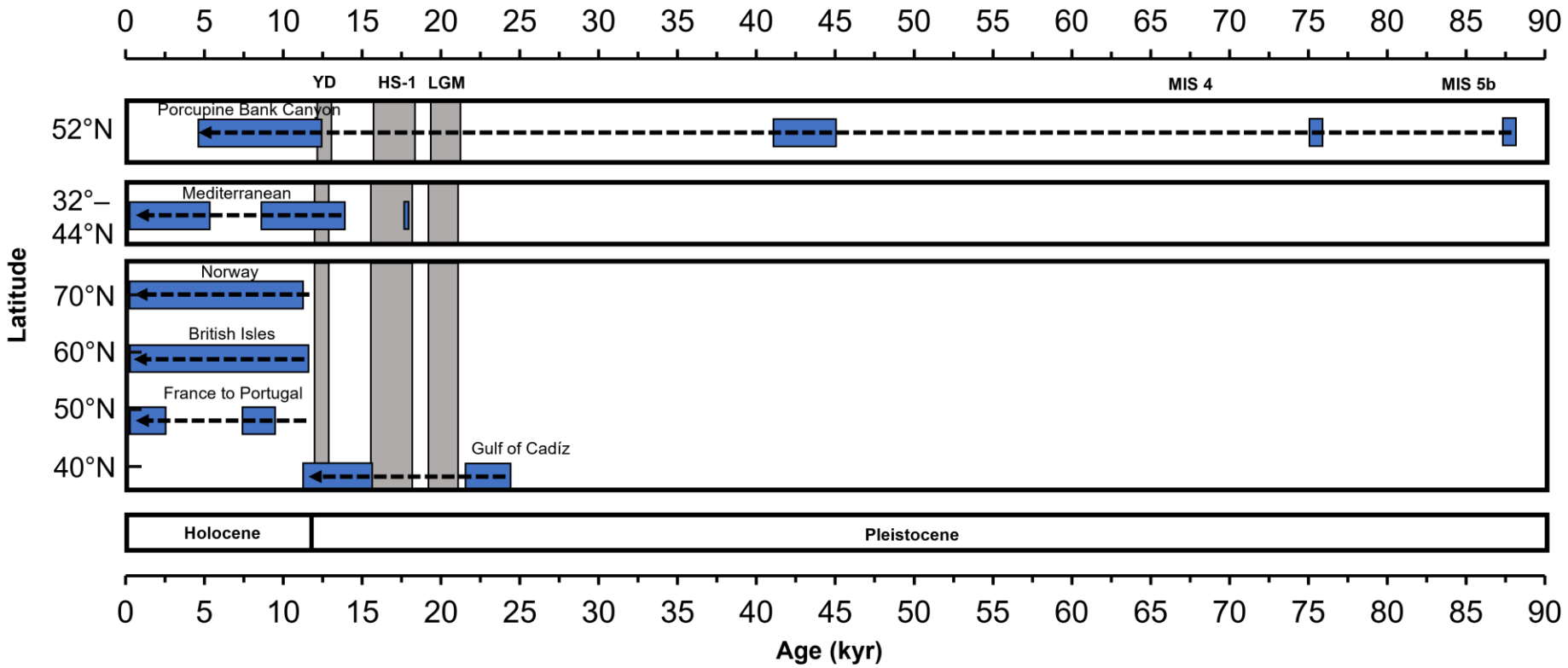


Figure 22: Adapted from Henry et al., (2014). Compilation of fossil chronology of D. pertusum in high latitudes covering the last 45 ka. Data taken from (Schröder-Ritzrau et al., 2003, Lindberg and Mienert, 2005, Roberts, 2005, Schröder-Ritzrau et al., 2005, Frank et al., 2009, Wienberg et al., 2009, Copard et al., 2010, Wienberg et al., 2010, De Mol et al., 2011, Eisele et al., 2011, Frank et al., 2011, López Correa et al., 2012, Douarin et al., 2013). Grey intervals show Younger Dryas (YD), Heinrich Stadial-1 (HS-1) and the Last Glacial Maxium (LGM).

4.5.2.1 Mechanism: Submarine Canyons Serve as CWC Refugia

Based on the glacial occurrence of CWCs, we propose that submarine canyons provided local refugia for corals along the NE Atlantic during ecologically demanded periods throughout the Late Pleistocene. Additionally, these canyon refugia might act as “stepping stones” for down-current larval transport and gene-flow during unfavourable conditions on the slope. Consequently, they play a vital role in the rapid expansive nature of CWCs in the NE Atlantic during the Holocene. Following the northern migration of the polar front, previously optimal environmental conditions for CWC growth were restored on the slopes (Frank et al., 2011), triggering enhanced surface ocean productivity (Rüggeberg et al., 2007). Furthermore, the return of the MOW enhanced bottom currents (Dorschel et al., 2005, Øvrebø et al., 2006, Rüggeberg et al., 2007). This reorganisation of the regional water column structure, combined with this enrichment in water productivity, increased the food supply to the corals during the Holocene (Frank et al., 2011), initiating the regional “tipping point” for CWC re-occurrence (Hebbeln et al., 2019). During these ecologically favourable conditions, coral larvae originating from the canyon refugia allowed the simultaneous CWC colonisation on the Rockall Bank and in the Porcupine Seabight 11.3 ka ago (Douarin et al., 2013, Wienberg et al., 2018). The slight delay of the coral colonisation of the Norwegian shelf at 10.9 ka (Stjernsund; see Frank et al., 2009, López Correa et al., 2012) might result from the limited data from this region and/or the delayed establishment of favourable conditions for the CWCs. The high abundance of submarine canyons incising the NE continental margin (Fig. 23), several of these with known occurrences of CWC (e.g. Huvenne et al., 2011, van den Beld et al., 2017), clearly shows the high potential of submarine canyons as coral refugia and local spreading centres for re-colonisation.

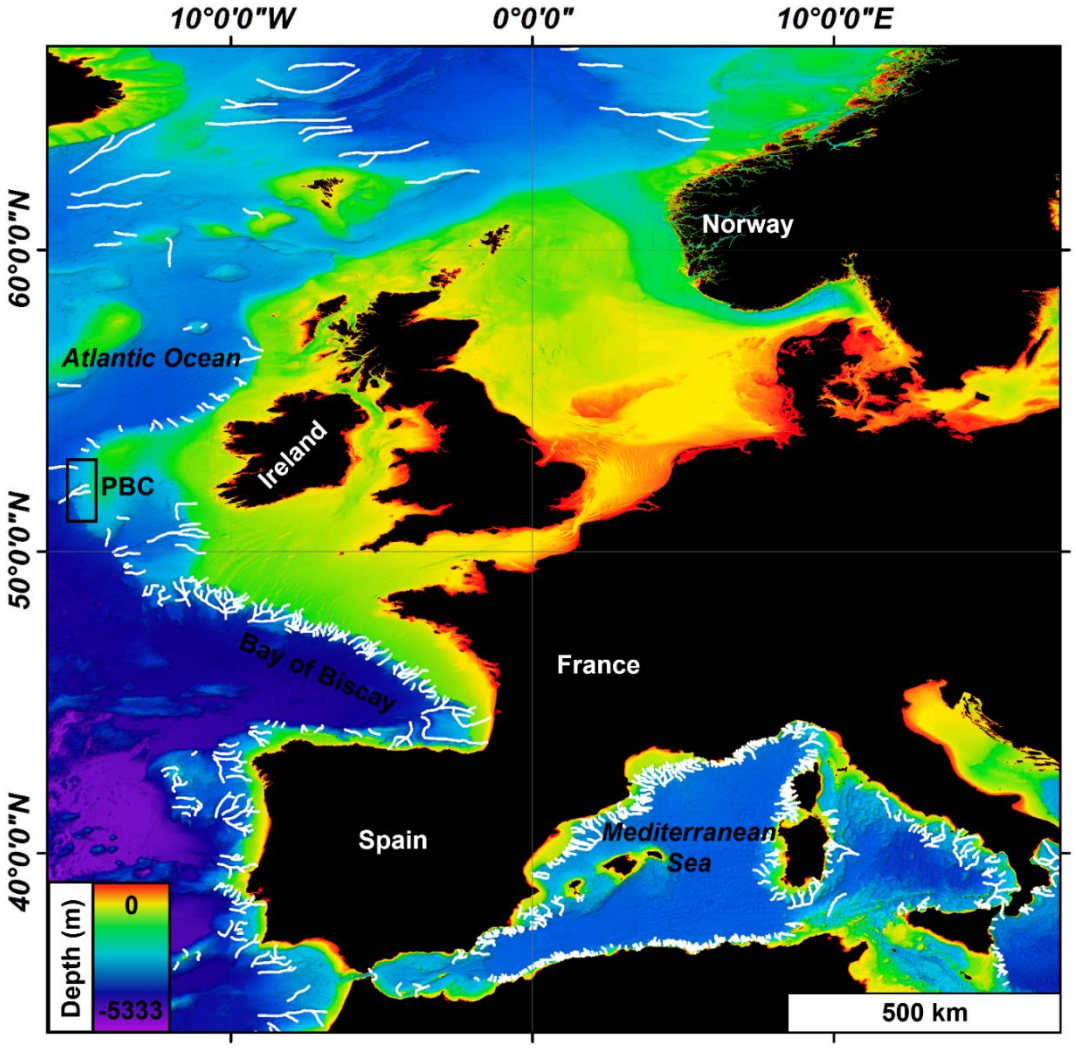


Figure 23: Submarine canyons (white; see Harris and Whiteway, 2011) located along the NE Atlantic continental margin. These settings represent ideal refugia to CWCs during environmental "tipping points" (Hebbeln et al., 2019). Maps created using ArcGIS Desktop v10.6 (www.arcgis.com). Bathymetry was taken from European Marine Observation and Data Network (EMODnet; https://emodnet.ec.europa.eu/en). Submarine canyon localities were taken from Harris and Whiteway (2011).

For CWC colonies occupying deeper water, breaking internal tides could promote increased bottom mixing and resuspension (Frederiksen et al., 1992) that enhance the vertical flux of particles (Sandstrom and Elliott, 1984), creating a constant food supply for benthic suspension feeders. Today, the boundary between the ENAW and the MOW occurs along the slope of the PBC at 800 m water depth (White and Bowyer, 1997, Mazzini et al., 2011). This boundary, or "transition zone", was linked with the re-initiation of CWCs in the Porcupine Seabight (Wienberg et al., 2020) that provided enhanced

particles, including food supply, to the corals. Furthermore, regular flushing of the canyon caused by turbidity flows further enhance the downslope transport of near-surface waters and POM from the continental shelf to the deep sea, further enriching food supply to corals occupying the slopes (Canals et al., 2006, Canals et al., 2009, Puig et al., 2014). The correlation of CWC proliferation with enhanced downslope transport has been described for corals in other submarine canyons in the NE Atlantic and the Mediterranean (Orejas et al., 2009, Huvenne et al., 2011, Morris et al., 2013, Taviani et al., 2015).

4.6. Conclusion

Novel coring techniques used in this study granted the acquisition of an array of cores from various geomorphological settings of the PBC and the adjacent wPB. Cores taken from the summits of coral mounds show mostly large and medium sized coral pieces orientated in a living position. In contrast, cores taken from the continental bank show smaller coral pieces with variable orientations, indicative of coral rubble. A brief period of mound development was captured on the continental bank (see Fig. 20b between 144–125 cmbsf), suggesting that the continental bank hosts brief periods of local mound development. This study is the first to assess cores from the steep slopes of a submarine canyon, documenting the past occurrence of CWCs. We discovered CWC presence in the region since at least 45.1 ka BP, extending the current estimates by 30 ka. U/Th dating of coral pieces reveal that CWCs were surviving along the canyon slopes during MIS 5b and MIS 4, likely facilitated by enriched particle availability along the ENAW-MOW water mass boundary. Furthermore, this study supports a new mechanism for the post-glacial biogeographical expansion of CWCs in the NE Atlantic. Alternative to the global ocean conveyor as the primary mechanism responsible for spreading post-glacial CWC populations (Henry et al., 2014), we propose that submarine canyons act as coral refugia during unfavourable conditions (such as periods of intense iceberg scouring and ice-rafting) and local spreading centres for re-colonisation. Regional paleoenvironmental change to water mass characteristics during the onset of the Holocene provided an ecological “tipping-point” that supported the rapid re-colonisation of the adjacent slope with larvae potentially supplied by corals living in the canyons. Mound aggradation ceased shortly after 5.6 ka, implying that present-day reef development on the open slope of the wPB is sub-optimal or prohibitive.

This study provides a brief and incomplete glimpse into the occurrence of CWC and coral mound development in a complex canyon system. Due to the small preservation window of CWCs, intensive coring campaigns of other CWC occupied submarine canyons are urgently needed to improve our understanding of submarine canyons as CWC refugia. We recommend using the sampling methods outlined in this study (i.e. ROV-mounted vibrocoring). It

offers strategic targeting of alternative CWC habitat types occurring across various geomorphological settings. In addition, it grants a visual observation of the seafloor before coring. Subsequent coring missions would be well suited with spatial surveys of the habitats (e.g. Appah et al., 2020) to contextualise geological interpretations.

Finally, we propose that canyon-created geomorphological settings be protected and continuously monitored. They likely play an essential role as spreading centres for regional CWC re-colonisation when favourable environmental conditions are established. Consequently, submarine canyons might play a definitive role as refugia for marine species under global climate warming conditions.

4.7 Acknowledgements

The authors would like to thank Mr Paddy O' Driscoll (P & O) for his assistance in developing the vibrocoring unit used in this study. All shiptime is funded under the National Development Plan (2019), National Grant-aided Shiptime Programme. Luke O'Reilly is funded by Science Foundation Ireland project "MMMonKey_Pro" ([grant number: 16/IA/4528]), which is co-funded by the Geological Survey Ireland and Marine Institute Ireland. Jürgen Titschack received funding from the Cluster of Excellence "The Ocean Floor—Earth's Uncharted Interface" (Germany's Excellence Strategy—EXC-2077-390741603 of the DFG). Felix Butschek is funded from the European Union's Horizon 2020 research and innovation program under grant agreement No 818123 (iAtlantic). The authors would like to thank the MMMonKey_Pro team members and members of the Marine Geosciences Research Group at UCC and the scientific parties, officers, and crew of cruise CE18011. All authors have read and approved the manuscript.

Chapter 5. Conclusions

Within the western Porcupine Bank (wPB) and Porcupine Bank Canyon (PBC), *D. pertusum* and *M. oculata* are the most abundant scleractinian framework-forming cold-water corals found today (Appah et al., 2020). They occur as individual reefs and accumulate as connected coral mounds along the lip and head of the canyon and are also form individual disconnected mounds along the continental bank. They occupy occur at depths as shallow as 600 m (Mazzini et al., 2011). The base of the Mediterranean Outflow Water (~1150 m) corresponds to the lower limit of mound distribution in the region (Mazzini et al., 2011). This study provided for the first time, insights into the temporal evolution of the coral mounds in the wPB and PBC.

To understand the environmental conditions affecting coral growth and mound development in the region, an off-mound was first investigated answering the following research questions: **What ice-ocean interactions occurred on the wPB?** and **Are similar signals seen in other regional records?** Non-destructive analysis of the core showed that several fluxes of ice-rafted debris (IRD) were deposited on the wPB. Using other regional records to infer these signals, it was found that the I**RD fluxes are, in part, concurrent with other NE Atlantic glacial reconstructions**, which ultimately captures BIIS (de)glaciation. This IRD material originated from glaciers that either a) followed the Malin Sea Ice Stream with minor input from the Irish Sea and Donegal Bay Ice Streams or b) from an alternative route originating from the Galway-Porcupine Lobe. In addition, a hiatus was identified from 27.3–17.2 ka BP and resulted from extensive iceberg scouring on the wPB. To further access paleoenvironmental conditions, the siliciclastic fraction of the sediment was analysis. Grain size distributions and mean sortable silt size illustrate that **during glaciated events, bottom currents decelerate**, which agrees with other studies from across the margin. Furthermore, end-member modelling showed that sediment deposition is mostly locally sourced (and sorted) by bottom currents. **During glacial interstadial phases, sediments contain abundant amounts of IRD**. Additional research outlined in this thesis (see Additional Material C), provides evidence that **the region remained decoupled throughout the Late Pleistocene, suggesting that the local**

PBC provided an enriched source of food supply for the occupying benthos. Each of these findings from the off-mound core, highlight that **the study site was significantly affected by the (de)glaciation of the BIIS.** This provided key information for accessing the temporal change seen in the coral bearing cores.

These findings framed chapter 3, allowing the following research questions to be answered: **Why are coral mounds mostly distributed along the canyon lip?** and **How do environmental influences differ with distance from the canyon lip? In addition, how does this impact mound development?** A Holocene comparison between two coral mounds was made, each within varying distance from the PBC. Both mounds showed low mean aggradation rates (ARs) compared to mounds in the Porcupine Seabight and Rockall Trough. A brief window of rapid mound development was captured in the wPB mound (394 cm ka^{-1}) between 7.1–6.7 ka BP and is comparable to other mound ARs from regional sites during favourable environmental periods. Mound AR rate appeared to respond to regional climatic shifts. Benthic foraminifera assemblages showed a similar response, highlighting the link between watermass change across many biological scales. Radiocarbon dating highlighted that the mounds development ceased during the mid-Holocene (5.6 ka BP), far sooner than in the Porcupine Seabight, Rockall Trough and off Norway. The study provided, for the first time, evidence of environmental forcing subjected by a submarine canyon on mound development. **Across a contemporaneous time period, the mound located along the lip of the canyon had an AR twice as great as the mound forming on the wPB, 1 km away. We link this with an enriched food supply provided by the canyon**, as evident from the multiproxy analysis (benthic foraminifera assemblages and stable isotopic signals). **This serves as the most likely rational behind mound clustering along the canyon lip.**

Chapter 4 focused on answering **Are submarine canyons refuges for CWCs during regionally unfavorable environmental conditions?** and **If so, does this realisation undermine established models of NE Atlantic Holocene CWC re-establishment during the early Holocene phase?** To answer these research questions, an array of cores acquired from alternative settings in the

canyon (bank, lip, slope and foot of slope). It was found that there are variances in the environmental control in different geomorphological settings on reef and mound formation. The majority of mounds are confined along the lip of the canyon, whereas coral rubble comprises the continental bank. Reefs occur on the continental bank today and briefly throughout the Late Pleistocene and is interpreted as their broader colonization of the bank during environmentally favourable conditions. Radiocarbon dates taken from the matrix sediment baffled by the framework of these reefs on the wPB, suggest that corals occupied the bank during the last glacial period. The coral pieces show weak evidence for bioerosion, suggesting they buried *in situ*. **These findings indicate that submarine canyons may act as a refugia to corals** during unfavourable conditions. In addition, **they operate as spreading centres for CWCs following the return of suitable environmental parameters. This study re-writes our understanding of reef re-initiation in the NE Atlantic during the onset of the Holocene.** The absence of reefs in the cores after 36.9 ka BP suggests that paleoenvironmental conditions reached an ecological tipping point. The off-mound core provides clues as to why this occurred. The interplay of sluggish currents caused by BIIS expansion, abundant IRD and intense scouring all likely play a role.

5.1 Recommendations for Future Studies

The off-mound core in Chapter 2, was used to interpret the background paleoenvironmental signal of the wPB. However, it contained a substantial hiatus, causing a lapse in our understanding of how conditions were in the region during the LGM. Yet, it granted a distinctive insight into BIIS deglaciation, as it was located proximal to the maximum extent of the ice sheet. Thus, collecting cores from similar proximal sites, would permit further unique reconstructions of its ice-margin.

While Chapter 3 provides insights into the most recent wPB and PBC coral mound development in the Holocene, the timing and environmental controls of mound development before 9.1 ka BP remains unknown. Only with further sampling of sedimentary records from the investigated site, may we further understand how these mounds responded throughout the last glaciation. This

highlights the need for an additional coring campaign to gain further insight into these limited periods of favourable paleoenvironmental conditions.

The findings of Chapter 4 (e.g. corals living in the PBC during the last glacial period), refocuses the importance of submarine canyons as imperative localities to access coral reefs and mounds. As such, corals occupying other submarine canyons today (e.g. Huvenne et al., 2011; van den Beld et al., 2017; Wienberg 2018) should be assessed using our novel sampling methods (i.e. ROV-vibrocoring). Temporal records from these settings would add valuable insights into the findings outlined in Chapter 4, and grant further clarification if canyons offer refugia to CWCs.

Appendices

Appendix I: Computed tomography processing procedures

The raw DICOM data were processed with the ZIB edition of Amira software (version 2018.36; Stalling *et al*., 2015; http://amira.zib.de). Within Amira, the CT scans of the cores liners, including approx. 2 mm of the core rims, were removed from the data set (using a combination of the segmentation editor and the *Arithmetic* tool) to remove density artefacts resulting from the coring process. Isotropic voxels were generated by reducing each voxel size to 0.2 mm in all dimensions, correcting for partial volume averaging errors. An isosurface was created to visualise the dataset in 3D space, which was then re-positioned interactively through the live module in the software, to account for any offsets during scanning. The resampled dataset was reformatted using the Lanczos interpolation method, which tries to approximate a low-pass filter that is in accordance with the sampling theorem, thus sharpening images (see *Amira Reference Guide*, *Visage Imaging*). The macroscopic sediment components (>*ca* 1 mm), dominated by IRD, were quantified in each CT-slice with the segmentation editor (Threshold value: 1400) and the *MaterialStatistics* module (volume per slice) to understand IRD deposition phases. Further evaluation of these components was performed with the *ContourTreeSegmentation* algorithm (Threshold: 1400; Persistence Value: 1100) which is based on the concept of contour trees and functions similar to hierarchical watershed segmentation and topological persistence (see (Titschack et al., 2015) and references therein). This created an automatic segmentation of the 3D macroscopic components. At this stage, the IRD CT results were visually checked to assess if the 3D segmentation was correctly applied. The *ShapeAnalysis* module and *GrainSizeDistribution* module were used to characterise each component. Clast length [unit: $\phi = \log_2$ [length (mm)/1 mm]] was used to analyse clast size. Therefore, every clast within a window of 51 CT-slices (about 1 cm) was counted and the result was added to a spreadsheet. The analysing window was moved slice by slice. Moreover, the *ShapeAnalysis* module and *GrainAngleDistribution* module were used to characterise the z-orientation of the major axis of each clast in a similar manner, whereby horizontal = 0° and vertical = 90°. Additionally, X-ray density

of the matrix sediment was determined by calculating the mean value and its standard deviation of the matrix sediment per slice. Modifications to the threshold values were made on a core-to-core basis, due to the variable nature of compaction of the cores (see table below). The final results were exported to a spreadsheet. For on-mound core CE_VC1, coral content and coral:matrix sediment were calculated using the finalised database. For core CE18011_VC2, IRD patterns were analysed using exported results from Amira (vol. % and clasts cm^{-3}).

Threshold values used during CT analysis.

Core	Segmentation Editor Parameters	Contour Tree Segmentation Parameters
RH17002-VC1	Threshold: 1400	Threshold: 1400; Persistence Value: 1100
RH17002-VC4	Threshold: 1400	Threshold: 1400; Persistence Value: 1100
RH17002-VC7	Threshold: 1400	Threshold: 1400; Persistence Value: 1100
RH17002-VC8	Threshold: 1400	Threshold: 1400; Persistence Value: 1100
RH17002-VC9	Threshold: 1400	Threshold: 1400; Persistence Value: 900
RH17002-VC12	Threshold: 1600	Threshold: 1600; Persistence Value: 1100
CE18011-VC1	Threshold: 1400	Threshold: 1400; Persistence Value: 1100
CE18011-VC2	Threshold: 1400	Threshold: 1400; Persistence Value: 1100
CE18011-VC3	Threshold: 1550	Threshold: 1550; Persistence Value: 1100
CE18011-VC4	Threshold: 1700	Threshold: 1700; Persistence Value: 1100
CE18011-VC5	Threshold: 1700	Threshold: 1700; Persistence Value: 1100
CE18011-VC8	Threshold: 1600	Threshold: 1600; Persistence Value: 1100

Appendix II: Organic matter and carbonate dissolution procedures

Subsamples of roughly 1 cm^3 of sediment were taken from the core at 5 cm intervals. Each sample was assigned to a pre-weighed beaker, and oven-dried at 60°C for 24 hours. When dry, the sample was left cool for 30 minutes. At this stage, any large bioclasts (>2 mm) which may have been extracted in the initial sampling stage were removed. 200 ml of distilled water and 10 ml of 10% HCl were added to each beaker and heated to 90°C for 2 hours to dissolve the carbonate fraction of the sample. If an incomplete reaction occurred, extra heat and HCl were added. The samples were given 1 hour to settle. Any remaining solution was removed with a syringe, taking care not to disturb any sediment on the bottom of the beaker. The samples were then oven dried at 60°C for 24 hours. Once dry, the sample was left cool for a further 30 minutes and weighed and the aforementioned steps repeated using a solution of 10 ml of 10% H_2O_2 to oxidise organic matter from the samples. When complete, the samples were dried at 60°C for 24 hours. When completely dry the sample was left cool again for a further 30 minutes and weighed again. This final weight represents the total lithic component of the sample. Each sample was sieved through a 2 mm sieve, removing larger lithoclasts from the sample. These clasts were weighed and stored in individual containers. The sieved samples were stored in individual test tubes with 30 ml of distilled water and a solution of 5.5 g l^{-1} sodium tetraphosphate for at least 24 hours. This chemical dispersant prevented grains from aggregating during the grain-size measurements as well as after sonication.

Appendix III: Grain size analysis and operating procedures

Prior to analysis, method building was required to ensure the best representative results were retrieved with the MS3000 by optimising the machine parameters. Variations on %obscuration, stirrer speed and ultrasonic duration were determined using a fine and coarse sediment fraction, insuring a representative control on the experiment. When a consistent relative standard deviation (RSD) value <2% was yielded, these parameters constructed standard operating procedures for the study (see table below). All samples showed stability using these methods. The measurement procedure in the MS3000 was carried out with deionized water. Prior to adding the sample to the MS3000 wet dispersion unit, the sample was shaken by hand for approximately 10 seconds to minimize flocculation of particles. The sample was then introduced into the wet dispersion unit using a 1 ml pipette, allowing the addition to occur in a controlled manner. Before accepting a grain size value, the data was first inspected for anomalous results which could be attributed to air bubbles or operational errors.

Operational procedures used during grain size analysis

PSA Operating Procedures		
Particle Type		
Non-spherical		
Material Properties		
Quartz		
Refractive Index: 1.543	*Absorption Index: 0.01*	*Density (g/cm^3): 1*
Dispersant Properties		
Water		
Refractive Index: 1.33	*Level Sensor threshold: 75*	
Measurement Duration (seconds)		
Red laser		
Background: 10	*Sample: 10*	
Blue laser		
Background: 10	*Sample: 10*	
Number of measurements		
5		
Clean Type		
Normal (3 clean cycles)		

Analysis settings

General purpose

Stirrer Speed (rmp)

Fine: 2400 Coarse: up to 3400

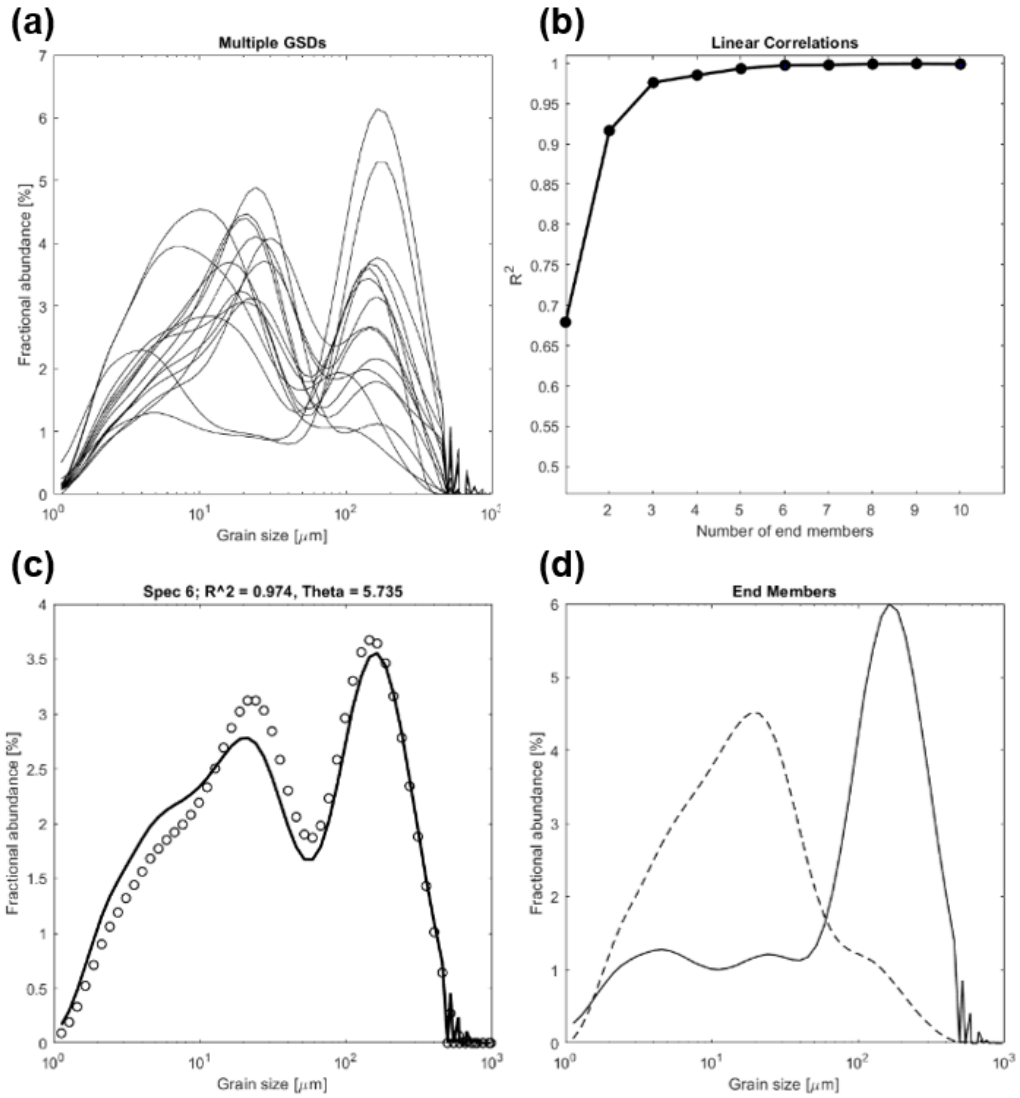
Obscuration%

Fine: 10 – 15% Coarse: 15 – 20%

Ultrasonication (seconds)

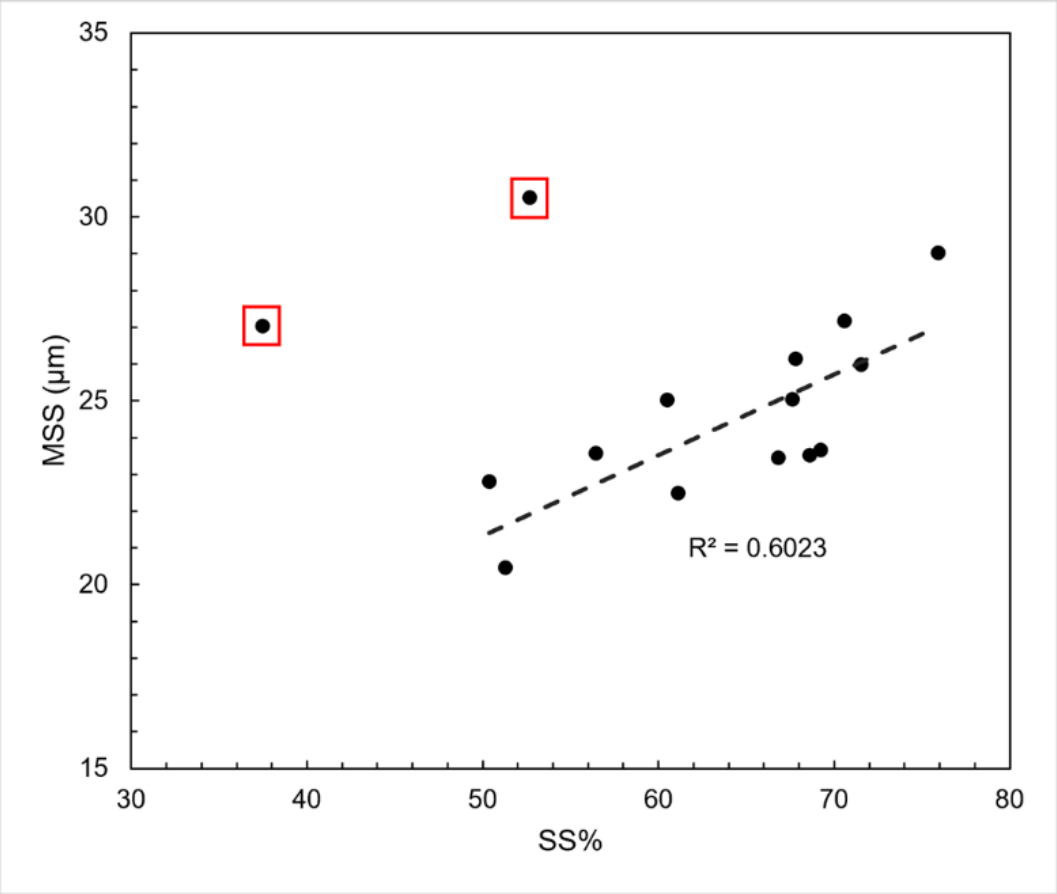
Fine: 120 Coarse: up to 240

Appendix IV: End-member modelling for core CE18011_VC2



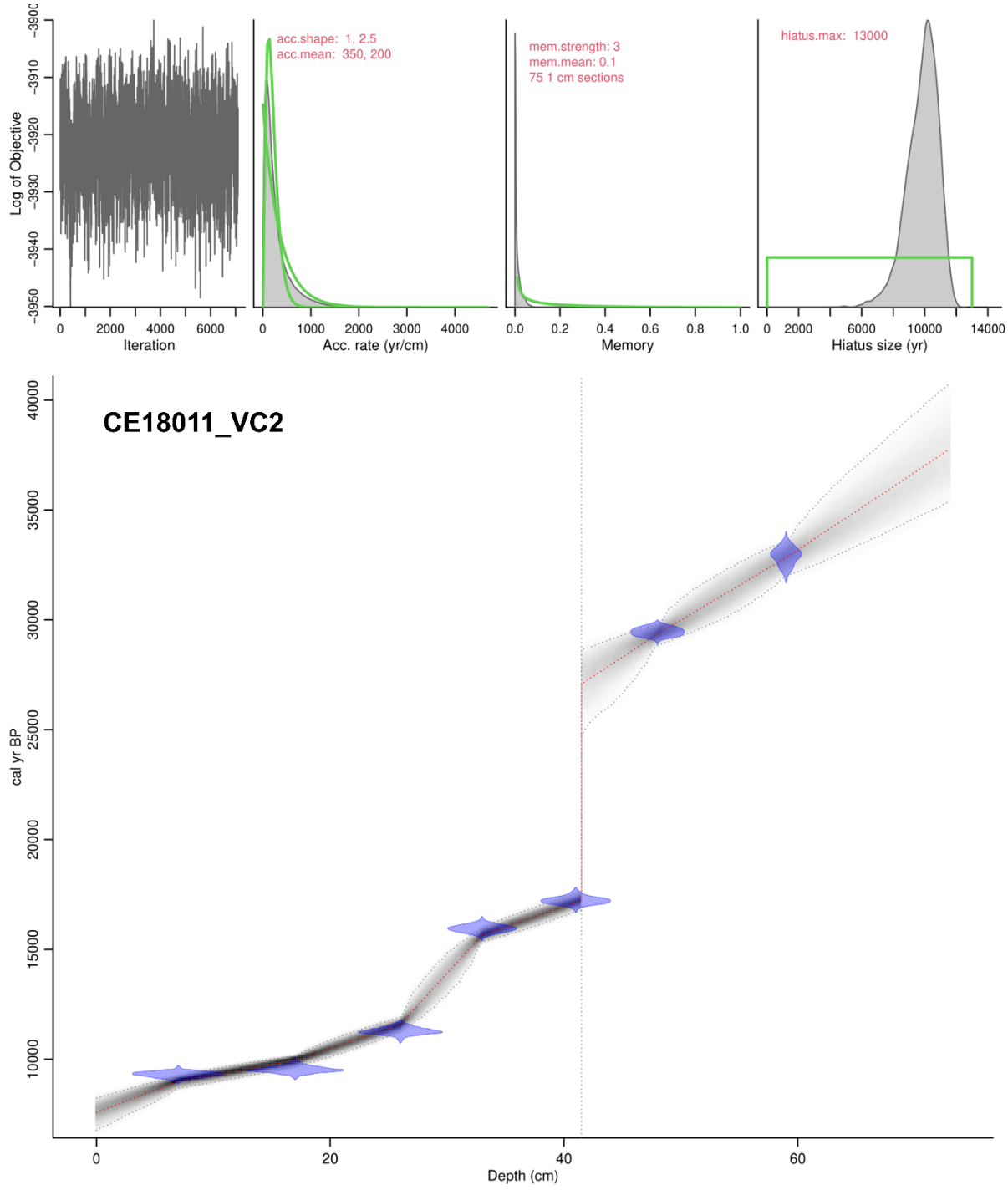
Goodness-of-fit statistics applied to estimate the number of end members. (a) all of the grain-size distributions used in the model; (b) r^2 values for CE18011_VC2 end-member models with 2–10 end members. With 2 end members a value of r^2=0.92 is acquired; (c) The application of the two end member model to grain size data from 30 cmbsf. Modelled (black) vs measured (circles); (d) Unmixed contributions of the model displaying EMa (dashed line) and EMb (black line).

Appendix V: Correlation of sortable silt (%) versus mean sortable silt (μm) for core CE18011_VC2



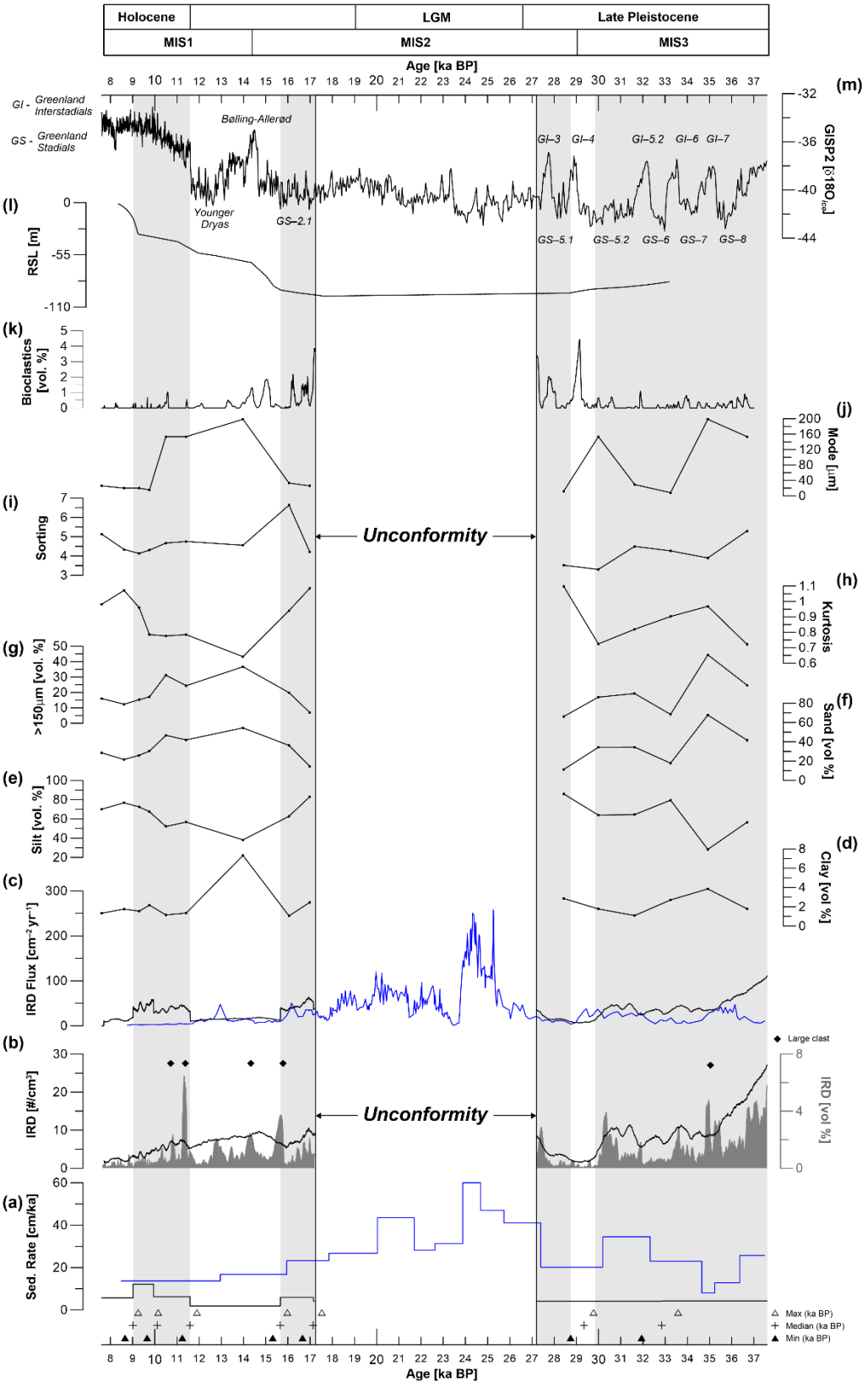
Two outliers were removed from this analysis (red boxes), which significantly increased the correlation coefficient by 0.5.

Appendix VI: Age model parameters for core CE18011_VC2



Raw age model parameters of Core CE18011_VC2 used in BACON, including iteration, estimated accumulation rate, memory and hiatus size

Appendix VII: Additional sedimentological data plot for core CE18011_VC2



Additional multi-proxy data obtained from core VC18011_VC2 excluded from Fig. 11. Compilation of multi-proxy data obtained from core VC18011_VC2 (in black and grey) plotted against time compared to the data of Peck et al. (2006) from the Porcupine Seabight (in blue). Includes an unconformity from 27.3–17.2 ka BP. Periods containing high IRD fluxes are shown as shaded grey areas. Modelled ages (in ka BP) at bottom are annotated by black cross (median), white triangles (maximum) and black triangles (minimum) (a) sedimentation rates; (b) IRD volume percentage (solid black line), IRD clasts per cubic centimetre (light grey filled in); (c) IRD flux (d–f) volume percentage derived from grain size analysis of clay, silt and sand (g) Volume percentage of grains >150 microns; (h) kurtosis (higher kurtosis indicate more peaked profiles; (i) sorting of grain size distributions. An increase in this proxy indicates sediments become less sorted (j) size of mode 1 of grain size distributions (k) volume percentage of biogenic clasts derived from CT-data; (l) Relative sea-level estimates in metres were calculated from models composed by Brooks et al. (2008) and was simulated by the glacial rebound model of Bradley et al. (2011) and applied to the area (personal communication Robin Edwards, Trinity College Dublin, 2021); (m) GISP Greenland Ice Core δ18O values.

Appendix VIII: Compilation of down core sedimentological data from each core analysed during this PhD

Cruise Code	Vibrocore Number	Depth (cmbsf)	Dry Sample Weight (100%)	Carbonate (wt. %)	Organic (wt%)	SiO_2 (wt. %)	Mean GS (µm)	Mean SS (µm)	Mode 1 (mm)	Sorting (µm)	Sorting	Skewness	Kurtosity
CE18011	1	0	3.0	45.0	0.3	54.7	10.2	18.5	8.2	1.6	P Sorted	C Skewed	Leptokurtic
CE18011	1	5	2.6	69.7	0.6	29.8	10.3	19.9	8.2	1.5	P Sorted	C Skewed	Mesokurtic
CE18011	1	10	2.8	44.3	0.7	54.9	7.9	17.6	6.3	1.7	P Sorted	C Skewed	Leptokurtic
CE18011	1	15	3.4	62.4	0.6	37.0	7.9	18.5	6.3	1.4	P Sorted	Symmetrical	Mesokurtic
CE18011	1	20	2.8	61.9	0.8	37.3	9.6	18.5	9.3	1.3	P Sorted	Symmetrical	Mesokurtic
CE18011	1	25	4.6	46.0	0.2	53.8	15.5	19.4	8.2	2.9	V P Sorted	C Skewed	Leptokurtic
CE18011	1	30	5.2	42.7	0.8	56.5	8.0	19.1	6.3	1.9	P Sorted	C Skewed	Leptokurtic
CE18011	1	35	2.3	80.1	0.5	19.4	8.8	20.2	6.3	1.6	P Sorted	Symmetrical	Mesokurtic
CE18011	1	40	3.4	67.2	0.4	32.4	8.6	17.7	8.2	1.4	P Sorted	C Skewed	Mesokurtic
CE18011	1	45	5.2	52.7	0.6	46.6	11.7	20.1	12.0	2.0	V P Sorted	C Skewed	Leptokurtic
CE18011	1	50	5.0	63.1	0.4	36.5	9.3	19.1	12.0	1.5	P Sorted	Symmetrical	Mesokurtic
CE18011	1	55	3.2	52.4	0.6	47.1	7.5	19.1	6.3	1.5	P Sorted	Symmetrical	Mesokurtic
CE18011	1	60	2.4	52.2	0.5	47.3	7.4	18.4	6.3	1.4	P Sorted	Symmetrical	Mesokurtic
CE18011	1	65	3.2	51.2	0.9	48.0	7.9	18.0	6.3	1.6	P Sorted	C Skewed	Leptokurtic
CE18011	1	70	3.2	47.6	1.1	51.2	8.1	18.0	6.3	1.5	P Sorted	Symmetrical	Mesokurtic
CE18011	1	75	2.4	57.4	0.9	41.7	9.2	18.5	8.2	1.8	P Sorted	C Skewed	Leptokurtic
CE18011	1	80	2.5	55.5	0.8	43.7	8.8	18.4	8.2	1.5	P Sorted	Symmetrical	Mesokurtic
CE18011	1	85	2.9	46.2	0.9	53.0	8.4	19.5	6.3	2.0	V P Sorted	C Skewed	Leptokurtic
CE18011	1	90	2.6	40.1	2.6	57.3	7.4	18.7	6.3	1.9	P Sorted	Symmetrical	Leptokurtic
CE18011	1	95	2.7	41.7	1.2	57.1	9.5	18.6	15.5	1.3	P Sorted	Symmetrical	Mesokurtic
CE18011	1	100	2.9	40.4	1.9	57.7	13.5	21.4	20.0	1.3	P Sorted	F Skewed	Mesokurtic
CE18011	1	105	4.0	54.6	0.6	44.8	8.1	19.2	6.3	2.2	V P Sorted	C Skewed	Leptokurtic
CE18011	1	110	3.3	30.5	2.5	67.0	11.5	20.0	15.5	1.3	P Sorted	F Skewed	Mesokurtic
CE18011	1	115	3.7	40.4	0.5	59.2	8.6	20.4	8.2	2.2	V P Sorted	Symmetrical	Leptokurtic
CE18011	1	120	3.7	39.7	1.6	58.7	7.2	17.1	6.3	1.3	P Sorted	Symmetrical	Mesokurtic
CE18011	1	125	3.6	42.3	1.8	55.9	7.1	18.3	6.3	1.6	P Sorted	C Skewed	Mesokurtic
CE18011	1	130	4.8	31.9	0.9	67.2	13.8	25.3	6.3	2.2	V P Sorted	Symmetrical	Mesokurtic
CE18011	2	0	5.0	40.6	2.4	57.0	30.1	26.0	25.8	2.0	V P Sorted	Symmetrical	Mesokurtic
CE18011	2	5	3.8	45.7	2.6	51.7	23.1	23.5	20.0	2.1	V P Sorted	C Skewed	Mesokurtic
CE18011	2	10	5.9	47.0	1.3	51.7	26.9	23.5	20.0	2.2	V P Sorted	C Skewed	Mesokurtic
CE18011	2	15	5.4	51.2	0.9	48.0	25.8	22.5	15.5	2.2	V P Sorted	C Skewed	Platykurtic
CE18011	2	20	5.9	51.2	1.0	47.8	46.0	23.7	153.5	2.2	V P Sorted	Symmetrical	Platykurtic
CE18011	2	25	6.1	39.0	1.7	59.3	38.0	26.1	153.5	2.7	V P Sorted	Symmetrical	Platykurtic
CE18011	2	30	3.5	26.6	0.4	73.0	42.2	27.0	198.5	2.1	V P Sorted	V F Skewed	Very Platykurtic
CE18011	2	35	5.9	46.6	0.6	52.9	38.5	29.0	33.2	1.8	V P Sorted	Symmetrical	Mesokurtic

Cruise Code	Vibrocore Number	Depth (cmbsf)	Dry Sample Weight (100%)	Carbonate (wt. %)	Organic (wt%)	SiO_2 (wt. %)	Mean GS (μm)	Mean SS (μm)	Mode 1 (mm)	Sorting (μm)	Sorting	Skewness	Kurtosity
CE18011	2	40	5.3	30.9	0.9	68.2	17.7	25.0	25.8	1.7	P Sorted	Symmetrical	Mesokurtic
CE18011	2	45	6.9	12.5	2.0	85.4	12.0	20.5	12.0	2.2	P Sorted	C Skewed	Mesokurtic
CE18011	2	50	6.1	31.0	0.9	68.2	27.5	25.0	153.5	2.1	V P Sorted	Symmetrical	Platykurtic
CE18011	2	55	5.0	43.0	0.3	56.7	33.8	27.2	29.3	2.0	V P Sorted	Symmetrical	Platykurtic
CE18011	2	60	6.0	24.8	0.9	74.4	15.2	22.8	8.2	2.4	P Sorted	C Skewed	Mesokurtic
CE18011	2	65	5.3	27.1	0.8	72.1	64.2	30.4	198.5	2.4	V P Sorted	V F Skewed	Mesokurtic
CE18011	2	70	3.4	29.1	1.7	69.1	32.7	23.6	153.5	2.1	V P Sorted	Symmetrical	Platykurtic
CE18011	3	0	3.9	26.2	2.0	71.8	108.5	29.2	198.5	2.5	P Sorted	V F Skewed	Very Leptokurtic
CE18011	3	5	3.3	40.7	1.8	57.5	28.2	20.1	198.5	2.4	V P Sorted	C Skewed	Very Platykurtic
CE18011	3	10	3.5	33.1	1.6	65.3	29.5	20.3	198.5	2.5	V P Sorted	C Skewed	Very Platykurtic
CE18011	3	15	3.8	34.7	1.9	63.4	19.4	22.5	15.5	2.5	V P Sorted	C Skewed	Platykurtic
CE18011	3	20	5.2	13.7	2.2	84.0	54.3	27.4	153.5	2.5	V P Sorted	V F Skewed	Platykurtic
CE18011	3	25	4.7	30.1	0.7	69.2	11.9	21.3	4.3	1.7	V P Sorted	V C Skewed	Mesokurtic
CE18011	3	30	3.0	28.5	1.0	70.5	15.9	23.6	20.0	2.5	P Sorted	Symmetrical	Mesokurtic
CE18011	3	35	4.0	31.4	0.4	68.2	11.6	22.2	4.3	2.6	V P Sorted	V C Skewed	Mesokurtic
CE18011	3	40	4.6	26.6	0.7	72.7	55.6	24.5	198.5	2.4	V P Sorted	V F Skewed	Very Platykurtic
CE18011	3	44	3.3	39.7	0.5	59.9	65.4	21.7	198.5	1.3	V P Sorted	V F Skewed	Platykurtic
CE18011	4.1	0	3.2	66.6	0.7	32.6	9.1	20.1	6.3	1.6	P Sorted	Symmetrical	Mesokurtic
CE18011	4.1	5	4.7	60.2	1.0	38.7	13.5	22.2	20.0	1.4	P Sorted	Symmetrical	Mesokurtic
CE18011	4.1	10	3.3	57.1	1.6	41.3	11.5	21.0	15.5	1.3	P Sorted	Symmetrical	Platykurtic
CE18011	4.1	15	2.2	71.7	1.2	27.0	11.7	21.0	15.5	1.3	P Sorted	F Skewed	Mesokurtic
CE18011	4.1	20	3.7	55.4	1.1	43.5	13.4	21.4	20.0	1.4	P Sorted	F Skewed	Mesokurtic
CE18011	4.1	25	3.0	57.2	0.8	42.0	10.7	19.7	15.5	1.4	P Sorted	Symmetrical	Mesokurtic
CE18011	4.1	30	2.7	56.8	0.9	42.3	10.8	20.2	15.5	1.4	P Sorted	Symmetrical	Mesokurtic
CE18011	4.1	35	3.3	64.2	0.9	34.9	13.0	21.4	20.0	1.5	P Sorted	Symmetrical	Mesokurtic
CE18011	4.1	40	4.0	82.1	0.6	17.4	17.8	23.9	20.0	1.3	P Sorted	Symmetrical	Leptokurtic
CE18011	4.1	45	4.9	76.5	0.8	22.7	18.2	24.2	22.7	1.4	P Sorted	F Skewed	Leptokurtic
CE18011	4.1	50	5.2	77.2	0.7	22.0	16.5	23.4	20.0	1.3	P Sorted	F Skewed	Mesokurtic
CE18011	4.1	55	5.9	78.6	0.9	20.5	15.0	22.1	20.0	1.3	P Sorted	F Skewed	Mesokurtic
CE18011	4.1	60	5.8	66.8	1.9	31.3	14.2	21.0	15.5	1.3	P Sorted	Symmetrical	Mesokurtic
CE18011	4.1	65	6.0	80.4	0.8	18.8	13.2	21.0	15.5	1.4	P Sorted	F Skewed	Mesokurtic
CE18011	4.1	70	2.9	73.4	1.3	25.4	16.1	22.5	20.0	1.4	P Sorted	Symmetrical	Mesokurtic
CE18011	4.1	75	4.2	76.4	1.1	22.6	15.5	22.1	20.0	1.3	P Sorted	Symmetrical	Mesokurtic
CE18011	4.2	80	10.7	67.6	1.7	30.8	12.1	19.3	15.5	1.4	P Sorted	Symmetrical	Leptokurtic
CE18011	4.2	85	2.7	82.4	0.2	17.5	11.1	18.9	15.5	1.3	P Sorted	Symmetrical	Mesokurtic
CE18011	4.2	90	3.2	63.6	1.6	34.8	12.8	19.3	15.5	1.7	P Sorted	C Skewed	Leptokurtic
CE18011	4.2	95	3.2	65.7	1.4	33.0	9.5	18.2	9.3	1.5	P Sorted	C Skewed	Leptokurtic
CE18011	4.2	100	3.3	70.4	1.1	28.5	9.3	18.4	8.2	1.6	P Sorted	C Skewed	Leptokurtic

Cruise Code	Vibrocore Number	Depth (cmbsf)	Dry Sample Weight (100%)	Carbonate (wt. %)	Organic (wt%)	SiO_2 (wt. %)	Mean GS (μm)	Mean SS (μm)	Mode 1 (mm)	Sorting (μm)	Sorting	Skewness	Kurtosity
CE18011	4.2	105	3.0	62.7	1.4	35.9	10.9	19.5	12.0	1.4	P Sorted	Symmetrical	Mesokurtic
CE18011	4.2	110	2.2	63.3	0.9	35.9	12.0	21.4	15.5	1.4	P Sorted	Symmetrical	Mesokurtic
CE18011	4.2	115	4.1	48.3	0.8	51.0	8.5	19.6	6.3	2.3	V P Sorted	C Skewed	Leptokurtic
CE18011	4.2	120	2.4	27.4	0.6	72.0	6.3	16.4	6.3	1.2	P Sorted	Symmetrical	Mesokurtic
CE18011	4.2	125	4.0	48.2	0.9	50.9	10.3	20.8	15.5	1.4	P Sorted	Symmetrical	Platykurtic
CE18011	4.2	130	3.3	33.4	0.4	66.1	5.7	16.6	5.6	1.4	P Sorted	C Skewed	Leptokurtic
CE18011	4.2	135	3.0	24.1	0.5	75.5	12.5	20.9	15.5	1.3	P Sorted	F Skewed	Mesokurtic
CE18011	4.2	140	2.7	24.1	0.6	75.2	7.7	17.2	6.3	1.3	P Sorted	Symmetrical	Mesokurtic
CE18011	4.2	145	2.9	36.2	0.4	63.4	16.7	18.7	5.6	2.7	V P Sorted	V C Skewed	Mesokurtic
CE18011	4.2	150	4.2	53.4	0.4	46.2	21.7	23.7	20.0	2.1	V P Sorted	C Skewed	Leptokurtic
CE18011	4.2	155	4.1	33.6	0.7	65.6	26.2	21.6	15.5	2.4	V P Sorted	C Skewed	Platykurtic
CE18011	4.2	160	4.9	75.8	1.2	23.0	20.1	26.9	29.3	1.4	P Sorted	F Skewed	Mesokurtic
CE18011	4.2	165	3.9	75.4	1.2	23.3	23.2	30.5	37.7	1.8	P Sorted	F Skewed	Leptokurtic
CE18011	5	0	2.3	82.5	1.3	16.2	32.3	26.4	29.3	2.0	V P Sorted	Symmetrical	Mesokurtic
CE18011	5	5	4.1	57.5	1.4	41.1	21.1	25.0	25.8	1.7	P Sorted	Symmetrical	Leptokurtic
CE18011	5	10	2.7	43.9	2.1	54.1	21.8	25.5	29.3	1.8	P Sorted	Symmetrical	Leptokurtic
CE18011	5	15	3.4	50.0	1.4	48.6	26.6	20.3	15.5	2.3	V P Sorted	C Skewed	Platykurtic
CE18011	5	20	4.2	56.9	0.8	42.2	42.7	25.5	153.5	2.5	V P Sorted	V F Skewed	Platykurtic
CE18011	5	25	4.7	56.3	0.7	43.1	26.1	19.9	15.5	2.3	V P Sorted	C Skewed	Platykurtic
CE18011	5	30	5.6	62.2	1.1	36.6	57.7	21.0	198.5	2.3	V P Sorted	V F Skewed	Platykurtic
CE18011	5	35	6.0	56.6	0.8	42.5	107.4	21.5	198.5	1.7	P Sorted	V F Skewed	Very Leptokurtic
CE18011	5	40	6.2	40.7	0.5	58.8	165.6	18.9	153.5	1.0	M Sorted	V F Skewed	Very Leptokurtic
CE18011	5	45	5.8	65.6	0.6	33.8	162.5	26.4	198.5	1.2	P Sorted	V F Skewed	Very Leptokurtic
CE18011	5	50	4.7	60.6	1.2	38.2	65.8	23.7	153.5	2.0	P Sorted	V F Skewed	Platykurtic
CE18011	5	55	4.8	73.8	0.7	25.5	36.9	28.0	104.6	2.0	P Sorted	Symmetrical	Platykurtic
CE18011	5	60	7.8	71.6	0.8	27.6	52.6	28.0	153.5	2.1	V P Sorted	V F Skewed	Platykurtic
CE18011	5	65	6.0	74.3	1.0	24.7	23.9	25.6	25.8	1.7	P Sorted	Symmetrical	Leptokurtic
CE18011	5	70	5.8	69.0	1.4	29.6	15.0	21.9	20.0	1.5	P Sorted	Symmetrical	Leptokurtic
CE18011	5	75	4.5	60.8	1.1	38.1	11.5	19.5	15.5	1.4	P Sorted	Symmetrical	Mesokurtic
CE18011	5	80	5.6	66.2	1.2	32.6	14.6	21.9	20.0	1.5	P Sorted	Symmetrical	Leptokurtic
CE18011	5	85	4.3	61.5	1.5	37.0	17.7	22.2	20.0	2.0	P Sorted	C Skewed	Leptokurtic
CE18011	5	90	6.4	61.0	0.9	38.0	30.8	20.4	256.0	2.6	V P Sorted	C Skewed	Very Platykurtic
CE18011	5	95	7.9	52.2	1.5	46.3	28.9	22.0	15.5	2.5	V P Sorted	C Skewed	Platykurtic
CE18011	5	100	8.1	70.2	0.6	29.2	28.9	21.6	15.5	2.7	V P Sorted	C Skewed	Platykurtic
CE18011	5	105	8.4	64.0	0.5	35.5	40.4	27.2	29.3	2.4	V P Sorted	Symmetrical	Platykurtic
CE18011	5	110	7.4	60.2	0.7	39.1	-	-	-	2.1	-	-	-
CE18011	6	0	2.5	36.1	2.4	61.5	14.2	22.0	20.0	1.4	P Sorted	F Skewed	Mesokurtic
CE18011	6	4	2.9	42.6	1.7	55.7	13.6	21.8	20.0	1.3	P Sorted	F Skewed	Mesokurtic

Cruise Code	Vibrocore Number	Depth (cmbsf)	Dry Sample Weight (100%)	Carbonate (wt. %)	Organic (wt%)	SiO_2 (wt. %)	Mean GS (μm)	Mean SS (μm)	Mode 1 (mm)	Sorting (μm)	Sorting	Skewness	Kurtosity
CE18011	6	6	2.4	34.2	2.8	63.0	12.0	20.7	15.5	1.4	P Sorted	Symmetrical	Mesokurtic
CE18011	6	12	2.8	38.9	1.9	59.3	14.0	21.8	20.0	1.3	P Sorted	F Skewed	Mesokurtic
CE18011	6	18	2.9	33.1	2.9	64.0	12.7	20.7	15.5	1.3	P Sorted	F Skewed	Mesokurtic
CE18011	6	24	3.1	27.9	3.3	68.8	12.3	21.0	20.0	1.3	P Sorted	F Skewed	Mesokurtic
CE18011	6	30	3.5	49.8	0.9	49.2	14.6	22.5	20.0	1.5	P Sorted	F Skewed	Mesokurtic
CE18011	6	36	4.2	56.3	1.0	42.7	19.2	24.4	25.8	1.8	P Sorted	Symmetrical	Leptokurtic
CE18011	8	0	3.5	44.2	1.9	54.0	12.6	25.2	6.3	3.3	V P Sorted	Symmetrical	Mesokurtic
CE18011	8	5	3.4	70.3	1.0	28.7	13.8	21.0	4.9	2.7	V P Sorted	C Skewed	Mesokurtic
CE18011	8	10	3.9	72.4	0.7	26.9	29.7	21.4	376.0	2.8	V P Sorted	V C Skewed	Very Platykurtic
CE18011	8	15	5.6	72.3	0.6	27.1	22.8	20.7	6.3	2.1	V P Sorted	V C Skewed	Mesokurtic
CE18011	8	20	7.2	49.7	2.5	47.8	14.8	20.5	15.5	2.7	V P Sorted	C Skewed	Leptokurtic
CE18011	8	25	8.0	70.2	1.0	28.8	31.9	22.2	15.5	1.8	V P Sorted	C Skewed	Mesokurtic
RH17002	1	0	4.6	56.4	0.9	42.8	16.3	24.4	25.8	1.5	P Sorted	F Skewed	Mesokurtic
RH17002	1	5	4.1	76.1	0.5	23.4	8.1	18.5	6.3	1.4	P Sorted	Symmetrical	Mesokurtic
RH17002	1	10	4.4	71.5	0.5	28.0	16.0	19.6	12.0	2.1	V P Sorted	C Skewed	Leptokurtic
RH17002	1	15	6.5	62.9	0.8	36.4	24.1	18.6	8.2	2.6	V P Sorted	V C Skewed	Mesokurtic
RH17002	1	18	4.2	69.4	0.5	30.1	14.1	21.4	20.0	1.4	P Sorted	Symmetrical	Leptokurtic
RH17002	1	20	5.8	66.4	0.4	33.3	8.1	18.5	6.3	1.4	P Sorted	Symmetrical	Mesokurtic
RH17002	1	23	7.5	62.5	0.1	37.4	13.9	21.1	15.5	1.7	P Sorted	Symmetrical	Leptokurtic
RH17002	1	25	6.7	50.4	1.1	48.5	11.2	20.1	15.5	1.4	P Sorted	Symmetrical	Mesokurtic
RH17002	1	27	3.7	59.9	-0.2	40.3	9.9	19.6	15.5	1.8	P Sorted	Symmetrical	Mesokurtic
RH17002	1	30	4.7	65.0	0.2	34.8	11.2	19.0	15.5	1.7	P Sorted	C Skewed	Leptokurtic
RH17002	1	32	4.4	69.5	0.6	29.9	13.2	21.0	20.0	1.4	P Sorted	F Skewed	Mesokurtic
RH17002	4	0	1.1	64.9	1.1	34.0	7.1	17.1	6.3	1.3	P Sorted	Symmetrical	Mesokurtic
RH17002	4	5	2.6	53.3	0.9	45.8	7.0	17.0	6.3	1.3	P Sorted	Symmetrical	Mesokurtic
RH17002	4	10	2.2	36.8	2.2	61.0	8.7	17.7	9.3	1.2	P Sorted	Symmetrical	Mesokurtic
RH17002	4	15	3.0	48.7	0.9	50.4	6.6	17.3	6.3	1.8	P Sorted	C Skewed	Leptokurtic
RH17002	4	20	2.7	49.4	0.5	50.1	8.5	18.8	6.3	2.1	V P Sorted	C Skewed	Leptokurtic
RH17002	4	25	2.8	46.2	0.0	53.9	7.3	17.8	8.2	1.8	P Sorted	Symmetrical	Leptokurtic
RH17002	4	30	1.6	54.9	1.4	43.7	7.0	16.6	6.3	1.2	P Sorted	Symmetrical	Mesokurtic
RH17002	4	35	1.9	60.7	1.3	37.9	8.3	17.5	8.2	1.3	P Sorted	Symmetrical	Mesokurtic
RH17002	4	40	1.5	58.8	1.2	40.1	7.8	17.1	8.2	1.2	P Sorted	Symmetrical	Mesokurtic
RH17002	4	45	3.7	43.3	0.7	56.0	8.1	18.1	6.3	2.1	V P Sorted	C Skewed	Leptokurtic
RH17002	4	50	2.2	56.3	1.1	42.6	7.0	16.6	6.3	1.2	P Sorted	Symmetrical	Mesokurtic
RH17002	4	55	2.2	54.5	1.1	44.4	6.8	16.6	6.3	1.2	P Sorted	Symmetrical	Mesokurtic
RH17002	4	60	3.4	49.4	0.8	49.9	8.4	18.1	8.2	2.2	V P Sorted	C Skewed	Very Leptokurtic
RH17002	4	65	3.0	45.3	0.5	54.1	9.7	20.6	6.3	2.3	V P Sorted	C Skewed	Leptokurtic
RH17002	7	0	2.6	56.3	1.1	42.6	10.5	19.4	15.5	1.3	P Sorted	Symmetrical	Mesokurtic

Cruise Code	Vibrocore Number	Depth (cmbsf)	Dry Sample Weight (100%)	Carbonate (wt. %)	Organic (wt%)	SiO_2 (wt. %)	Mean GS (μm)	Mean SS (μm)	Mode 1 (mm)	Sorting (μm)	Sorting	Skewness	Kurtosity
RH17002	7	5	3.5	47.8	1.1	51.1	12.1	20.5	20.0	1.3	P Sorted	F Skewed	Mesokurtic
RH17002	7	10	1.2	30.3	3.1	66.6	12.3	21.4	20.0	1.3	P Sorted	F Skewed	Mesokurtic
RH17002	7	15	2.8	51.1	1.2	47.7	9.4	18.6	12.0	1.2	P Sorted	Symmetrical	Mesokurtic
RH17002	7	20	2.4	46.8	1.4	51.9	10.7	19.1	15.5	1.3	P Sorted	F Skewed	Mesokurtic
RH17002	7	25	2.3	52.2	3.0	44.9	8.2	18.2	6.3	1.3	P Sorted	Symmetrical	Mesokurtic
RH17002	7	30	3.0	36.2	1.8	62.1	10.7	19.7	15.5	1.4	P Sorted	F Skewed	Platykurtic
RH17002	7	35	1.8	46.6	0.2	53.1	10.7	20.3	15.5	1.3	P Sorted	Symmetrical	Platykurtic
RH17002	7	40	1.7	33.4	2.3	64.3	12.4	21.2	20.0	1.3	P Sorted	F Skewed	Mesokurtic
RH17002	7	45	3.4	26.9	3.0	70.1	11.8	20.9	20.0	1.3	P Sorted	F Skewed	Platykurtic
RH17002	7	50	2.4	38.8	1.7	59.5	11.5	20.2	15.5	1.2	P Sorted	F Skewed	Mesokurtic
RH17002	7	55	2.2	56.6	1.6	41.7	9.9	18.7	15.5	1.3	P Sorted	F Skewed	Platykurtic
RH17002	7	60	2.7	46.2	1.3	52.5	10.0	18.9	15.5	1.3	P Sorted	F Skewed	Platykurtic
RH17002	7	65	2.8	37.1	1.9	61.0	12.3	20.8	20.0	1.3	P Sorted	F Skewed	Mesokurtic
RH17002	7	70	4.1	46.6	1.6	51.9	8.3	17.9	9.3	1.4	P Sorted	Symmetrical	Mesokurtic
RH17002	7	75	2.1	55.6	0.1	44.4	11.5	20.9	15.5	1.5	P Sorted	Symmetrical	Mesokurtic
RH17002	8	0	2.5	60.5	0.7	38.9	11.2	20.2	15.5	1.3	P Sorted	Symmetrical	Mesokurtic
RH17002	8	5	3.4	76.8	0.3	22.8	13.4	21.8	20.0	1.3	P Sorted	F Skewed	Mesokurtic
RH17002	8	10	3.4	58.6	0.7	40.7	9.8	18.7	15.5	1.3	P Sorted	Symmetrical	Mesokurtic
RH17002	8	15	3.1	51.1	0.4	48.5	10.4	19.4	15.5	1.3	P Sorted	Symmetrical	Mesokurtic
RH17002	8	20	3.1	50.2	0.6	49.2	8.8	18.2	9.3	1.3	P Sorted	Symmetrical	Mesokurtic
RH17002	8	25	3.0	51.8	0.5	47.6	8.9	18.5	9.3	1.3	P Sorted	Symmetrical	Mesokurtic
RH17002	8	30	3.0	37.7	1.4	60.9	13.7	22.5	20.0	1.3	P Sorted	F Skewed	Mesokurtic
RH17002	8	35	2.7	26.9	2.5	70.6	18.8	26.4	29.3	1.3	P Sorted	V F Skewed	Mesokurtic
RH17002	8	40	3.3	13.8	3.8	82.4	13.0	22.5	20.0	1.6	P Sorted	Symmetrical	Mesokurtic
RH17002	8	45	3.5	36.2	2.2	61.6	16.2	24.4	25.8	1.3	P Sorted	F Skewed	Mesokurtic
RH17002	8	50	3.0	22.9	1.9	75.1	9.7	19.0	15.5	1.3	P Sorted	Symmetrical	Platykurtic
RH17002	8	55	3.6	30.4	2.6	67.0	14.3	23.0	20.0	1.4	P Sorted	F Skewed	Mesokurtic
RH17002	8	60	3.4	39.4	1.6	58.9	16.5	23.7	25.8	1.2	P Sorted	F Skewed	Mesokurtic
RH17002	8	67	3.3	48.1	1.3	50.6	13.1	22.1	20.0	1.3	P Sorted	F Skewed	Mesokurtic
RH17002	9	0	2.5	39.2	2.6	58.2	26.9	30.9	37.7	1.6	P Sorted	F Skewed	Leptokurtic
RH17002	9	5	1.8	52.9	0.6	46.4	7.1	18.2	6.3	1.3	P Sorted	Symmetrical	Mesokurtic
RH17002	9	10	2.6	47.8	1.1	51.1	11.1	20.1	15.5	1.3	P Sorted	F Skewed	Platykurtic
RH17002	9	15	2.0	20.9	3.4	75.7	10.4	18.5	15.5	1.2	P Sorted	F Skewed	Mesokurtic
RH17002	9	20	2.3	52.1	1.0	46.9	9.8	18.7	15.5	1.3	P Sorted	Symmetrical	Mesokurtic
RH17002	9	25	2.4	55.7	0.6	43.7	9.9	19.2	15.5	1.3	P Sorted	Symmetrical	Platykurtic
RH17002	9	30	2.5	53.0	0.5	46.5	8.5	18.4	9.3	1.3	P Sorted	Symmetrical	Platykurtic
RH17002	9	35	2.9	51.6	0.9	47.4	8.2	18.2	8.2	1.3	P Sorted	Symmetrical	Mesokurtic
RH17002	9	40	2.5	53.2	0.8	46.1	8.9	18.5	12.0	1.3	P Sorted	Symmetrical	Mesokurtic

Cruise Code	Vibrocore Number	Depth (cmbsf)	Dry Sample Weight (100%)	Carbonate (wt. %)	Organic (wt%)	SiO_2 (wt. %)	Mean GS (μm)	Mean SS (μm)	Mode 1 (mm)	Sorting (μm)	Sorting	Skewness	Kurtosity
RH17002	9	45	3.7	49.6	1.2	49.2	14.4	23.6	25.8	1.4	P Sorted	F Skewed	Mesokurtic
RH17002	9	50	3.6	46.4	0.9	52.7	7.4	17.8	6.3	1.4	P Sorted	Symmetrical	Mesokurtic
RH17002	9	55	2.6	51.6	1.2	47.2	10.0	19.2	15.5	1.3	P Sorted	Symmetrical	Platykurtic
RH17002	9	60	3.5	52.7	1.1	46.3	7.3	17.6	6.3	1.3	P Sorted	Symmetrical	Mesokurtic
RH17002	9	65	3.2	64.1	0.4	35.5	9.2	18.4	12.0	1.3	P Sorted	Symmetrical	Mesokurtic
RH17002	9	70	2.9	58.4	0.8	40.8	11.3	20.6	15.5	1.3	P Sorted	F Skewed	Platykurtic
RH17002	12	0	6.6	59.4	2.4	38.2	25.6	19.6	15.5	2.7	V P Sorted	V C Skewed	Leptokurtic
RH17002	12	5	3.2	41.4	1.5	57.1	12.0	21.3	20.0	1.3	P Sorted	F Skewed	Platykurtic
RH17002	12	10	3.2	32.6	3.3	64.1	17.6	25.1	29.3	1.9	P Sorted	Symmetrical	Leptokurtic
RH17002	12	15	2.7	31.6	2.5	65.9	16.0	23.9	22.7	1.8	P Sorted	Symmetrical	Leptokurtic
RH17002	12	20	3.2	41.4	2.4	56.3	17.9	25.7	29.3	1.4	P Sorted	F Skewed	Mesokurtic
RH17002	12	25	4.0	56.0	0.9	43.1	9.8	19.2	15.5	1.4	P Sorted	Symmetrical	Mesokurtic

Cruise Code	Vibrocore Number	Depth (cmbsf)	Critical current velocity for erosion at 100 cm above the bed (m/s)	Settling Velocity (m/s)	Notes
CE18011	1	0	0.25	0.19	coral framework
CE18011	1	5	0.26	0.22	coral framework
CE18011	1	10	0.25	0.17	coral framework
CE18011	1	15	0.25	0.19	coral framework
CE18011	1	20	0.25	0.19	less coral relative to above
CE18011	1	25	0.26	0.21	few coral pieces
CE18011	1	30	0.25	0.20	muds and silts
CE18011	1	35	0.26	0.22	coral framework
CE18011	1	40	0.25	0.17	coral framework
CE18011	1	45	0.26	0.22	coral framework
CE18011	1	50	0.25	0.20	coral framework
CE18011	1	55	0.25	0.20	coral framework
CE18011	1	60	0.25	0.18	coral framework
CE18011	1	65	0.25	0.18	coral framework
CE18011	1	70	0.25	0.18	coral framework
CE18011	1	75	0.25	0.19	coral framework
CE18011	1	80	0.25	0.19	coral framework
CE18011	1	85	0.26	0.21	silty muds with coral
CE18011	1	90	0.25	0.19	large coral pieces

Cruise Code	Vibrocore Number	Depth (cmbsf)	Critical current velocity for erosion at 100 cm above the bed (m/s)	Settling Velocity (m/s)	Notes
CE18011	1	95	0.25	0.19	silty muds with coral pieces
CE18011	1	100	0.26	0.25	Bright yellow colour during carbonate dissolving. Muds. Taken with relative ease.
CE18011	1	105	0.26	0.20	Muds. Taken with relative ease.
CE18011	1	110	0.26	0.22	Muds with madrepora framework
CE18011	1	115	0.26	0.23	Muds with madrepora framework
CE18011	1	120	0.25	0.16	Clay rich muds
CE18011	1	125	0.25	0.18	Muds with broken coral pieces.
CE18011	1	130	0.27	0.35	Muds with broken coral pieces.
CE18011	2	0	0.28	0.37	Silty muds
CE18011	2	5	0.27	0.30	Grey silty muds
CE18011	2	10	0.27	0.30	Grey silty muds
CE18011	2	15	0.27	0.28	Grey silty muds
CE18011	2	20	0.27	0.31	Grey silty muds
CE18011	2	25	0.28	0.37	Grey silty muds
CE18011	2	30	0.28	0.40	Light brown muds. Saturated in water
CE18011	2	35	0.28	0.46	Light brown muds with shells
CE18011	2	40	0.27	0.34	Light brown muds. High clay %
CE18011	2	45	0.26	0.23	Orange muds
CE18011	2	50	0.27	0.34	Orange muds
CE18011	2	55	0.28	0.40	Orange muds with sand
CE18011	2	60	0.27	0.29	Orange muds with sand
CE18011	2	65	0.29	0.51	Orange muds with sand
CE18011	2	70	0.27	0.30	Light brown sands with black clasts <2mm sub-rounded to sub-angular
CE18011	3	0	0.28	0.47	Grey silty muds
CE18011	3	5	0.26	0.22	Grey silty muds
CE18011	3	10	0.26	0.23	Grey silty muds
CE18011	3	15	0.27	0.28	Grey sandy silty muds
CE18011	3	20	0.28	0.41	Brown sandy silty muds
CE18011	3	25	0.26	0.25	Orange/Brown Silty muds. Large bivalve present
CE18011	3	30	0.27	0.31	Orange muds. High moisture content. Clay rich?
CE18011	3	35	0.27	0.27	Orange muds. High moisture content. Clay rich? Higher amount of lithoclasts than above
CE18011	3	40	0.27	0.33	Orange muds. High moisture content. Clay rich? Higher sand content than above
CE18011	3	44	0.26	0.26	Orange sandy muds. High moisture content.
CE18011	4.1	0	0.26	0.22	Small extraction. Abundant coral framework
CE18011	4.1	5	0.27	0.27	Easier extraction than above. Light grey muds
CE18011	4.1	10	0.26	0.24	Grey muds in between coral frameworks

Cruise Code	Vibrocore Number	Depth (cmbsf)	Critical current velocity for erosion at 100 cm above the bed (m/s)	Settling Velocity (m/s)	Notes
CE18011	4.1	15	0.26	0.24	Grey muds in between coral frameworks
CE18011	4.1	20	0.26	0.25	Grey muds in between coral frameworks
CE18011	4.1	25	0.26	0.21	Grey muds in between coral frameworks
CE18011	4.1	30	0.26	0.22	Grey muds in between coral frameworks
CE18011	4.1	35	0.26	0.25	At boundary between grey muds and white muds
CE18011	4.1	40	0.27	0.31	White calcareous muds/silts (?) Framework
CE18011	4.1	45	0.27	0.32	White calcareous muds/silts (?) Framework
CE18011	4.1	50	0.27	0.30	White calcareous muds/silts (?) Framework
CE18011	4.1	55	0.26	0.27	White calcareous muds/silts (?) Framework
CE18011	4.1	60	0.26	0.24	White calcareous muds/silts (?) Framework
CE18011	4.1	65	0.26	0.24	White calcareous muds/silts (?) Framework
CE18011	4.1	70	0.27	0.28	Small extraction. Large coral piece present
CE18011	4.1	75	0.27	0.27	Large coral piece. White muds
CE18011	4.2	80	0.26	0.20	White muds. Minor coral pieces
CE18011	4.2	85	0.25	0.20	White muds. Minor coral pieces
CE18011	4.2	90	0.26	0.20	White muds. Easy extraction
CE18011	4.2	95	0.25	0.18	White muds. Easy extraction
CE18011	4.2	100	0.25	0.19	White muds. Easy extraction
CE18011	4.2	105	0.26	0.21	Creamy grey muds. Minor coral pieces present
CE18011	4.2	110	0.26	0.25	Creamy grey muds. Coral present was breaking apart
CE18011	4.2	115	0.26	0.21	Light grey-brown clay rich silts. Trace of biogenics
CE18011	4.2	120	0.24	0.15	Brown clay rich silts. Coral pieces present
CE18011	4.2	125	0.26	0.24	Brown clay rich silts. Large coral piece moved to extract sediment
CE18011	4.2	130	0.25	0.15	Orangey-brown clay rich silts. Coral pieces (*Madrepora* sp.) very brittle
CE18011	4.2	135	0.26	0.24	Orangey-brown clay rich silts. Coral pieces (*Madrepora* sp.) very brittle
CE18011	4.2	140	0.25	0.16	Brown clay-rich silts
CE18011	4.2	145	0.25	0.19	Brown clay rich silts. Biogenics present
CE18011	4.2	150	0.27	0.31	Rich in biogenics. Almost shelly hash. Tough extraction of sediment as a result
CE18011	4.2	155	0.26	0.26	Browny-orange fine sands (?) rich in biogenics. From
CE18011	4.2	160	0.28	0.40	White carbonate rich sediments
CE18011	4.2	165	0.29	0.51	White carbonate rich sediments. Red mottling present throughout
CE18011	5	0	0.28	0.38	Medium sands. No coral
CE18011	5	5	0.27	0.34	Medium Sands with minor coral pieces
CE18011	5	10	0.27	0.36	Medium sands with minor silts
CE18011	5	15	0.26	0.23	Medium sands and abundant shelly hash
CE18011	5	20	0.27	0.36	Medium sands and abundant shelly hash

Cruise Code	Vibrocore Number	Depth (cmbsf)	Critical current velocity for erosion at 100 cm above the bed (m/s)	Settling Velocity (m/s)	Notes
CE18011	5	25	0.26	0.22	Medium light brown sands
CE18011	5	30	0.26	0.24	Medium sands
CE18011	5	35	0.26	0.25	Medium sands
CE18011	5	40	0.25	0.20	Medium sands
CE18011	5	45	0.28	0.38	Medium sands
CE18011	5	50	0.27	0.31	Medium sands
CE18011	5	55	0.28	0.43	Medium sands
CE18011	5	60	0.28	0.43	Abundant shelly hash with <2mm sub angular black clasts
CE18011	5	65	0.27	0.36	Fine light brown sands
CE18011	5	70	0.26	0.26	With clays/muds. Corals present
CE18011	5	75	0.26	0.21	With clays/muds. Corals present
CE18011	5	80	0.26	0.26	With clays/muds. Corals present
CE18011	5	85	0.27	0.27	Muds taken from between framework
CE18011	5	90	0.26	0.23	Sandy
CE18011	5	95	0.26	0.26	Sandy with shell
CE18011	5	100	0.26	0.26	Shelly hash
CE18011	5	105	0.28	0.41	Shelly hash with minor corals
CE18011	5	110	-	-	Shelly hash with minor corals
CE18011	6	0	0.26	0.27	Grey muds
CE18011	6	6	0.26	0.23	Grey muds
CE18011	6	12	0.26	0.26	Grey muds
CE18011	6	18	0.26	0.23	Grey muds
CE18011	6	24	0.26	0.24	Grey muds
CE18011	6	30	0.27	0.28	Grey muds extracted at boundary above carbonate debris
CE18011	6	36	0.27	0.33	Large black basalt clast. Tallus deposits. Grey muds
CE18011	7	4	0.26	0.26	Sample taken from middle of core plug. Dark grey muds.
CE18011	8	0	0.27	0.35	Light brown sands with abundant biogenic material
CE18011	8	5	0.26	0.24	Brown sands with minor biogenic material
CE18011	8	10	0.26	0.25	Sands with abundant biogenics
CE18011	8	15	0.26	0.23	Abundant biogenics
CE18011	8	20	0.26	0.23	Abundant biogenics
CE18011	8	25	0.27	0.27	Large clasts > 4cm (Lithic and biogenic)
RH17002	1	0	0.27	0.33	silts
RH17002	1	5	0.25	0.19	Fine-medium biogenics
RH17002	1	10	0.26	0.21	Medium-coarse biogenics
RH17002	1	15	0.25	0.19	Medium-coarse biogenics

Cruise Code	Vibrocore Number	Depth (cmbsf)	Critical current velocity for erosion at 100 cm above the bed (m/s)	Settling Velocity (m/s)	Notes
RH17002	1	18	0.26	0.25	Coarse shelly hash
RH17002	1	20	0.25	0.19	Large coral pieces
RH17002	1	23	0.26	0.24	Silts with biogenics
RH17002	1	25	0.26	0.22	Large coral pieces
RH17002	1	27	0.26	0.21	Silts with large coral branches
RH17002	1	30	0.25	0.20	Large coral pieces
RH17002	1	32	0.26	0.24	Coarse biogenics with coral
RH17002	4	0	0.25	0.16	Small yield due to coral
RH17002	4	5	0.25	0.16	Small yield due to coral
RH17002	4	10	0.25	0.17	Relatively easier to retrieve. Muds
RH17002	4	15	0.25	0.16	Muds, no coral
RH17002	4	20	0.25	0.19	Muds around large coral pieces.
RH17002	4	25	0.25	0.17	Large coral pieces
RH17002	4	30	0.25	0.15	Difficult yield. Intricate coral growth
RH17002	4	35	0.25	0.17	Large coral piece
RH17002	4	40	0.25	0.16	Coral framework. Small yield
RH17002	4	45	0.25	0.18	Small yield. Dark grey muds
RH17002	4	50	0.25	0.15	Good yield. No coral. Dark grey muds
RH17002	4	55	0.25	0.15	Coral framework. Dark grey muds
RH17002	4	60	0.25	0.18	Coral framework. Dark grey muds
RH17002	4	65	0.26	0.23	Coral framework. Dark grey muds
RH17002	7	0	0.26	0.21	Large coral clasts. Grey muds
RH17002	7	5	0.26	0.23	Large coral clasts. Grey muds
RH17002	7	10	0.26	0.25	Large coral clasts. Grey muds
RH17002	7	15	0.25	0.19	Tough extraction. Had to dig around large framework present. Grey muds
RH17002	7	20	0.25	0.20	Tough extraction. Had to dig around large framework present. Grey muds
RH17002	7	25	0.25	0.18	Less framework than above. Grey muds
RH17002	7	30	0.26	0.21	Framework present. Grey muds
RH17002	7	35	0.26	0.23	Framework present. Grey muds
RH17002	7	40	0.26	0.25	Framework present. Grey muds
RH17002	7	45	0.26	0.24	Had to remove large coral piece to retrieve sediment. Grey muds
RH17002	7	50	0.26	0.22	Framework present. Grey muds
RH17002	7	55	0.25	0.19	Framework present. Grey muds
RH17002	7	60	0.25	0.19	Framework present. Grey muds
RH17002	7	65	0.26	0.24	Less framework than above. Grey muds
RH17002	7	70	0.25	0.18	Abundant framework. Grey muds

Cruise Code	Vibrocore Number	Depth (cmbsf)	Critical current velocity for erosion at 100 cm above the bed (m/s)	Settling Velocity (m/s)	Notes
RH17002	7	75	0.26	0.24	Abundant framework. Grey muds
RH17002	8	0	0.26	0.22	Small extraction. Grey muds. Note: abundant in plastic pieces from core liner
RH17002	8	5	0.26	0.26	Small extraction. Moved large coral branch too access sediment. Grey muds.
RH17002	8	10	0.25	0.19	Small extraction. Moved large coral branch too access sediment. Grey muds.
RH17002	8	15	0.26	0.21	Grey muds from between gap in coral branching.
RH17002	8	20	0.25	0.18	Grey muds from between gap in coral branching.
RH17002	8	25	0.25	0.19	Grey muds from between gap in coral branching.
RH17002	8	30	0.27	0.28	Grey muds from between gap in coral branching.
RH17002	8	35	0.28	0.38	Grey muds. Easy extraction
RH17002	8	40	0.27	0.28	Grey muds from between gap in coral branching.
RH17002	8	45	0.27	0.33	Grey muds from between gap in coral branching.
RH17002	8	50	0.25	0.20	Grey muds. Easy extraction
RH17002	8	55	0.27	0.29	Grey muds. Easy extraction
RH17002	8	60	0.27	0.31	Grey muds. Easy extraction
RH17002	8	67	0.26	0.27	Grey muds from between gap in coral branching.
RH17002	9	0	0.29	0.52	Sample crumbly from dryness. Grey muds.
RH17002	9	5	0.25	0.18	Grey muds
RH17002	9	10	0.26	0.22	Grey muds. Clay rich (?)
RH17002	9	15	0.25	0.19	Grey muds. Clay rich
RH17002	9	20	0.25	0.19	Grey muds. Clay rich
RH17002	9	25	0.26	0.20	Grey muds. Clay rich
RH17002	9	30	0.25	0.19	Grey muds. Clay rich
RH17002	9	35	0.25	0.18	Grey muds. Clay rich
RH17002	9	40	0.25	0.19	Grey muds. Clay rich
RH17002	9	45	0.27	0.31	Grey muds. Clay rich
RH17002	9	50	0.25	0.17	Grey muds. Clay rich
RH17002	9	55	0.26	0.20	Grey muds. Clay rich
RH17002	9	60	0.25	0.17	Grey muds. Trace black mottling.
RH17002	9	65	0.25	0.19	Fractionally lighter grey muds
RH17002	9	70	0.26	0.23	Fractionally lighter grey muds
RH17002	12	0	0.26	0.21	Tallus
RH17002	12	5	0.26	0.25	Muds. High clay (?)
RH17002	12	10	0.27	0.35	Muds. High clay (?)
RH17002	12	15	0.27	0.31	Muds. High clay (?)
RH17002	12	20	0.28	0.36	Muds. High clay (?)
RH17002	12	25	0.26	0.20	Muds. High clay (?)

Appendix IX: Species list and raw quantitative data of benthic foraminifera for core CE18011_VC1 and RH17002_VC7

Core	Core CE18011_VC1																			Total
Depth (cm)	6	11	16	21	26	31	36	41	56	66	71	76	81	86	96	101	106	116	121	
Amphycorina scalaris	1	1	0	0	0	1	1	0	3	0	3	1	3	0	1	0	0	5	10	30
Alabaminella weddellensis	0	0	0	0	0	0	0	0	0	0	0	0	0	0	0	0	0	2	0	2
Anomalina globulosa	0	1	2	1	0	0	0	0	0	0	0	0	2	0	1	0	0	0	0	7
Astrononion stelligerum	0	3	1	0	6	0	2	3	2	0	4	0	6	0	3	5	3	5	6	49
Astrononion tumidum	2	0	0	1	8	3	1	3	0	1	3	1	0	2	2	3	3	2	2	37
Biloculinella depressa	0	0	0	0	1	0	0	1	0	0	0	0	0	0	0	0	0	0	0	2
Biloculinella globula	8	35	41	24	59	33	28	50	28	17	54	35	28	38	17	11	21	3	8	538
Bolivina dilatata	0	0	0	0	0	0	0	0	0	0	0	0	0	0	0	0	0	0	0	0
Bolivina pseudopunctata	0	0	0	0	0	0	0	0	0	0	1	0	1	0	0	0	1	1	0	4
Bulimina aculeata	1	0	0	0	0	0	0	0	0	0	0	0	0	0	0	0	0	0	0	1
Bulimina marginata	4	5	5	1	7	5	3	9	2	0	6	6	1	2	2	2	1	3	3	67
Bulimina pupoides	0	0	0	0	0	0	0	0	0	0	1	1	0	0	0	0	2	1	3	8
Cassidulina carinata	0	0	0	0	0	1	0	0	0	0	0	1	0	0	0	0	0	0	0	2
Cassidulina laevigata	0	0	0	0	3	0	0	1	0	0	0	0	0	0	0	0	0	0	1	5
Cassidulina reniforme	1	7	1	3	9	8	3	6	4	1	12	8	14	4	6	6	3	4	10	110
Cassidulina teretis	6	9	7	3	16	13	5	14	5	0	6	6	5	12	7	6	3	4	9	136
Chilostomella oolina	0	0	0	1	0	0	0	0	0	0	0	0	0	0	0	0	0	0	0	1
Cibicides aravaensis	0	0	0	0	0	0	0	0	0	0	0	0	0	0	0	0	0	1	0	1
Cibicides mundulus	1	1	3	0	1	0	1	0	0	0	1	0	1	0	1	0	1	0	0	11
Cibicides pachyderma	21	36	26	13	32	18	16	40	22	24	54	37	25	22	24	10	5	16	10	451
Cibicides refulgens	4	1	5	3	0	0	2	1	1	1	2	2	4	0	0	1	0	2	0	29
Cibicides ungerianus	0	3	2	2	0	3	0	2	1	0	2	1	0	0	0	1	0	0	0	17
Cibicides wuellestorfi	0	0	0	0	0	0	0	1	0	0	0	0	0	0	0	0	1	0	0	2
Cornuspira involvens	0	0	0	0	0	0	0	0	0	0	0	0	0	0	0	0	0	0	0	0
Cycloforina laevigata	0	0	0	0	0	0	0	0	0	1	0	1	0	1	0	3	0	0	0	6
Dentalina cuvieri	0	0	1	0	0	0	0	0	0	0	0	0	0	0	0	0	0	0	0	1
Dentalina sp. identified	0	0	0	0	0	0	0	0	0	0	0	0	1	0	1	2	0	0	1	5
Discanomalina coronata	11	12	4	2	14	5	8	10	10	33	34	21	37	33	51	97	87	75	43	587
Discanomalina japonica	0	0	0	0	0	0	0	0	0	0	0	0	0	0	0	0	0	0	0	0
Discorbina bertheloti	0	0	0	0	0	0	0	0	0	0	3	0	0	0	2	0	0	0	0	5

Core	Core CE18011_VC1																			Total
Depth (cm)	6	11	16	21	26	31	36	41	56	66	71	76	81	86	96	101	106	116	121	
Eggerella humboldti	2	8	2	3	5	5	4	6	3	7	12	9	5	7	2	2	2	0	2	86
Elphidium excavatum	0	0	0	0	0	0	0	0	0	0	0	0	2	0	1	0	2	1	0	6
Favulina squamosa	0	0	5	0	0	0	0	0	0	0	0	0	0	0	0	0	0	0	0	5
Fissurina agassizi	0	0	0	0	0	0	0	0	0	0	0	0	0	0	0	0	0	0	0	0
Fissurina annectens	0	2	0	2	0	1	2	0	0	1	1	0	0	0	0	0	1	0	0	10
Fissurina eburnea	2	0	0	0	0	2	1	1	0	0	1	0	1	0	1	0	0	0	0	9
Fissurina lucida	0	0	0	0	0	0	0	2	0	0	0	0	0	0	0	0	0	0	0	2
Fissurina pseudolucida	0	0	1	0	0	0	0	0	0	0	0	0	0	0	0	0	0	0	0	1
Fissurina submarginata	0	0	0	0	0	0	0	0	0	0	0	0	0	0	0	0	1	0	0	1
Fissurina sp.1	0	0	0	0	0	0	0	0	0	0	0	0	1	0	0	0	0	0	0	1
Gaudryna pseudotrochus	0	2	0	0	0	0	0	0	0	1	1	0	1	0	2	0	0	0	0	7
Gaudryna rudis	0	0	4	3	0	3	1	0	0	3	2	6	3	5	3	0	1	1	4	39
Gavelinopsis praegeri	0	1	0	1	0	1	2	2	3	0	0	3	1	1	0	2	0	0	1	18
Glandulina ovula	0	3	0	4	5	3	2	0	3	4	5	5	2	0	1	14	6	6	2	65
Glandulonodosaria calomorpha	1	1	0	0	0	0	0	0	0	0	0	1	0	0	1	0	0	0	0	4
Globocassidulina subglobosa	2	7	4	5	11	5	6	6	6	2	8	11	6	5	12	10	13	10	12	141
Globobulimina affinis	0	0	0	0	0	0	0	0	0	0	0	0	0	0	0	0	0	0	0	0
Globulina minuta	0	6	0	1	3	1	1	5	1	3	6	3	10	3	1	3	16	14	8	85
Globulina rotundata	0	0	0	0	2	0	0	0	0	0	2	0	0	0	3	2	6	0	2	17
Gyroidina lamarckiana	0	0	2	0	1	0	0	0	0	0	0	0	0	0	0	0	0	0	0	3
Gyroidina soldanii	5	6	3	2	5	3	2	5	2	0	2	1	2	2	2	7	1	3	2	55
Hanzawaia boueana	3	13	7	12	14	8	6	11	6	0	5	2	4	1	7	5	6	2	1	113
Homalohedra apiopleura	1	0	0	1	0	0	0	0	0	1	0	0	0	0	0	0	0	0	0	3
Homalohedra eucostata	1	0	0	3	4	1	1	3	0	0	2	0	0	2	1	6	1	0	2	27
Homalohedra williamsoni	5	13	8	4	13	7	5	6	9	5	19	12	7	10	6	9	4	11	20	173
Hyalinea balthica	6	0	1	1	1	1	0	2	0	0	0	0	0	0	2	0	0	0	0	14
Hyrrokkin sarcophaga	8	16	15	16	18	12	13	17	11	24	22	21	31	20	14	28	27	13	33	359
Karreriella bradyi	3	0	0	1	0	0	0	1	0	3	3	0	1	2	1	1	0	1	0	17
Lagena squamosalata	3	0	0	0	1	0	2	0	0	0	2	1	0	0	0	0	0	0	1	10
Lenticulina orbicularis	2	8	2	0	1	1	1	3	2	0	6	1	5	0	4	0	11	11	0	58
Lenticulina gibba	0	0	0	0	0	0	0	0	2	0	0	2	0	4	0	1	0	0	3	12
Melonis barleeanum	26	50	28	30	42	21	28	45	23	9	43	43	31	30	37	84	47	46	47	710
Melonis pompiloides	0	0	1	0	0	0	0	0	0	0	0	0	0	0	0	0	0	0	0	1
Nonionella turgida	0	2	0	0	2	1	0	0	1	0	0	0	0	0	0	0	0	0	0	6

Core	Core CE18011_VC1																			Total
Depth (cm)	6	11	16	21	26	31	36	41	56	66	71	76	81	86	96	101	106	116	121	
Nuttalides umbonifer	0	0	0	1	2	0	0	0	0	0	1	0	1	0	0	1	1	1	1	9
Oolina acuticosta	0	0	1	0	0	0	0	0	0	0	0	0	2	0	0	0	0	0	0	3
Oolina globosa	1	0	1	0	0	1	2	0	0	0	1	4	1	0	1	4	1	0	0	17
Oolina lineata	2	1	1	0	0	0	0	2	0	0	1	0	0	1	1	0	3	1	0	13
Oolina melo	4	13	3	2	4	7	4	10	2	0	8	4	2	4	4	3	2	2	1	79
Oolina sp. unidentified	0	0	0	0	0	0	0	0	0	0	0	0	1	0	0	0	0	0	0	1
Orthomorphina jedlitschkai	0	0	0	0	0	0	0	0	0	0	0	0	0	0	0	0	1	0	0	1
Palliolatella semimarginata	1	0	2	0	0	0	0	0	1	0	0	1	4	0	1	0	0	0	0	10
Parafissurina lateralis	0	0	1	0	0	1	0	0	0	0	0	1	0	0	0	0	0	0	0	3
Pattellina corrugata	0	0	0	0	0	0	0	0	0	0	0	0	0	0	0	0	0	0	0	0
Planulina ariminensis	16	10	2	0	1	2	3	4	1	0	1	1	0	0	9	1	0	0	0	51
Procerolagena gracillima	0	0	1	0	0	0	0	0	0	0	0	0	0	0	0	0	0	0	0	1
Pullenia bulloides	0	0	0	0	0	0	0	0	0	0	0	0	0	0	0	0	1	0	0	1
Pullenia subcarinata	5	18	7	10	18	18	11	9	4	0	11	9	10	15	7	10	7	9	7	185
Pyrgo comata	1	0	0	0	0	0	0	0	0	0	0	0	0	0	0	0	0	0	1	2
Pyrgo elongata	1	0	0	0	1	0	1	1	2	0	0	0	0	0	0	2	1	1	3	13
Pyrgo sarsi	1	3	1	0	0	1	0	1	0	3	1	3	3	1	2	1	0	1	0	22
Pyrgo williamsoni	0	0	1	0	0	0	0	0	0	0	0	0	0	0	0	0	0	0	0	1
Pyrulina fusiformis	0	0	0	0	0	0	0	0	0	0	0	0	0	0	0	0	1	0	0	1
Quinqueloculina bosciana	0	0	0	0	0	0	0	1	0	0	2	0	0	0	0	0	0	0	0	3
Quinqueloculina laevigata	0	0	0	0	0	0	0	0	0	0	0	0	0	0	0	0	0	0	0	0
Quinqueloculina semiluna	0	3	2	0	1	1	0	0	1	0	3	1	4	0	1	1	2	2	1	23
Quinqueloculina viennensis	0	1	1	1	2	0	0	1	1	3	0	1	0	1	0	0	0	1	4	17
Robertinoides bradyi	1	2	0	0	3	0	1	0	1	1	4	1	1	4	1	5	3	3	1	32
Rosalina globularis	0	1	2	1	2	0	0	2	1	0	1	0	1	0	4	0	1	1	0	17
Sigmoilopsis schlumbergeri	0	0	1	0	2	0	0	3	1	0	0	1	0	0	0	0	0	0	0	8
Siphonina reticulata	0	7	0	1	3	0	1	2	0	0	1	0	0	0	0	0	0	0	0	15
Siphonotextularia obesa	2	0	0	0	0	0	0	0	0	0	0	0	0	0	0	0	0	0	0	2
Sphaeroidina bulloides	1	0	0	0	0	0	0	0	0	0	0	0	0	0	0	0	0	0	0	1
Spiroloculina dilatata	0	0	0	0	0	0	0	0	0	0	1	1	0	2	0	0	0	0	0	4
Spiroloculina tenuisepta	0	0	1	0	0	0	0	0	0	0	0	0	1	0	0	0	0	0	0	2
Spirillina vivipara	0	0	1	0	0	1	1	0	0	1	0	0	2	1	0	0	0	0	0	7
Spiroplectinella sagitulla	7	17	20	12	27	16	8	29	17	2	42	26	13	22	2	8	7	3	3	281
Spiroplectinella wrightii	8	17	9	10	4	6	8	2	9	10	20	14	6	15	2	5	5	3	8	161

Core	Core CE18011_VC1																			Total
Depth (cm)	6	11	16	21	26	31	36	41	56	66	71	76	81	86	96	101	106	116	121	
Stomatorbina concentrica	0	0	0	0	0	0	0	0	0	0	0	0	1	0	0	0	0	0	0	1
Textularia agglutinans	0	0	0	1	0	0	0	0	0	0	0	0	0	0	0	0	0	0	0	1
Trifarina angulosa	38	63	57	38	56	30	45	86	60	3	76	61	27	18	22	24	18	24	23	769
Trifarina bradyi	0	1	0	0	0	0	0	0	0	0	0	0	0	0	0	0	0	0	0	1
Triloculina marioni	0	0	1	0	0	0	0	0	0	0	0	0	0	0	0	0	0	0	0	1
Triloculina tricarinta	0	0	0	0	0	0	0	0	0	0	0	0	0	0	0	0	0	0	0	0
Triloculina trigonula	1	2	0	0	0	1	0	1	0	2	1	1	0	0	0	0	0	0	0	9
Unknown 2	0	0	0	0	0	0	0	0	0	0	1	0	0	0	0	0	0	0	0	1
Uvigerina auberiana	10	4	5	2	6	2	2	4	4	0	2	1	2	0	0	0	0	1	0	45
Uvigerina mediterranea	49	59	42	28	41	26	29	60	38	20	69	51	24	15	6	7	7	1	4	576
Uvigerina pygmae	30	28	19	33	20	17	21	29	32	16	47	30	30	16	4	17	13	12	0	414
Total	309	502	363	283	477	296	284	503	325	202	622	454	377	321	286	410	350	309	303	6976

Core	Core RH17002_VC7												Total
Depth (cm)	5	10	20	30	35	40	45	50	55	60	70	75	
Amphycorina scalaris	1	0	0	1	0	0	0	0	1	0	0	1	4
Alabaminella weddellensis	2	2	0	0	0	0	1	0	0	0	0	1	6
Anomalina globulosa	0	0	0	0	0	0	0	0	0	0	0	0	0
Astrononion stelligerum	4	2	0	6	3	1	6	1	6	0	0	0	29
Astrononion tumidum	4	3	6	11	7	5	0	4	3	3	3	1	50
Biloculinella depressa	0	0	0	0	0	0	0	0	0	0	0	0	0
Biloculinella globula	33	21	33	64	46	34	23	53	49	41	29	22	448
Bolivina dilatata	0	3	0	1	0	0	0	0	0	0	0	0	4
Bolivina pseudopunctata	1	1	1	3	0	0	0	0	0	0	1	1	8
Bulimina aculeata	0	0	1	0	0	0	0	0	0	0	0	0	1
Bulimina marginata	0	1	3	2	0	1	3	4	2	2	5	3	26
Bulimina pupoides	0	0	0	0	0	0	0	0	0	0	0	0	0
Cassidulina carinata	1	7	0	0	1	4	4	5	8	0	5	1	36
Cassidulina laevigata	0	0	1	0	0	0	0	0	0	0	0	0	1
Cassidulina reniforme	1	2	2	13	3	1	2	1	0	6	5	1	37
Cassidulina teretis	11	12	17	16	18	8	9	4	15	5	9	11	135
Chilostomella oolina	0	0	0	0	1	0	0	0	1	0	0	0	2
Cibicides aravaensis	0	0	0	0	0	0	0	0	0	0	0	0	0
Cibicides mundulus	0	0	2	7	0	2	0	0	0	0	0	0	11
Cibicides pachyderma	5	13	13	22	24	8	24	14	15	19	23	30	210
Cibicides refulgens	2	0	3	0	5	5	1	2	2	8	1	3	32
Cibicides ungerianus	0	0	0	0	0	1	1	0	0	0	0	0	2
Cibicides wuellestorfi	0	0	0	0	0	0	0	0	0	0	0	0	0
Cornuspira involvens	0	0	0	0	0	0	1	0	0	0	0	0	1
Cycloforina laevigata	1	0	0	0	4	0	0	1	0	0	1	0	7
Dentalina cuvieri	0	0	0	0	0	3	0	0	0	1	0	0	4
Dentalina sp. identified	1	0	0	0	1	0	0	0	1	0	1	0	4
Discanomalina coronata	24	30	18	26	21	7	8	9	11	10	19	30	213
Discanomalina japonica	0	0	0	2	0	0	0	0	0	0	0	0	2
Discorbina bertheloti	0	0	0	1	0	0	0	0	0	0	0	0	1
Eggerella humboldti	1	1	2	7	5	2	3	3	6	7	10	15	62
Elphidium excavatum	0	0	2	0	0	0	0	0	0	0	0	0	2
Favulina squamosa	0	0	0	0	0	0	0	0	0	0	0	0	0
Fissurina agassizi	0	0	0	0	0	0	0	1	1	0	1	0	3

Core	Core RH17002_VC7												Total
Depth (cm)	5	10	20	30	35	40	45	50	55	60	70	75	
Fissurina annectens	0	1	3	3	3	0	0	1	0	0	0	0	11
Fissurina eburnea	0	1	0	0	2	1	1	1	0	2	3	2	13
Fissurina lucida	0	0	0	0	0	0	0	0	0	0	0	0	0
Fissurina pseudolucida	0	0	0	0	0	0	0	0	0	0	0	0	0
Fissurina submarginata	0	0	0	0	0	0	0	0	0	0	0	0	0
Fissurina sp.1	0	1	0	0	0	0	0	0	0	0	0	0	1
Gaudryna pseudotrochus	0	0	0	1	0	0	0	0	0	0	0	0	1
Gaudryna rudis	1	0	0	0	2	1	0	1	1	1	1	4	12
Gavelinopsis praegeri	3	0	4	0	1	0	0	2	1	1	1	1	14
Glandulina ovula	4	3	1	7	3	2	1	1	4	0	0	0	26
Glandulonodosaria calomorpha	0	0	0	0	0	0	0	0	0	0	0	0	0
Globocassidulina subglobosa	48	58	53	92	140	45	54	47	57	45	58	36	733
Globobulimina affinis	0	0	3	0	0	0	0	0	0	0	0	0	3
Globulina minuta	0	4	0	2	4	4	1	2	2	3	2	3	27
Globulina rotundata	0	0	0	0	1	0	0	0	0	0	0	1	2
Gyroidina lamarckiana	0	0	0	0	0	0	0	0	0	0	0	0	0
Gyroidina soldanii	0	4	0	0	3	1	1	4	2	2	4	4	25
Hanzawaia boueana	4	3	0	10	15	8	10	10	22	16	13	9	120
Homalohedra apiopleura	0	0	0	0	0	0	1	0	0	0	0	0	1
Homalohedra eucostata	2	0	1	3	1	1	1	4	2	1	0	1	17
Homalohedra williamsoni	12	15	13	21	14	7	9	5	12	8	9	6	131
Hyalinea balthica	6	1	3	6	6	0	1	0	1	1	1	0	26
Hyrrokkin sarcophaga	20	22	24	40	28	18	11	11	12	14	20	24	244
Karreriella bradyi	0	0	1	0	0	0	0	0	0	0	0	0	1
Lagena squamosalata	0	0	1	0	0	0	0	0	1	0	0	0	2
Lenticulina orbicularis	0	0	1	5	0	7	0	0	0	3	0	0	16
Lenticulina gibba	3	2	0	0	8	0	1	7	4	1	1	1	28
Melonis barleeanum	12	19	40	35	26	25	11	20	26	34	8	28	284
Melonis pompiloides	0	0	0	0	0	0	0	0	0	0	0	0	0
Nonionella turgida	0	0	0	0	0	1	0	0	1	0	0	0	2
Nuttalides umbonifer	30	41	7	19	28	9	5	9	11	5	6	2	172
Oolina acuticosta	0	0	0	0	0	0	0	0	0	0	0	0	0
Oolina globosa	4	3	0	4	1	1	4	1	2	1	2	0	23
Oolina lineata	0	2	2	0	0	1	0	0	0	0	0	0	5

Core	Core RH17002_VC7												Total
Depth (cm)	5	10	20	30	35	40	45	50	55	60	70	75	
Oolina melo	4	4	6	3	4	1	2	3	2	4	1	0	34
Oolina sp. unidentified	0	0	0	0	0	0	0	0	0	0	0	0	0
Orthomorphina jedlitschkai	0	0	0	0	0	0	0	0	0	0	0	0	0
Palliolatella semimarginata	0	2	1	4	6	2	1	3	8	3	1	0	31
Parafissurina lateralis	0	0	0	0	0	0	0	0	0	0	0	0	0
Pattellina corrugata	0	0	0	0	0	1	0	1	2	1	0	0	5
Planulina ariminensis	8	6	12	48	28	7	7	9	3	7	2	3	140
Procerolagena gracillima	0	0	0	0	0	0	0	0	0	0	0	0	0
Pullenia bulloides	0	0	0	0	0	0	0	0	0	0	0	0	0
Pullenia subcarinata	2	6	8	8	11	5	5	4	11	3	5	4	72
Pyrgo comata	0	0	0	0	0	0	0	0	0	0	0	2	2
Pyrgo elongata	0	0	0	1	0	0	0	0	0	0	0	0	1
Pyrgo sarsi	0	1	0	0	0	0	0	0	0	0	0	3	4
Pyrgo williamsoni	0	0	0	0	0	0	0	0	0	0	0	0	0
Pyrulina fusiformis	0	0	0	0	0	0	0	0	0	0	0	0	0
Quinqueloculina bosciana	0	0	0	0	0	1	0	0	0	0	0	0	1
Quinqueloculina laevigata	0	0	0	0	0	1	0	0	0	0	0	0	1
Quinqueloculina semiluna	1	0	2	3	2	2	1	5	1	2	1	1	21
Quinqueloculina viennensis	0	0	0	0	0	0	0	0	0	0	1	0	1
Robertinoides bradyi	1	0	0	0	0	0	0	0	0	0	1	1	3
Rosalina globularis	1	6	1	0	5	1	4	0	0	0	1	1	20
Sigmoilopsis schlumbergeri	0	0	0	0	0	0	0	0	0	0	0	0	0
Siphonina reticulata	1	4	0	0	1	0	0	0	0	0	3	0	9
Siphonotextularia obesa	0	0	0	0	0	0	0	0	0	0	0	0	0
Sphaeroidina bulloides	0	0	0	1	0	0	0	0	0	0	0	0	1
Spiroloculina dilatata	0	0	0	0	0	0	0	0	0	1	0	0	1
Spiroloculina tenuisepta	0	0	0	0	0	0	0	0	0	0	0	0	0
Spirillina vivipara	13	10	2	6	9	6	9	6	11	11	1	1	85
Spiroplectinella sagitulla	12	10	0	1	5	3	3	1	5	4	3	8	55
Spiroplectinella wrightii	5	4	10	12	2	2	8	7	4	4	9	6	73
Stomatorbina concentrica	0	0	0	0	0	0	0	0	0	0	0	0	0
Textularia agglutinans	0	0	0	0	0	0	1	0	1	0	0	0	2
Trifarina angulosa	19	26	43	46	21	14	15	12	19	14	20	27	276
Trifarina bradyi	5	13	3	24	14	5	2	0	4	3	2	1	76

Core	Core RH17002_VC7												Total
Depth (cm)	5	10	20	30	35	40	45	50	55	60	70	75	
Triloculina marioni	0	0	0	0	0	0	0	0	0	0	0	0	0
Triloculina tricarinta	0	0	0	0	0	0	0	0	1	0	0	0	1
Triloculina trigonula	0	0	0	0	0	0	0	0	0	1	1	0	2
Unknown 2	0	0	0	0	0	0	0	0	0	0	0	0	0
Uvigerina auberiana	46	39	43	72	32	14	9	10	11	11	6	9	302
Uvigerina mediterranea	2	11	47	48	0	9	15	13	16	18	16	27	222
Uvigerina pygmae	4	3	2	2	14	3	5	7	6	3	12	17	78
Total	365	423	441	709	579	291	285	309	387	330	328	353	4800

Appendix X: Species list and relative abundance data of benthic foraminifera for core CE18011_VC1 and RH17002_VC7

Core	Core CE18011_VC1																		
Depth (cm)	6	11	16	21	26	31	36	41	56	66	71	76	81	86	96	101	106	116	121
Amphycorina scalaris	0.32	0.20	0.00	0.00	0.00	0.34	0.35	0.00	0.92	0.00	0.48	0.22	0.80	0.00	0.35	0.00	0.00	1.62	3.30
Alabaminella weddellensis	0.00	0.00	0.00	0.00	0.00	0.00	0.00	0.00	0.00	0.00	0.00	0.00	0.00	0.00	0.00	0.00	0.00	0.65	0.00
Anomalina globulosa	0.00	0.20	0.55	0.35	0.00	0.00	0.00	0.00	0.00	0.00	0.00	0.00	0.53	0.00	0.35	0.00	0.00	0.00	0.00
Astrononion stelligerum	0.00	0.60	0.28	0.00	1.26	0.00	0.70	0.60	0.62	0.00	0.64	0.00	1.59	0.00	1.05	1.22	0.86	1.62	1.98
Astrononion tumidum	0.65	0.00	0.00	0.35	1.68	1.01	0.35	0.60	0.00	0.50	0.48	0.22	0.00	0.62	0.70	0.73	0.86	0.65	0.66
Biloculinella depressa	0.00	0.00	0.00	0.00	0.21	0.00	0.00	0.20	0.00	0.00	0.00	0.00	0.00	0.00	0.00	0.00	0.00	0.00	0.00
Biloculinella globula	2.59	6.97	11.29	8.48	12.37	11.15	9.86	9.94	8.62	8.42	8.68	7.71	7.43	11.84	5.94	2.68	6.00	0.97	2.64
Bolivina dilatata	0.00	0.00	0.00	0.00	0.00	0.00	0.00	0.00	0.00	0.00	0.00	0.00	0.00	0.00	0.00	0.00	0.00	0.00	0.00
Bolivina pseudopunctata	0.00	0.00	0.00	0.00	0.00	0.00	0.00	0.00	0.00	0.00	0.16	0.00	0.27	0.00	0.00	0.00	0.29	0.32	0.00
Bulimina aculeata	0.32	0.00	0.00	0.00	0.00	0.00	0.00	0.00	0.00	0.00	0.00	0.00	0.00	0.00	0.00	0.00	0.00	0.00	0.00
Bulimina marginata	1.29	1.00	1.38	0.35	1.47	1.69	1.06	1.79	0.62	0.00	0.96	1.32	0.27	0.62	0.70	0.49	0.29	0.97	0.99
Bulimina pupoides	0.00	0.00	0.00	0.00	0.00	0.00	0.00	0.00	0.00	0.00	0.16	0.22	0.00	0.00	0.00	0.00	0.57	0.32	0.99
Cassidulina carinata	0.00	0.00	0.00	0.00	0.00	0.34	0.00	0.00	0.00	0.00	0.00	0.22	0.00	0.00	0.00	0.00	0.00	0.00	0.00
Cassidulina laevigata	0.00	0.00	0.00	0.00	0.63	0.00	0.00	0.20	0.00	0.00	0.00	0.00	0.00	0.00	0.00	0.00	0.00	0.00	0.33
Cassidulina reniforme	0.32	1.39	0.28	1.06	1.89	2.70	1.06	1.19	1.23	0.50	1.93	1.76	3.71	1.25	2.10	1.46	0.86	1.29	3.30
Cassidulina teretis	1.94	1.79	1.93	1.06	3.35	4.39	1.76	2.78	1.54	0.00	0.96	1.32	1.33	3.74	2.45	1.46	0.86	1.29	2.97
Chilostomella oolina	0.00	0.00	0.00	0.35	0.00	0.00	0.00	0.00	0.00	0.00	0.00	0.00	0.00	0.00	0.00	0.00	0.00	0.00	0.00
Cibicides aravaensis	0.00	0.00	0.00	0.00	0.00	0.00	0.00	0.00	0.00	0.00	0.00	0.00	0.00	0.00	0.00	0.00	0.00	0.32	0.00
Cibicides mundulus	0.32	0.20	0.83	0.00	0.21	0.00	0.35	0.00	0.00	0.00	0.16	0.00	0.27	0.00	0.35	0.00	0.29	0.00	0.00
Cibicides pachyderma	6.80	7.17	7.16	4.59	6.71	6.08	5.63	7.95	6.77	11.88	8.68	8.15	6.63	6.85	8.39	2.44	1.43	5.18	3.30
Cibicides refulgens	1.29	0.20	1.38	1.06	0.00	0.00	0.70	0.20	0.31	0.50	0.32	0.44	1.06	0.00	0.00	0.24	0.00	0.65	0.00
Cibicides ungerianus	0.00	0.60	0.55	0.71	0.00	1.01	0.00	0.40	0.31	0.00	0.32	0.22	0.00	0.00	0.00	0.24	0.00	0.00	0.00
Cibicides wuellestorfi	0.00	0.00	0.00	0.00	0.00	0.00	0.00	0.20	0.00	0.00	0.00	0.00	0.00	0.00	0.00	0.00	0.29	0.00	0.00
Cornuspira involvens	0.00	0.00	0.00	0.00	0.00	0.00	0.00	0.00	0.00	0.00	0.00	0.00	0.00	0.00	0.00	0.00	0.00	0.00	0.00
Cycloforina laevigata	0.00	0.00	0.00	0.00	0.00	0.00	0.00	0.00	0.00	0.50	0.00	0.22	0.00	0.31	0.00	0.73	0.00	0.00	0.00
Dentalina cuvieri	0.00	0.00	0.28	0.00	0.00	0.00	0.00	0.00	0.00	0.00	0.00	0.00	0.00	0.00	0.00	0.00	0.00	0.00	0.00
Dentalina sp. identified	0.00	0.00	0.00	0.00	0.00	0.00	0.00	0.00	0.00	0.00	0.00	0.00	0.27	0.00	0.35	0.49	0.00	0.00	0.33
Discanomalina coronata	3.56	2.39	1.10	0.71	2.94	1.69	2.82	1.99	3.08	16.34	5.47	4.63	9.81	10.28	17.83	23.66	24.86	24.27	14.19

Core	Core CE18011_VC1																		
Depth (cm)	6	11	16	21	26	31	36	41	56	66	71	76	81	86	96	101	106	116	121
Discanomalina japonica	0.00	0.00	0.00	0.00	0.00	0.00	0.00	0.00	0.00	0.00	0.00	0.00	0.00	0.00	0.00	0.00	0.00	0.00	0.00
Discorbina bertheloti	0.00	0.00	0.00	0.00	0.00	0.00	0.00	0.00	0.00	0.00	0.48	0.00	0.00	0.00	0.70	0.00	0.00	0.00	0.00
Eggerella humboldti	0.65	1.59	0.55	1.06	1.05	1.69	1.41	1.19	0.92	3.47	1.93	1.98	1.33	2.18	0.70	0.49	0.57	0.00	0.66
Elphidium excavatum	0.00	0.00	0.00	0.00	0.00	0.00	0.00	0.00	0.00	0.00	0.00	0.00	0.53	0.00	0.35	0.00	0.57	0.32	0.00
Favulina squamosa	0.00	0.00	1.38	0.00	0.00	0.00	0.00	0.00	0.00	0.00	0.00	0.00	0.00	0.00	0.00	0.00	0.00	0.00	0.00
Fissurina agassizi	0.00	0.00	0.00	0.00	0.00	0.00	0.00	0.00	0.00	0.00	0.00	0.00	0.00	0.00	0.00	0.00	0.00	0.00	0.00
Fissurina annectens	0.00	0.40	0.00	0.71	0.00	0.34	0.70	0.00	0.00	0.50	0.16	0.00	0.00	0.00	0.00	0.00	0.29	0.00	0.00
Fissurina eburnea	0.65	0.00	0.00	0.00	0.00	0.68	0.35	0.20	0.00	0.00	0.16	0.00	0.27	0.00	0.35	0.00	0.00	0.00	0.00
Fissurina lucida	0.00	0.00	0.00	0.00	0.00	0.00	0.00	0.40	0.00	0.00	0.00	0.00	0.00	0.00	0.00	0.00	0.00	0.00	0.00
Fissurina pseudolucida	0.00	0.00	0.28	0.00	0.00	0.00	0.00	0.00	0.00	0.00	0.00	0.00	0.00	0.00	0.00	0.00	0.00	0.00	0.00
Fissurina submarginata	0.00	0.00	0.00	0.00	0.00	0.00	0.00	0.00	0.00	0.00	0.00	0.00	0.00	0.00	0.00	0.00	0.29	0.00	0.00
Fissurina sp.1	0.00	0.00	0.00	0.00	0.00	0.00	0.00	0.00	0.00	0.00	0.00	0.00	0.27	0.00	0.00	0.00	0.00	0.00	0.00
Gaudryna pseudotrochus	0.00	0.40	0.00	0.00	0.00	0.00	0.00	0.00	0.00	0.50	0.16	0.00	0.27	0.00	0.70	0.00	0.00	0.00	0.00
Gaudryna rudis	0.00	0.00	1.10	1.06	0.00	1.01	0.35	0.00	0.00	1.49	0.32	1.32	0.80	1.56	1.05	0.00	0.29	0.32	1.32
Gavelinopsis praegeri	0.00	0.20	0.00	0.35	0.00	0.34	0.70	0.40	0.92	0.00	0.00	0.66	0.27	0.31	0.00	0.49	0.00	0.00	0.33
Glandulina ovula	0.00	0.60	0.00	1.41	1.05	1.01	0.70	0.00	0.92	1.98	0.80	1.10	0.53	0.00	0.35	3.41	1.71	1.94	0.66
Glandulonodosaria calomorpha	0.32	0.20	0.00	0.00	0.00	0.00	0.00	0.00	0.00	0.00	0.00	0.22	0.00	0.00	0.35	0.00	0.00	0.00	0.00
Globocassidulina subglobosa	0.65	1.39	1.10	1.77	2.31	1.69	2.11	1.19	1.85	0.99	1.29	2.42	1.59	1.56	4.20	2.44	3.71	3.24	3.96
Globobulimina affinis	0.00	0.00	0.00	0.00	0.00	0.00	0.00	0.00	0.00	0.00	0.00	0.00	0.00	0.00	0.00	0.00	0.00	0.00	0.00
Globulina minuta	0.00	1.20	0.00	0.35	0.63	0.34	0.35	0.99	0.31	1.49	0.96	0.66	2.65	0.93	0.35	0.73	4.57	4.53	2.64
Globulina rotundata	0.00	0.00	0.00	0.00	0.42	0.00	0.00	0.00	0.00	0.00	0.32	0.00	0.00	0.00	1.05	0.49	1.71	0.00	0.66
Gyroidina lamarckiana	0.00	0.00	0.55	0.00	0.21	0.00	0.00	0.00	0.00	0.00	0.00	0.00	0.00	0.00	0.00	0.00	0.00	0.00	0.00
Gyroidina soldanii	1.62	1.20	0.83	0.71	1.05	1.01	0.70	0.99	0.62	0.00	0.32	0.22	0.53	0.62	0.70	1.71	0.29	0.97	0.66
Hanzawaia boueana	0.97	2.59	1.93	4.24	2.94	2.70	2.11	2.19	1.85	0.00	0.80	0.44	1.06	0.31	2.45	1.22	1.71	0.65	0.33
Homalohedra apiopleura	0.32	0.00	0.00	0.35	0.00	0.00	0.00	0.00	0.00	0.50	0.00	0.00	0.00	0.00	0.00	0.00	0.00	0.00	0.00
Homalohedra eucostata	0.32	0.00	0.00	1.06	0.84	0.34	0.35	0.60	0.00	0.00	0.32	0.00	0.00	0.62	0.35	1.46	0.29	0.00	0.66
Homalohedra boueana	1.62	2.59	2.20	1.41	2.73	2.36	1.76	1.19	2.77	2.48	3.05	2.64	1.86	3.12	2.10	2.20	1.14	3.56	6.60
Hyalinea balthica	1.94	0.00	0.28	0.35	0.21	0.34	0.00	0.40	0.00	0.00	0.00	0.00	0.00	0.00	0.70	0.00	0.00	0.00	0.00
Hyrrokkin sarcophaga	2.59	3.19	4.13	5.65	3.77	4.05	4.58	3.38	3.38	11.88	3.54	4.63	8.22	6.23	4.90	6.83	7.71	4.21	10.89
Karreriella bradyi	0.97	0.00	0.00	0.35	0.00	0.00	0.00	0.20	0.00	1.49	0.48	0.00	0.27	0.62	0.35	0.24	0.00	0.32	0.00
Lagena squamosalata	0.97	0.00	0.00	0.00	0.21	0.00	0.70	0.00	0.00	0.00	0.32	0.22	0.00	0.00	0.00	0.00	0.00	0.00	0.33

Core	Core CE18011_VC1																		
Depth (cm)	6	11	16	21	26	31	36	41	56	66	71	76	81	86	96	101	106	116	121
Lenticulina orbicularis	0.65	1.59	0.55	0.00	0.21	0.34	0.35	0.60	0.62	0.00	0.96	0.22	1.33	0.00	1.40	0.00	3.14	3.56	0.00
Lenticulina gibba	0.00	0.00	0.00	0.00	0.00	0.00	0.00	0.00	0.62	0.00	0.00	0.44	0.00	1.25	0.00	0.24	0.00	0.00	0.99
Melonis barleeanum	8.41	9.96	7.71	10.60	8.81	7.09	9.86	8.95	7.08	4.46	6.91	9.47	8.22	9.35	12.94	20.49	13.43	14.89	15.51
Melonis pompiloides	0.00	0.00	0.28	0.00	0.00	0.00	0.00	0.00	0.00	0.00	0.00	0.00	0.00	0.00	0.00	0.00	0.00	0.00	0.00
Nonionella turgida	0.00	0.40	0.00	0.00	0.42	0.34	0.00	0.00	0.31	0.00	0.00	0.00	0.00	0.00	0.00	0.00	0.00	0.00	0.00
Nuttalides umbonifer	0.00	0.00	0.00	0.35	0.42	0.00	0.00	0.00	0.00	0.00	0.16	0.00	0.27	0.00	0.00	0.24	0.29	0.32	0.33
Oolina acuticosta	0.00	0.00	0.28	0.00	0.00	0.00	0.00	0.00	0.00	0.00	0.00	0.00	0.53	0.00	0.00	0.00	0.00	0.00	0.00
Oolina globosa	0.32	0.00	0.28	0.00	0.00	0.34	0.70	0.00	0.00	0.00	0.16	0.88	0.27	0.00	0.35	0.98	0.29	0.00	0.00
Oolina lineata	0.65	0.20	0.28	0.00	0.00	0.00	0.00	0.40	0.00	0.00	0.16	0.00	0.00	0.31	0.35	0.00	0.86	0.32	0.00
Oolina melo	1.29	2.59	0.83	0.71	0.84	2.36	1.41	1.99	0.62	0.00	1.29	0.88	0.53	1.25	1.40	0.73	0.57	0.65	0.33
Oolina sp. unidentified	0.00	0.00	0.00	0.00	0.00	0.00	0.00	0.00	0.00	0.00	0.00	0.00	0.27	0.00	0.00	0.00	0.00	0.00	0.00
Orthomorphina jedlitschkai	0.00	0.00	0.00	0.00	0.00	0.00	0.00	0.00	0.00	0.00	0.00	0.00	0.00	0.00	0.00	0.00	0.29	0.00	0.00
Palliolatella semimarginata	0.32	0.00	0.55	0.00	0.00	0.00	0.00	0.00	0.31	0.00	0.00	0.22	1.06	0.00	0.35	0.00	0.00	0.00	0.00
Parafissurina lateralis	0.00	0.00	0.28	0.00	0.00	0.34	0.00	0.00	0.00	0.00	0.00	0.22	0.00	0.00	0.00	0.00	0.00	0.00	0.00
Pattellina corrugata	0.00	0.00	0.00	0.00	0.00	0.00	0.00	0.00	0.00	0.00	0.00	0.00	0.00	0.00	0.00	0.00	0.00	0.00	0.00
Planulina ariminensis	5.18	1.99	0.55	0.00	0.21	0.68	1.06	0.80	0.31	0.00	0.16	0.22	0.00	0.00	3.15	0.24	0.00	0.00	0.00
Procerolagena gracillima	0.00	0.00	0.28	0.00	0.00	0.00	0.00	0.00	0.00	0.00	0.00	0.00	0.00	0.00	0.00	0.00	0.00	0.00	0.00
Pullenia bulloides	0.00	0.00	0.00	0.00	0.00	0.00	0.00	0.00	0.00	0.00	0.00	0.00	0.00	0.00	0.00	0.00	0.29	0.00	0.00
Pullenia subcarinata	1.62	3.59	1.93	3.53	3.77	6.08	3.87	1.79	1.23	0.00	1.77	1.98	2.65	4.67	2.45	2.44	2.00	2.91	2.31
Pyrgo comata	0.32	0.00	0.00	0.00	0.00	0.00	0.00	0.00	0.00	0.00	0.00	0.00	0.00	0.00	0.00	0.00	0.00	0.00	0.33
Pyrgo elongata	0.32	0.00	0.00	0.00	0.21	0.00	0.35	0.20	0.62	0.00	0.00	0.00	0.00	0.00	0.00	0.49	0.29	0.32	0.99
Pyrgo sarsi	0.32	0.60	0.28	0.00	0.00	0.34	0.00	0.20	0.00	1.49	0.16	0.66	0.80	0.31	0.70	0.24	0.00	0.32	0.00
Pyrgo williamsoni	0.00	0.00	0.28	0.00	0.00	0.00	0.00	0.00	0.00	0.00	0.00	0.00	0.00	0.00	0.00	0.00	0.00	0.00	0.00
Pyrulina fusiformis	0.00	0.00	0.00	0.00	0.00	0.00	0.00	0.00	0.00	0.00	0.00	0.00	0.00	0.00	0.00	0.00	0.29	0.00	0.00
Quinqueloculina bosciana	0.00	0.00	0.00	0.00	0.00	0.00	0.00	0.20	0.00	0.00	0.32	0.00	0.00	0.00	0.00	0.00	0.00	0.00	0.00
Quinqueloculina laevigata	0.00	0.00	0.00	0.00	0.00	0.00	0.00	0.00	0.00	0.00	0.00	0.00	0.00	0.00	0.00	0.00	0.00	0.00	0.00
Quinqueloculina semiluna	0.00	0.60	0.55	0.00	0.21	0.34	0.00	0.00	0.31	0.00	0.48	0.22	1.06	0.00	0.35	0.24	0.57	0.65	0.33
Quinqueloculina viennensis	0.00	0.20	0.28	0.35	0.42	0.00	0.00	0.20	0.31	1.49	0.00	0.22	0.00	0.31	0.00	0.00	0.00	0.32	1.32
Robertinoides bradyi	0.32	0.40	0.00	0.00	0.63	0.00	0.35	0.00	0.31	0.50	0.64	0.22	0.27	1.25	0.35	1.22	0.86	0.97	0.33
Rosalina globularis	0.00	0.20	0.55	0.35	0.42	0.00	0.00	0.40	0.31	0.00	0.16	0.00	0.27	0.00	1.40	0.00	0.29	0.32	0.00
Sigmoilopsis schlumbergeri	0.00	0.00	0.28	0.00	0.42	0.00	0.00	0.60	0.31	0.00	0.00	0.22	0.00	0.00	0.00	0.00	0.00	0.00	0.00
Siphonina reticulata	0.00	1.39	0.00	0.35	0.63	0.00	0.35	0.40	0.00	0.00	0.16	0.00	0.00	0.00	0.00	0.00	0.00	0.00	0.00

Core	Core CE18011_VC1																		
Depth (cm)	6	11	16	21	26	31	36	41	56	66	71	76	81	86	96	101	106	116	121
Siphonotextularia obesa	0.65	0.00	0.00	0.00	0.00	0.00	0.00	0.00	0.00	0.00	0.00	0.00	0.00	0.00	0.00	0.00	0.00	0.00	0.00
Sphaeroidina bulloides	0.32	0.00	0.00	0.00	0.00	0.00	0.00	0.00	0.00	0.00	0.00	0.00	0.00	0.00	0.00	0.00	0.00	0.00	0.00
Spiroloculina dilatata	0.00	0.00	0.00	0.00	0.00	0.00	0.00	0.00	0.00	0.00	0.16	0.22	0.00	0.62	0.00	0.00	0.00	0.00	0.00
Spiroloculina tenuisepta	0.00	0.00	0.28	0.00	0.00	0.00	0.00	0.00	0.00	0.00	0.00	0.00	0.27	0.00	0.00	0.00	0.00	0.00	0.00
Spirillina vivipara	0.00	0.00	0.28	0.00	0.00	0.34	0.35	0.00	0.00	0.50	0.00	0.00	0.53	0.31	0.00	0.00	0.00	0.00	0.00
Spiroplectinella sagitulla	2.27	3.39	5.51	4.24	5.66	5.41	2.82	5.77	5.23	0.99	6.75	5.73	3.45	6.85	0.70	1.95	2.00	0.97	0.99
Spiroplectinella wrightii	2.59	3.39	2.48	3.53	0.84	2.03	2.82	0.40	2.77	4.95	3.22	3.08	1.59	4.67	0.70	1.22	1.43	0.97	2.64
Stomatorbina concentrica	0.00	0.00	0.00	0.00	0.00	0.00	0.00	0.00	0.00	0.00	0.00	0.00	0.27	0.00	0.00	0.00	0.00	0.00	0.00
Textularia agglutinans	0.00	0.00	0.00	0.35	0.00	0.00	0.00	0.00	0.00	0.00	0.00	0.00	0.00	0.00	0.00	0.00	0.00	0.00	0.00
Trifarina angulosa	12.30	12.55	15.70	13.43	11.74	10.14	15.85	17.10	18.46	1.49	12.22	13.44	7.16	5.61	7.69	5.85	5.14	7.77	7.59
Trifarina bradyi	0.00	0.20	0.00	0.00	0.00	0.00	0.00	0.00	0.00	0.00	0.00	0.00	0.00	0.00	0.00	0.00	0.00	0.00	0.00
Triloculina marioni	0.00	0.00	0.28	0.00	0.00	0.00	0.00	0.00	0.00	0.00	0.00	0.00	0.00	0.00	0.00	0.00	0.00	0.00	0.00
Triloculina tricarinta	0.00	0.00	0.00	0.00	0.00	0.00	0.00	0.00	0.00	0.00	0.00	0.00	0.00	0.00	0.00	0.00	0.00	0.00	0.00
Triloculina trigonula	0.32	0.40	0.00	0.00	0.00	0.34	0.00	0.20	0.00	0.99	0.16	0.22	0.00	0.00	0.00	0.00	0.00	0.00	0.00
Unknown 2	0.00	0.00	0.00	0.00	0.00	0.00	0.00	0.00	0.00	0.00	0.16	0.00	0.00	0.00	0.00	0.00	0.00	0.00	0.00
Uvigerina auberiana	3.24	0.80	1.38	0.71	1.26	0.68	0.70	0.80	1.23	0.00	0.32	0.22	0.53	0.00	0.00	0.00	0.00	0.32	0.00
Uvigerina mediterranea	15.86	11.75	11.57	9.89	8.60	8.78	10.21	11.93	11.69	9.90	11.09	11.23	6.37	4.67	2.10	1.71	2.00	0.32	1.32
Uvigerina pygmae	9.71	5.58	5.23	11.66	4.19	5.74	7.39	5.77	9.85	7.92	7.56	6.61	7.96	4.98	1.40	4.15	3.71	3.88	0.00
Total Relative Abundance	100	100	100	100	100	100	100	100	100	100	100	100	100	100	100	100	100	100	100
Evenness Hill's Ratio	0.49	0.52	0.43	0.49	0.52	0.56	0.50	0.43	0.47	0.55	0.41	0.44	0.51	0.60	0.47	0.41	0.41	0.42	0.51
Rarefied Species Richness	38.65	35.65	39.64	35.22	35.32	36.64	36.57	34.74	33.44	28.91	36.23	33.99	40.13	30.37	41.18	33.51	36.68	36.02	34.68

Core	Core RH 17002_VC7											
Depth (cm)	5	10	20	30	35	40	45	50	55	60	70	75
Amphycorina scalaris	0.27	0.00	0.00	0.14	0.00	0.00	0.00	0.00	0.26	0.00	0.00	0.28
Alabaminella weddellensis	0.55	0.47	0.00	0.00	0.00	0.00	0.35	0.00	0.00	0.00	0.00	0.28
Anomalina globulosa	0.00	0.00	0.00	0.00	0.00	0.00	0.00	0.00	0.00	0.00	0.00	0.00
Astrononion stelligerum	1.10	0.47	0.00	0.85	0.52	0.34	2.11	0.32	1.55	0.00	0.00	0.00
Astrononion tumidum	1.10	0.71	1.36	1.55	1.21	1.72	0.00	1.29	0.78	0.91	0.91	0.28
Biloculinella depressa	0.00	0.00	0.00	0.00	0.00	0.00	0.00	0.00	0.00	0.00	0.00	0.00
Biloculinella globula	9.04	4.96	7.48	9.03	7.94	11.68	8.07	17.15	12.66	12.42	8.84	6.23
Bolivina dilatata	0.00	0.71	0.00	0.14	0.00	0.00	0.00	0.00	0.00	0.00	0.00	0.00

Core	Core RH 17002_VC7											
Depth (cm)	5	10	20	30	35	40	45	50	55	60	70	75
Bolivina pseudopunctata	0.27	0.24	0.23	0.42	0.00	0.00	0.00	0.00	0.00	0.00	0.30	0.28
Bulimina aculeata	0.00	0.00	0.23	0.00	0.00	0.00	0.00	0.00	0.00	0.00	0.00	0.00
Bulimina marginata	0.00	0.24	0.68	0.28	0.00	0.34	1.05	1.29	0.52	0.61	1.52	0.85
Bulimina pupoides	0.00	0.00	0.00	0.00	0.00	0.00	0.00	0.00	0.00	0.00	0.00	0.00
Cassidulina carinata	0.27	1.65	0.00	0.00	0.17	1.37	1.40	1.62	2.07	0.00	1.52	0.28
Cassidulina laevigata	0.00	0.00	0.23	0.00	0.00	0.00	0.00	0.00	0.00	0.00	0.00	0.00
Cassidulina reniforme	0.27	0.47	0.45	1.83	0.52	0.34	0.70	0.32	0.00	1.82	1.52	0.28
Cassidulina teretis	3.01	2.84	3.85	2.26	3.11	2.75	3.16	1.29	3.88	1.52	2.74	3.12
Chilostomella oolina	0.00	0.00	0.00	0.00	0.17	0.00	0.00	0.00	0.26	0.00	0.00	0.00
Cibicides aravaensis	0.00	0.00	0.00	0.00	0.00	0.00	0.00	0.00	0.00	0.00	0.00	0.00
Cibicides mundulus	0.00	0.00	0.45	0.99	0.00	0.69	0.00	0.00	0.00	0.00	0.00	0.00
Cibicides pachyderma	1.37	3.07	2.95	3.10	4.15	2.75	8.42	4.53	3.88	5.76	7.01	8.50
Cibicides refulgens	0.55	0.00	0.68	0.00	0.86	1.72	0.35	0.65	0.52	2.42	0.30	0.85
Cibicides ungerianus	0.00	0.00	0.00	0.00	0.00	0.34	0.35	0.00	0.00	0.00	0.00	0.00
Cibicides wuellestorfi	0.00	0.00	0.00	0.00	0.00	0.00	0.00	0.00	0.00	0.00	0.00	0.00
Cornuspira involvens	0.00	0.00	0.00	0.00	0.00	0.00	0.35	0.00	0.00	0.00	0.00	0.00
Cycloforina laevigata	0.27	0.00	0.00	0.00	0.69	0.00	0.00	0.32	0.00	0.00	0.30	0.00
Dentalina cuvieri	0.00	0.00	0.00	0.00	0.00	1.03	0.00	0.00	0.00	0.30	0.00	0.00
Dentalina sp. identified	0.27	0.00	0.00	0.00	0.17	0.00	0.00	0.00	0.26	0.00	0.30	0.00
Discanomalina coronata	6.58	7.09	4.08	3.67	3.63	2.41	2.81	2.91	2.84	3.03	5.79	8.50
Discanomalina japonica	0.00	0.00	0.00	0.28	0.00	0.00	0.00	0.00	0.00	0.00	0.00	0.00
Discorbina bertheloti	0.00	0.00	0.00	0.14	0.00	0.00	0.00	0.00	0.00	0.00	0.00	0.00
Eggerella humboldti	0.27	0.24	0.45	0.99	0.86	0.69	1.05	0.97	1.55	2.12	3.05	4.25
Elphidium excavatum	0.00	0.00	0.45	0.00	0.00	0.00	0.00	0.00	0.00	0.00	0.00	0.00
Favulina squamosa	0.00	0.00	0.00	0.00	0.00	0.00	0.00	0.00	0.00	0.00	0.00	0.00
Fissurina agassizi	0.00	0.00	0.00	0.00	0.00	0.00	0.00	0.32	0.26	0.00	0.30	0.00
Fissurina annectens	0.00	0.24	0.68	0.42	0.52	0.00	0.00	0.32	0.00	0.00	0.00	0.00
Fissurina eburnea	0.00	0.24	0.00	0.00	0.35	0.34	0.35	0.32	0.00	0.61	0.91	0.57
Fissurina lucida	0.00	0.00	0.00	0.00	0.00	0.00	0.00	0.00	0.00	0.00	0.00	0.00
Fissurina pseudolucida	0.00	0.00	0.00	0.00	0.00	0.00	0.00	0.00	0.00	0.00	0.00	0.00
Fissurina submarginata	0.00	0.00	0.00	0.00	0.00	0.00	0.00	0.00	0.00	0.00	0.00	0.00
Fissurina sp.1	0.00	0.24	0.00	0.00	0.00	0.00	0.00	0.00	0.00	0.00	0.00	0.00
Gaudryna pseudotrochus	0.00	0.00	0.00	0.14	0.00	0.00	0.00	0.00	0.00	0.00	0.00	0.00
Gaudryna rudis	0.27	0.00	0.00	0.00	0.35	0.34	0.00	0.32	0.26	0.30	0.30	1.13

Core	Core RH 17002_VC7											
Depth (cm)	5	10	20	30	35	40	45	50	55	60	70	75
Gavelinopsis praegeri	0.82	0.00	0.91	0.00	0.17	0.00	0.00	0.65	0.26	0.30	0.30	0.28
Glandulina ovula	1.10	0.71	0.23	0.99	0.52	0.69	0.35	0.32	1.03	0.00	0.00	0.00
Glandulonodosaria calomorpha	0.00	0.00	0.00	0.00	0.00	0.00	0.00	0.00	0.00	0.00	0.00	0.00
Globocassidulina subglobosa	13.15	13.71	12.02	12.98	24.18	15.46	18.95	15.21	14.73	13.64	17.68	10.20
Globobulimina affinis	0.00	0.00	0.68	0.00	0.00	0.00	0.00	0.00	0.00	0.00	0.00	0.00
Globulina minuta	0.00	0.95	0.00	0.28	0.69	1.37	0.35	0.65	0.52	0.91	0.61	0.85
Globulina rotundata	0.00	0.00	0.00	0.00	0.17	0.00	0.00	0.00	0.00	0.00	0.00	0.28
Gyroidina lamarckiana	0.00	0.00	0.00	0.00	0.00	0.00	0.00	0.00	0.00	0.00	0.00	0.00
Gyroidina soldanii	0.00	0.95	0.00	0.00	0.52	0.34	0.35	1.29	0.52	0.61	1.22	1.13
Hanzawaia boueana	1.10	0.71	0.00	1.41	2.59	2.75	3.51	3.24	5.68	4.85	3.96	2.55
Homalohedra apiopleura	0.00	0.00	0.00	0.00	0.00	0.00	0.35	0.00	0.00	0.00	0.00	0.00
Homalohedra eucostata	0.55	0.00	0.23	0.42	0.17	0.34	0.35	1.29	0.52	0.30	0.00	0.28
Homalohedra boueana	3.29	3.55	2.95	2.96	2.42	2.41	3.16	1.62	3.10	2.42	2.74	1.70
Hyalinea balthica	1.64	0.24	0.68	0.85	1.04	0.00	0.35	0.00	0.26	0.30	0.30	0.00
Hyrrokkin sarcophaga	5.48	5.20	5.44	5.64	4.84	6.19	3.86	3.56	3.10	4.24	6.10	6.80
Karreriella bradyi	0.00	0.00	0.23	0.00	0.00	0.00	0.00	0.00	0.00	0.00	0.00	0.00
Lagena squamosalata	0.00	0.00	0.23	0.00	0.00	0.00	0.00	0.00	0.26	0.00	0.00	0.00
Lenticulina orbicularis	0.00	0.00	0.23	0.71	0.00	2.41	0.00	0.00	0.00	0.91	0.00	0.00
Lenticulina gibba	0.82	0.47	0.00	0.00	1.38	0.00	0.35	2.27	1.03	0.30	0.30	0.28
Melonis barleeanum	3.29	4.49	9.07	4.94	4.49	8.59	3.86	6.47	6.72	10.30	2.44	7.93
Melonis pompiloides	0.00	0.00	0.00	0.00	0.00	0.00	0.00	0.00	0.00	0.00	0.00	0.00
Nonionella turgida	0.00	0.00	0.00	0.00	0.00	0.34	0.00	0.00	0.26	0.00	0.00	0.00
Nuttalides umbonifer	8.22	9.69	1.59	2.68	4.84	3.09	1.75	2.91	2.84	1.52	1.83	0.57
Oolina acuticosta	0.00	0.00	0.00	0.00	0.00	0.00	0.00	0.00	0.00	0.00	0.00	0.00
Oolina globosa	1.10	0.71	0.00	0.56	0.17	0.34	1.40	0.32	0.52	0.30	0.61	0.00
Oolina lineata	0.00	0.47	0.45	0.00	0.00	0.34	0.00	0.00	0.00	0.00	0.00	0.00
Oolina melo	1.10	0.95	1.36	0.42	0.69	0.34	0.70	0.97	0.52	1.21	0.30	0.00
Oolina sp. unidentified	0.00	0.00	0.00	0.00	0.00	0.00	0.00	0.00	0.00	0.00	0.00	0.00
Orthomorphina jedlitschkai	0.00	0.00	0.00	0.00	0.00	0.00	0.00	0.00	0.00	0.00	0.00	0.00
Palliolatella semimarginata	0.00	0.47	0.23	0.56	1.04	0.69	0.35	0.97	2.07	0.91	0.30	0.00
Parafissurina lateralis	0.00	0.00	0.00	0.00	0.00	0.00	0.00	0.00	0.00	0.00	0.00	0.00
Pattellina corrugata	0.00	0.00	0.00	0.00	0.00	0.34	0.00	0.32	0.52	0.30	0.00	0.00
Planulina ariminensis	2.19	1.42	2.72	6.77	4.84	2.41	2.46	2.91	0.78	2.12	0.61	0.85
Procerolagena gracillima	0.00	0.00	0.00	0.00	0.00	0.00	0.00	0.00	0.00	0.00	0.00	0.00

Core	Core RH 17002_VC7											
Depth (cm)	5	10	20	30	35	40	45	50	55	60	70	75
Pullenia bulloides	0.00	0.00	0.00	0.00	0.00	0.00	0.00	0.00	0.00	0.00	0.00	0.00
Pullenia subcarinata	0.55	1.42	1.81	1.13	1.90	1.72	1.75	1.29	2.84	0.91	1.52	1.13
Pyrgo comata	0.00	0.00	0.00	0.00	0.00	0.00	0.00	0.00	0.00	0.00	0.00	0.57
Pyrgo elongata	0.00	0.00	0.00	0.14	0.00	0.00	0.00	0.00	0.00	0.00	0.00	0.00
Pyrgo sarsi	0.00	0.24	0.00	0.00	0.00	0.00	0.00	0.00	0.00	0.00	0.00	0.85
Pyrgo williamsoni	0.00	0.00	0.00	0.00	0.00	0.00	0.00	0.00	0.00	0.00	0.00	0.00
Pyrulina fusiformis	0.00	0.00	0.00	0.00	0.00	0.00	0.00	0.00	0.00	0.00	0.00	0.00
Quinqueloculina bosciana	0.00	0.00	0.00	0.00	0.00	0.34	0.00	0.00	0.00	0.00	0.00	0.00
Quinqueloculina laevigata	0.00	0.00	0.00	0.00	0.00	0.34	0.00	0.00	0.00	0.00	0.00	0.00
Quinqueloculina semiluna	0.27	0.00	0.45	0.42	0.35	0.69	0.35	1.62	0.26	0.61	0.30	0.28
Quinqueloculina viennensis	0.00	0.00	0.00	0.00	0.00	0.00	0.00	0.00	0.00	0.00	0.30	0.00
Robertinoides bradyi	0.27	0.00	0.00	0.00	0.00	0.00	0.00	0.00	0.00	0.00	0.30	0.28
Rosalina globularis	0.27	1.42	0.23	0.00	0.86	0.34	1.40	0.00	0.00	0.00	0.30	0.28
Sigmoilopsis schlumbergeri	0.00	0.00	0.00	0.00	0.00	0.00	0.00	0.00	0.00	0.00	0.00	0.00
Siphonina reticulata	0.27	0.95	0.00	0.00	0.17	0.00	0.00	0.00	0.00	0.00	0.91	0.00
Siphonotextularia obesa	0.00	0.00	0.00	0.00	0.00	0.00	0.00	0.00	0.00	0.00	0.00	0.00
Sphaeroidina bulloides	0.00	0.00	0.00	0.14	0.00	0.00	0.00	0.00	0.00	0.00	0.00	0.00
Spiroloculina dilatata	0.00	0.00	0.00	0.00	0.00	0.00	0.00	0.00	0.00	0.30	0.00	0.00
Spiroloculina tenuisepta	0.00	0.00	0.00	0.00	0.00	0.00	0.00	0.00	0.00	0.00	0.00	0.00
Spirillina vivipara	3.56	2.36	0.45	0.85	1.55	2.06	3.16	1.94	2.84	3.33	0.30	0.28
Spiroplectinella sagitulla	3.29	2.36	0.00	0.14	0.86	1.03	1.05	0.32	1.29	1.21	0.91	2.27
Spiroplectinella wrightii	1.37	0.95	2.27	1.69	0.35	0.69	2.81	2.27	1.03	1.21	2.74	1.70
Stomatorbina concentrica	0.00	0.00	0.00	0.00	0.00	0.00	0.00	0.00	0.00	0.00	0.00	0.00
Textularia agglutinans	0.00	0.00	0.00	0.00	0.00	0.00	0.35	0.00	0.26	0.00	0.00	0.00
Trifarina angulosa	5.21	6.15	9.75	6.49	3.63	4.81	5.26	3.88	4.91	4.24	6.10	7.65
Trifarina bradyi	1.37	3.07	0.68	3.39	2.42	1.72	0.70	0.00	1.03	0.91	0.61	0.28
Triloculina marioni	0.00	0.00	0.00	0.00	0.00	0.00	0.00	0.00	0.00	0.00	0.00	0.00
Triloculina tricarinta	0.00	0.00	0.00	0.00	0.00	0.00	0.00	0.00	0.26	0.00	0.00	0.00
Triloculina trigonula	0.00	0.00	0.00	0.00	0.00	0.00	0.00	0.00	0.00	0.30	0.30	0.00
Unknown 2	0.00	0.00	0.00	0.00	0.00	0.00	0.00	0.00	0.00	0.00	0.00	0.00
Uvigerina auberiana	12.60	9.22	9.75	10.16	5.53	4.81	3.16	3.24	2.84	3.33	1.83	2.55
Uvigerina mediterranea	0.55	2.60	10.66	6.77	0.00	3.09	5.26	4.21	4.13	5.45	4.88	7.65
Uvigerina pygmae	1.10	0.71	0.45	0.28	2.42	1.03	1.75	2.27	1.55	0.91	3.66	4.82
Total Relative Abundance	100	100	100	100	100	100	100	100	100	100	100	100

Core	Core RH 17002_VC7											
Depth (cm)	5	10	20	30	35	40	45	50	55	60	70	75
Evenness Hill's Ratio	0.51	0.54	0.48	0.51	0.47	0.53	0.54	0.54	0.53	0.55	0.51	0.53
Rarefied Species Richness	36.02	36.79	33.01	33.48	35.35	41.29	38.15	37.51	38.83	36.93	38.46	34.42

Appendix XI: Paleoenvironmental information derived from cores CE18011_VC1, CE18011_VC2, CE18011_VC5 and RH17002_VC7

Core	Depth [cmbsf]	Planktic $\delta^{13}C$ [VPDB]	Planktic $\Delta^{18}O$ [VPDB Calcite]	Benthic $\delta^{13}C$ [VPDB]	Benthic $\Delta^{18}O$ [VPDB Calcite]
CE_VC1	0	-0.46	1.03	1.17	1.45
	5	-0.29	0.79	1.36	1.53
	10	-0.17	1.19	1.44	1.81
	15	-0.19	1.24	1.5	1.68
	20	-0.26	1.24	1.52	1.6
	25	-0.18	1.15	1.48	1.56
	30	-0.29	1.31	1.51	1.54
	35	-0.48	1.2	1.39	1.75
	40	-0.14	1.63	1.49	1.6
	45	-0.21	1.12	1.51	1.64
	50	-0.09	1.14	1.57	1.66
	55	-0.16	1.09	1.47	1.64
	60	-0.27	1.34	1.65	1.63
	65	-0.1	1.33	1.55	1.67
	70	-0.32	1.05	2.08	2.11
	75	-0.03	1.24	1.7	1.65
	80	0.03	1.27	1.47	1.63
	85	-0.3	1.03	1.41	1.61
	90	-0.33	1.28	1.44	1.65
	95	-0.34	1.16	1.46	1.83
	100	-0.4	0.82	-	-
	105	-0.05	1.06	-	-
	110	-0.59	1.19	-	-
	115	-0.55	1.43	-	-
	120	-0.37	1.14	-	-
	125	-0.43	0.96	-	-
CE_VC5	0	-0.38	1.96	1.06	2.77
	5	-0.68	1.28	1.91	3.6
	10	-0.37	1.89	1.47	2.93
	15	-0.28	2.32	1.33	3.28
	20	-0.17	2.92	1.44	3.16
	25	-0.13	2.52	1.29	3.02
	30	-0.21	2.62	1.63	2.75

Core	Depth [cmbsf]	Planktic $\delta^{13}C$ [VPDB]	Planktic $\Delta^{18}O$ [VPDB Calcite]	Benthic $\delta^{13}C$ [VPDB]	Benthic $\Delta^{18}O$ [VPDB Calcite]
CE_VC2	35	-0.05	2.55	1.27	2.77
	40	-0.18	2.57	1.47	2.75
	45	-0.16	2.56	1.37	2.73
	50	-0.2	2.61	1.39	2.87
	55	0.02	2.58	1.39	3.26
	60	-0.07	2.35	1.28	2.81
	65	-0.37	2.04	0.78	2.6
	70	-0.62	2.28	0.86	2.36
	75	-0.18	2.54	-0.26	2.8
	80	-0.39	1.99	1.08	3.12
	85	-0.41	2.42	1	3.31
	90	-0.5	2.5	1.27	3.42
	95	-0.4	2.98	1.61	3.76
	100	-0.76	3.1	1.11	3.58
	105	-0.69	2.96	1.74	3.77
	110	-0.66	2.93	1.7	3.84
	1	-0.64	1.61	1.35	2.18
	6	-0.39	1.73	1.51	2.59
	11	-0.28	2.17	1.36	2.28
	16	-0.36	2.00	1.27	2.15
	21	-0.19	2.03	1.66	3.14
	26	-0.35	1.93	1.28	2.05
	31	-0.28	2.56	1.78	3.74
	36	-0.56	2.76	1.55	2.80
	41	-0.48	2.68	1.62	3.06
	46	0.15	2.92	1.81	3.71
	51	0.07	2.89	1.69	3.56
	56	0.15	3.14	1.57	3.15
	61	-0.03	2.73	1.67	3.32
	66	0.32	2.78	1.71	3.18
	71	0.24	2.82	1.62	2.71
RH_VC7	0	-0.70	0.90	1.10	1.60
	5	-0.74	0.84	1.43	1.37
	10	-	-	-	-
	15	-	-	-	-
	20	-	-	-	-

Core	Depth [cmbsf]	Planktic		Benthic	
		$\delta^{13}C$ [VPDB]	$\Delta^{18}O$ [VPDB Calcite]	$\delta^{13}C$ [VPDB]	$\Delta^{18}O$ [VPDB Calcite]
	25	-0.84	0.87	1.47	1.75
	30	-0.60	1.11	1.53	1.79
	35	-	-	-	-
	40	-0.52	1.32	1.61	1.71
	45	-0.42	1.25	1.52	1.73
	50	-0.65	1.17	1.64	1.84
	55	-	-	-	-
	60	-0.58	1.16	1.51	1.73
	65	-0.60	1.33	1.62	1.93
	70	-0.56	1.17	1.48	1.80
	75	-0.33	1.11	1.53	1.77

Appendix XII: Relative abundance of all benthic foraminifera species in BFAs for core CE18011_VC1 and RH17002_VC7

Species	PBCMiddle relative abundance (%)	wPBMiddle relative abundance (%)	wPBearly relative abundance (%)	Mean relative abudnance (%)
Discanomalina coronata	5.49	5.48	20.65	10.54
Melonis barleeanum	6.50	8.94	15.43	10.29
Trifarina angulosa	6.07	12.11	6.91	8.36
Biloculinella globula	8.82	8.41	4.06	7.10
Globocassidulina subglobosa	14.04	1.88	3.56	6.49
Cibicides pachyderma	5.55	7.31	4.88	5.91
Hyrrokkin sarcophaga	5.49	4.71	6.49	5.56
Uvigerina mediterranea	5.15	9.87	1.65	5.56
Uvigerina pygmae	2.57	6.88	2.53	3.99
Homalohedra williamsoni	2.43	2.35	2.80	2.53
Spiroplectinella sagitulla	1.51	4.66	1.26	2.48
Cassidulina teretis	2.88	1.86	1.90	2.22
Pullenia subcarinata	1.45	2.64	2.43	2.17
Hanzawaia boueana	2.75	1.52	1.52	1.93
Uvigerina auberiana	4.76	0.70	0.04	1.83
Spiroplectinella wrightii	1.54	2.64	1.23	1.80
Eggerella humboldti	2.13	1.49	0.53	1.38
Cassidulina reniforme	0.58	1.66	1.83	1.36
Planulina ariminensis	2.01	0.86	1.16	1.34
Globulina minuta	0.71	0.78	1.94	1.14
Nuttalides umbonifer	2.85	0.08	0.19	1.04
Glandulina ovula	0.38	0.72	1.53	0.88
Oolina melo	0.50	1.15	0.88	0.84
Bulimina marginata	0.66	1.00	0.67	0.78
Gyroidina soldanii	0.75	0.65	0.91	0.77
Lenticulina orbicularis	0.29	0.59	1.44	0.77
Astrononion stelligerum	0.43	0.49	1.27	0.73
Astrononion tumidum	0.82	0.43	0.72	0.66
Gaudryna rudis	0.50	0.72	0.63	0.62
Spirillina vivipara	1.47	0.12	0.00	0.53
Cibicides refulgens	0.77	0.50	0.15	0.47
Amphycorina scalaris	0.13	0.31	0.80	0.41
Homalohedra eucostata	0.34	0.28	0.60	0.41
Robertinoides bradyi	0.12	0.36	0.71	0.40
Rosalina globularis	0.39	0.23	0.57	0.40
Trifarina bradyi	1.13	0.01	0.00	0.38
Quinqueloculina semiluna	0.41	0.30	0.40	0.37
Oolina globosa	0.36	0.34	0.39	0.36
Globulina rotundata	0.10	0.12	0.82	0.35
Pyrgo sarsi	0.29	0.39	0.35	0.34
Lenticulina gibba	0.54	0.20	0.19	0.31
Palliolatella semimarginata	0.52	0.21	0.12	0.29
Cassidulina carinata	0.78	0.06	0.00	0.28
Hyalinea balthica	0.32	0.23	0.24	0.27
Gavelinopsis praegeri	0.28	0.34	0.16	0.26

Species	PBCMiddle relative abundance (%)	wPBMiddle relative abundance (%)	wPBearly relative abundance (%)	Mean relative abudnance (%)
Fissurina eburnea	0.38	0.16	0.12	0.22
Oolina lineata	0.08	0.13	0.29	0.17
Karreriella bradyi	0.01	0.25	0.22	0.16
Pyrgo elongata	0.01	0.10	0.34	0.15
Cibicides mundulus	0.13	0.15	0.16	0.15
Quinqueloculina viennensis	0.02	0.18	0.22	0.14
Dentalina sp identified	0.07	0.04	0.28	0.13
Gaudryna pseudotrochus	0.01	0.11	0.24	0.12
Cycloforina laevigata	0.11	0.07	0.17	0.12
Siphonina reticulata	0.17	0.18	0.00	0.12
Discorbina bertheloti	0.01	0.09	0.24	0.12
Elphidium excavatum	0.02	0.07	0.25	0.11
Cibicides ungerianus	0.04	0.23	0.06	0.11
Bulimina pupoides	0.00	0.06	0.26	0.11
Fissurina annectens	0.13	0.15	0.04	0.10
Bolivina pseudopunctata	0.18	0.04	0.09	0.10
Lagena squamosalata	0.03	0.21	0.04	0.09
Alabaminella weddellensis	0.17	0.00	0.09	0.09
Pyrgo comata	0.18	0.02	0.04	0.08
Anomalina globulosa	0.00	0.11	0.12	0.08
Glandulonodosaria calomorpha	0.00	0.10	0.12	0.07
Triloculina trigonula	0.04	0.14	0.00	0.06
Sigmoilopsis schlumbergeri	0.00	0.12	0.00	0.04
Nonionella turgida	0.05	0.07	0.00	0.04
Spiroloculina dilatata	0.02	0.10	0.00	0.04
Pattellina corrugata	0.11	0.00	0.00	0.04
Dentalina cuvieri	0.10	0.01	0.00	0.04
Cassidulina laevigata	0.01	0.04	0.04	0.03
Quinqueloculina bosciana	0.03	0.04	0.00	0.02
Parafissurina lateralis	0.00	0.07	0.00	0.02
Bolivina dilatata	0.06	0.00	0.00	0.02
Fissurina agassizi	0.06	0.00	0.00	0.02
Homalohedra apiopleura	0.01	0.05	0.00	0.02
Textularia agglutinans	0.03	0.02	0.00	0.02
Chilostomella oolina	0.03	0.02	0.00	0.02
Oolina acuticosta	0.00	0.05	0.00	0.02
Siphonotextularia obesa	0.00	0.04	0.00	0.01
Fissurina sp. 1	0.02	0.02	0.00	0.01
Favulina squamosa	0.00	0.04	0.00	0.01
Spiroloculina tenuisepta	0.00	0.03	0.00	0.01
Bulimina aculeata	0.01	0.02	0.00	0.01
Sphaeroidina bulloides	0.01	0.02	0.00	0.01
Globobulimina affinis	0.03	0.00	0.00	0.01
Gyroidina lamarckiana	0.00	0.03	0.00	0.01
Quinqueloculina laevigata	0.03	0.00	0.00	0.01
Triloculina tricarinta	0.02	0.00	0.00	0.01
Discanomalina japonica	0.02	0.00	0.00	0.01
Cornuspira involvens	0.01	0.00	0.00	0.00

Appendix XIII: Ecological preferences of dominant benthic foraminifera

Ecological preferences (when known) of dominant benthic foraminiferal species identified in this study. In alphabetical order based on species dominant at both sites, then species dominant only in CE_VC1, then species dominant only in RH_VC7

Species	Living strategy	Feeding strategy	Energy	Other ecological preferences	References
Biloculinella globula	epifaunal	?	?	identified in the Mediterranean Sea, the Alboran Sea and the Porcupine Seabight	(Kaminski et al., 2002, Stalder et al., 2015, Fentimen et al., 2018)
Cibicides pachyderma	epifaunal/ shallow infaunal	passive suspension feeder, prefers labile components of organic matter	high	oligotrophic, found in stable physicochemical conditions	(Miao and Thunell, 1993, Almogi-Labin et al., 2000, Schmiedl et al., 2000, Murray, 2006b)
Discanomalina coronata	epifaunal attached	?	strong bottom currents up to 26–50 cm/s	attached on hydroids and octocorals	(Schönfeld, 1997, Schönfeld, 2002a, Schönfeld, 2002b, Hawkes and Scott, 2005)
Hyrrokkin sarcophaga	epifaunal	parasitic	high	found in aphotic environments. Attaches to large suspension feeders living in deep water, even where metabolic rates are low	(Cedhagen, 1994)
Melonis barleeanum	infaunal	may feed on low and intermediate quality organic matter	?	found in waters <10°C which are high in POM, lives in high productivity waters, lives on the redox front	(Corliss, 1985, Gooday, 1986, Caralp, 1989, Loubere, 1991, Fontanier et al., 2005, Murray, 2006a, Fontanier et al., 2008, Koho et al., 2008, Morigi et al., 2012)
Planulina ariminensis	epifaunal attached	suspension feeder	high	live on elevated substrates directly exposed to the water masses and flourish where strong currents mobilize suspended food particles	(Corliss, 1985, Lutze and Thiel, 1989, Schönfeld, 1997, Schönfeld, 2002a, Schönfeld, 2002b)

Trifarina angulosa	infaunal	?	high	associated with shelf-edge–upper-slope areas under the influence of strong bottom currents	(Sejrup et al., 1981, Hald and Vorren, 1984, Mackensen et al., 1985, Qvale and Weering, 1985, Austin and Evans, 2000, Schönfeld, 2002a, Mojtahid et al., 2021)
Uvigerina mediterranea	shallow, infaunal	?	?	Dominantly eutrophic. More abundant in the pelagic sediments overlying coral-fragment rich horizons	(de Stigter et al., 1998, Altenbach et al., 1999, Fontanier et al., 2002, Murray, 2006a)
Hanzawaia boueana	epifaunal attached	epiphytic	high	identified in the Alboran Sea and Porcupine Seabight	(Spezzaferri and Coric, 2001, Murray, 2006a, Stalder et al., 2015, Fentimen et al., 2018)
Pullenia subcarinata	infaunal	?	?	?	
Spiroplectinella sagitulla	epifaunal	?	?	?	
Uvigerina pygmae	infaunal	?	?	very tolerant of low oxygen levels	(Phleger and Soutar, 1973, Boltovskoy and Wright, 1976, Brolsma, 1978, Streeter and Shackleton, 1979, Woodruff and Douglas, 1981, Van der Zwaan, 1982)
Globocassidulina subglobosa	infaunal	phytodetritus feeder, preferentially ingests fresh diatoms	?	oligotrophic; organic matter rich sediments, indicative of organic matter fluxes of 0.8–60 g m^{-2} yr^{-1}	(Corliss, 1979, Gooday, 1993, Mackensen et al., 1995, Fariduddin and Loubere, 1997, Altenbach et al., 1999, Fontanier et al., 2002, Suhr et al., 2003, Fontanier et al., 2005, Murray, 2006a, Alve, 2010)
Homalohedra borealis		?	?	trace amounts identified in the Porcupine Seabight	(Fentimen et al., 2018)
Nuttalides umbonifer	infaunal	?	?	?	(Corliss, 1979, Schnitker, 1980, Corliss, 1985, Corliss and Chen, 1988)
Uvigerina auberiana	infaunal	?	?	very tolerant of low oxygen levels and indicates high organic matter	(Phleger and Soutar, 1973, Boltovskoy and Wright, 1976, Brolsma, 1978, Streeter and Shackleton, 1979, Woodruff and Douglas, 1981, Van der Zwaan, 1982, Singh et al., 2021)

Appendix XIV: ROV-vibrocorer



Photograph of Holland 1 ROV with the vibrocoring rig mounted on the front of the vehicle

Appendix XV: Coral preservation patterns in core CE18011_VC1, CE18011_VC4, CE18011_VC5 and RH17002_VC7

Characteristics of cold-water coral preservation patterns (CPPs) identified for cores RH_VC1, CE_VC5 and CE_VC5 based on CT data analyses. Data sets include average coral content (vol.%), average CWC clast size (unit: Φ; Φ=−log2[length(mm)/1 mm] and cm), the CWC clast orientation (0-90°) and assigned CPPs. CPP A: CWC framework in living position; CPP B: Slightly collapsed CWC framework; CPP C: CWC rubble; CPP D: Barren of CWC

Core ID	Core Depth [cmbsf]	Average Coral Content [vol.%]	Average CWC Clast Size [Φ]	CWC Clast Orientation [°]	Assigned CPP
CE_VC1	0–36	11.9	-4.5	<45	C
	36–73	8.5	-5	<60	A
	73–130	7.6	-4.8	up to 90	B
CE_VC4	0–83	10.6	-4.3	<45	C
	83–125	1.4	-3.3	-	D
	125–144	6.2	-4.8	<60	B
	144–165	9.1	-4.1	<45	C
	165–180	1.8	-0.8	-	D
CE_VC5	0–33	8.6	-3.5	<45	C
	33–79	1.9	-2.5	-	D
	79–115	6.4	-2.7	<45	C
RH_VC7	0–56	14.3	-4.9	up to 90	A
	56–80	7.9	-4.2	<60	B

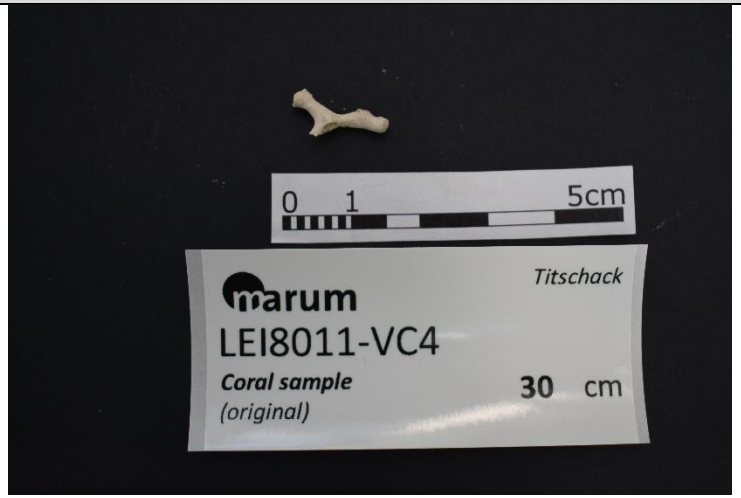
Appendix XVI: Corals used for U/Th dating

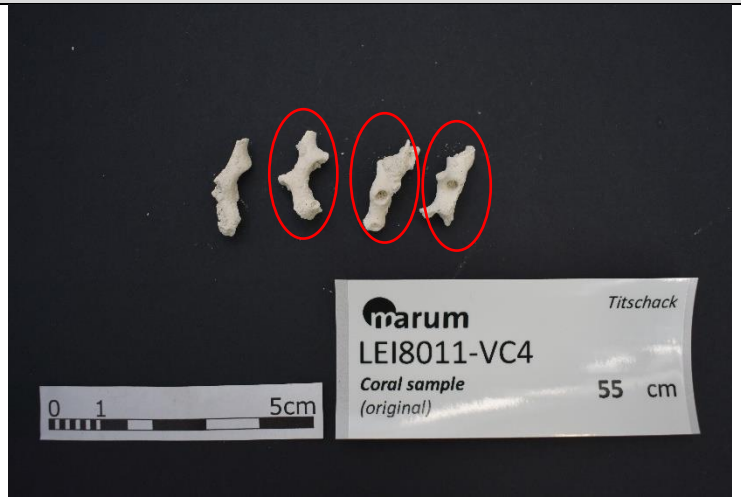
Corals used for U/Th were submitted on the basis of their thickness, bioerosion and dissolution. In the event 2 or more coral fragments were extracted (e.g. from cores CE_VC8 and RH_VC1) based on their suitability, the final submitted pieces are marked with a cirlce.

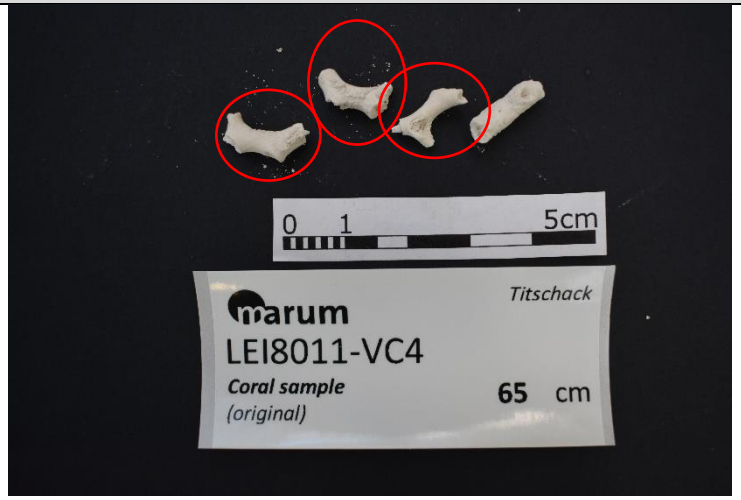
Sample ID [GeoB]	Species	Picture	Theka thickness			Bioerosion				Dissolution			
			thin	moderate	thick	none	weak	moderate	intense	none	weak	moderate	intense
CE18011-VC4_2 cm	*Madrepora oculata*				x				x			x	

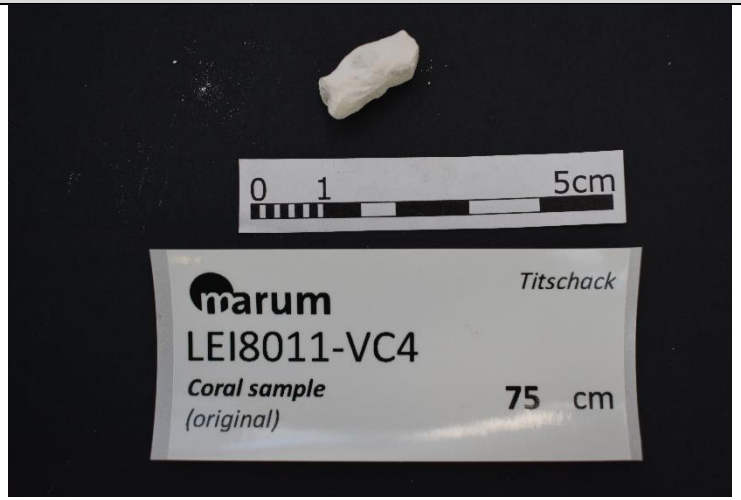
Sample ID [GeoB]	Species	Picture	Theka thickness			Bioerosion				Dissolution			
			thin	moderate	thick	none	weak	moderate	intense	none	weak	moderate	intense
CE18011-VC4_10 cm	*Madrepora* oculata			x				x			x		

Sample ID [GeoB]	Species	Picture	Theka thickness			Bioerosion				Dissolution			
			thin	moderate	thick	none	weak	moderate	intense	none	weak	moderate	intense
CE18011-VC4_20 cm	*Coral fragment*		x						x				x

Sample ID [GeoB]	Species	Picture	Theka thickness			Bioerosion				Dissolution			
			thin	moderate	thick	none	weak	moderate	intense	none	weak	moderate	intense
CE18011-VC4_30 cm	*Desmophyllum pertusum?*						x				x		
		very small sample											

Sample ID [GeoB]	Species	Picture	Theka thickness			Bioerosion				Dissolution			
			thin	moderate	thick	none	weak	moderate	intense	none	weak	moderate	intense
CE18011-VC4_55 cm	*Madrepora oculata*		x						x				x

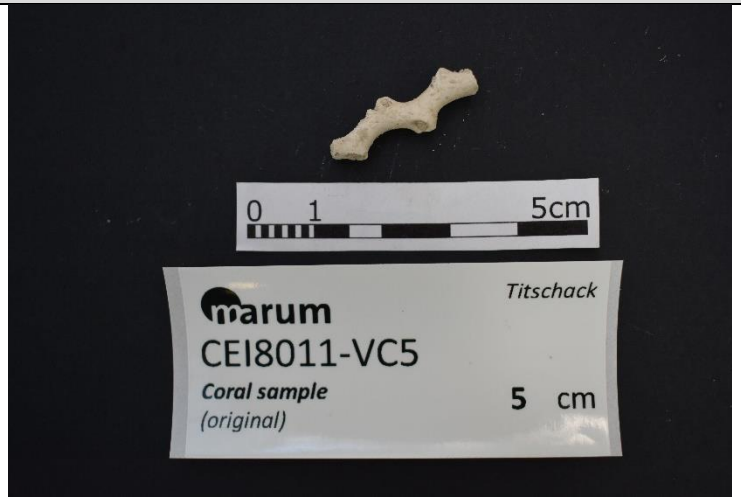
Sample ID [GeoB]	Species	Picture	Theka thickness			Bioerosion				Dissolution			
			thin	moderate	thick	none	weak	moderate	intense	none	weak	moderate	intense
CE18011-VC4_65 cm	*3 x Madrepora oculata?*		x					x					x

Sample ID [GeoB]	Species	Picture	Theka thickness			Bioerosion				Dissolution			
			thin	moderate	thick	none	weak	moderate	intense	none	weak	moderate	intense
CE18011-VC4_75 cm	*Coral fragment (potentially Madrepora oculata)*						x						x

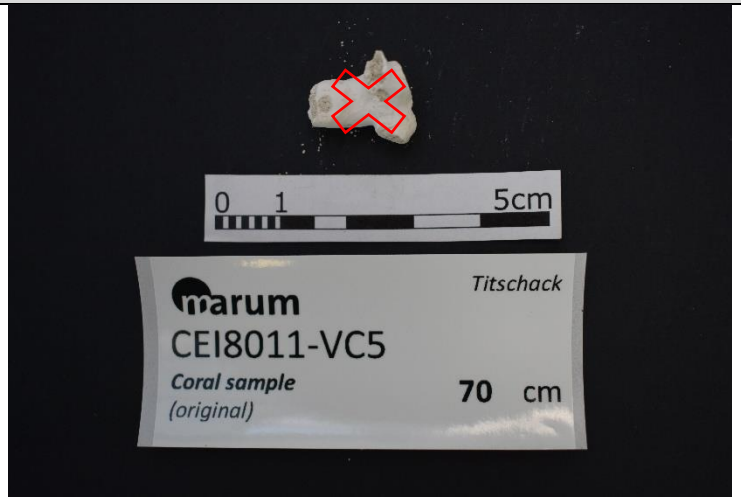
Sample ID [GeoB]	Species	Picture	Theka thickness			Bioerosion				Dissolution			
			thin	moderate	thick	none	weak	moderate	intense	none	weak	moderate	intense
CE18011-VC4_125 cm	*Desmophyllum pertusum*				x			x					x

Sample ID [GeoB]	Species	Picture	Theka thickness			Bioerosion				Dissolution			
			thin	moderate	thick	none	weak	moderate	intense	none	weak	moderate	intense
CE18011-VC4_135 cm	*Desmophyllum pertusum*		x					x					x

Sample ID [GeoB]	Species	Picture	Theka thickness			Bioerosion				Dissolution			
			thin	moderate	thick	none	weak	moderate	intense	none	weak	moderate	intense
CE18011-VC4_150 cm	*Desmophyllum pertusum?* (in the centre; left and right pieces could be also *Madrepora oculata*)	 completely altered											x

Sample ID [GeoB]	Species	Picture	Theka thickness			Bioerosion				Dissolution			
			thin	moderate	thick	none	weak	moderate	intense	none	weak	moderate	intense
CE18011-VC5_5 cm	*Madrepora oculata*		x						x				x

Sample ID [GeoB]	Species	Picture	Theka thickness			Bioerosion				Dissolution			
			thin	moderate	thick	none	weak	moderate	intense	none	weak	moderate	intense
CE18011-VC5_10 cm	*Madrepora oculata*			x				x			x		

Sample ID [GeoB]	Species	Picture	Theka thickness			Bioerosion				Dissolution			
			thin	moderate	thick	none	weak	moderate	intense	none	weak	moderate	intense
CE18011-VC5_70 cm	*Madrepora oculata*	 completely altered											x

Sample ID [GeoB]	Species	Picture	Theka thickness			Bioerosion				Dissolution			
			thin	moderate	thick	none	weak	moderate	intense	none	weak	moderate	intense
CE18011-VC5_80 cm	*Madrepora oculata*	 completely altered											x

Sample ID [GeoB]	Species	Picture	Theka thickness			Bioerosion				Dissolution			
			thin	moderate	thick	none	weak	moderate	intense	none	weak	moderate	intense
CE18011-VC5_100 cm	*Desmophyllum pertusum*								x				
		too much bioerosion											

Sample ID [GeoB]	Species	Picture	Theka thickness			Bioerosion				Dissolution			
			thin	moderate	thick	none	weak	moderate	intense	none	weak	moderate	intense
RH17002-VC1	*Madrepora oculata* (selected, red circle), only two pieces of *Desmophyllum pertusum* (yellow circles)				x		x					x	

Sample ID [GeoB]	Species	Picture	Theka thickness			Bioerosion				Dissolution			
			thin	moderate	thick	none	weak	moderate	intense	none	weak	moderate	intense
CE18011-VC6	Selected pieces are *Desmophyllum pertusum* (red circles), pieces in		x				x					x	

Sample ID [GeoB]	Species	Picture	Theka thickness			Bioerosion				Dissolution			
			thin	moderate	thick	none	weak	moderate	intense	none	weak	moderate	intense
CE18011-VC8	*Madrepora oculata*and a caryophyllid coral or *Desmophyllum dianthus* (yellow circle)			x	1				x				x
					2	x			x			x	

Appendix XVII: Courses completed during PhD

2022

- Professional Diploma in Project Management – University College Dublin Professional Academy. End of course exam grade: 94%. Project management project (Title: Sediment Analysis Lab for Renewable Energy – SEALREENY) grade: pending

2021

- Innovating Field Trips (IFiT) “Training the Trainers” (TTT) course hosted by CERES, in Aljezur, Portugal – No grade

2020

- Statistical Analysis for Palaeontology and Archaeology organised by Transmitting Science. This course was equivalent to 1 European Credit Transfer System – Grade: pass (pass or fail grading system)

2019

- 10 credits of Quantitative Skills for Biologists using R (BL6024) – Grade: 1:1
- 5 credits of Teaching and Demonstrating Skills for Biological, Earth and Environmental Sciences (BEES) Postgraduate Students (PG6017) – Grade: pass (pass or fail grading system)
- 5 credits of Geoinformatics for Environmental Geology (GL6025) – Grade: pass (pass or fail grading system)
- 5 credit postgraduate module in science communications and outreach (PG6014) – Grade: pass (pass or fail grading system)

2018

- ECORD training course 2018: MARUM – No grade

Appendix XIII: Research cruises undertook as part of, and during, the PhD

CE20011 (Leg 2) – Systematic Monitoring Survey of the Moira Mound Chain (Chief Scientist)

CE20011 (Leg 1) – Systematic Monitoring Survey of the Moira Mound Chain (Night shift leader)

CE19014 – Monitoring Changes in Submarine Canyon Coral Habitats II (Night shift leader)

CE19008 – Monitoring Changes in Submarine Canyon Coral Habitats I (Night shift leader)

CV19026 – De-risking Offshore Wind Energy Development Potential in Irish Waters II (Scientist)

CE18011 – Controls of Cold-Water Coral Habitats in Submarine Canyons II (Night shift leader)

CV18034 - AggreWind Research Survey (Scientist)

RV Belgica 2018/14 – GOLLUM: Research into the potential for "silent tsunamis" generated through mass-wasting in the Gollum Canal System, offshore SW Ireland (Foreign Vessel Observer)

RH17002 – Controls of Cold-Water Coral Habitats in Submarine Canyons (Geoscientist)

CV17020 – Quantifying Irish Marine Placer Resources (Geoscientist)

Appendix XIX: Awards and grants received during PhD

Awards

2020

- EES Education and Public Engagement (EPE) Prize – based on my involvement in numerous, diverse and/or innovative EPE activities across a 12-month period. Luke was the inaugural winner of this award across the school.
- Best oral presentation (including post-doctoral researchers) – Irish Geological Research Meeting

2019

- Honourable mention (Poster Presentation) – Irish Geological Research Meeting

2018

- Honourable Mention (Poster Presentation) – Irish Geological Research Meeting

Grants

2022

- Networking and Travel Award – Marine Institute – €2000 – I organized for a world expert in spatial data and GIS (Prof. Sam Purkis) to give a keynote talk at iGEO2022

2020

- Networking and Travel Award – Marine Institute 2020 for the amount of €2000 – I organized for a world expert in spatial data, GIS and machine learning (Prof. Luis Conti) to give a workshop at iGEO2020

2019

- Bill Watts 14CHRONO Award – Awarded 3 AMS dates on behalf of the Irish Quaternary Association
- Networking and Travel Award – Marine Institute – €750

2018

- Networking and Travel Award – Marine Institute – €1200
- Networking and Travel Award – Marine Institute – €550

Appendix XX: Conferences attended during PhD

2022

- Irish Geological Research Meeting 2022 – Online – In attendance

2021

- International Network for Submarine Canyon Investigation and Scientific Exchange 2021 – Online – Poster Presentation (The MMMonKey_Pro Research Program)
- Irish Geological Research Meeting 2021 – Online – In Attendance

2020

- Irish Geological Research Meeting 2020 – Athlone – Oral Presentation (The Controls of Cold-water Coral Habitats in Submarine Canyons: Preliminary Results)

2019

- Irish Geological Research Meeting 2019 – Dublin – Poster Presentation (The Controls of Cold-water Coral Habitats in Submarine Canyons: Preliminary CT results and Grain Size Analysis)
- International Association of Sedimentologists 2019 – Rome – Oral Presentation (The Controls of Cold-water Coral Habitats in Submarine Canyons: Preliminary Results)
- 13th International Symposium on Fossil Cnidaria and Porifera 2019 – Moderna – Oral Presentation (The Controls of Cold-water Coral Habitats in Submarine Canyons: Preliminary Results)
- Irish Quaternary association Spring Symposium 2019– Dublin – In Attendance

2018

- Irish Geological Research Meeting 2018 – Cork – Poster Presentation (The Controls of Cold-water Coral Habitats in Submarine Canyons: Introduction)
- Irish Quaternary association Spring Symposium 2018 – Dublin

- International Network for Submarine Canyon Investigation and Scientific Exchange 2018 – Shenzhen – Poster presentation (The Controls of Cold-water Coral Habitats in Submarine Canyons: Preliminary CT Results and Grain Size Analysis)

Appendix XXI: Conferences organized during PhD

2021/2022

- iGEO 2022 – I was elected as Chair for the upcoming early career symposium being held in University College Cork. Using the skills I have gained over the duration of the PhD, I now oversee all organizational tasks of the event

2020

- iGEO 2020 – I was lead social media representative of the event. I also was the official photographer of the event
- International Network for Submarine Canyon Investigation and Scientific Exchange 2020 – Prior to its cancellation due to the COVID-19 pandemic, I was a member of the organizing committee. My main task was to organize a field trip for delegates
- International Coral Reef Symposium 2020 – I was a social media representative for the event. I transcribed numerous documents into the Irish language for social media and blog posts

2018

- Irish Geological Research Meeting 2018 – Assisted with registration desk and miscellaneous tasked given to me by the organizing committee

Appendix XXII: Outreach during PhD

I gave a radio presentation in my native language (Irish) on national radio. Link: https://www.rte.ie/radio/radioplayer/html5/#/rnag/11071144

I was an invited guest on the iCRAG-o-rama podcast, where I talked about my research. Link: https://www.icrag-centre.org/news-and-media/podcasts/

I organised, hosted, and published a series of live webinars throughout the COVID-19 pandemic, to raise the awareness of the multidisciplinary nature of marine geology. The invited guests were from diverse backgrounds with expertise in many niches of the science and were delivered using transmittable language. They are available to view on my YouTube page (https://www.youtube.com/channel/UC8eBXpzBAzr7AdG4bfUfSkQ) and are listed below:

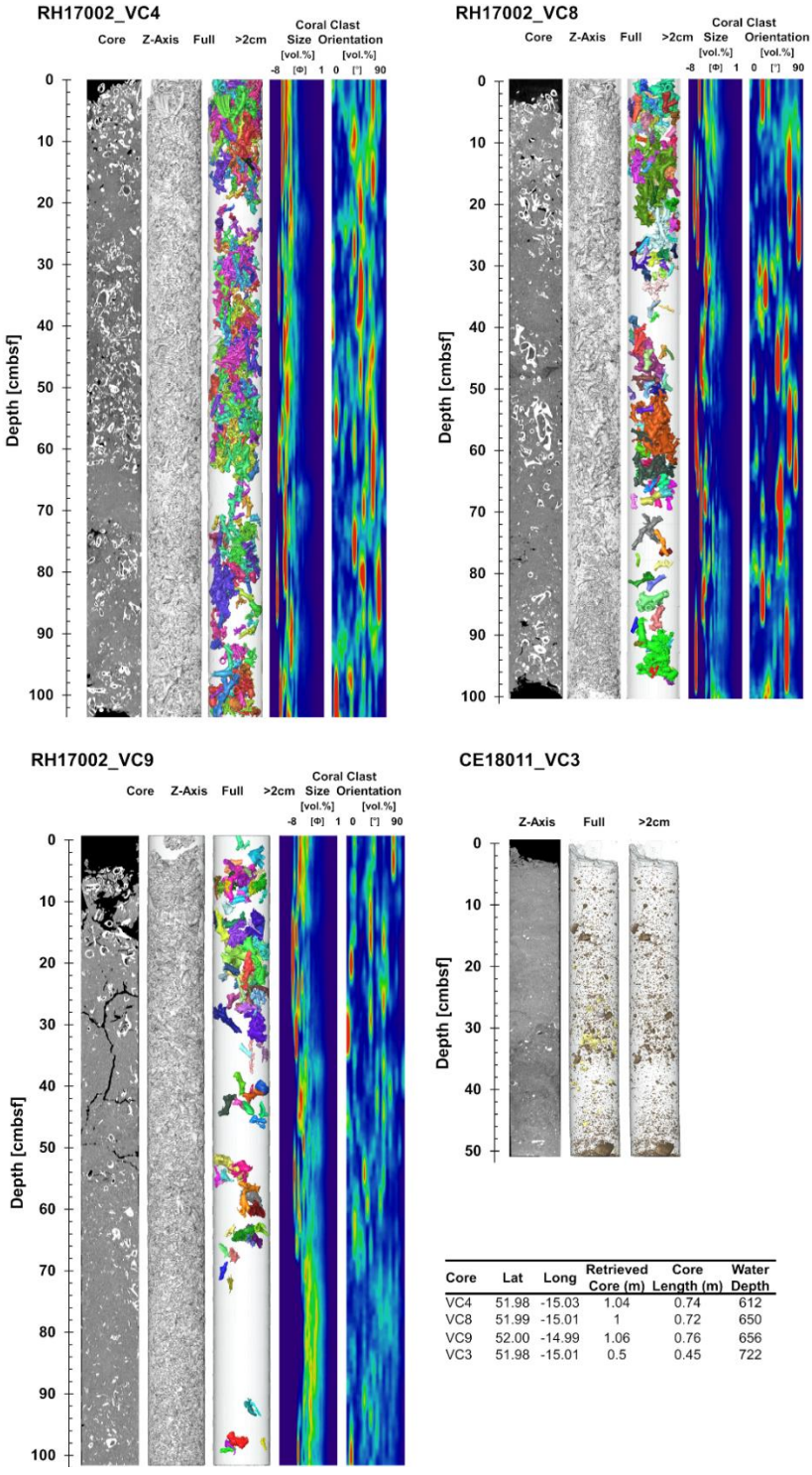
- 07.10.2020 - SEAROVER - A Comprehensive Assessment of Irelands Offshore Reef Biodiversity (David O'Sullivan)
- 09.09.2020 - Youth for the Atlantic Ocean: How to Make a Real Change (Eimear Manning and Eugénia Barroca)
- 02.09.2020 - Marine Geology in Context: Ordering the Ocean Through Science, Law & Politics (Philip E. Steinberg)
- 26.08.2020 - Living on the Edge: From Deep Sea to Outer Space (André Antunes)
- 29.07.2020 - Microplastic Transport, Dispersal & Accumulation in Seafloor Sediments (Florian Pohl)
- 22.07.2020 - Tectonic Evolution of the Falklands Plateau: Insights from Offshore Data (Dave McCarthy)
- 15.07.2020 - Studying Corals *as a geologist (Luke O'Reilly and Evan O'Mahony)
- 24.06.2020 - Mapping our Oceans: Earth's Final Frontier (Vicki Ferrini)
- 17.06.2020 - Mapping the Seafloor: From Inshore Ireland to the Abyss (Aileen Bohan)
- 10.06.2020 - Tiny Fossils, Big Currents: Pliocene Reconstruction of Kuroshio Current Extension (Adriane Lam)

- 03.06.2020 - Marine Palaeoglaciology: a cold and salty whodunnit (Jared Peters)
- 27.05.2020 - Building Offshore Windfarms in the Quaternary (Mark Coughlan)
- 20.05.2020 - Deep sea Microfossils: Whats the Story in Ireland & the Mediterranean? (Robin Fentimen)
- 13.05.2020 - Deep sea Corals The Best Storytellers (Matthias López Correa)

Additional Material

A: Additional cores and corresponding logs

These cores were not analysed further as the deemed unnecessary to the research following three-dimenstional CT analysis.



Core	Lat	Long	Retrieved Core (m)	Core Length (m)	Water Depth
VC4	51.98	-15.03	1.04	0.74	612
VC8	51.99	-15.01	1	0.72	650
VC9	52.00	-14.99	1.06	0.76	656
VC3	51.98	-15.01	0.5	0.45	722

Additional Material I: 3D-segmented computer tomography of additional cores collected during the RH17002 and CE18011 research cruises (see Wheeler, 2017 and Lim, 2018). See

summary table on lower right for acquisition details. Cores RH17002_VC4, RH17002_VC8, and RH17002_VC9 are coral bearing, whereas core CE18011_VC3 is mostly composed of IRD (brown) with trace amounts of bioclastic material (yellow).

B: Additional discussion on stable isotopes from core CE18011_VC2

The following section was removed from Chapter 2 (Using novel methods to track British and Irish Ice Sheet dynamics since the Late Pleistocene, along the west Porcupine Bank, NE Atlantic), as it broadened the focus of the study. During revision of the manuscript, it was recommended by both reviewers and editor that, although scientifically valid, appeared outside the target of the research scope.

Palaeoceanographic change

Oxygen and carbon stable isotope analysis in core CE18011_VC2 indicate variable patterns downcore (see figure below; see also Appendix XV). According to the planktonic $\delta^{18}O$ record, sediments during the Late Pleistocene have high $\delta^{18}O$ values (2.6 to 3.1 ‰), whereas Holocene sediments are characterised by low $\delta^{18}O$ values (1.6 to 2.2 ‰). A similar trend is seen in benthic $\delta^{18}O$ where higher values (2.7 to 3.7 ‰) are recorded in the Late Pleistocene and lower values (2 to 3.1 ‰) exist in the Holocene. This disparity becomes more evident if outliers are removed, whereby $\delta^{18}O$ values of 3 to 3.7 ‰ represent the Late Pleistocene and $\delta^{18}O$ values of 2.1 to 2.6 ‰ represent the Holocene. Other studies show that this glacial to interglacial shift of 1 ‰ is typical for benthic $\delta^{18}O$ records from the NE Atlantic (Peck et al., 2006; Peck et al., 2007). Peck *et al*. (2006) show that fully glacial conditions in the adjoining Porcupine Seabight at the same latitude are represented by benthic $\delta^{18}O$ values higher than 3 ‰, while fully interglacial conditions are represented by benthic $\delta^{18}O$ values lower than 2 ‰. Values ranging between these two thresholds correspond to intermediate climatic environments.

Canyon Decoupling

The environmental signals of cores CE_VC2 and CE_VC5 are used and compared to regional environmental signals from the Porcupine Seabight (see Peck et al., 2006) where CWCs also occur. In doing so, we ascertain the mechanism behind the succession of glacial CWCs in the PBC.

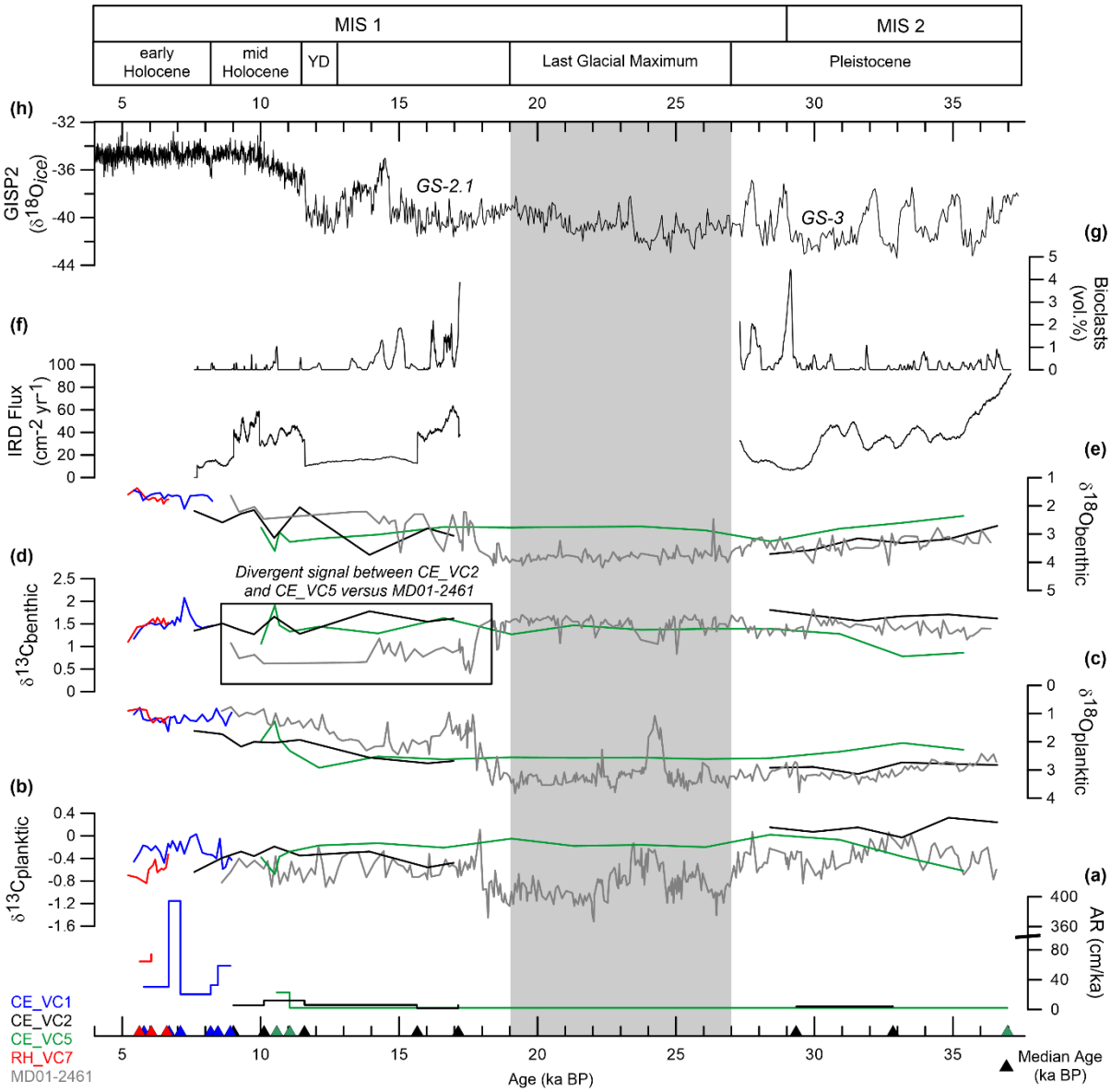
The changes in benthic $\delta^{13}C$ values could indicate changes in the bottom waters on the wPB (see figure below - d). Benthic $\delta^{18}O$ and $\delta^{13}C$ values are higher in CE_VC2 and CE_VC5 following the IRD fluxes at 30.1 and 15.7 ka event, providing evidence that a colder water body becomes prevalent during glacial periods of MIS 2 (GS–5.1 and GS–2.1) on the wPB. This is contemporaneous with abundant bioclastic material (see figure below - g), suggesting higher relative bioproductivity allowed for increased $\delta^{13}C$ dissolved inorganic carbon (DIC) values. From this, it is inferred that fully marine conditions were established, creating a suitable habitat for filter-feeding vagile benthic megafauna such as bivalves. The higher benthic $\delta^{13}C$ values suggest the presence of a new water mass or a notable change in the bottom-water $\delta^{13}C_{DIC}$ due to changes in primary production and remineralisation throughout the water column (see figure below - d). Planktic $\delta^{13}C$ values increase (up to 0.5 ‰), suggesting that surface waters are coupled to the bottom waters in the wPB during this period. This enrichment in ^{13}C of the DIC could result from an introduction of a new bottom water source with higher $\delta^{13}C$ and $\delta^{18}O$ values. On a regional scale, the wPB has higher benthic $\delta^{13}C$ values during MIS 2 when compared to the PS, where benthic $\delta^{13}C$ values >1.6 ‰ during glacial periods account for enhanced ventilation caused by the northerly sourced Glacial North Atlantic Intermediate Water (GNAIW; see figure below - d; see Peck et al., 2007). In contrast, benthic $\delta^{13}C$ values recorded in the PS during the Holocene are lower (<0.7 ‰), reflecting the collapse in the influence of the GNAIW. On the wPB, benthic $\delta^{13}C$ values remain constant across the Late Pleistocene and Holocene, suggesting water masses operated separately to the PS. These differences suggest a local effect, most likely from the nearby PBC.

It is expected that benthic $\delta^{13}C$ values would be lower than planktic δ13C values if both species grow in equilibrium with the given seawater DIC source. Nonetheless, this is not the case with the wPB (see figure below - d). In a homogenous water body with similar origins for the surface and bottom waters, a higher bioproductivity in the photic zone may increase the $\delta^{13}C$ values for the DIC. Concurrently, respiration of sinking organic matter in the water column lowers the $\delta^{13}C$ in sea water through remineralisation of the carbon

(Cavan et al., 2017). Intrinsically, the carbon isotopic composition of planktic foraminifera is commonly higher in ^{13}C compared to that for the benthic foraminifera (e.g. Duplessy et al., 1988). However, it is also known that different foraminifera have different vital effects that may cause an offset from equilibrium values for the foraminifera (e.g. Wefer and Berger, 1991). Even when considering the vital effects (estimated at -0.3 ‰ for *C. pachyderma* and about -1 ‰ for *G. bulloides;* Howard Spero, personal communication, 2021) the difference in carbon isotopic composition reduces somewhat, but the benthic species still maintain marginally higher or similar $\delta^{13}C$ values compared to the planktic foraminiferal species. This may further be complicated when considering that these vital offsets may change as a function of the concentration of DIC in seawater, which could be of particular importance for surface waters and hence planktic foraminifera compared to benthic foraminifera (e.g. Spero, 1997). The depositional records in CE_VC2 and CE_VC5 cover numerous glacial stadial/interstadial periods (see figure below). Hence, the change in vital effect for *G. bulloides* could indeed be considerable, especially when compared to the benthic record.

Nonetheless, an alternative explanation for these planktic-benthic differences in $\delta^{13}C$ values, as well as the critical changes in benthic $\delta^{13}C$ values with time, could be related to the origins of the surface and/or deep waters (e.g. Sarnthein et al., 2001) and changes therein with time at the present site. In the case of the wPB, the water column is naturally stratified (Mazzini et al., 2011). A potential source for the higher $\delta^{13}C$ values of the benthic records here could be the northerly flowing ENAW, which could account for an enriched ^{13}C isotopic composition originating from a different source than the surface waters. Today, this wPB is known for intensified currents on a local level (Lim et al., 2020bb), which may explain why the benthic foraminifera are relatively enriched in ^{13}C compared to the planktic foraminifera. The predominance of colder meltwater at the surface may also prevent productivity, consequently reducing planktic $\delta^{13}C$ values. Therefore, a divergent $\delta^{13}C$ record supports the hypothesis that surface and deep waters in the wPB were decoupled throughout the deglaciation of the BIIS. This source of enrichment would, in

turn, provide the most likely rational for the presence of glacial CWCs in the region during glacial periods.



Additional figure: Compilation of data obtained from cold-water coral bearing cores CE_VC1 (blue), CE_VC5 (green), RH_VC7 (red) and offmound core CE_VC2 (black) plotted against time. Data from CE_VC2 a hiatus in data between 27.3–17.2 ka BP (see O'Reilly et al., 2022). Data from MD01-2461 (grey; Peck et al., (2006) was recalibrated using the MARINE20 calibration curve (Heaton et al., 2020) to exclude any potential offsets. Modelled ages (in kilo annum before present) at the bottom of the figure are annotated by triangles. (a) sedimentation rates; (b–e) $\delta^{13}C$ and $\delta^{18}O$ of benthic and planktic foraminifers. A divergent signal is evident between CE_VC2 and CE_VC5

versus MD01-2461 and is annotated by a black rectangle; (f) IRD flux derived from CT-data (see O'Reilly et al., 2022); (g) volume percentage of biogenic clasts derived from CT-data (see O'Reilly et al., 2022); (h) Greenland Ice Core $\delta^{18}O$ values (GS – Greenland Stadials).

C: Additional benthic foraminifera picked from CE18011_VC5

During the exploratory phase of the data, it was determined that Core CE18011_VC5 broadened the scope of the study. It was decided as Cores CE18011_VC1 and RH17002_VC7 were from the same geomorphological setting (coral mound summits) and were somewhat contemporaneous, that they contained sufficient information to base a thesis chapter on. As such, benthic foraminifera counted from Core CE18011_VC5 were removed and presented as additional data in this thesis. Multivariate analysis of the assemblages was carried out, which is displayed below. Furthermore, SEM images of 5 dominant species were also acquired and are included.

Benthic foraminiferal assemblages were investigated from core CE18011_VC5 from 31 samples sampled at 5 to 10 cm intervals from the >125 μm fraction. Foraminifera were picked under a light stereomicroscope at Laboratory of Geology, University of Lyon (France). Taxonomic identification follows Margreth (2010) and Spezzaferri (2015). For the subsamples where foraminifera were very abundant, they were split with an Otto microsplitter and the whole splits were counted (see tables below). To help with the taxonomical identification Scanning Electron Microscope (SEM) photographs were acquired at the Department of Geosciences, University of Fribourg (Switzerland), using a Thermo Fischer SEM FEIXL30SFEG (see Fig. 14; see also images below) Benthic foraminiferal data was statistically treaded using the software PAST (PAleontological STatistics; Version 4.08; Hammer et al., 2001). Input for the PCA consisted of species' relative abundance data (correlation matrix). Only taxa occurring with ≥5% in at least one sample were retained in these statistical analyses (Mojtahid et al., 2021). Similarity Percentage Analysis (SIMPER) was obtained with the PRIMER 6 software (Clarke and Gorlet 2006). Data for non-metric MultiDimensional Scaling (nMDS) analysis were square root transformed. Clusters identified in the nMDS plot, both based on the Bray–Curtis Dissimilarity, underwent a non-parametric MANOVA test (NPMANOVA) and SIMPER. The SIMPER allowed to reveal the contribution of each species to the total dissimilarity/similarity, their individual contribution to each group (Clarke and Gorley 2006), and to highlight ecological differences in benthic foraminiferal assemblages. The ratio

between the average contribution of a species ($\bar{\delta_i}$) and the standard deviation of the species average contribution [SD ($\bar{\delta_i}$)], defined as follows: $\bar{\delta_i}$/SD ($\bar{\delta_i}$) (Clarke and Gorley 2006) was used to recognize discriminating species, e.g. the higher the value, the better the species is as a discriminator.

Species list and raw quantitative data of benthic foraminifera

Vibrocore	CE18011_VC5																						
Sample Number	290	291	292	293	294	295	297	298	299	300	301	302	303	304	305	306	307	308	309	310	311	312	Tot.
Depth (cm)	0	5	10	15	20	25	35	40	45	50	55	60	65	70	75	80	85	90	95	100	105	110	
Alabaminella weddellensis	1	1	0	0	0	0	0	0	0	0	0	0	0	0	0	0	1	0	0	0	0	0	3
Amphycorina scalaris	11	2	4	1	3	0	0	0	0	1	0	1	2	2	3	1	0	1	2	0	0	0	34
Astrononion stelligerum	2	1	4	3	0	1	0	0	1	0	0	0	2	4	2	2	0	2	2	0	0	0	26
Astrononion tumidum	0	0	2	1	0	0	0	0	0	0	0	0	0	1	0	1	0	0	0	0	0	0	5
Biloculinella globula	1	1	6	15	6	5	3	3	3	4	10	0	0	2	1	5	3	12	14	7	17	14	132
Bolivina dilatata	2	0	0	0	0	0	1	1	1	1	1	3	3	2	5	1	3	2	3	0	0	0	29
Bolivina pseudopunctata	0	0	0	0	0	0	0	0	0	0	0	0	0	1	0	0	0	0	0	0	0	0	1
Bolivina subspinescens	1	0	0	1	1	1	0	1	0	0	0	1	0	0	1	0	0	0	1	0	0	0	8
Bulimina aculeata	1	1	1	0	1	6	4	1	3	3	2	5	1	0	0	1	1	10	9	13	5	9	77
Bulimina marginata	10	4	6	10	18	9	23	16	24	25	12	38	39	36	21	23	21	18	30	29	50	46	508
Bulimina pupoides	1	1	0	0	2	0	1	0	0	1	0	2	1	0	0	0	0	1	2	1	0	1	14
Cassidulina carinata	1	0	0	0	0	0	0	0	0	0	0	0	0	0	0	0	0	0	0	0	0	0	1
Cassidulina reniforme	10	13	30	7	10	3	10	15	34	17	47	20	14	17	13	15	18	13	4	0	0	0	310
Cassidulina teretis	9	14	12	39	13	12	2	4	5	1	5	4	10	6	2	8	7	13	8	2	6	1	183
Chilostomella oolina	0	0	0	0	0	0	0	0	0	0	1	0	0	0	0	0	0	0	0	0	0	0	1
Cibicides aravaensis	0	0	0	1	0	0	0	0	0	0	0	0	0	0	0	1	0	0	0	0	0	0	2
Cibicides mundulus	2	3	0	2	5	3	4	2	4	0	0	3	1	0	0	1	5	3	0	0	4	4	46
Cibicides pachyderma	18	22	28	40	63	34	56	52	47	50	24	26	19	22	21	18	32	79	78	57	113	119	1018
Cibicides refulgens	4	7	2	9	9	11	24	16	22	16	18	9	3	8	7	8	34	25	48	31	70	49	430
Cibicides ungerianus	0	0	3	5	6	10	13	11	17	15	2	4	5	2	3	2	0	7	2	6	6	11	130
Cycloforina laevigata	0	1	0	0	1	0	0	0	0	0	0	0	0	0	0	0	0	1	0	0	0	1	4
Discanomalina coronata	11	9	11	10	7	6	6	4	7	5	16	11	3	5	10	7	11	9	18	6	19	11	202
Discorbina bertheloti	0	0	0	0	0	0	0	1	0	0	0	0	0	0	0	0	0	0	0	0	0	0	1
Eggerella humboldti	0	0	0	0	0	0	0	0	0	0	2	1	0	0	0	2	0	0	1	1	1	0	8
Fissurina annectens	2	4	0	2	1	0	1	0	0	0	4	2	0	4	2	1	2	3	1	1	0	0	30
Fissurina eburnea	2	5	1	12	1	1	0	1	0	0	2	3	0	2	3	1	2	1	1	0	2	0	40
Gaudryna pseudotrochus	0	0	0	0	0	0	0	0	0	0	0	0	0	0	0	0	1	0	2	0	0	0	3
Gaudryna rudis	0	0	1	1	0	1	0	0	0	0	0	0	0	0	0	0	0	1	0	0	0	0	4
Gavelinopsis praegeri	1	3	4	4	3	2	3	0	2	3	5	11	10	5	10	3	12	17	13	7	9	4	131
Glandulina ovula	0	3	2	1	1	0	0	0	0	0	0	0	0	0	0	0	0	1	0	0	0	0	8
Globocassidulina subglobosa	52	98	39	24	7	5	4	3	6	5	22	8	16	9	17	27	19	10	7	0	1	0	379
Globulina minuta	0	0	0	0	1	0	0	1	0	0	0	0	0	0	0	0	0	0	0	0	0	0	2
Gyroidina soldanii	7	14	9	14	16	7	12	7	10	18	8	13	8	5	6	7	3	11	14	11	12	11	223
Hanzawaia boueana	5	3	2	3	0	1	3	0	0	1	3	2	2	7	3	7	2	5	3	0	1	0	53

Vibrocore	CE18011_VC5																						
Sample Number	290	291	292	293	294	295	297	298	299	300	301	302	303	304	305	306	307	308	309	310	311	312	Tot.
Depth (cm)	0	5	10	15	20	25	35	40	45	50	55	60	65	70	75	80	85	90	95	100	105	110	
Hoeglundina elegans	1	0	0	3	0	1	3	1	3	3	1	3	3	0	0	1	2	4	1	0	2	2	34
Homalohedra apiopleura	0	0	0	0	0	0	0	0	0	0	0	2	1	0	0	0	0	0	0	0	0	0	3
Homalohedra williamsoni	0	0	1	0	0	1	1	1	0	0	0	0	0	5	2	1	2	1	0	1	1	2	19
Hyalinea balthica	2	1	0	2	1	0	1	1	2	0	1	7	3	2	2	3	4	1	0	1	0	0	34
Hyrrokkin sarcophaga	2	3	0	0	1	0	0	1	1	0	0	0	0	1	1	3	1	0	1	0	2	2	19
Karreriella bradyi	1	4	0	5	11	5	4	1	9	9	1	4	3	2	0	3	4	5	0	1	1	2	75
Lagena meridionalis	0	0	0	0	0	0	0	0	0	0	0	0	0	0	1	0	0	0	0	0	0	0	1
Lagena squamosalata	3	1	0	3	0	0	0	0	0	1	0	0	0	1	0	0	0	0	0	0	2	1	12
Lagena substriata	0	0	0	0	0	0	0	0	1	0	0	0	0	0	0	0	0	0	0	0	0	0	1
Lenticulina gibba	6	2	0	1	1	2	6	0	2	2	0	2	0	0	3	4	0	4	0	1	0	0	36
Lenticulina orbicularis	1	0	3	0	0	0	0	4	0	0	1	0	0	1	0	0	7	2	1	0	1	1	22
Melonis barleeanum	31	37	26	25	37	21	25	16	19	17	19	25	18	25	19	13	17	16	6	5	6	2	425
Neolenticulina peregrina	0	1	0	1	0	0	1	0	0	0	0	2	0	0	0	0	0	0	0	0	0	0	5
Nonion commune	0	0	0	1	0	0	0	0	0	0	0	0	0	0	0	0	0	1	0	0	0	0	2
Nuttalides umbonifer	4	3	0	1	0	0	0	0	2	0	0	1	3	0	1	7	1	2	0	1	0	0	26
Oolina globosa	3	0	2	0	0	0	0	0	0	0	0	0	0	2	0	0	0	1	0	0	0	0	8
Oolina lineata	0	0	0	0	0	0	0	1	0	0	1	0	0	0	0	0	2	0	0	0	0	0	4
Oolina melo	1	5	0	0	0	0	0	0	0	0	1	0	0	3	2	3	2	3	2	0	0	0	22
Palliolatella semimarginata	4	1	0	0	0	0	0	0	0	0	0	0	0	2	0	0	3	0	1	0	0	0	11
Pattellina corrugata	0	0	0	0	0	0	0	0	0	0	0	0	0	1	0	0	0	0	0	0	0	0	1
Planulina ariminensis	6	11	5	1	9	2	5	3	5	2	0	3	2	0	1	2	4	5	1	1	3	0	71
Pullenia bulloides	0	0	1	0	0	0	0	0	0	0	0	0	0	0	0	0	0	0	0	0	3	0	4
Pullenia subcarinata	1	6	5	12	3	3	0	0	8	2	1	3	4	4	10	7	3	1	0	2	2	2	79
Pyrgo comata	2	1	0	0	0	0	1	0	0	0	0	0	0	1	0	0	0	0	0	0	0	0	5
Pyrgo elongata	0	1	0	0	0	0	0	0	0	0	0	0	0	0	0	0	0	1	1	0	0	0	3
Pyrgo sarsi	3	4	1	2	1	1	1	1	0	2	0	2	0	0	2	1	1	1	3	0	0	1	27
Pyrulina angusta	0	0	1	0	0	0	0	0	0	0	0	0	0	0	0	0	0	0	0	0	0	0	1
Quinqueloculina bosciana	0	0	0	0	0	0	0	0	0	0	0	0	0	0	0	0	2	0	0	0	0	0	2
Quinqueloculina semiluna	1	2	2	2	3	0	3	1	4	3	6	3	1	0	1	0	3	4	4	0	2	4	49
Quinqueloculina viennensis	2	0	2	0	0	1	2	1	2	5	3	3	1	0	3	1	7	4	7	5	16	4	69
Reophax agglutinans	0	0	0	0	0	1	2	1	0	4	0	1	0	0	0	0	0	0	0	2	0	0	11
Robertinoides bradyi	0	2	1	0	0	0	0	0	1	0	0	0	1	1	1	1	4	1	1	1	0	0	15
Schakoinella spina	1	0	0	0	0	0	0	0	0	0	0	0	0	1	0	0	0	0	0	0	0	0	2
Sigmoilopsis schlumbergeri	3	2	0	4	2	4	5	7	7	5	8	4	1	5	2	1	2	5	2	6	6	3	84
Siphonina reticulata	0	0	1	0	0	0	0	0	0	0	0	0	0	0	1	0	0	0	0	0	0	0	2
Sphaeroidina bulloides	1	3	0	1	0	1	0	0	0	0	0	0	0	0	1	0	0	0	0	0	0	0	7
Spirillina vivipara	1	0	0	0	0	1	0	0	0	0	0	0	0	1	0	0	0	0	0	0	0	0	3
Spiroloculina dilatata	0	1	0	1	0	0	0	0	0	0	0	0	0	0	0	1	0	1	0	1	0	0	5

Vibrocore	CE18011_VC5																						
Sample Number	290	291	292	293	294	295	297	298	299	300	301	302	303	304	305	306	307	308	309	310	311	312	Tot.
Depth (cm)	0	5	10	15	20	25	35	40	45	50	55	60	65	70	75	80	85	90	95	100	105	110	
Spiroloculina tenuisepta	0	0	0	0	0	0	0	0	0	0	0	0	0	1	0	0	0	0	0	0	0	0	1
Spiroplectinella sagitulla	8	8	2	3	3	0	1	1	3	1	2	2	5	1	4	1	5	6	5	0	2	0	63
Spiroplectinella wrightii	9	6	0	1	3	4	0	1	2	3	1	0	0	0	0	1	1	2	3	3	0	0	40
Textularia agglutinans	0	0	0	0	2	1	0	0	2	1	0	0	0	0	1	0	0	0	0	0	0	0	7
Textularia pseudorugosa	0	0	0	0	0	0	0	0	0	0	0	0	0	1	0	0	1	0	0	0	0	0	2
Textularia truncata	0	2	0	1	1	3	1	0	0	3	1	4	1	0	1	1	0	14	17	37	40	27	154
Trifarina angulosa	49	49	30	54	22	36	10	9	8	10	54	159	99	90	73	88	78	87	42	12	18	8	1085
Trifarina bradyi	0	1	0	0	0	0	0	0	0	0	0	0	0	0	0	0	0	0	0	0	0	0	1
Triloculina marioni	0	0	0	0	0	0	0	0	0	0	0	0	0	0	0	0	0	0	1	0	0	0	1
Triloculina tricarinta	2	0	0	0	0	1	0	0	1	0	0	0	0	0	0	0	0	1	0	0	0	1	6
Triloculina trigonula	0	0	0	0	1	1	0	0	0	0	0	0	0	0	0	0	0	1	1	0	0	0	4
Uvigerina auberiana	12	11	2	4	2	0	0	0	1	0	0	1	2	0	0	3	3	1	0	0	0	0	42
Uvigerina mediterranea	50	43	29	47	123	74	136	82	77	68	30	52	41	29	15	24	54	49	53	29	74	45	1224
Uvigerina pygmae	11	19	5	1	16	7	14	9	20	8	7	10	11	9	11	7	6	12	5	4	5	3	200
Total																							8075

Species list and relative abundance of benthic foraminifera from core CE18011_VC5

Core	CE18011_VC5																					
Depth (cm)	0	5	10	15	20	25	35	40	45	50	55	60	65	70	75	80	85	90	95	100	105	110
Alabaminella weddellensis	0.27	0.23	0	0	0	0	0	0	0	0	0	0	0	0	0	0	0.25	0	0	0	0	0
Amphycorina scalaris	2.93	0.45	1.4	0.26	0.72	0	0	0	0	0.32	0	0.22	0.59	0.61	1.04	0.31	0	0.21	0.48	0	0	0
Astrononion stelligerum	0.53	0.23	1.4	0.79	0	0.35	0	0	0.27	0	0	0	0.59	1.22	0.69	0.63	0	0.42	0.48	0	0	0
Astrononion tumidum	0	0	0.7	0.26	0	0	0	0	0	0	0	0	0	0.3	0	0.31	0	0	0	0	0	0
Biloculinella globula	0.27	0.23	2.1	3.94	1.44	1.73	0.77	1.07	0.82	1.27	3.11	0	0	0.61	0.35	1.57	0.76	2.49	3.33	2.46	3.39	3.58
Bolivina dilatata	0.53	0	0	0	0	0	0.26	0.36	0.27	0.32	0.31	0.65	0.88	0.61	1.74	0.31	0.76	0.42	0.71	0	0	0
Bolivina pseudopunctata	0	0	0	0	0	0	0	0	0	0	0	0	0	0.3	0	0	0	0	0	0	0	0
Bolivina subspinescens	0.27	0	0	0.26	0.24	0.35	0	0.36	0	0	0	0.22	0	0	0.35	0	0	0	0.24	0	0	0
Bulimina aculeata	0.27	0.23	0.35	0	0.24	2.08	1.02	0.36	0.82	0.95	0.62	1.09	0.29	0	0	0.31	0.25	2.08	2.14	4.56	1	2.3
Bulimina marginata	2.67	0.91	2.1	2.62	4.32	3.11	5.87	5.69	6.56	7.94	3.73	8.26	11.5	10.9	7.29	7.21	5.3	3.74	7.13	10.2	9.96	11.8
Bulimina pupoides	0.27	0.23	0	0	0.48	0	0.26	0	0	0.32	0	0.43	0.29	0	0	0	0	0.21	0.48	0.35	0	0.26
Cassidulina carinata	0.27	0	0	0	0	0	0	0	0	0	0	0	0	0	0	0	0	0	0	0	0	0
Cassidulina reniforme	2.67	2.95	10.5	1.84	2.4	1.04	2.55	5.34	9.29	5.4	14.6	4.35	4.13	5.17	4.51	4.7	4.55	2.7	0.95	0	0	0
Cassidulina teretis	2.4	3.18	4.2	10.2	3.12	4.15	0.51	1.42	1.37	0.32	1.55	0.87	2.95	1.82	0.69	2.51	1.77	2.7	1.9	0.7	1.2	0.26

Core	CE18011_VC5																					
Depth (cm)	0	5	10	15	20	25	35	40	45	50	55	60	65	70	75	80	85	90	95	100	105	110
Chilostomella oolina	0	0	0	0	0	0	0	0	0	0	0.31	0	0	0	0	0	0	0	0	0	0	0
Cibicides aravaensis	0	0	0	0.26	0	0	0	0	0	0	0	0	0	0	0	0.31	0	0	0	0	0	0
Cibicides mundulus	0.53	0.68	0	0.52	1.2	1.04	1.02	0.71	1.09	0	0	0.65	0.29	0	0	0.31	1.26	0.62	0	0	0.8	1.02
Cibicides pachyderma	4.8	5	9.79	10.5	15.1	11.8	14.3	18.5	12.8	15.9	7.45	5.65	5.6	6.69	7.29	5.64	8.08	16.4	18.5	20	22.5	30.4
Cibicides refulgens	1.07	1.59	0.7	2.36	2.16	3.81	6.12	5.69	6.01	5.08	5.59	1.96	0.88	2.43	2.43	2.51	8.59	5.2	11.4	10.9	13.9	12.5
Cibicides ungerianus	0	0	1.05	1.31	1.44	3.46	3.32	3.91	4.64	4.76	0.62	0.87	1.47	0.61	1.04	0.63	0	1.46	0.48	2.11	1.2	2.81
Cycloforina laevigata	0	0.23	0	0	0.24	0	0	0	0	0	0	0	0	0	0	0	0	0.21	0	0	0	0.26
Discanomalina coronata	2.93	2.05	3.85	2.62	1.68	2.08	1.53	1.42	1.91	1.59	4.97	2.39	0.88	1.52	3.47	2.19	2.78	1.87	4.28	2.11	3.78	2.81
Discorbina bertheloti	0	0	0	0	0	0	0	0.36	0	0	0	0	0	0	0	0	0	0	0	0	0	0
Eggerella humboldti	0	0	0	0	0	0	0	0	0	0	0.62	0.22	0	0	0	0.63	0	0	0.24	0.35	0.2	0
Fissurina annectens	0.53	0.91	0	0.52	0.24	0	0.26	0	0	0	1.24	0.43	0	1.22	0.69	0.31	0.51	0.62	0.24	0.35	0	0
Fissurina eburnea	0.53	1.14	0.35	3.15	0.24	0.35	0	0.36	0	0	0.62	0.65	0	0.61	1.04	0.31	0.51	0.21	0.24	0	0.4	0
Gaudryna pseudotrochus	0	0	0	0	0	0	0	0	0	0	0	0	0	0	0	0	0.25	0	0.48	0	0	0
Gaudryna rudis	0	0	0.35	0.26	0	0.35	0	0	0	0	0	0	0	0	0	0	0	0.21	0	0	0	0
Gavelinopsis praegeri	0.27	0.68	1.4	1.05	0.72	0.69	0.77	0	0.55	0.95	1.55	2.39	2.95	1.52	3.47	0.94	3.03	3.53	3.09	2.46	1.79	1.02
Glandulina ovula	0	0.68	0.7	0.26	0.24	0	0	0	0	0	0	0	0	0	0	0	0	0.21	0	0	0	0
Globocassidulina subglobosa	13.9	22.3	13.6	6.3	1.68	1.73	1.02	1.07	1.64	1.59	6.83	1.74	4.72	2.74	5.9	8.46	4.8	2.08	1.66	0	0.2	0
Globulina minuta	0	0	0	0	0.24	0	0	0.36	0	0	0	0	0	0	0	0	0	0	0	0	0	0
Gyroidina soldanii	1.87	3.18	3.15	3.67	3.84	2.42	3.06	2.49	2.73	5.71	2.48	2.83	2.36	1.52	2.08	2.19	0.76	2.29	3.33	3.86	2.39	2.81
Hanzawaia boueana	1.33	0.68	0.7	0.79	0	0.35	0.77	0	0	0.32	0.93	0.43	0.59	2.13	1.04	2.19	0.51	1.04	0.71	0	0.2	0
Hoeglundina elegans	0.27	0	0	0.79	0	0.35	0.77	0.36	0.82	0.95	0.31	0.65	0.88	0	0	0.31	0.51	0.83	0.24	0	0.4	0.51
Homalohedra apiopleura	0	0	0	0	0	0	0	0	0	0	0	0.43	0.29	0	0	0	0	0	0	0	0	0
Homalohedra williamsoni	0	0	0.35	0	0	0.35	0.26	0.36	0	0	0	0	0	1.52	0.69	0.31	0.51	0.21	0	0.35	0.2	0.51
Hyalinea balthica	0.53	0.23	0	0.52	0.24	0	0.26	0.36	0.55	0	0.31	1.52	0.88	0.61	0.69	0.94	1.01	0.21	0	0.35	0	0
Hyrrokkin sarcophaga	0.53	0.68	0	0	0.24	0	0	0.36	0.27	0	0	0	0	0.3	0.35	0.94	0.25	0	0.24	0	0.4	0.51
Karreriella bradyi	0.27	0.91	0	1.31	2.64	1.73	1.02	0.36	2.46	2.86	0.31	0.87	0.88	0.61	0	0.94	1.01	1.04	0	0.35	0.2	0.51
Lagena meridionalis	0	0	0	0	0	0	0	0	0	0	0	0	0	0	0.35	0	0	0	0	0	0	0
Lagena squamosalata	0.8	0.23	0	0.79	0	0	0	0	0	0.32	0	0	0	0.3	0	0	0	0	0	0	0.4	0.26
Lagena substriata	0	0	0	0	0	0	0	0	0.27	0	0	0	0	0	0	0	0	0	0	0	0	0
Lenticulina gibba	1.6	0.45	0	0.26	0.24	0.69	1.53	0	0.55	0.63	0	0.43	0	0	1.04	1.25	0	0.83	0	0.35	0	0
Lenticulina orbicularis	0.27	0	1.05	0	0	0	0	1.42	0	0	0.31	0	0	0.3	0	0	1.77	0.42	0.24	0	0.2	0.26
Melonis barleeanum	8.27	8.41	9.09	6.56	8.87	7.27	6.38	5.69	5.19	5.4	5.9	5.43	5.31	7.6	6.6	4.08	4.29	3.33	1.43	1.75	1.2	0.51
Neolenticulina peregrina	0	0.23	0	0.26	0	0	0.26	0	0	0	0	0.43	0	0	0	0	0	0	0	0	0	0
Nonion commune	0	0	0	0.26	0	0	0	0	0	0	0	0	0	0	0	0	0	0.21	0	0	0	0
Nuttalides umbonifer	1.07	0.68	0	0.26	0	0	0	0	0.55	0	0	0.22	0.88	0	0.35	2.19	0.25	0.42	0	0.35	0	0
Oolina globosa	0.8	0	0.7	0	0	0	0	0	0	0	0	0	0	0.61	0	0	0	0.21	0	0	0	0
Oolina lineata	0	0	0	0	0	0	0	0.36	0	0	0.31	0	0	0	0	0	0.51	0	0	0	0	0
Oolina melo	0.27	1.14	0	0	0	0	0	0	0	0	0.31	0	0	0.91	0.69	0.94	0.51	0.62	0.48	0	0	0

Core	CE18011_VC5																					
Depth (cm)	0	5	10	15	20	25	35	40	45	50	55	60	65	70	75	80	85	90	95	100	105	110
Palliolatella semimarginata	1.07	0.23	0	0	0	0	0	0	0	0	0	0	0	0.61	0	0	0.76	0	0.24	0	0	0
Pattellina corrugata	0	0	0	0	0	0	0	0	0	0	0	0	0	0.3	0	0	0	0	0	0	0	0
Planulina ariminensis	1.6	2.5	1.75	0.26	2.16	0.69	1.28	1.07	1.37	0.63	0	0.65	0.59	0	0.35	0.63	1.01	1.04	0.24	0.35	0.6	0
Pullenia bulloides	0	0	0.35	0	0	0	0	0	0	0	0	0	0	0	0	0	0	0	0	0	0.6	0
Pullenia subcarinata	0.27	1.36	1.75	3.15	0.72	1.04	0	0	2.19	0.63	0.31	0.65	1.18	1.22	3.47	2.19	0.76	0.21	0	0.7	0.4	0.51
Pyrgo comata	0.53	0.23	0	0	0	0	0.26	0	0	0	0	0	0	0.3	0	0	0	0	0	0	0	0
Pyrgo elongata	0	0.23	0	0	0	0	0	0	0	0	0	0	0	0	0	0	0	0.21	0.24	0	0	0
Pyrgo sarsi	0.8	0.91	0.35	0.52	0.24	0.35	0.26	0.36	0	0.63	0	0.43	0	0	0.69	0.31	0.25	0.21	0.71	0	0	0.26
Pyrulina angusta	0	0	0.35	0	0	0	0	0	0	0	0	0	0	0	0	0	0	0	0	0	0	0
Quinqueloculina bosciana	0	0	0	0	0	0	0	0	0	0	0	0	0	0	0	0	0.51	0	0	0	0	0
Quinqueloculina semiluna	0.27	0.45	0.7	0.52	0.72	0	0.77	0.36	1.09	0.95	1.86	0.65	0.29	0	0.35	0	0.76	0.83	0.95	0	0.4	1.02
Quinqueloculina viennensis	0.53	0	0.7	0	0	0.35	0.51	0.36	0.55	1.59	0.93	0.65	0.29	0	1.04	0.31	1.77	0.83	1.66	1.75	3.19	1.02
Reophax agglutinans	0	0	0	0	0	0.35	0.51	0.36	0	1.27	0	0.22	0	0	0	0	0	0	0	0.7	0	0
Robertinoides bradyi	0	0.45	0.35	0	0	0	0	0	0.27	0	0	0	0.29	0.3	0.35	0.31	1.01	0.21	0.24	0.35	0	0
Schakoinella spina	0.27	0	0	0	0	0	0	0	0	0	0	0	0	0.3	0	0	0	0	0	0	0	0
Sigmoilopsis schlumbergeri	0.8	0.45	0	1.05	0.48	1.38	1.28	2.49	1.91	1.59	2.48	0.87	0.29	1.52	0.69	0.31	0.51	1.04	0.48	2.11	1.2	0.77
Siphonina reticulata	0	0	0.35	0	0	0	0	0	0	0	0	0	0	0	0.35	0	0	0	0	0	0	0
Sphaeroidina bulloides	0.27	0.68	0	0.26	0	0.35	0	0	0	0	0	0	0	0	0.35	0	0	0	0	0	0	0
Spirillina vivipara	0.27	0	0	0	0	0.35	0	0	0	0	0	0	0	0.3	0	0	0	0	0	0	0	0
Spiroloculina dilatata	0	0.23	0	0.26	0	0	0	0	0	0	0	0	0	0	0	0.31	0	0.21	0	0.35	0	0
Spiroloculina tenuisepta	0	0	0	0	0	0	0	0	0	0	0	0	0	0.3	0	0	0	0	0	0	0	0
Spiroplectinella sagitulla	2.13	1.82	0.7	0.79	0.72	0	0.26	0.36	0.82	0.32	0.62	0.43	1.47	0.3	1.39	0.31	1.26	1.25	1.19	0	0.4	0
Spiroplectinella wrightii	2.4	1.36	0	0.26	0.72	1.38	0	0.36	0.55	0.95	0.31	0	0	0	0	0.31	0.25	0.42	0.71	1.05	0	0
Textularia agglutinans	0	0	0	0	0.48	0.35	0	0	0.55	0.32	0	0	0	0	0.35	0	0	0	0	0	0	0
Textularia pseudorugosa	0	0	0	0	0	0	0	0	0	0	0	0	0	0.3	0	0	0.25	0	0	0	0	0
Textularia truncata	0	0.45	0	0.26	0.24	1.04	0.26	0	0	0.95	0.31	0.87	0.29	0	0.35	0.31	0	2.91	4.04	13	7.97	6.91
Trifarina angulosa	13.1	11.1	10.5	14.2	5.28	12.5	2.55	3.2	2.19	3.17	16.8	34.6	29.2	27.4	25.3	27.6	19.7	18.1	9.98	4.21	3.59	2.05
Trifarina bradyi	0	0.23	0	0	0	0	0	0	0	0	0	0	0	0	0	0	0	0	0	0	0	0
Triloculina marioni	0	0	0	0	0	0	0	0	0	0	0	0	0	0	0	0	0	0	0.24	0	0	0
Triloculina tricarinta	0.53	0	0	0	0	0.35	0	0	0.27	0	0	0	0	0	0	0	0	0.21	0	0	0	0.26
Triloculina trigonula	0	0	0	0	0.24	0.35	0	0	0	0	0	0	0	0	0	0	0	0.21	0.24	0	0	0
Uvigerina auberiana	3.2	2.5	0.7	1.05	0.48	0	0	0	0.27	0	0	0.22	0.59	0	0	0.94	0.76	0.21	0	0	0	0
Uvigerina mediterranea	13.3	9.77	10.1	12.3	29.5	25.6	34.7	29.2	21	21.6	9.32	11.3	12.1	8.81	5.21	7.52	13.6	10.2	12.6	10.2	14.7	11.5
Uvigerina pygmae	2.93	4.32	1.75	0.26	3.84	2.42	3.57	3.2	5.46	2.54	2.17	2.17	3.24	2.74	3.82	2.19	1.52	2.49	1.19	1.4	1	0.77

Results of Simper Analysis using Bray Curtis similarity describing the similarity between benthic foraminifera assemblages in core CE18011_VC5. Cut off for low contributions set at 90,00% For interpretation see figures below these tables

Red group Average similarity: 79,15					
Species	Av.Abund	Av.Sim	Sim/SD	Contrib%	Cum.%
Cibicides pachyderma	4.91	10.39	20.07	13.12	13.12
Cibicides refulgens	3.52	7.69	17.69	9.72	22.84
Uvigerina mediterranea	3.47	7.42	19.52	9.37	32.21
Bulimina marginata	3.26	7.21	45.49	9.11	41.32
Textularia truncata	3.02	6.13	43.79	7.74	49.06
Biloculinella globula	1.77	3.78	9.12	4.77	53.83
Gyroidina soldanii	1.73	3.62	17.7	4.57	58.41
Trifarina angulosa	1.79	3.6	6.74	4.55	62.95
Discanomalina coronata	1.69	3.48	9.98	4.39	67.35
Cibicides ungerianus	1.41	2.76	5.64	3.49	70.84
Bulimina aculeata	1.55	2.67	3.81	3.37	74.21
Gavelinopsis praegeri	1.31	2.55	6.74	3.22	77.42
Quinqueloculina viennensis	1.37	2.53	7.06	3.2	80.62
Sigmoilopsis schlumbergeri	1.14	2.15	8.91	2.72	83.35
Uvigerina pygmae	1.02	2.08	17.44	2.63	85.98
Melonis barleeanum	1.04	1.91	4.19	2.41	88.39
Pullenia subcarinata	0.73	1.5	12.27	1.9	90.29

Blue group Average similarity: 77,80					
Species	Av.Abund	Av.Sim	Sim/SD	Contrib%	Cum.%
Uvigerina mediterranea	5.17	10.07	11.72	12.95	12.95
Cibicides pachyderma	3.83	7.54	14.42	9.69	22.64
Melonis barleeanum	2.53	4.91	17.39	6.31	28.95
Bulimina marginata	2.34	4.38	6.66	5.63	34.58
Cibicides refulgens	2.16	4.03	4.85	5.17	39.76
Uvigerina pygmae	1.85	3.49	10.3	4.48	44.24
Trifarina angulosa	2.08	3.45	7.77	4.43	48.68
Cibicides ungerianus	1.87	3.45	4.7	4.43	53.11
Gyroidina soldanii	1.81	3.38	13.85	4.35	57.46
Cassidulina reniforme	1.97	3.18	3.19	4.09	61.55
Discanomalina coronata	1.3	2.57	36.69	3.31	64.86
Globocassidulina subglobosa	1.2	2.32	10.52	2.98	67.83
Karreriella bradyi	1.3	2.16	2.82	2.77	70.61
Sigmoilopsis schlumbergeri	1.2	2.13	4.01	2.74	73.34
Biloculinella globula	1.08	2.01	9.14	2.58	75.92
Planulina ariminensis	1.07	1.91	6.05	2.46	78.38
Cassidulina teretis	1.24	1.84	2.51	2.36	80.74
Bulimina aculeata	0.9	1.45	3.33	1.86	82.6
Cibicides mundulus	0.84	1.31	1.35	1.68	84.29
Gavelinopsis praegeri	0.71	1.1	1.35	1.41	85.7
Quinqueloculina semiluna	0.72	1.06	1.31	1.36	87.06
Spiroplectinella wrightii	0.72	0.99	1.32	1.28	88.34
Hoeglundina elegans	0.66	0.94	1.29	1.21	89.54
Lenticulina gibba	0.68	0.9	1.28	1.16	90.71

Cyan group Average similarity: 73,16	Green group Average similarity: 71,38

Species	Av.Abund	Av.Sim	Sim/SD	Contrib %	Cum. %
Trifarina angulosa	4.75	8.26	5.47	11.29	11.29
Uvigerina mediterranea	3.15	5.59	6.68	7.65	18.93
Cibicides pachyderma	2.93	4.91	9.42	6.71	25.65
Bulimina marginata	2.64	4.53	5.36	6.19	31.84
Melonis barleeanum	2.17	3.69	4.11	5.04	36.88
Cassidulina reniforme	2.14	3.42	3.65	4.67	41.55
Globocassidulina subglobosa	2	3.19	3.78	4.36	45.91
Cibicides refulgens	2	2.96	3.4	4.04	49.95
Uvigerina pygmae	1.53	2.66	6.32	3.63	53.58
Gavelinopsis praegeri	1.55	2.64	4.61	3.61	57.19
Discanomalina coronata	1.6	2.61	4.69	3.57	60.76
Gyroidina soldanii	1.46	2.54	4.65	3.47	64.24
Cassidulina teretis	1.34	2.24	4.58	3.06	67.3
Hanzawaia boueana	0.99	1.58	5.11	2.16	69.46
Spiroplectinella sagitulla	0.92	1.47	3.27	2.01	71.47
Sigmoilopsis schlumbergeri	0.9	1.36	4.05	1.86	73.33
Bolivina dilatata	0.81	1.32	5.05	1.81	75.14
Cibicides ungerianus	0.82	1.22	1.76	1.67	76.81
Pullenia subcarinata	0.91	1.13	1.46	1.55	78.36
Quinqueloculina viennensis	0.83	1.13	1.61	1.54	79.9
Hyalinea balthica	0.75	1.05	1.57	1.44	81.35
Biloculinella globula	0.96	1.03	1	1.41	82.76
Fissurina annectens	0.7	0.96	1.66	1.31	84.07
Karreriella bradyi	0.69	0.9	1.12	1.23	85.3
Fissurina eburnea	0.62	0.88	1.64	1.2	86.5
Quinqueloculina semiluna	0.67	0.8	1.11	1.09	87.59
Oolina melo	0.61	0.77	1.14	1.05	88.64
Bulimina aculeata	0.7	0.75	1.03	1.02	89.66
Planulina ariminensis	0.61	0.74	1.1	1.01	90.68

Species	Av.Abund	Av.Sim	Sim/SD	Contrib %	Cum. %
Trifarina angulosa	3.49	6.11	30.17	8.56	8.56
Uvigerina mediterranea	3.37	5.88	21.53	8.24	16.8
Globocassidulina subglobosa	3.66	5.69	4.8	7.97	24.77
Melonis barleeanum	2.84	4.99	14.42	6.99	31.77
Cibicides pachyderma	2.7	4.34	5.34	6.09	37.85
Cassidulina teretis	2.15	3.14	6.82	4.41	42.26
Gyroidina soldanii	1.71	2.89	5.97	4.05	46.31
Discanomalina coronata	1.68	2.83	10.73	3.96	50.26
Cassidulina reniforme	1.99	2.77	8.53	3.87	54.14
Bulimina marginata	1.41	2.26	3.93	3.16	57.3
Uvigerina auberiana	1.31	1.86	3.98	2.61	59.91
Uvigerina pygmae	1.41	1.79	1.88	2.51	62.43
Cibicides refulgens	1.17	1.78	6.22	2.49	64.92
Spiroplectinella sagitulla	1.13	1.71	5.31	2.4	67.32
Planulina ariminensis	1.17	1.64	2.13	2.3	69.62
Pullenia subcarinata	1.2	1.61	2.12	2.25	71.87
Hanzawaia boueana	0.93	1.54	28.54	2.16	74.03
Fissurina eburnea	1.04	1.31	4.05	1.84	75.86
Gavelinopsis praegeri	0.89	1.3	2.96	1.82	77.69
Pyrgo sarsi	0.79	1.25	6.8	1.76	79.44
Amphycorina scalaris	1.02	1.24	2.59	1.74	81.18
Biloculinella globula	1.11	1.21	1.58	1.69	82.87
Astrononion stelligerum	0.82	1.16	3.34	1.62	84.5
Quinqueloculina semiluna	0.69	1.11	5.32	1.56	86.05
Sigmoilopsis schlumbergeri	0.65	0.67	0.9	0.94	86.99
Spiroplectinella wrightii	0.81	0.65	0.79	0.91	87.9
Cibicides mundulus	0.57	0.65	0.91	0.91	88.81
Fissurina annectens	0.6	0.65	0.91	0.91	89.72
Karreriella bradyi	0.65	0.59	0.83	0.83	90.55

Green and blue groups Average dissimilarity = 35,97							Green and cyan groups Average dissimilarity = 31,72						
Species	Green Av.Abund	Blue Av.Abund	Av.Diss	Diss/SD	Contrib%	Cum.%	Species	Green Av.Abund	Cyan Av.Abund	Av.Diss	Diss/SD	Contrib%	Cum.%
Globocassidulina subglobosa	3.66	1.2	2.39	3.06	6.65	6.65	*Globocassidulina subglobosa*	3.66	2	1.58	1.83	4.99	4.99
Uvigerina mediterranea	3.37	5.17	1.76	3.25	4.89	11.55	*Trifarina angulosa*	3.49	4.75	1.26	1.85	3.99	8.98
Trifarina angulosa	3.49	2.08	1.41	2.21	3.93	15.47	*Bulimina marginata*	1.41	2.64	1.17	2.09	3.67	12.65
Cibicides ungerianus	0.54	1.87	1.28	2.11	3.55	19.02	*Uvigerina auberiana*	1.31	0.39	0.86	1.74	2.72	15.37
Cibicides pachyderma	2.7	3.83	1.09	2	3.03	22.05	*Cibicides refulgens*	1.17	2	0.84	1.23	2.65	18.02
Uvigerina auberiana	1.31	0.2	1.07	2.29	2.97	25.02	*Cassidulina reniforme*	1.99	2.14	0.8	1.36	2.52	20.54
Cibicides refulgens	1.17	2.16	0.98	2.23	2.72	27.74	*Cassidulina teretis*	2.15	1.34	0.78	1.2	2.47	23.02
Cassidulina teretis	2.15	1.24	0.96	1.32	2.68	30.42	*Biloculinella globula*	1.11	0.96	0.73	1.41	2.29	25.3
Bulimina marginata	1.41	2.34	0.9	2.09	2.5	32.93	*Cibicides pachyderma*	2.7	2.93	0.66	1.39	2.08	27.38
Amphycorina scalaris	1.02	0.24	0.81	1.62	2.24	35.17	*Melonis barleeanum*	2.84	2.17	0.64	1.5	2.02	29.4
Cassidulina reniforme	1.99	1.97	0.77	1.29	2.15	37.32	*Planulina ariminensis*	1.17	0.61	0.63	1.63	1.99	31.39
Fissurina eburnea	1.04	0.28	0.74	1.38	2.06	39.38	*Gavelinopsis praegeri*	0.89	1.55	0.63	1.88	1.99	33.38
Karreriella bradyi	0.65	1.3	0.72	1.48	1.99	41.37	*Bolivina dilatata*	0.18	0.81	0.62	1.86	1.96	35.35
Pullenia subcarinata	1.2	0.69	0.7	1.42	1.96	43.33	*Spiroplectinella wrightii*	0.81	0.35	0.62	1.38	1.96	37.3
Astrononion stelligerum	0.82	0.19	0.64	1.78	1.77	45.1	*Textularia truncata*	0.3	0.77	0.59	1.07	1.84	39.15
Biloculinella globula	1.11	1.08	0.59	2.41	1.65	46.75	*Pullenia subcarinata*	1.2	0.91	0.58	1.42	1.82	40.96
Sigmoilopsis schlumbergeri	0.65	1.2	0.59	1.34	1.64	48.39	*Amphycorina scalaris*	1.02	0.53	0.56	1.28	1.75	42.72
Uvigerina pygmae	1.41	1.85	0.59	1.2	1.64	50.03	*Quinqueloculina viennensis*	0.39	0.83	0.54	1.4	1.7	44.41
Spiroplectinella wrightii	0.81	0.72	0.58	1.52	1.61	51.64	*Cibicides ungerianus*	0.54	0.82	0.53	1.39	1.68	46.09
Hanzawaia boueana	0.93	0.34	0.58	1.61	1.6	53.24	*Lenticulina gibba*	0.61	0.41	0.52	1.37	1.64	47.73

Green and blue groups Average dissimilarity = 35,97							Green and cyan groups Average dissimilarity = 31,72						
Species	Green Av.Abund	Blue Av.Abund	Av.Diss	Diss/SD	Contrib%	Cum.%	Species	Green Av.Abund	Cyan Av.Abund	Av.Diss	Diss/SD	Contrib%	Cum.%
Spiroplectinella sagitulla	1.13	0.57	0.55	1.46	1.53	54.77	*Lagena squamosalata*	0.56	0.06	0.5	1.48	1.58	49.31
Nuttalides umbonifer	0.59	0.12	0.53	1.42	1.47	56.24	*Uvigerina pygmae*	1.41	1.53	0.5	1.38	1.56	50.87
Lagena squamosalata	0.56	0.09	0.5	1.45	1.4	57.64	*Glandulina ovula*	0.54	0.05	0.49	1.52	1.56	52.43
Bulimina aculeata	0.4	0.9	0.5	1.37	1.39	59.04	*Fissurina eburnea*	1.04	0.62	0.48	1.1	1.52	53.94
Fissurina annectens	0.6	0.17	0.5	1.58	1.39	60.43	*Oolina melo*	0.4	0.61	0.47	1.45	1.49	55.43
Glandulina ovula	0.54	0.08	0.49	1.48	1.37	61.8	*Nuttalides umbonifer*	0.59	0.51	0.46	1.34	1.46	56.89
Reophax agglutinans	0	0.5	0.49	1.24	1.37	63.17	*Bulimina aculeata*	0.4	0.7	0.46	1.22	1.46	58.35
Lenticulina gibba	0.61	0.68	0.47	1.31	1.3	64.47	*Karreriella bradyi*	0.65	0.69	0.44	1.21	1.37	59.73
Hoeglundina elegans	0.35	0.66	0.46	1.33	1.29	65.76	*Lenticulina orbicularis*	0.39	0.4	0.43	1.16	1.37	61.09
Quinqueloculina viennensis	0.39	0.65	0.46	1.27	1.27	67.03	*Sigmoilopsisschlumbergeri*	0.65	0.9	0.42	1.14	1.31	62.4
Lenticulina orbicularis	0.39	0.2	0.45	0.97	1.25	68.28	*Astrononion stelligerum*	0.82	0.54	0.42	1.24	1.31	63.71
Cibicides mundulus	0.57	0.84	0.45	1.26	1.24	69.52	*Hoeglundina elegans*	0.35	0.55	0.41	1.31	1.29	65
Oolina globosa	0.43	0	0.42	0.98	1.17	70.69	*Sphaeroidina bulloides*	0.46	0.07	0.41	1.46	1.29	66.29
Textularia truncata	0.3	0.5	0.42	1.27	1.16	71.85	*Cibicides mundulus*	0.57	0.42	0.41	1.27	1.29	67.58
Textularia agglutinans	0	0.43	0.41	1.36	1.15	73.01	*Oolina globosa*	0.43	0.14	0.41	1.06	1.29	68.87
Sphaeroidina bulloides	0.46	0.1	0.41	1.41	1.14	74.15	*Hyalinea balthica*	0.48	0.75	0.41	1.3	1.28	70.15
Planulina ariminensis	1.17	1.07	0.4	1.74	1.1	75.25	*Palliolatella semimarginata*	0.38	0.24	0.39	1.07	1.22	71.38
Oolina melo	0.4	0	0.38	0.87	1.05	76.3	*Homalohedra williamsoni*	0.15	0.42	0.39	1.05	1.22	72.6
Hyrrokkin sarcophaga	0.39	0.27	0.38	1.28	1.05	77.35	*Pyrgo sarsi*	0.79	0.43	0.39	1.29	1.21	73.81
Discanomalina coronata	1.68	1.3	0.37	1.72	1.04	78.39	*Hyrrokkin sarcophaga*	0.39	0.34	0.38	1.28	1.21	75.02
Melonis barleeanum	2.84	2.53	0.36	1.65	1	79.38	*Uvigerina mediterranea*	3.37	3.15	0.38	1.22	1.19	76.21

Green and blue groups
Average dissimilarity = 35,97

Species	Green Av.Abund	Blue Av.Abund	Av.Diss	Diss/SD	Contrib%	Cum.%
Palliolatella semimarginata	0.38	0	0.36	0.87	0.99	80.38
Bolivina dilatata	0.18	0.36	0.36	1.38	0.99	81.37
Astrononion tumidum	0.34	0	0.34	0.92	0.94	82.3
Gavelinopsis praegeri	0.89	0.71	0.33	1.08	0.92	83.22
Hyalinea balthica	0.48	0.39	0.32	1.18	0.88	84.1
Robertinoides bradyi	0.32	0.09	0.31	1.02	0.86	84.96
Pyrgo sarsi	0.79	0.5	0.31	1.24	0.85	85.81
Quinqueloculina semiluna	0.69	0.72	0.29	1.36	0.81	86.62
Pyrgo comata	0.3	0.08	0.29	1	0.81	87.43
Bulimina pupoides	0.25	0.29	0.29	1.11	0.8	88.22
Gyroidina soldanii	1.71	1.81	0.28	1.3	0.79	89.01
Homalohedra williamsoni	0.15	0.28	0.28	1	0.79	89.8
Gaudryna rudis	0.28	0.1	0.28	0.99	0.77	90.58

Green and cyan groups
Average dissimilarity = 31,72

Species	Green Av.Abund	Cyan Av.Abund	Av.Diss	Diss/SD	Contrib%	Cum.%
Fissurina annectens	0.6	0.7	0.36	1.14	1.13	77.34
Spiroplectinella sagitulla	1.13	0.92	0.35	1.63	1.09	78.43
Discanomalina coronata	1.68	1.6	0.34	1.39	1.08	79.52
Robertinoides bradyi	0.32	0.47	0.33	1.25	1.05	80.57
Quinqueloculina semiluna	0.69	0.67	0.33	1.32	1.05	81.62
Astrononion tumidum	0.34	0.12	0.33	1.01	1.03	82.65
Gyroidina soldanii	1.71	1.46	0.32	1.38	1	83.64
Pyrgo comata	0.3	0.06	0.28	0.99	0.89	84.53
Bulimina pupoides	0.25	0.26	0.28	1.12	0.87	85.4
Eggerella humboldti	0	0.28	0.27	0.84	0.84	86.25
Gaudryna rudis	0.28	0.05	0.26	1.01	0.84	87.08
Neolenticulina peregrina	0.25	0.07	0.25	1.03	0.79	87.87
Bolivina subspinescens	0.26	0.17	0.25	1.04	0.78	88.65
Spiroloculina dilatata	0.25	0.11	0.24	1.02	0.75	89.41
Hanzawaia boueana	0.93	0.99	0.24	1.27	0.75	90.16

Blue and green groups
Average dissimilarity = 32,54

Species	Blue Av.Abund	Green Av.Abund	Av.Diss	Diss/SD	Contrib%	Cum.%
Trifarina angulosa	2.08	4.75	2.7	2.54	8.29	8.29
Uvigerina mediterranea	5.17	3.15	2.03	3.16	6.23	14.52
Cibicides pachyderma	3.83	2.93	1.08	2.12	3.31	17.83
Cibicides ungerianus	1.87	0.82	1.04	2.23	3.2	21.03
Gavelinopsis praegeri	0.71	1.55	0.84	1.84	2.58	23.61

Green and red groups
Average dissimilarity = 47,38

Species	Green Av.Abund	Red Av.Abund	Av.Diss	Diss/SD	Contrib%
Globocassidulina subglobosa	3.66	0.15	3.56	4.2	7.52
Textularia truncata	0.3	3.02	2.76	5.14	5.83
Cibicides refulgens	1.17	3.52	2.4	6.5	5.06
Cibicides pachyderma	2.7	4.91	2.24	3.26	4.73
Cassidulina reniforme	1.99	0	2.03	2.39	4.29

	Blue and green groups Average dissimilarity = 32,54							Green and red groups Average dissimilarity = 47,38				
Globocassidulina subglobosa	1.2	2	0.81	1.38	2.48	26.09	*Bulimina marginata*	1.41	3.26	1.88	5.64	3.96
Cassidulina reniforme	1.97	2.14	0.77	1.25	2.38	28.47	*Melonis barleeanum*	2.84	1.04	1.83	5.13	3.86
Cibicides refulgens	2.16	2	0.72	1.53	2.2	30.67	*Trifarina angulosa*	3.49	1.79	1.72	4.66	3.64
Karreriella bradyi	1.3	0.69	0.69	1.52	2.11	32.78	*Cassidulina teretis*	2.15	0.81	1.36	1.85	2.88
Hanzawaia boueana	0.34	0.99	0.67	1.59	2.06	34.84	*Uvigerina auberiana*	1.31	0	1.32	3.48	2.78
Pullenia subcarinata	0.69	0.91	0.63	1.3	1.92	36.77	*Bulimina aculeata*	0.4	1.55	1.17	2.15	2.47
Textularia truncata	0.5	0.77	0.62	1.2	1.9	38.67	*Amphycorina scalaris*	1.02	0	1.03	2.14	2.18
Oolina melo	0	0.61	0.6	1.74	1.86	40.52	*Quinqueloculina viennensis*	0.39	1.37	0.99	1.88	2.09
Biloculinella globula	1.08	0.96	0.59	1.6	1.82	42.35	*Spiroplectinella sagitulla*	1.13	0.21	0.93	2.24	1.97
Cibicides mundulus	0.84	0.42	0.58	1.45	1.77	44.12	*Cibicides ungerianus*	0.54	1.41	0.88	1.46	1.85
Fissurina annectens	0.17	0.7	0.57	1.64	1.74	45.85	*Fissurina eburnea*	1.04	0.21	0.85	1.49	1.8
Bulimina marginata	2.34	2.64	0.55	1.39	1.7	47.55	*Astrononion stelligerum*	0.82	0	0.84	2.84	1.77
Lenticulina gibba	0.68	0.41	0.55	1.43	1.69	49.25	*Hanzawaia boueana*	0.93	0.15	0.79	3.05	1.66
Cassidulina teretis	1.24	1.34	0.52	1.63	1.59	50.83	*Planulina ariminensis*	1.17	0.46	0.79	1.7	1.66
Bulimina aculeata	0.9	0.7	0.51	1.42	1.56	52.4	*Biloculinella globula*	1.11	1.77	0.77	1.43	1.63
Spiroplectinella wrightii	0.72	0.35	0.51	1.41	1.56	53.96	*Spiroplectinella wrightii*	0.81	0.34	0.73	1.31	1.53
Nuttalides umbonifer	0.12	0.51	0.5	1.13	1.53	55.49	*Uvigerina pygmae*	1.41	1.02	0.65	2.03	1.36
Planulina ariminensis	1.07	0.61	0.5	1.23	1.53	57.02	*Pyrgo sarsi*	0.79	0.17	0.63	2.22	1.32
Reophax agglutinans	0.5	0.05	0.49	1.26	1.5	58.53	*Pullenia subcarinata*	1.2	0.73	0.59	1.71	1.24
Hyalinea balthica	0.39	0.75	0.48	1.45	1.47	59.99	*Glandulina ovula*	0.54	0	0.56	1.52	1.18
Astrononion stelligerum	0.19	0.54	0.48	1.32	1.46	61.46	*Sigmoilopsis schlumbergeri*	0.65	1.14	0.53	1.13	1.13
Lenticulina orbicularis	0.2	0.4	0.47	1.04	1.43	62.89	*Lenticulina gibba*	0.61	0.2	0.53	1.22	1.12
Melonis barleeanum	2.53	2.17	0.46	1.13	1.42	64.31	*Nuttalides umbonifer*	0.59	0.2	0.51	1.37	1.08
Amphycorina scalaris	0.24	0.53	0.46	1.4	1.4	65.71	*Fissurina annectens*	0.6	0.2	0.51	1.4	1.07
Quinqueloculina viennensis	0.65	0.83	0.45	1.35	1.39	67.1	*Sphaeroidina bulloides*	0.46	0	0.46	1.5	0.98
Bolivina dilatata	0.36	0.81	0.45	1.34	1.39	68.48	*Homalohedra williamsoni*	0.15	0.58	0.46	1.87	0.98
Sigmoilopsis schlumbergeri	1.2	0.9	0.44	1.57	1.36	69.84	*Cibicides mundulus*	0.57	0.63	0.45	1.21	0.96
Fissurina eburnea	0.28	0.62	0.43	1.4	1.32	71.16	*Gavelinopsis praegeri*	0.89	1.31	0.45	1.51	0.95
Quinqueloculina semiluna	0.72	0.67	0.42	1.18	1.3	72.46	*Oolina globosa*	0.43	0	0.44	0.96	0.93
Spiroplectinella sagitulla	0.57	0.92	0.42	1.36	1.3	73.76	*Karreriella bradyi*	0.65	0.58	0.42	1.79	0.88
Robertinoides bradyi	0.09	0.47	0.42	1.41	1.29	75.04	*Hoeglundina elegans*	0.35	0.45	0.41	1.28	0.87
Textularia agglutinans	0.43	0.07	0.41	1.31	1.25	76.29	*Lagena squamosalata*	0.56	0.38	0.41	1.39	0.87
Homalohedra williamsoni	0.28	0.42	0.4	1.16	1.24	77.53	*Hyalinea balthica*	0.48	0.2	0.41	1.32	0.86
Discanomalina coronata	1.3	1.6	0.4	1.33	1.24	78.77	*Hyrrokkin sarcophaga*	0.39	0.45	0.4	1.14	0.84
Uvigerina auberiana	0.2	0.39	0.39	1.14	1.2	79.97	*Lenticulina orbicularis*	0.39	0.32	0.4	1.23	0.84
Gyroidina soldanii	1.81	1.46	0.39	1.11	1.19	81.16	*Oolina melo*	0.4	0	0.39	0.85	0.83

Blue and green groups Average dissimilarity = 32,54						
Uvigerina pygmae	1.85	1.53	0.39	1.32	1.19	82.35
Hoeglundina elegans	0.66	0.55	0.37	1.19	1.13	83.48
Hyrrokkin sarcophaga	0.27	0.34	0.33	1.11	1	84.48
Pyrgo sarsi	0.5	0.43	0.33	1.23	1	85.48
Bulimina pupoides	0.29	0.26	0.32	1.11	0.97	86.45
Eggerella humboldti	0	0.28	0.28	0.84	0.87	87.32
Bolivina subspinescens	0.28	0.17	0.28	1.06	0.87	88.19
Palliolatella semimarginata	0	0.24	0.24	0.68	0.72	88.92
Triloculina trigonula	0.18	0.1	0.21	0.84	0.65	89.57
Oolina lineata	0.1	0.14	0.2	0.68	0.61	90.18

Green and red groups Average dissimilarity = 47,38					
Quinqueloculina semiluna	0.69	0.55	0.38	1.4	0.8
Palliolatella semimarginata	0.38	0	0.37	0.85	0.79
Astrononion tumidum	0.34	0	0.35	0.9	0.74
Eggerella humboldti	0	0.35	0.35	1.32	0.73
Robertinoides bradyi	0.32	0.2	0.32	0.99	0.68
Pullenia bulloides	0.15	0.26	0.31	0.87	0.66
Uvigerina mediterranea	3.37	3.47	0.3	1.37	0.64

Blue and red groups

Average dissimilarity = 34,10

	Blue	Red				
Species	Av.Abund	Av.Abund	Av.Diss	Diss/SD	Contrib%	Cum.%
Textularia truncata	0.5	3.02	2.73	4.26	8	8
Cassidulina reniforme	1.97	0	2.14	2.94	6.28	14.28
Uvigerina mediterranea	5.17	3.47	1.85	2.98	5.41	19.69
Melonis barleeanum	2.53	1.04	1.62	3.96	4.74	24.43
Cibicides refulgens	2.16	3.52	1.47	3.36	4.32	28.75
Cibicides pachyderma	3.83	4.91	1.18	1.97	3.46	32.21
Globocassidulina subglobosa	1.2	0.15	1.14	4.21	3.34	35.54
Bulimina marginata	2.34	3.26	1	2.5	2.93	38.47

Cyan and red groups

Average dissimilarity = 38,89

	Cyan	Red				
Species	Av.Abund	Av.Abund	Av.Diss	Diss/SD	Contrib%	Cum.%
Trifarina angulosa	4.75	1.79	3.11	3.3	7.99	7.99
Textularia truncata	0.77	3.02	2.36	2.87	6.06	14.05
Cassidulina reniforme	2.14	0	2.25	2.83	5.78	19.83
Cibicides pachyderma	2.93	4.91	2.1	2.28	5.39	25.21
Globocassidulina subglobosa	2	0.15	1.94	2.98	4.99	30.21
Cibicides refulgens	2	3.52	1.61	1.93	4.15	34.36
Melonis barleeanum	2.17	1.04	1.19	2.23	3.07	37.42
Bulimina aculeata	0.7	1.55	0.96	1.53	2.46	39.89

Blue and red groups						
Average dissimilarity = 34,10						
Uvigerina pygmae	1.85	1.02	0.91	2.8	2.66	41.13
Quinqueloculina viennensis	0.65	1.37	0.81	1.67	2.38	43.51
Karreriella bradyi	1.3	0.58	0.78	1.89	2.3	45.81
Bulimina aculeata	0.9	1.55	0.76	1.38	2.22	48.03
Biloculinella globula	1.08	1.77	0.75	3.05	2.21	50.23
Planulina ariminensis	1.07	0.46	0.67	1.47	1.98	52.21
Spiroplectinella wrightii	0.72	0.34	0.65	1.47	1.91	54.11
Gavelinopsis praegeri	0.71	1.31	0.64	1.43	1.89	56
Cassidulina teretis	1.24	0.81	0.62	1.29	1.82	57.82
Lenticulina gibba	0.68	0.2	0.61	1.44	1.79	59.62
Trifarina angulosa	2.08	1.79	0.61	0.97	1.78	61.39
Cibicides ungerianus	1.87	1.41	0.58	1.84	1.71	63.1
Reophax agglutinans	0.5	0.28	0.52	1.26	1.53	64.63
Spiroplectinella sagitulla	0.57	0.21	0.49	1.42	1.45	66.08
Pullenia subcarinata	0.69	0.73	0.49	1.45	1.45	67.52
Quinqueloculina semiluna	0.72	0.55	0.48	1.21	1.41	68.93

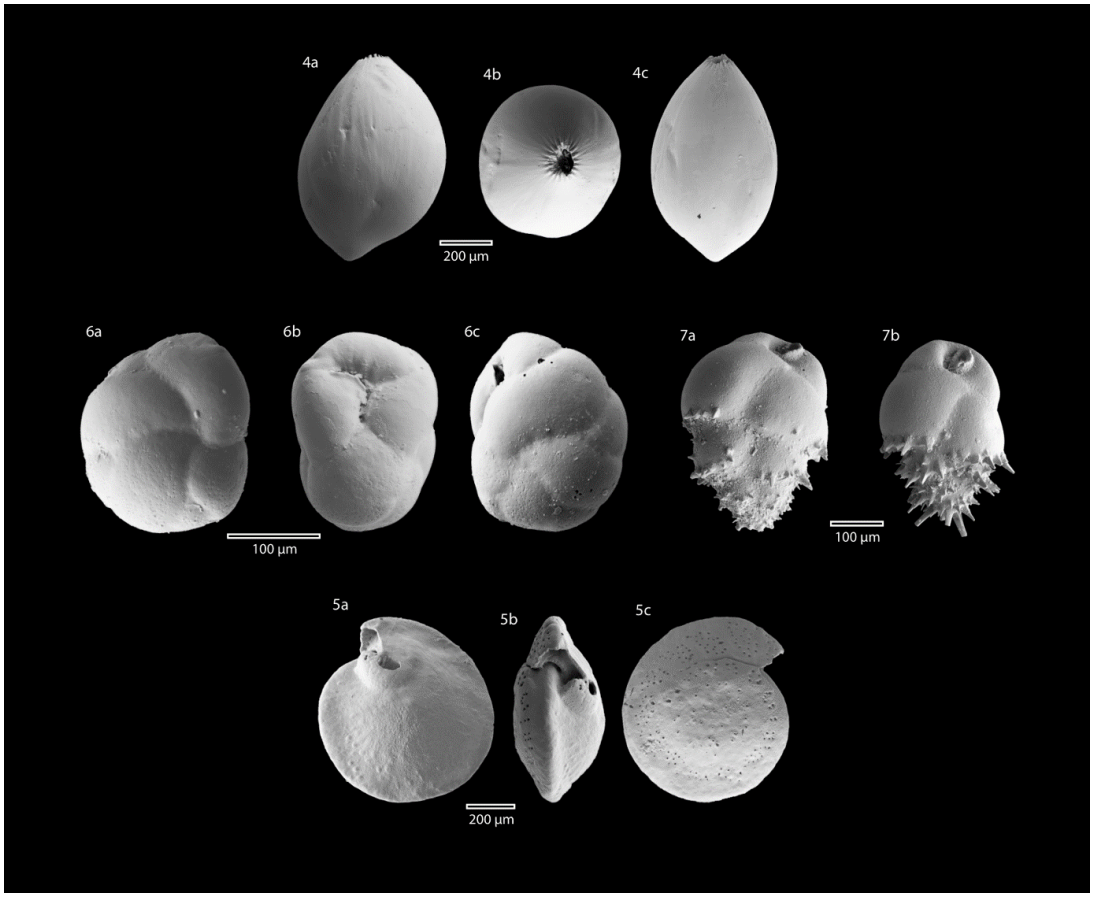
Cyan and red groups						
Average dissimilarity = 38,89						
Biloculinella globula	0.96	1.77	0.89	1.27	2.29	42.17
Hanzawaia boueana	0.99	0.15	0.88	2.37	2.26	44.44
Bolivina dilatata	0.81	0	0.85	3.6	2.19	46.63
Spiroplectinella sagitulla	0.92	0.21	0.75	1.88	1.94	48.57
Bulimina marginata	2.64	3.26	0.69	1.5	1.78	50.35
Hyalinea balthica	0.75	0.2	0.64	1.63	1.66	52.01
Oolina melo	0.61	0	0.63	1.73	1.62	53.63
Cibicides ungerianus	0.82	1.41	0.63	1.51	1.61	55.25
Quinqueloculina viennensis	0.83	1.37	0.62	1.3	1.6	56.84
Cassidulina teretis	1.34	0.81	0.58	1.65	1.5	58.34
Fissurina annectens	0.7	0.2	0.58	1.52	1.49	59.83
Astrononion stelligerum	0.54	0	0.56	1.32	1.44	61.27
Amphycorina scalaris	0.53	0	0.55	1.58	1.42	62.69
Cibicides mundulus	0.42	0.63	0.54	1.32	1.4	64.09
Uvigerina pygmae	1.53	1.02	0.54	1.85	1.39	65.48
Fissurina eburnea	0.62	0.21	0.51	1.52	1.32	66.79

Blue and red groups						
Average dissimilarity = 34,10						
Cibicides mundulus	0.84	0.63	0.47	0.95	1.38	70.31
Textularia agglutinans	0.43	0	0.46	1.35	1.35	71.66
Lenticulina orbicularis	0.2	0.32	0.45	1.29	1.32	72.98
Discanomalina coronata	1.3	1.69	0.42	1.72	1.24	74.22
Hoeglundina elegans	0.66	0.45	0.42	1.23	1.24	75.47
Pyrgo sarsi	0.5	0.17	0.42	1.38	1.22	76.69
Bolivina dilatata	0.36	0	0.4	1.36	1.17	77.85
Hyrrokkin sarcophaga	0.27	0.45	0.39	1.24	1.15	79
Lagena squamosalata	0.09	0.38	0.39	1.26	1.13	80.13
Hyalinea balthica	0.39	0.2	0.37	1.19	1.1	81.23
Eggerella humboldti	0	0.35	0.37	1.34	1.09	82.32
Homalohedra williamsoni	0.28	0.58	0.37	1.29	1.08	83.4
Hanzawaia boueana	0.34	0.15	0.37	1.08	1.08	84.48
Sigmoilopsis schlumbergeri	1.2	1.14	0.33	1.49	0.98	85.46
Bulimina pupoides	0.29	0.37	0.33	1.14	0.97	86.43
Fissurina eburnea	0.28	0.21	0.33	1.04	0.96	87.4

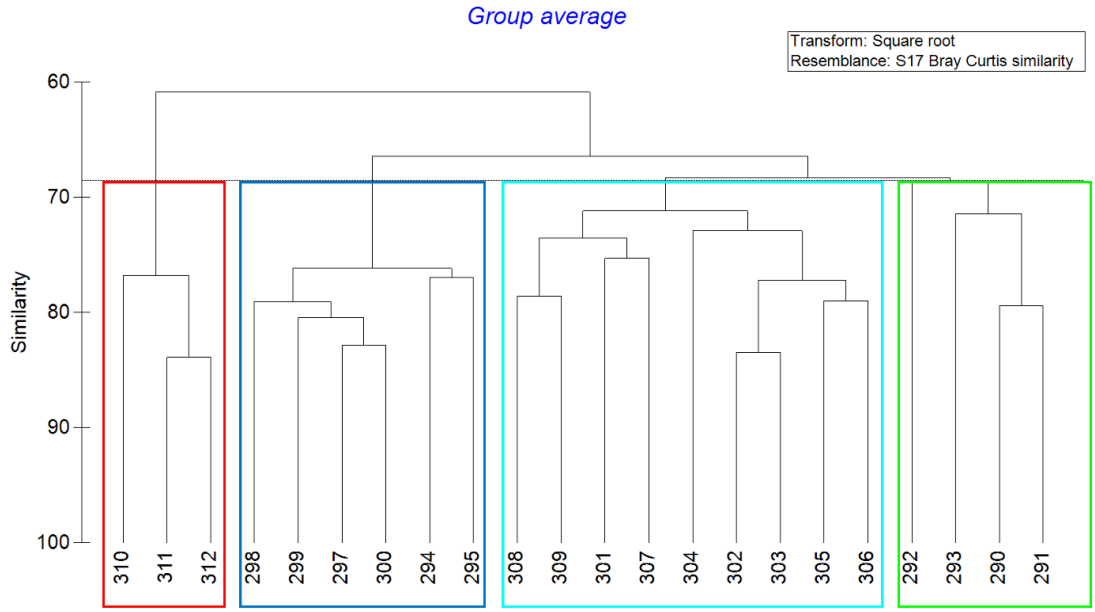
Cyan and red groups						
Average dissimilarity = 38,89						
Quinqueloculina semiluna	0.67	0.55	0.5	1.27	1.29	68.09
Nuttalides umbonifer	0.51	0.2	0.49	1.08	1.25	69.33
Uvigerina mediterranea	3.15	3.47	0.48	1.24	1.25	70.58
Spiroplectinella wrightii	0.35	0.34	0.47	1.24	1.22	71.8
Pullenia subcarinata	0.91	0.73	0.47	1.3	1.2	73
Lenticulina gibba	0.41	0.2	0.45	1.06	1.15	74.16
Homalohedra williamsoni	0.42	0.58	0.42	1.55	1.09	75.25
Planulina ariminensis	0.61	0.46	0.42	1.2	1.07	76.32
Uvigerina auberiana	0.39	0	0.41	1	1.05	77.37
Sigmoilopsis schlumbergeri	0.9	1.14	0.41	1.51	1.05	78.42
Gavelinopsis praegeri	1.55	1.31	0.4	1.56	1.03	79.45
Robertinoides bradyi	0.47	0.2	0.4	1.27	1.03	80.48
Hyrrokkin sarcophaga	0.34	0.45	0.4	1.28	1.02	81.5
Karreriella bradyi	0.69	0.58	0.39	2.05	1.01	82.51
Pyrgo sarsi	0.43	0.17	0.39	1.23	1	83.52
Discanomalina coronata	1.6	1.69	0.39	1.38	0.99	84.51

Blue and red groups						
Average dissimilarity = 34,10						
Bolivina subspinescens	0.28	0	0.3	0.96	0.89	88.28
Gyroidina soldanii	1.81	1.73	0.28	1.08	0.82	89.11
Pullenia bulloides	0	0.26	0.28	0.69	0.81	89.92
Fissurina annectens	0.17	0.2	0.27	0.93	0.8	90.72

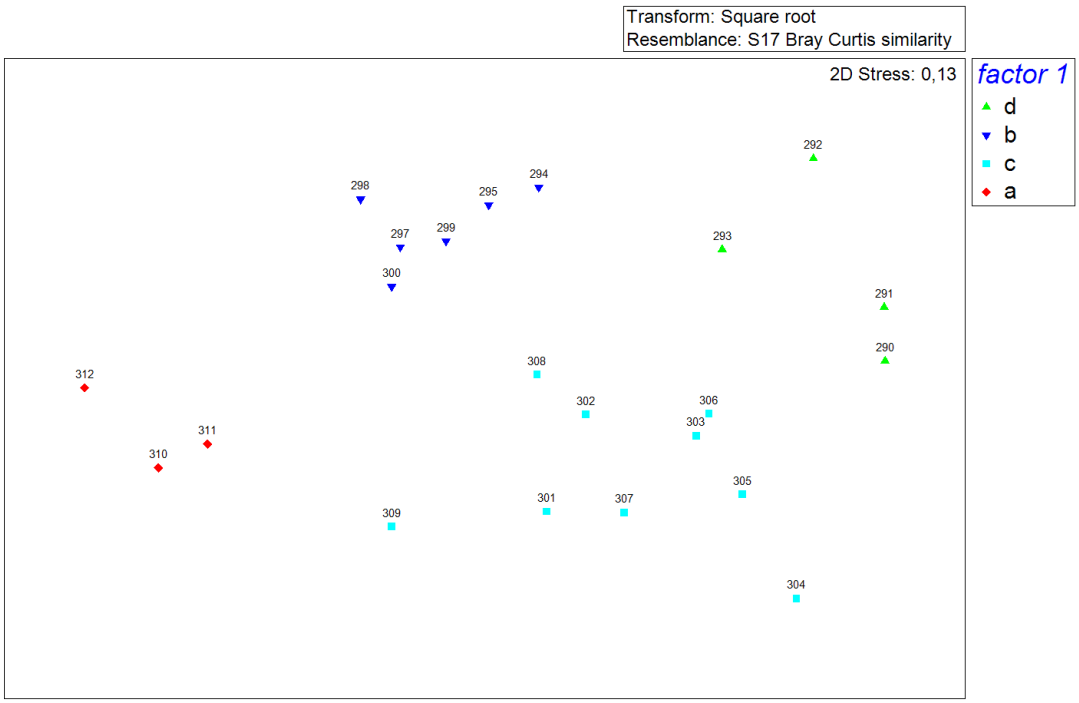
Cyan and red groups						
Average dissimilarity = 38,89						
Hoeglundina elegans	0.55	0.45	0.38	1.21	0.98	85.49
Lagena squamosalata	0.06	0.38	0.38	1.3	0.98	86.46
Lenticulina orbicularis	0.4	0.32	0.38	1.11	0.97	87.43
Eggerella humboldti	0.28	0.35	0.35	1.3	0.9	88.34
Bulimina pupoides	0.26	0.37	0.33	1.21	0.86	89.2
Gyroidina soldanii	1.46	1.73	0.32	1.16	0.83	90.03



Additional SEMs images taken of other benthic foraminifera which were noted as dominant in CE18011_VC5. **4**. *Globulina minuta* (Roemer, 1838) a. side view; b. apertural view, c. peripheral view; **6**. *Cassidulina reniforme* (Norvang, 1945) a. side view 1, b. apertural view, c. side view 2; **7**. *Bulimina marginata* (d'Orbigny, 1826) a. morphotype 1, b. morphotype 2; **5**. *Cibicides mundulus* (Brady, Parker and Jones, 1888) a. spiral side, b. peripheral view, c. umbilical side;



Dendrogram of benthic foraminifera assemblages See table above for sample numbers. Four clusters were defined at 69% similarity



Multivariate analysis performed on the complete and standardized dataset reveals variations in the total number of individuals from one sample to another. Species contributing to the average dissimilarity/similarity and their individual abundances are listed in the tables above.

The hierarchical cluster analysis distinguished 4 clusters (red, blue, cyan and green composed of 4, 6, 9 and 3 samples, respectively) at 68% similarity. Each cluster relates to a specific benthic foraminiferal assemblage (BFA). The red

cluster groups all samples from 0–15 cmbsf and will be hereafter referred to as the "BFA_1 Assemblage". The blue cluster groups samples from 20–50 cmbsf and will be hereafter referred to as the "BFA_2 Assemblage". The cyan cluster groups all samples from 55–95 cmbsf and will be hereafter referred to as the "BFA_3 Assemblage". The green cluster groups all samples from 100–110 cmbsf and will be hereafter referred to as the "BFA_4 Assemblage".

The BFA_1 Assemblage is characterised by *Trifarina angulosa* and *Uvigerina mediterranea*, which contribute 16.8% of the total abundance. *T. angulosa* is the most dominant species (6.1% of the average similarity). Less contributing species are *U. mediterranea* (5.9% of the average similarity), *Globocassidulina subglobosa* (5.7% of the average similarity), *Melonis barleeanum* (5.0% of the average similarity), *Cibicides pachyderma* (4.3% of the average similarity), *Cassidulina teretis* (3.1% of the average similarity) and *Gyroidina soldanii* (2.9% of the average similarity; see tables above).

The BFA_2 Assemblage is characterised by *U. mediterranea* and *C. pachyderma*, which contribute 22.6% of the total abundance. *U. mediterranea* is the most dominant species (13.0% of the average similarity). Less contributing species are *C. pachyderma* (9.7% of the average similarity), *M. barleeanum* (6.3% of the average similarity), *Bulimina marginata* (5.6% of the average similarity), *Cibicides refulgens* (5.2% of the average similarity), *Uvigerina pygmae* (4.5% of the average similarity) and *T. angulosa* (4.4% of the average similarity; see tables above).

The BFA_3 Assemblage is characterised by *T. angulosa* and *U. mediterranea*, which contribute 18.9% of the total abundance. *T. angulosa* is the most dominant species (11.3% of the average similarity). Less contributing species are *U. mediterranea* (7.7% of the average similarity), *C. pachyderma* (6.7% of the average similarity), *B. marginata* (6.2% of the average similarity), *M. barleeanum* (5.0% of the average similarity), *Cassidulina reniforme* (4.7% of the average similarity) and *Globocassidulina subglobosa* (4.4% of the average similarity; see tables above).

The BFA_4 Assemblage is characterised by *C. pachyderma* and *C. refulgens*, which contribute 22.8% of the total abundance. *C.pachyderma* is the most

dominant species (13.1% of the average similarity). Less contributing species are *C. refulgens* (9.7% of the average similarity), *U. mediterranea* (9.4% of the average similarity), *B. marginata* (9.4% of the average similarity), *Textularia. truncata* (7.7% of the average similarity), *Biloculinella globula* (4.8% of the average similarity) and *G. soldanii* (4.6% of the average similarity; see tables above).

Discriminating species (i.e. have the highest $\bar{\delta_i}$/SD ($\bar{\delta_i}$) ratios) between the assemblages are *U. mediterranea* and *G. subglobosa* for BFA_1 and BFA_2, *B. marginata* and *Gavelinopsis praegeri* for BFA_1 and BFA_3, *U. mediterranea* and *T. angulosa* for BFA_2 and BFA_3, *C. refulgens* and *T. truncata* for BFA_1 and BFA_4, *T. truncata* and *G. subglobosa* for BFA_2 and BFA_4 and *Bolivina dilatata* and *T. angulosa* for BFA_3 and BFA_4.

Thesis References

Addamo, A. M., Vertino, A., Stolarski, J., García-Jiménez, R., Taviani, M. & Machordom, A. 2016. Merging Scleractinian Genera: The Overwhelming Genetic Similarity between Solitary Desmophyllum and Colonial Lophelia. BMC Evolutionary Biology, 16. http://dx.doi.org/10.1186/s12862-016-0654-8

Adkins, J. F., Griffin, S., Kashgarian, M., Cheng, H., Druffel, E. R. M., Boyle, E. A., Lawrence Edwards, R. & Shen, C.-C. 2002. Radiocarbon Dating of Deep-Sea Corals. Radiocarbon, 44, 567 - 580. http://dx.doi.org/10.1017/S0033822200031921

Alatalo, R. V. 1981. Problems in the Measurement of Evenness in Ecology. Oikos, 37, 199-204. http://dx.doi.org/10.2307/3544465

Allen, S. E. & De Madron, X. D. 2009. A Review of the Role of Submarine Canyons in Deep-Ocean Exchange with the Shelf. Ocean Science, 5, 607–620. http://dx.doi.org/10.5194/os-5-607-2009

Allen, S. E. & Hickey, B. M. 2010. Dynamics of Advection-Driven Upwelling over a Shelf Break Submarine Canyon. Journal of Geophysical Research, 115. http://dx.doi.org/10.1029/2009JC005731

Allen, S. E., Vindeirinho, C. & Thomsen, R. E. 2001. Physical and Biological Processes over a Submarine Canyon During an Upwelling Event. Canadian Journal of Fisheries and Aquatic Sciences, 58, 671. http://dx.doi.org/10.1139/f01-008

Almogi-Labin, A., Schmiedl, G., Hemleben, C., Siman-Tov, R., Segl, M. & Meischner, D. 2000. The Influence of the North East Winter Monsoon on Productivity Changes in the Gulf of Aden, NW Arabian Sea, During the Last 530 Ka as Recorded by Foraminifera. Marine Micropaleontology, 40, 295-319. http://dx.doi.org/10.1016/S0377-8398(00)00043-8

Altenbach, A. V., Pflaumann, U., Schiebel, R., Thies, A., Timm, S. & Trauth, M. H. 1999. Scaling Percentages and Distributional Patterns of Benthic

Foraminifera with Flux Rates of Organic Carbon. Journal of Foraminiferal Research, 29, 173-185.

Alve, E. 2010. Benthic Foraminiferal Responses to Absence of Fresh Phytodetritus: A Two-Year Experiment. Marine Micropaleontology, 76, 67-75. http://dx.doi.org/10.1016/j.marmicro.2010.05.003

Amaro, T., Huvenne, V. a. I., Allcock, A. L., Aslam, T., Davies, J. S., Danovaro, R., Stigter, H. C. D., Duineveld, G., Gambi, C., Gooday, A. J., Gunton, L. M., Hall, R. A., Howell, K. L., Ingels, J., Kiriakoulakis, K., Kershaw, C. E., Lavaleye, M. S. S., Robert, K., Stewart, H. A., Rooij, D. V., White, M. & Wilson, A. M. 2016. The Whittard Canyon: A Case Study of Submarine Canyon Processes. Progress in Oceanography, 146, 38-57. http://dx.doi.org/10.1016/j.pocean.2016.06.003

Amblas, D., Ceramicola, S., Gerber, T. P. D., Canals, M., Chiocci, F. L., Dowdeswell, J. A., Harris, P. T., Huvenne, V. a. I., Lai, S. Y. J., Lastras, G., Iacono, C. L., Micallef, A., Mountjoy, J. J., Paull, C. K., Puig, P. & Sànchez-Vidal, A. 2018. Submarine Canyons and Gullies. Submarine Geomorphology, 251–272. http://dx.doi.org/10.1007/978-3-319-57852-1_14

Andresen, C. S., McCarthy, D. J., Dylmer, C. V., Seidenkrantz, M.-S., Kuijpers, A. & Lloyd, J. M. 2011. Interaction between Subsurface Ocean Waters and Calving of the Jakobshavn Isbrae During the Late Holocene. Holocene, 21, 211-224. 10.1177/0959683610378877

Andrews, J. 2000. Icebergs and Iceberg Rafted Detritus (Ird) in the North Atlantic: Facts and Assumptions. Oceanography, 13, 100-108.

Appah, J., Lim, A., Harris, K., O'Riordan, R., O'Reilly, L. & Wheeler, A. 2020. Are Non-Reef Habitats as Important to Benthic Diversity and Composition as Coral Reef and Rubble Habitats in Submarine Canyons? Analysis of Controls on Benthic Megafauna Distribution in the Porcupine Bank Canyon, NE Atlantic. Frontiers in Marine Science, 7. http://dx.doi.org/10.3389/fmars.2020.571820

Armishaw, J. E., Holmes, R. L. & Stow, D. a. V. 2000. The Barra Fan: A Bottom-Current Reworked, Glacially-Fed Submarine Fan System. Marine and Petroleum Geology, 17, 219-238. http://dx.doi.org/10.1016/S0264-8172(99)00049-5

Arosio, R., Crocket, K. C., Nowell, G. M., Callard, S. L., Howe, J. A., Benetti, S., Fabel, D., Moreton, S. G. & Clark, C. D. 2017. Weathering Fluxes and Sediment Provenance on the SW Scottish Shelf During the Last Deglaciation. Marine Geology, 402, 81-98.

Arzola, R. G., Wynn, R. B., Lastras, G., Masson, D. G. & Weaver, P. P. E. 2008. Sedimentary Features and Processes in the Nazaré and Setúbal Submarine Canyons, West Iberian Margin. Marine Geology, 250, 64-88. http://dx.doi.org/10.1016/j.margeo.2007.12.006

Aslam, T., Hall, R. A. & Dye, S. R. 2018. Internal Tides in a Dendritic Submarine Canyon. Progress in Oceanography, 169, 20-32. http://dx.doi.org/10.1016/j.pocean.2017.10.005

Austin, W. E. N. & Evans, J. R. 2000. NE Atlantic Benthic Foraminifera: Modern Distribution Patterns and Palaeoecological Significance. Journal of the Geological Society, 157, 679 - 691. http://dx.doi.org/10.1144/jgs.157.3.679

Austin, W. E. N. & Kroon, D. 2001. Deep Sea Ventilation of the Northeastern Atlantic During the Last 15,000 Years. Global and Planetary Change, 30, 13-31. http://dx.doi.org/10.1016/S0921-8181(01)00074-1

Ballantyne, C. & Cofaigh, C. Ó. The Last Irish Ice Sheet: Extent and Chronology. 2017.

Barber, D. C., Dyke, A., Hillaire-Marcel, C., Jennings, A. E., Andrews, J. T., Kerwin, M. W., Bilodeau, G., Mcneely, R., Southon, J., Morehead, M. D. & Gagnon, J.-M. 1999. Forcing of the Cold Event of 8,200 Years Ago by Catastrophic Drainage of Laurentide Lakes. Nature, 400, 344-348. http://dx.doi.org/10.1038/22504

Bartels, M., Titschack, J., Fahl, K., Stein, R. & Hebbeln, D. 2018. Wahlenbergfjord, Eastern Svalbard: A Glacier Surrounded Fjord Reflecting Regional Hydrographic Variability During the Holocene? Boreas, 47, 1003-1021.

Bateman, M. D., Evans, D. J. A., Roberts, D. H., Medialdea, A., Ely, J. C. & Clark, C. D. 2017. The Timing and Consequences of the Blockage of the Humber Gap by the Last Britisš Irish Ice Sheet. Boreas, 47, 41-61.

Benetti, S., Chiverrell, R. C., Ó Cofaigh, C., Burke, M. J., Medialdea, A., Small, D. L., Ballantyne, C. K., Bateman, M. D., Callard, S. L., Wilson, P., Fabel, D., Clark, C. D., Arosio, R., Bradley, S. L., Dunlop, P., Ely, J. C., Gales, J., Livingstone, S. J., Moreton, S. G., Purcell, C., Saher, M., Schiele, K., Van Landeghem, K. J. J. & Weilbach, K. 2021. Exploring Controls of the Early and Stepped Deglaciation on the Western Margin of the British Irish Ice Sheet. Journal of Quaternary Science.

Benson, L., Burdett, J., Lund, S., Kashgarian, M. & Mensing, S. 1997. Nearly Synchronous Climate Change in the Northern Hemisphere During the Last Glacial Termination. Nature, 388, 263-265. http://dx.doi.org/10.1038/40838

Benson, S. R., Croll, D. A., Marinovic, B., Chavez, F. P. & Harvey, J. T. 2002. Changes in the Cetacean Assemblage of a Coastal Upwelling Ecosystem During El Niño 1997–98 and La Niña 1999. Progress in Oceanography, 54, 279-291. http://dx.doi.org/10.1016/S0079-6611(02)00054-X

Bigg, G. R., Clark, C. D., Greenwood, S. L., Haflidason, H., Hughes, A. L. C., Levine, R. C., Nygård, A. & Sejrup, H. P. 2012. Sensitivity of the North Atlantic Circulation to Break-up of the Marine Sectors of the NW European Ice Sheets During the Last Glacial: A Synthesis of Modelling and Palaeoceanography. Global and Planetary Change, 98-99, 153-165. http://dx.doi.org/10.1016/j.gloplacha.2012.09.004

Blaauw, M. & Christen, J. A. 2011. Flexible Paleoclimate Age-Depth Models Using an Autoregressive Gamma Process. Bayesian Analysis, 6, 457-474. http://dx.doi.org/10.1214/11-BA618

Blaauw, M., Christen, J. A. & Aquino, A. Age-Depth Modelling Using Bayesian Statistics [R Package Rbacon Version 2.5.0]. 2020.

Blott, S. J. & Pye, K. 2001. Gradistat: A Grain Size Distribution and Statistics Package for the Analyses of Unconsolidated Sediments. Earth Surface Processes and Landforms, 26, 1237-1248. DOI: 10.1002/esp.261

Boltovskoy, E. & Wright, R. C. 1976. Recent Foraminifera.

Bond, G. C., Broecker, W. S., Johnsen, S. J., Mcmanus, J. F., Labeyrie, L., Jouzel, J. & Bonani, G. G. 1993. Correlations between Climate Records from North Atlantic Sediments and Greenland Ice. Nature, 365, 143-147.

Bond, G. C., Showers, W. J., Cheseby, M., Lotti, R., Almasi, P. F., Demenocal, P. B., Priore, P., Cullen, H. M., Hajdas, I. & Bonani, G. 1997. A Pervasive Millennial-Scale Cycle in North Atlantic Holocene and Glacial Climates. Science, 278, 1257-1266.

Bonneau, L., Colin, C., Pons-Branchu, E., Mienis, F., Tisnérat-Laborde, N., Blamart, D., Elliot, M., Collart, T., Frank, N., Foliot, L. & Douville, E. 2018. Imprint of Holocene Climate Variability on Cold-Water Coral Reef Growth at the SW Rockall Trough Margin, NE Atlantic. Geochemistry Geophysics Geosystems, 19, 2437-2452. http://dx.doi.org/10.1029/2018GC007502

Bosley, K. L., Lavelle, J. W., Brodeur, R. D., Wakefield, W. W., Emmett, R. L., Baker, E. T. & Rehmke, K. M. 2004. Biological and Physical Processes in and around Astoria Submarine Canyon, Oregon, USA. Journal of Marine Systems, 50, 21-37. http://dx.doi.org/10.1016/j.jmarsys.2003.06.006

Boulton, G. 1996. The Origin of Till Sequences by Subglacial Sediment Deformation beneath Mid-Latitude Ice Sheets. Annals of Glaciology, 22, 75-84.

Bowen, D. Q., Rose, J., Mccabe, A. & Sutherland, D. G. 1986. Correlation of Quaternary Glaciations in England, Ireland, Scotland and Wales. Quaternary Science Reviews, 5, 299-340. http://dx.doi.org/10.1016/S0277-3791(86)80024-5

Bradwell, T., Small, D. L., Fabel, D., Smedley, R. K., Clark, C. D., Saher, M. H., Callard, S. L., Chiverrell, R. C., Dove, D., Moreton, S. G., Roberts, D. H., Duller, G. a. T. & Ó Cofaigh, C. 2019. Ice-Stream Demise Dynamically Conditioned by Trough Shape and Bed Strength. Science Advances, 5.

Bradwell, T., Stoker, M. S. & Larter, R. 2007. Geomorphological Signature and Flow Dynamics of the Minch Palaeo-Ice Stream, Northwest Scotland. Journal of Quaternary Science, 22, 609–617. https://doi.org/10.1002/jqs.1080

Brodeur, R. D. 2001. Habitat-Specific Distribution of Pacific Ocean Perch (Sebastes Alutus) in Pribilof Canyon, Bering Sea. Continental Shelf Research, 21, 207-224. http://dx.doi.org/10.1016/S0278-4343(00)00083-2

Brolsma, M. J. 1978. Quantitative Forminiferal Analysis and Environmental Interpretation of the Pliocene and Topmost Miocene on the South Coast of Sicily.

Brooks, A., Bradley, S., Edwards, R., Milne, G., Horton, B. & Shennan, I. 2008. Postglacial Relative Sea Level Observations from Ireland and Their Role in Glacial Rebound Modelling. Journal of Quaternary Science, 23, 821-825.

Buhl-Mortensen, L., Vanreusel, A., Gooday, A. J., Levin, L. A., Priede, I. G., Buhl-Mortensen, P., Gheerardyn, H., King, N. J. & Raes, M. 2010. Biological Structures as a Source of Habitat Heterogeneity and

Biodiversity on the Deep Ocean Margins. Marine Ecology, 31, 21-50. http://dx.doi.org/10.1111/j.1439-0485.2010.00359.x

Buhl-Mortensen, P., Buhœ Mortensen, L. & Purser, A. 2016. Trophic Ecology and Habitat Provision in Cold-Water Coral Ecosystems. In: ROSSI S., B. L., GORI A., OREJAS C. (ed.) Marine Animal Forests. Springer, Cham.

Butzin, M., Köhler, P. & Lohmann, G. 2017. Marine Radiocarbon Reservoir Age Simulations for the Past 50000 Years. Geophysical Research Letters, 44, 8473–8480. doi:10.1002/2017GL074688

Cairns, S. D. 2001. A Brief History of Taxonomic Research on Azooxanthellate Scleractinia (Cnidaria: Anthozoa). Bulletin of the Biological Society of Washington, 10, 191–203.

Callard, S. L., Ó Cofaigh, C., Benetti, S., Chiverrell, R., Landeghem, K. V., Saher, M., Livingstone, S., Clark, C., Small, D., Fabel, D. & Moreton, S. 2020. Oscillating Retreat of the Last British-Irish Ice Sheet on the Continental Shelf Offshore Galway Bay, Western Ireland. Marine Geology, 420, 106087.

Callard, S., Ó Cofaigh, C., Benetti, S., Chiverrell, R., Landeghem, K. V., Saher, M. H., Gales, J., Small, D., Clark, C., Stephen, J. L., Fabel, D. & Moreton, S. G. 2018. Extent and Retreat History of the Barra Fan Ice Stream Offshore Western Scotland and Northern Ireland During the Last Glaciation. Quaternary Science Reviews, 201, 280-302.

Canals, M., Danovaro, R., Heussner, S., Lykousis, V., Puig, P., Trincardi, F., Calafat, A. M., Durrieu De Madron, X., Panlanques, A. & Sanchez-Vidal, A. 2009. Cascades in Mediterranean Submarine Grand Canyons. Oceanography, 22, 26-43. http://dx.doi.org/10.5670/oceanog.2009.03

Canals, M., Puig, P., Durrieu De Madron, X., Heussner, S., Palanques, A. & Fabres, J. 2006. Flushing Submarine Canyons. Nature, 444, 354-357. doi:10.1038/nature05271

Caralp, M. H. 1989. Size and Morphology of the Benthic Foraminifer Melonis Barleeanum; Relationships with Marine Organic Matter. Journal of Foraminiferal Research, 19, 235-245. http://dx.doi.org/10.2113/gsjfr.19.3.235

Carlier, A., Le Guilloux, E., Olu-Le Roy, K., Sarrazin, J., Mastrototaro, F., Taviani, M. & Clavier, J. 2010. Trophic Relationships in a Deep Mediterranean Cold-Water Coral Bank (Santa Maria Di Leuca, Ionian Sea). Marine Ecology Progress Series, 397, 125-137. doi: 10.3354/meps08361

Carlson, A. E., Anslow, F. S., Obbink, E. A., Legrande, A. N., Ullman, D. J. & Licciardi, J. M. 2009. Surface-Melt Driven Laurentide Ice Sheet Retreat During the Early Holocene. Geophysical Research Letters, 36. http://dx.doi.org/10.1029/2009GL040948

Carlson, A. E., Legrande, A. N., Oppo, D. W., Came, R. E., Schmidt, G. A., Anslow, F. S., Licciardi, J. M. & Obbink, E. A. 2008. Rapid Early Holocene Deglaciation of the Laurentide Ice Sheet. Nature Geoscience, 1, 620-624. http://dx.doi.org/10.1038/ngeo285

Carr, J. R., Vieli, A. & Stokes, C. R. 2013. Influence of Sea Ice Decline, Atmospheric Warming, and Glacier Width on Marine-Terminating Outlet Glacier Behavior in Northwest Greenland at Seasonal to Interannual Timescales. Journal of Geophysical Research, 118, 1210-1226.

Cavan, E., Trimmer, M., Shelley, F., Sanders, R., 2017. Remineralization Of Particulate Organic Carbon In An Ocean Oxygen Minimum Zone. Nature Communications, 8, 1, http://dx.doi.org/10.1038/ncomms14847

Cedhagen, T. 1994. Taxonomy and Biology of Hyrrokkin Sarcophaga Gen. Et Sp. N., a Parasitic Foraminiferan (Rosalinidae). Sarsia, 79, 65-82. 10.1080/00364827.1994.10413549

Chapman, M. 2010. Seasonal Production Patterns of Planktonic Foraminifera in the NE Atlantic Ocean: Implications for Paleotemperature and Hydrographic Reconstructions. Paleoceanography, 25. http://dx.doi.org/10.1029/2008PA001708

Chenin, P., Manatschal, G., Lavier, L. L. & Erratt, D. 2015. Assessing the Impact of Orogenic Inheritance on the Architecture, Timing and Magmatic Budget of the North Atlantic Rift System: A Mapping Approach. Journal of the Geological Society, 172, 711 - 720.

Chiverrell, R. C., Smedley, R. K., Small, D. L., Ballantyne, C. K., Burke, M. J., Callard, S. L., Clark, C. D., Duller, G. a. T., Evans, D. J. A., Fabel, D., Landeghem, K. J. J. V., Livingstone, S. J., Ó Cofaigh, C., Thomas, G. S. P., Roberts, D. H., Saher, M. H., Scourse, J. D. & Wilson, P. 2018. Ice Margin Oscillations During Deglaciation of the Northern Irish Sea Basin. Journal of Quaternary Science, 33, 739-762.

Chiverrell, R. C., Thrasher, I. M., Thomas, G. S. P., Lang, A., Scourse, J. D., Van Landeghem, K. J. J., Mccarroll, D., Clark, C. D., Cofaigh, C. Ó., Evans, D. J. A. & Ballantyne, C. K. 2013. Bayesian Modelling the Retreat of the Irish Sea Ice Stream. Journal of Quaternary Science, 28, 200-209. http://dx.doi.org/10.1002/jqs.2616

Clark, C. D., Hughes, A. L. C., Greenwood, S. L., Jordan, C. J. & Sejrup, H. P. 2012. Pattern and Timing of Retreat of the Last British-Irish Ice Sheet. Quaternary Science Reviews, 44, 112-146. http://dx.doi.org/10.1016/j.quascirev.2010.07.019

Clarke, K.R. and Gorley, R.N. (2006) PRIMER v6: User Manual/Tutorial (Plymouth Routines in Multivariate Ecological Research). PRIMER-E, Plymouth

Colin, C., Frank, N., Copard, K. & Douville, E. 2010. Neodymium Isotopic Composition of Deep-Sea Corals from the NE Atlantic: Implications for Past Hydrological Changes During the Holocene. Quaternary Science Reviews, 29, 2509-2517. http://dx.doi.org/10.1016/j.quascirev.2010.05.012

Company, J. B., Puig, P., Sardà, F., Palanques, A., Latasa, M. & Scharek, R. 2008. Climate Influence on Deep Sea Populations. PLoS ONE, 3, e1431. http://dx.doi.org/10.1371/journal.pone.0001431

Copard, K., Colin, C., Douville, E., Freiwald, A., Gudmundsson, G., De Mol, B. & Frank, N. 2010. Nd Isotopes in Deep-Sea Corals in the North-Eastern Atlantic. Quaternary Science Reviews, 29, 2499-2508. 10.1016/j.quascirev.2010.05.025

Copard, K., Colin, C., Henderson, G. M., Scholten, J., Douville, E., Sicre, M. A. & Frank, N. 2012. Late Holocene Intermediate Water Variability in the Northeastern Atlantic as Recorded by Deep-Sea Corals. Earth and Planetary Science Letters, 313-314, 34-44. 10.1016/j.epsl.2011.09.047

Corbera, G., Lo Iacono, C., Gràcia, E., Grinyó, J., Pierdomenico, M., Huvenne, V. a. I., Aguilar, R. & Gili, J. M. 2019. Ecological Characterisation of a Mediterranean Cold-Water Coral Reef: Cabliers Coral Mound Province (Alboran Sea, Western Mediterranean). Progress in Oceanography, 175, 245-262. http://dx.doi.org/10.1016/j.pocean.2019.04.010

Corliss, B. H. & Chen, C. 1988. Morphotype Patterns of Norwegian Sea Deep-Sea Benthic Foraminifera and Ecological Implications. Geology, 16, 716-719. http://dx.doi.org/10.1130/0091-7613(1988)016%3C0716:MPONSD%3E2.3.CO;2

Corliss, B. H. 1979. Quaternary Antarctic Bottom-Water History: Deep-Sea Benthonic Foraminiferal Evidence from the Southeast Indian Ocean – Inferred Bottom-Water Routes and Ecological Implications. Quaternary Research, 12, 271 - 289. https://doi.org/10.1016/0033-5894(79)90062-0

Corliss, B. H. 1985. Microhabitats of Benthic Foraminifera within Deep-Sea Sediments. Nature, 314, 435-438. http://dx.doi.org/10.1038/314435a0

Cowan, E., Hillenbrand, C., Hassler, L. & Ake, M. T. 2008. Coarse-Grained Terrigenous Sediment Deposition on Continental Rise Drifts: A Record of Plio-Pleistocene Glaciation on the Antarctic Peninsula. Palaeogeography, Palaeoclimatology, Palaeoecology, 265, 275-291.

Croll, D. A., Marinovic, B., Benson, S. R., Chavez, F. P., Black, N. A., Ternullo, R. & Tershy, B. R. 2005. From Wind to Whales: Trophic Links in a

Coastal Upwelling System. Marine Ecology Progress Series, 289, 117-130. http://dx.doi.org/10.3354/meps289117

Damiani, D., Giorgetti, G. & Turbanti, I. 2006. Clay Mineral Fluctuations and Surface Textural Analysis of Quartz Grains in Pliocece Quaternary Marine Sediments from Wilkes Land Continental Rise (East-Antarctica): Paleoenvironmental Significance. Marine Geology, 226, 281-295.

Danovaro, R., Company, J. B., Corinaldesi, C., D Onghia, G., Galil, B. S., Danovaro, R., Bianchelli, S., Gambi, C., Mea, M. & Zeppilli, D. 2009. α-, β-, γ-, δ-and ε-Diversity of Deep-Sea Nematodes in Canyons and Open Slopes of Northeast Atlantic and Mediterranean Margins. Marine Ecology Progress Series, 396, 197-209. 10.3354/meps08269

Davies, A. J. & Guinotte, J. M. 2011. Global Habitat Suitability for Framework-Forming Cold-Water Corals. PLoS ONE, 6, e18483. 10.1371/journal.pone.0018483

Davies, A. J., Duineveld, G. C., Lavaleye, M. S., Bergman, M. J., Van Haren, H. & Roberts, J. M. 2009. Downwelling and Deep-Water Bottom Currents as Food Supply Mechanisms to the Cold-Water Coral Lophelia Pertusa (Scleractinia) at the Mingulay Reef Complex. Limnology and Oceanography, 54, 620-629. http://dx.doi.org/10.4319/lo.2009.54.2.0620

Davies, A. J., Wisshak, M., Orr, J. C. & Roberts, J. M. 2008. Predicting Suitable Habitat for the Cold-Water Coral Lophelia Pertusa (Scleractinia). Deep-Sea Research I, 55, 1048-1062. http://dx.doi.org/10.1016/j.dsr.2008.04.010

Davies, J. S., Howell, K. L., Stewart, H. A., Guinan, J. & Golding, N. 2014. Defining Biological Assemblages (Biotopes) of Conservation Interest in the Submarine Canyons of the South West Approaches (Offshore United Kingdom) for Use in Marine Habitat Mapping. Deep Sea Research Part II: Topical Studies in Oceanography, 104, 208-229. https://doi.org/10.1016/j.dsr2.2014.02.001

Davies, J. S., Stewart, H. A., Narayanaswamy, B. E., Jacobs, C. L., Spicer, J. I., Golding, N. & Howell, K. L. 2015. Benthic Assemblages of the Anton Dohrn Seamount (NE Atlantic): Defining Deep-Sea Biotopes to Support Habitat Mapping and Management Efforts with a Focus on Vulnerable Marine Ecosystems. PLoS ONE, 10. http://dx.doi.org/10.1371/journal.pone.0124815

Davies, J., Guillaumont, B., Tempera, F., Vertino, A., Beuck, L., Olafsdottir, S. H., Smith, C. J., Fosså, J., Beld, I. V. D., Savini, A., Rengstorf, A. M., Bayle, C., Bourillet, J., Arnaud-Haond, S. & Grehan, A. 2017. A New Classification Scheme of European Cold-Water Coral Habitats: Implications for Ecosystem-Based Management of the Deep Sea. Deep-sea Research Part Ii-topical Studies in Oceanography, 145, 102-109. http://dx.doi.org/10.1016/j.dsr2.2017.04.014

De Haas, H., Mienis, F., Frank, N., Richter, T. O., Steinacher, R., De Stigter, H. C., Van Der Land, C. & Van Weering, T. C. E. 2009. Morphology and Sedimentology of (Clustered) Cold-Water Coral Mounds at the South Rockall Trough Margins, NE Atlantic Ocean. Facies, 55, 1-26. DOI 10.1007/s10347-008-0157-1

De Leo, F. C., Drazen, J. C., Vetter, E. W., Rowden, A. A. & Smith, C. R. 2012. The Effects of Submarine Canyons and the Oxygen Minimum Zone on Deep-Sea Fish Assemblages Off Hawai'i. Deep Sea Research Part I: Oceanographic Research Papers, 64, 54-70. 10.1016/j.dsr.2012.01.014

De Leo, F. C., Smith, C. R., Rowden, A. A., Bowden, D. A. & Clark, M. R. 2010. Submarine Canyons: Hotspots of Benthic Biomass and Productivity in the Deep Sea. Proceedings of the Royal Society B: Biological Sciences, 277, 2783 - 2792. http://dx.doi.org/10.1098/rspb.2010.0462

De Mol, B., Henriet, J.-P. & Canals, M. 2005. Development of Coral Banks in Porcupine Seabight: Do They Have Mediterranean Ancestors? In: FREIWALD, A. & ROBERTS, J. M. (eds.) Cold-Water Corals and Ecosystems. Berlin, Heidelberg, New York: Springer.

De Mol, B., Huvenne, V. a. I. & Canals, M. 2009. Cold-Water Coral Banks and Submarine Landslides: A Review. International Journal of Earth Sciences, 98, 885-899.

De Mol, B., Kozachenko, M., Wheeler, A. J., Alvares, H., Henriet, J.-P. & Olu-Le Roy, K. 2007. Thérèse Mound: A Case Study of Coral Bank Development in the Belgica Mound Province, Porcupine Seabight. International Journal of Earth Sciences, 96, 103-120. http://dx.doi.org/10.1007/s00531-005-0496-x

De Mol, B., Van Rensbergen, P., Pillen, S., Van Herreweghe, K., Van Rooij, D., Mcdonnell, A., Huvenne, V. a. I., Ivanov, M. K., Swennen, R. & Henriet, J.-P. 2002. Large Deep-Water Coral Banks in the Porcupine Basin, Southwest of Ireland. Marine Geology, 188, 193-231.

De Mol, L., Rooij, D. V., Pirlet, H., Greinert, J., Frank, N., Quemmerais, F. & Henriet, J. P. 2011. Cold-Water Coral Habitats in the Penmarc'h and Guilvinec Canyons (Bay of Biscay): Deep-Water Versus Shallow-Water Settings. Marine Geology, 282, 40-52. http://dx.doi.org/10.1016/j.margeo.2010.04.011

De Stigter, H. C., Boer, W., Mendes, P., Jesus, C. C., Thomsen, L., Bergh, G. D. V. D. & Weering, T. C. E. V. 2007. Recent Sediment Transport and Deposition in the Nazaré Canyon, Portuguese Continental Margin. Marine Geology, 246, 144-164. http://dx.doi.org/10.1016/j.margeo.2007.04.011

De Stigter, H. C., Jorissen, F. J. & Zwaan, G. J. V. D. 1998. Bathymetric Distribution and Microhabitat Partitioning of Live (Rose Bengal Stained) Benthic Foraminifera Along a Shelf to Bathyal Transect in the Southern Adriatic Sea. Journal of Foraminiferal Research, 28, 40-65.

Degelleke, L., Hill, P., Kienast, M. & Piper, D. J. 2013. Sediment Dynamics During Heinrich Event H1 Inferred from Grain Size. Marine Geology, 336, 160-169.

Demopoulos, A. W. J., Mcclain-Counts, J. P., Ross, S. W., Brooke, S. D. & Mienis, F. 2017. Food-Web Dynamics and Isotopic Niches in Deep-Sea

Communities Residing in a Submarine Canyon and on the Adjacent Open Slopes. Marine Ecology Progress Series, 578, 19-33. http://dx.doi.org/10.3354/meps12231

Dickson, R. R. & Mccave, I. N. 1986. Nephloid Layer on the Continental Slope West of Porcupine Bank. Deep Sea Research Part A. Oceanographic Research Papers, 33, 791-818. https://doi.org/10.1016/0198-0149(86)90089-0

Dodds, L. A., Roberts, J. M., Taylor, A. C. & Marubini, F. 2007. Metabolic Tolerance of the Cold-Water Coral Lophelia Pertusa (Scleractinia) to Temperature and Dissolved Oxygen Change. Journal of Experimental Marine Biology and Ecology, 349, 205-214. http://dx.doi.org/10.1016/j.jembe.2007.05.013

Dorschel, B., Hebbeln, D., Foubert, A. T. G., White, M. & Wheeler, A. J. 2007a. Hydrodynamics and Cold-Water Coral Facies Distribution Related to Recent Sedimentary Processes at Galway Mound West of Ireland. Marine Geology, 244, 184-195. doi:10.1016/j.margeo.2007.06.010

Dorschel, B., Hebbeln, D., Rüggeberg, A. & Dullo, W.-C. 2007b. Carbonate Budget of a Cold-Water Coral Carbonate Mound: Propeller Mound, Porcupine Seabight. International Journal of Earth Sciences, 96, 73-83. http://dx.doi.org/10.1007/s00531-005-0493-0

Dorschel, B., Hebbeln, D., Rüggeberg, A., Dullo, W.-C. & Freiwald, A. 2005. Growth and Erosion of a Cold-Water Coral Covered Carbonate Mound in the Northeast Atlantic During the Late Pleistocene and Holocene. Earth and Planetary Science Letters, 233, 33-44. http://dx.doi.org/10.1016/j.epsl.2005.01.035

Dorschel, B., Wheeler, A. J., Huvenne, V. a. I. & De Haas, H. 2009. Cold-Water Coral Mounds in an Erosive Environmental Setting: Tobi Side-Scan Sonar Data and Rov Video Footage from the Northwest Porcupine Bank, NE Atlantic. Marine Geology, 264, 218-229. 10.1016/j.margeo.2009.06.005

Dorschel, B., Wheeler, A. J., Monteys, X. & Verbruggen, K. 2010. Atlas of the Deep-Water Seabed: Ireland, Dordrecht Heidelberg London New York Springer.

Douarin, M., Elliot, M., Noble, S. R., Moreton, S. G., Long, D., Sinclair, D. J., Henry, L. A. & Roberts, J. M. 2016. North Atlantic Ecosystem Sensitivity to Holocene Shifts in Meridional Overturning Circulation. Geophysical Research Letters, 43, 291-298. http://dx.doi.org/10.1002/2015GL065999

Douarin, M., Elliot, M., Noble, S. R., Sinclair, D., Henry, L.-A., Long, D., Moreton, S. G. & Murray Roberts, J. 2013. Growth of North-East Atlantic Cold-Water Coral Reefs and Mounds During the Holocene: A High Resolution U-Series and 14c Chronology. Earth and Planetary Science Letters, 375, 176-187. https://doi.org/10.1016/j.epsl.2013.05.023

Douarin, M., Sinclair, D. J., Elliot, M., Henry, L.-A., Long, D., Mitchison, F. & Roberts, J. M. 2014. Changes in Fossil Assemblage in Sediment Cores from Mingulay Reef Complex (NE Atlantic): Implications for Coral Reef Build-Up. Deep Sea Research Part II: Topical Studies in Oceanography, 99, 286-296. http://dx.doi.org/10.1016/j.dsr2.2013.07.022

Dowdeswell, J. A., Elverhøi, A., Andrews, J. T. & Hebbeln, D. 1999. Asynchronous Deposition of Ice-Rafted Layers in the Nordic Seas and North Atlantic Ocean. Nature, 400. http://dx.doi.org/10.1038/22510

Duineveld, G. C. A., Lavaleye, M. S. S., Bergman, M. J. N., De Stigter, H. C. & Mienis, F. 2007. Trophic Structure of a Cold-Water Coral Mound Community (Rockall Bank, NE Atlantic) in Relation to the near-Bottom Particle Supply and Current Regime. Bulletin of Marine Science, 81, 449-467.

Duineveld, G., Lavaleye, M. & Berghuis, E. 2004. Particle Flux and Food Supply to a Seamount Cold-Water Coral Community (Galicia Bank, NW

Spain). Marine Ecology Progress Series, 277, 13-23. http://dx.doi.org/10.3354/meps277013

Dullo, W.-C., Flögel, S. & Rüggeberg, A. 2008. Cold-Water Coral Growth in Relation to the Hydrography of the Celtic and Nordic European Continental Margin. Marine Ecology Progress Series, 371, 165-176. 10.3354/meps07623

Dunlop, P., Shannon, R., Mccabe, M., Quinn, R. & Doyle, E. 2010. Marine Geophysical Evidence for Ice Sheet Extension and Recession on the Malin Shelf: New Evidence for the Western Limits of the British Irish Ice Sheet. Marine Geology, 276, 86-99. http://dx.doi.org/10.1016/j.margeo.2010.07.010

Duplessy, J., Shackleton, N., Fairbanks, R., Labeyrie, L., Oppo, D., Kallel, N., 1988. Deepwater Source Variations During The Last Climatic Cycle And Their Impact On The Global Deepwater Circulation. Paleoceanoraphy, 3, 343-360.

Eisele, M. H., Frank, N., Wienberg, C., Titschack, J., Mienis, F., Beuck, L., Tisnérat-Laborde, N. & Hebbeln, D. 2014. Sedimentation Patterns on a Cold-Water Coral Mound Off Mauritania. Deep-sea Research Part II: Topical Studies in Oceanography, 99, 307-315. http://dx.doi.org/10.1016/j.dsr2.2013.07.004

Eisele, M., Frank, N., Wienberg, C., Hebbeln, D., López Correa, M., Douville, E. & Freiwald, A. 2011. Productivity Controlled Cold-Water Coral Growth Periods During the Last Glacial Off Mauritania. Marine Geology, 280, 143-149. http://dx.doi.org/10.1016/j.margeo.2010.12.007

Eisele, M., Hebbeln, D. & Wienberg, C. 2008. Growth History of a Cold-Water Coral Covered Carbonate Mound - Galway Mound, Porcupine Seabight, Ne-Atlantic. Marine Geology, 253, 160-169. 10.1016/j.margeo.2008.05.006

Eldrett, J., Harding, I., Wilson, P., Butler, E. & Roberts, A. P. 2007. Continental Ice in Greenland During the Eocene and Oligocene. Nature, 446, 176-179.

Ellett, D. J. & Martin, J. H. A. 1973. The Physical and Chemical Oceanography of the Rockall Channel. Deep Sea Research and Oceanographic Abstracts, 20, 585-625. http://dx.doi.org/10.1016/0011-7471(73)90030-2

Elliot, M., Colin, C., Douarin, M., Pons-Branchu, E., Tisnérat-Laborde, N., Schmidt, F., Michel, E., Dubois-Dauphin, Q., Dapoigny, A., Foliot, L., Miska, S., Thil, F., Long, D. & Douville, E. 2019. Onset and Demise of Coral Reefs, Relationship with Regional Ocean Circulation on the Wyville Thomson Ridge. Marine Geology. http://dx.doi.org/10.1016/j.margeo.2019.105969

Elliott, G. M., Shannon, P. M., Haughton, P. D. W., Praeg, D. & O'Reilly, B. 2006. Mid- to Late Cenozoic Canyon Development on the Eastern Margin of the Rockall Trough, Offshore Ireland. Marine Geology, 229, 113-132.

Evans, D. J. A., Bateman, M. D., Roberts, D. H., Medialdea, A., Hayes, L., Duller, G. a. T., Fabel, D. & Clark, C. D. 2017. Glacial Lake Pickering: Stratigraphy and Chronology of a Proglacial Lake Dammed by the North Sea Lobe of the British Irish Ice Sheet. Journal of Quaternary Science, 32, 295-310.

Evans, D. J. A., Livingstone, S. J., Vieli, A. & Cofaigh, C. Ó. 2009. The Palaeoglaciology of the Central Sector of the British and Irish Ice Sheet: Reconciling Glacial Geomorphology and Preliminary Ice Sheet Modelling. Quaternary Science Reviews, 28, 739-757. http://dx.doi.org/10.1016/j.quascirev.2008.05.011

Evans, D. J. A., Roberts, D. H., Bateman, M. D., Ely, J. C., Medialdea, A., Burke, M. J., Chiverrell, R. C., Clark, C. D. & Fabel, D. 2019. A Chronology for North Sea Lobe Advance and Recession on the Lincolnshire and Norfolk Coasts During MIS 2 and 6. Proceedings of the Geologists' Association.

Evans, D. J. A., Roberts, D. H., Bateman, M. D., Medialdea, A., Ely, J. C., Moreton, S. G., Clark, C. D. & Fabel, D. 2018. Sedimentation During

MIS 3 at the Eastern Margins of the Glacial Lake Humber Basin, England. Journal of Quaternary Science, 33, 8, 871-891, https://doi.org/10.1002/jqs.3066

Eyles, N. & Mccabe, A. 1989. The Late Devensian (<22,000 BP) Irish Sea Basin: The Sedimentary Record of a Collapsed Ice Sheet Margin. Quaternary Science Reviews, 8, 307-351. http://dx.doi.org/10.1016/0277-3791(89)90034-6

Fariduddin, M. & Loubere, P. W. 1997. The Surface Ocean Productivity Response of Deeper Water Benthic Foraminifera in the Atlantic Ocean. Marine Micropaleontology, 32, 289-310. http://dx.doi.org/10.1016/S0377-8398(97)00026-1

Fentimen, R., Feenstra, E. J., Rüggeberg, A., Vennemann, T. W., Hajdas, I., Adatte, T., Van Rooij, D. & Foubert, A. 2020a. Cold-Water Coral Mound Archive Provides Unique Insights into Intermediate Water Mass Dynamics in the Alboran Sea During the Last Deglaciation. Frontiers in Marine Science, 7. http://dx.doi.org/10.3389/fmars.2020.00354

Fentimen, R., Lim, A., Rüggeberg, A., Wheeler, A. J., Van Rooij, D. & Foubert, A. 2020b. Impact of Bottom Water Currents on Benthic Foraminiferal Assemblages in a Cold-Water Coral Environment: The Moira Mounds (NE Atlantic). Marine Micropaleontology, 154, 101799. http://dx.doi.org/10.1016/j.marmicro.2019.101799

Fentimen, R., Rüggeberg, A., Lim, A., Kateb, A. E., Foubert, A., Wheeler, A. J. & Spezzaferri, S. 2018. Benthic Foraminifera in a Deep-Sea High-Energy Environment: The Moira Mounds (Porcupine Seabight, SW of Ireland). Swiss Journal of Geosciences, 111, 561-572. http://dx.doi.org/10.1007/s00015-018-0317-4

Fentimen, R., Schmiedl, G., Rüggeberg, A. & Foubert, A. 2021. Benthic Foraminiferal Faunas Associated with Cold-Water Coral Environments in the North Atlantic Realm. The Depositional Record, 7, 223 - 255. https://doi.org/10.1002/dep2.149

Fernandez-Arcaya, U., Ramírez-Llodra, E., Aguzzi, J., Allcock, A. L., Davies, J. S., Dissanayake, A., Harris, P. T., Howell, K. L., Huvenne, V. a. I., Macmillan-Lawler, M., Martín, J., Menot, L., Nizinski, M. S., Puig, P., Rowden, A. A., Sanchez, F. & Van Den Beld, I. M. J. 2017. Ecological Role of Submarine Canyons and Need for Canyon Conservation: A Review. Frontiers in Marine Science, 4, 1-26. http://dx.doi.org/10.3389/fmars.2017.00005

Findlay, H. S., Hennige, S. J., Wicks, L. C., Navas, J. M., Woodward, E. M. S. & Roberts, J. M. 2014. Fine-Scale Nutrient and Carbonate System Dynamics around Cold-Water Coral Reefs in the Northeast Atlantic. Scientific Reports, 4, 3671. 10.1038/srep03671

Fink, H. G., Wienberg, C., Hebbeln, D., Mcgregor, H. V., Schmiedl, G., Taviani, M. & Freiwald, A. 2012. Oxygen Control on Holocene Cold-Water Coral Development in the Eastern Mediterranean Sea. Deep Sea Research Part I: Oceanographic Research Papers, 62, 89-96. http://dx.doi.org/10.1016/j.dsr.2011.12.013

Flögel, S., Dullo, W. C., Pfannkuche, O., Kiriakoulakis, K. & Rüggeberg, A. 2014. Geochemical and Physical Constraints for the Occurrence of Living Cold-Water Corals. Deep-sea Research Part II: Topical Studies in Oceanography, 99, 19-26. http://dx.doi.org/10.1016/j.dsr2.2013.06.006

Flügel, E. A. 2004. Microfacies of Carbonate Rocks: Analysis, Interpretation and Application, Springer, Berlin, Heidelberg.

Folk, R. L. & Ward, W. 1957. Brazos River Bar [Texas]; a Study in the Significance of Grain Size Parameters. Journal of Sedimentary Research, 27, 3-26.

Font, J., Salat, J. & Tintoré, J. 1988. Permanent Features of the Circulation in the Catalan Sea. Oceanologica Acta, Special issue, 16-20. https://archimer.ifremer.fr/doc/00267/37808/

Fontanier, C., Jorissen, F. J., Chaillou, G., Anschutz, P., Grémare, A. & Griveaud, C. 2005. Live Foraminiferal Faunas from a 2800 M Deep

Lower Canyon Station from the Bay of Biscay: Faunal Response to Focusing of Refractory Organic Matter. Deep Sea Research Part I: Oceanographic Research Papers, 52, 1189-1227. https://doi.org/10.1016/j.dsr.2005.01.006

Fontanier, C., Jorissen, F. J., Lansard, B., Mouret, A., Buscail, R., Schmidt, S., Kerhervé, P., Buron, F. F., Zaragosi, S., Hunault, G., Ernoult, E., Artero, C., Anschutz, P. & Rabouille, C. 2008. Live Foraminifera from the Open Slope between Grand Rhône and Petit Rhône Canyons (Gulf of Lions, NW Mediterranean). Deep Sea Research Part I: Oceanographic Research Papers, 55, 1532-1553. http://dx.doi.org/10.1016/j.dsr.2008.07.003

Fontanier, C., Jorissen, F. J., Licari, L., Alexandre, A., Anschutz, P. & Carbonel, P. 2002. Live Benthic Foraminiferal Faunas from the Bay of Biscay: Faunal Density, Composition, and Microhabitats. Deep Sea Research Part I: Oceanographic Research Papers, 49, 751-785. http://dx.doi.org/10.1016/S0967-0637(01)00078-4

Fosså, J. H., Mortensen, P. B. & Furevik, D. M. 2002. The Deep-Water Coral Lophelia Pertusa in Norwegian Waters: Distribution and Fishery Impacts. Hydrobiologia, 471, 1-12. https://doi.org/10.1023/A:1016504430684

Foubert, A. T. G., Beck, T., Wheeler, A. J., Opderbecke, J., Grehan, A., Klages, M., Thiede, J., Henriet, J.-P. & Polarstern Ark-Xix/3a Shipboard Party 2005. New View of the Belgica Mounds, Porcupine Seabight, NE Atlantic: Preliminary Results from the Polarstern Ark-Xix/3a Rov Cruise. In: FREIWALD, A. & ROBERTS, J. M. (eds.) Deep-Water Corals and Ecosystems, . Berlin Heidelberg: Springer-Verlag.

Foubert, A. T. G., Depreiter, D., Beck, T., Maignien, L., Pannemans, B., Frank, N., Blamart, D. & Henriet, J.-P. 2008. Carbonate Mounds in a Mud Volcano Province Off North-West Morocco: Key to Processes and Controls. Marine Geology, 248, 74-96. http://dx.doi.org/10.1016/j.margeo.2007.10.012

Frank, N., Freiwald, A., López Correa, M., Wienberg, C., Eisele, M., Hebbeln, D., Van Rooij, D., Henriet, J.-P., Colin, C., Van Weering, T. C. E., De Haas, H., Buhl-Mortensen, P., Roberts, J. M., De Mol, B., Douville, E., Blamart, D. & Hatté, C. 2011. Northeastern Atlantic Cold-Water Coral Reefs and Climate. Geology, 39, 743-746. 10.1130/G31825.1

Frank, N., Lutringer, A., Paterne, M., Blamart, D., Henriet, J.-P., Van Rooij, D. & Van Weering, T. C. E. 2005. Deep-Water Corals of the Northeastern Atlantic Margin: Carbonate Mound Evolution and Upper Intermediate Water Ventilation During the Holocene. In: FREIWALD, A. & ROBERTS, J. M. (eds.) Cold-Water Corals and Ecosystems. Berlin, Heidelberg, New York: Springer.

Frank, N., Ricard, E., Lutringer-Paquet, A., Van Der Land, C., Colin, C., Blamart, D., Foubert, A. T. G., Van Rooij, D., Henriet, J.-P., De Haas, H. & Van Weering, T. C. E. 2009. The Holocene Occurrence of Cold Water Corals in the NE Atlantic: Implications for Coral Carbonate Mound Evolution. Marine Geology, 266, 129-142. http://dx.doi.org/10.1016/j.margeo.2009.08.007

Frederiksen, R., Jensen, A. & Westerberg, H. 1992. The Distribution of the Scleractinian Coral Lophelia Pertusa around the Faroe Islands and the Relation to Internal Tidal Mixing. Sarsia, 77, 157-171. https://doi.org/10.1080/00364827.1992.10413502

Freiwald, A. & Schönfeld, J. 1996. Substrate Pitting and Boring Pattern of Hyrrokkin Sarcophaga Cedhagen, 1994 (Foraminifera) in a Modern Deep-Water Coral Reef Mound. Marine Micropaleontology, 28, 199-207. http://dx.doi.org/10.1016/0377-8398(96)00002-3

Freiwald, A. 1998. Modern Nearshore Cold-Temperate Calcareous Sediments in the Troms District, Northern Norway. Journal of Sedimentary Research, 68, 763-776.

Freiwald, A. 2002. Reef-Forming Cold-Water Corals. In: WEFER, G., BILLETT, D. S. M., HEBBELN, D., JØRGENSEN, B. B. & VAN WEERING, T. C. E. (eds.) Ocean Margin Systems. Hanse Conference

on Ocean Margin Systems (2000: Delmenhorst, Germany) ed. Berlin Heidelberg New York: Springer.

Freiwald, A., Fosså, J. H., Grehan, A., Koslow, T. & Roberts, J. M. 2004. Cold-Water Coral Reefs. http://www.unep-wcmc.org/resources/publications/

García, R., Oevelen, D. V., Soetaert, K., Thomsen, L., Stigter, H. C. D. & Epping, E. 2008. Deposition Rates, Mixing Intensity and Organic Content in Two Contrasting Submarine Canyons. Progress in Oceanography, 76, 192-215. http://dx.doi.org/10.1016/j.pocean.2008.01.001

Geikie, J. 1864. The Great Ice Age and Its Relation to the Antiquity of Man.

Genin, A. 2004. Bio-Physical Coupling in the Formation of Zooplankton and Fish Aggregations over Abrupt Topographies. Journal of Marine Systems, 50, 3-20. 10.1016/j.jmarsys.2003.10.008

Genin, A., Dayton, P. K., Lonsdale, P. F. & Spiess, F. N. 1986. Corals on Seamount Peaks Provide Evidence of Current Acceleration over Deep-Sea Topography. Nature, 322, 59-61. http://dx.doi.org/10.1038/322059a0

Georgiopoulou, A., Benetti, S., Shannon, P. M., Haughton, P. D. & McCarron, S. 2012. Gravity Flow Deposits in the Deep Rockall Trough, Northeast Atlantic. Submarine Mass Movements and Their Consequences. Springer.

Gooday, A. J. & Hughes, J. 2002. Foraminifera Associated with Phytodetritus Deposits at a Bathyal Site in the Northern Rockall Trough (NE Atlantic): Seasonal Contrasts and a Comparison of Stained and Dead Assemblages. Marine Micropaleontology, 46, 83-110. http://dx.doi.org/10.1016/S0377-8398(02)00050-6

Gooday, A. J. 1986. Meiofaunal Foraminiferans from the Bathyal Porcupine Seabight (Northeast Atlantic): Size Structure, Standing Stock, Taxonomic Composition, Species Diversity and Vertical Distribution in the Sediment. Deep Sea Research Part A. Oceanographic Research

Papers 33, 1345-1373. http://dx.doi.org/10.1016/0198-0149(86)90040-3

Gooday, A. J. 1993. The Biology of Deep-Sea Foraminifera; a Review of Some Advances and Their Applications in Paleoceanography. PALAIOS, 9, 14-31. http://dx.doi.org/10.2307/3515075

Gooday, A. J. 1994. The Biology of Deep-Sea Foraminifera; a Review of Some Advances and Their Applications in Paleoceanography. PALAIOS, 9, 14-31. http://dx.doi.org/10.2307/3515075

Gooday, A. J. 2019. Deep-Sea Benthic Foraminifera.

Granata, T., Vidondo, B., Duarte, C. M., Satta, M. P. & García, M. A. 1999. Hydrodynamics and Particle Transport Associated with a Submarine Canyon Off Blanes (Spain), NW Mediterranean Sea. Continental Shelf Research, 19, 1249-1263. http://dx.doi.org/10.1016/S0278-4343(98)00118-6

Greenwood, S. & Clark, C. 2009. Reconstructing the Last Irish Ice Sheet 1 : Changing Flow Geometries and Ice Flow Dynamics Deciphered from the Glacial Landform Record. Quaternary Science Reviews, 28, 3085-3100.

Gregoire, L. J., Payne, A. J. & Valdes, P. J. 2012. Deglacial Rapid Sea Level Rises Caused by Ice-Sheet Saddle Collapses. Nature, 487, 219-222. http://dx.doi.org/10.1038/nature11257

Guihen, D., White, M. & Lundälv, T. 2013. Boundary Layer Flow Dynamics at a Cold-Water Coral Reef. Journal of Sea Research, 78, 36-44. http://dx.doi.org/10.1016/j.seares.2012.12.007

Haapaniemi, A. I., Scourse, J., Peck, V. L., Kennedy, H., Kennedy, P., Hemming, S., Furze, M. F., Pifdkowski, A. J., Austin, W., Walden, J. B., Wadsworth, E. & Hall, I. 2010. Source, Timing, Frequency and Flux of Ice Rafted Detritus to the Northeast Atlantic Margin, 3p 12 Ka: Testing the Heinrich Precursor Hypothesis. Boreas, 39, 576-591.

Hald, M. & Vorren, T. O. 1984. Modern and Holocene Foraminifera and Sediments on the Continental Shelf Off Troms, North Norway. Boreas, 13, 133-154. http://dx.doi.org/10.1111/j.1502-3885.1984.tb00067.x

Hall, I. & Mccave, I. N. 1998a. Glacial-Interglacial Variation in Organic Carbon Burial on the Slope of the N.W. European Continental Margin (48° 50°N). Progress in Oceanography, 42, 37-60.

Hall, I. & Mccave, I. N. 1998b. Late Glacial to Recent Accumulation Fluxes of Sediments at the Shelf Edge and Slope of NW Europe, 4x 50°N. Geological Society, London, Special Publications, 129, 339 - 350.

Hall, I. R., Colmenero-Hidalgo, E., Zahn, R., Peck, V. L. & Hemming, S. R. 2011. Centennial- to Millennial-Scale Ice-Ocean Interactions in the Subpolar Northeast Atlantic 18-41 Kyr Ago. Paleoceanography, 26. http://dx.doi.org/10.1029/2010PA002084

Hall, R. A., Alford, M. H., Carter, G. S., Gregg, M. C., Lien, R. C., Wain, D. J. & Zhao, Z. K. 2014. Transition from Partly Standing to Progressive Internal Tides in Monterey Submarine Canyon. Deep-sea Research Part II: Topical Studies in Oceanography, 104, 164-173. http://dx.doi.org/10.1016/j.dsr2.2013.05.039

Hall, R. A., Aslam, T. & Huvenne, V. a. I. 2017. Partly Standing Internal Tides in a Dendritic Submarine Canyon Observed by an Ocean Glider. Deep Sea Research Part I: Oceanographic Research Papers, 126, 73-84. http://dx.doi.org/10.1016/j.dsr.2017.05.015

Hammer, Øyvind, Harper, David A.T., and Paul D. Ryan, 2001. Past: Paleontological Statistics Software Package for Education and Data Analysis. Palaeontologia Electronica, vol. 4, issue 1, art. 4: 9pp., 178kb. http://palaeo-electronica.org/2001_1/past/issue1_01.htm

Hanz, U., Wienberg, C., Hebbeln, D., Duineveld, G., Lavaleye, M. S. S., Juva, K., Dullo, W. C., Freiwald, A., Tamborrino, L., Reichart, G. J., Flögel, S. & Mienis, F. 2019. Environmental Factors Influencing Cold-Water Coral Ecosystems in the Oxygen Minimum Zones on the Angolan and

Namibian Margins. Biogeosciences Discussions, 16, 1-37. https://doi.org/10.5194/bg-16-4337-2019

Harris, P. T. & Whiteway, T. 2011. Global Distribution of Large Submarine Canyons: Geomorphic Differences between Active and Passive Continental Margins. Marine Geology, 285, 69-86. http://dx.doi.org/10.1016/j.margeo.2011.05.008

Hateren, J. a. V., Prins, M. & Balen, R. V. 2017. On the Genetically Meaningful Decomposition of Grain-Size Distributions: A Comparison of Different End-Member Modelling Algorithms. Sedimentary Geology, 375, 49-71.

Hawkes, A. D. & Scott, D. B. 2005. Attached Benthic Foraminifera as Indicators of Past and Present Distribution of the Coral Primnoa Resedaeformis on the Scotian Margin, Springer, Berlin, Heidelberg.

Heaton, T. J., Koehler, P., Butzin, M., Bard, É., Reimer, R., Austin, W., Ramsey, C., Grootes, P., Hughen, K., Kromer, B., Reimer, P. J., Adkins, J., Burke, A., Cook, M., Olsen, J. V. & Skinner, L. 2020. Marine20 the Marine Radiocarbon Age Calibration Curve (0 55,000 Cal Bp). Radiocarbon, 62, 779-820.

Hebbeln, D. & Samankassou, E. 2015. Where Did Ancient Carbonate Mounds Grow — in Bathyal Depths or in Shallow Shelf Waters? Earth-Science Reviews, 145, 56-65. http://dx.doi.org/10.1016/j.earscirev.2015.03.001

Hebbeln, D., Portilho-Ramos, R. D. C., Wienberg, C. & Titschack, J. 2019. The Fate of Cold-Water Corals in a Changing World: A Geological Perspective. Frontiers in Marine Science, 6. http://dx.doi.org/10.3389/fmars.2019.00119

Hebbeln, D., Van Rooij, D. & Wienberg, C. 2016. Good Neighbours Shaped by Vigorous Currents: Cold-Water Coral Mounds and Contourites in the North Atlantic. Marine Geology, 378, 171-185. http://dx.doi.org/10.1016/j.margeo.2016.01.014

Heindel, K., Titschack, J., Dorschel, B., Huvenne, V. a. I. & Freiwald, A. 2010. The Sediment Composition and Predictive Mapping of Facies on the

Propeller Mound—a Cold-Water Coral Mound (Porcupine Seabight, NE Atlantic). Continental Shelf Research, 30, 1814-1829. doi:10.1016/j.csr.2010.08.007

Heinrich, H. 1988. Origin and Consequences of Cyclic Ice Rafting in the Northeast Atlantic Ocean During the Past 130,000 Years. Quaternary Research, 29, 142-152.

Helland, P. E. & Holmes, M. 1997. Surface Textural Analysis of Quartz Sand Grains from Odp Site 918 Off the Southeast Coast of Greenland Suggests Glaciation of Southern Greenland at 11 Ma. Palaeogeography, Palaeoclimatology, Palaeoecology, 135, 109-121.

Henriet, J., De Mol, B., Pillen, S. T., Vanneste, M., Van Rooij, D., Versteeg, W., Croker, P., Shannon, P., Unnithan, V. & Bouriak, S. 1998. Gas Hydrate Crystals May Help Build Reefs. Nature, 391, 648-649. http://dx.doi.org/10.1038/35530

Henriet, J.-P., De Mol, B., Pillen, S., Vanneste, M., Van Rooij, D., Versteeg, W., Croker, P. F., Shannon, P. M., Unnithan, V., Bouriak, S., Chachkine, P. & Belgica 97 Shipboard Scientific Crew 1998. Gas Hydrate Crystals May Help Build Reefs. Nature, 391, 648-649. Doi 10.1038/35530

Henry, L. A., Frank, N., Hebbeln, D., Wienberg, C., Robinson, L. F., Flierdt, T. V. D., Dahl, M., Douarin, M., Morrison, C. L., Correa, M. L., Rogers, A., Ruckelshausen, M. & Roberts, J. M. 2014. Global Ocean Conveyor Lowers Extinction Risk in the Deep Sea. Deep Sea Research Part I: Oceanographic Research Papers, 88, 8-16. http://dx.doi.org/10.1016/j.dsr.2014.03.004

Henry, L.-A. & Roberts, J. M. 2007. Biodiversity and Ecological Composition of Macrobenthos on Cold-Water Coral Mounds and Adjacent Off-Mound Habitat in the Bathyal Porcupine Seabight, NE Atlantic. Deep Sea Research Part I: Oceanographic Research Papers, 54, 654-672. doi:10.1016/j.dsr.2007.01.005

Hibbert, F. D., Austin, W. E. N., Leng, M. J. J. & Gatliff, R. 2010. British Ice Sheet Dynamics Inferred from North Atlantic Ice Rafted Debris Records Spanning the Last 175 000 Years. Journal of Quaternary Science, 25, 461-482. http://dx.doi.org/10.1002/jqs.1331

Hickey, B. M. 1997. The Response of a Steep-Sided, Narrow Canyon to Time-Variable Wind Forcing. Journal of Physical Oceanography, 27, 697–726. http://dx.doi.org/10.1175/1520-0485(1997)027%3C0697:TROASS%3E2.0.CO;2

Hill, M. O. 1973. Diversity and Evenness: A Unifying Notation and Its Consequences. Ecology, 54, 427-432. http://dx.doi.org/10.2307/1934352

Hovland, M., Croker, P. F. & Martin, M. 1994. Fault-Associated Seabed Mounds (Carbonate Knolls?) Off Western Ireland and North-West Australia. Marine and Petroleum Geology, 11, 232-246. http://dx.doi.org/10.1016/0264-8172(94)90099-X

Howe, J. A. 1996. Turbidite and Contourite Sediment Waves in the Northern Rockall Trough, North Atlantic Ocean. Sedimentology, 43, 219-234. http://dx.doi.org/10.1046/j.1365-3091.1996.d01-1.x

Howe, J. A., Stoker, M. S. & Stow, D. a. V. 1994. Late Cenozoic Sediment Drift Complex, Northeast Rockall Trough, North Atlantic. Paleoceanography, 9, 989-999. http://dx.doi.org/10.1029/94PA01440

Hubbard, A., Bradwell, T., Golledge, N. R., Hall, A. M., Patton, H., Sugden, D. E., Cooper, R. & Stoker, M. S. 2009. Dynamic Cycles, Ice Streams and Their Impact on the Extent, Chronology and Deglaciation of the British-Irish Ice Sheet. Quaternary Science Reviews, 28, 758-776. http://dx.doi.org/10.1016/j.quascirev.2008.12.026

Huthnance, J. M. 1995. Circulation, Exchange and Water Masses at the Ocean Margin: The Role of Physical Processes at the Shelf Edge. Progress in Oceanography, 35, 353-431. http://dx.doi.org/10.1016/0079-6611(95)80003-C

Huvenne, V. a. I. & Davies, J. S. 2014. Towards a New and Integrated Approach to Submarine Canyon Research. . Deep-sea Research Part II: Topical Studies in Oceanography, 104, 1-5. http://dx.doi.org/10.1016/j.dsr2.2013.09.012

Huvenne, V. a. I., Beyer, A., De Haas, H., Dekindt, K., Henriet, J.-P., Kozachenko, M., Olu-Le Roy, K., Wheeler, A. J., Participants, T. P. C. & Participants, C. C. 2005. The Seabed Appearance of Different Coral Bank Provinces in the Porcupine Seabight, NE Atlantic: Results from Sidescan Sonar and Rov Seabed Mapping. In: FREIWALD, A. & ROBERTS, J. M. (eds.) Cold-Water Corals and Ecosystems. Berlin Heidelberg: Springer-Verlag.

Huvenne, V. a. I., Blondel, P. & Henriet, J.-P. 2002. Textural Analyses of Sidescan Sonar Imagery from Two Mound Provinces in the Porcupine Seabight. Marine Geology, 189, 323-341. Pii S0025-3227(02)00420-6

Huvenne, V. a. I., De Mol, B. & Henriet, J.-P. 2003. A 3d Seismic Study of the Morphology and Spatial Distribution of Buried Coral Banks in the Porcupine Basin, SW of Ireland. Marine Geology, 198, 5-25. http://dx.doi.org/10.1016/S0025-3227(03)00092-6

Huvenne, V. a. I., Masson, D. G. & Wheeler, A. J. 2009a. Sediment Dynamics of a Sandy Contourite: The Sedimentary Context of the Darwin Cold-Water Coral Mounds, Northern Rockall Trough. International Journal of Earth Sciences, 98, 865-884. 10.1007/s00531-008-0312-5

Huvenne, V. a. I., Shannon, P. M., Naeth, J., Di Primio, R., Henriet, J.-P., Horsfield, B., De Haas, H., Wheeler, A. J. & Olu-Le Roy, K. 2007. The Magellan Mound Province in the Porcupine Basin. International Journal of Earth Sciences, 96, 85-101. http://dx.doi.org/10.1007/s00531-005-0494-z

Huvenne, V. a. I., Van Rooij, D., De Mol, B., Thierens, M., O'Donnell, R. & Foubert, A. T. G. 2009b. Sediment Dynamics and Palaeo-Environmental Context at Key Stages in the Challenger Cold-Water Coral Mound Formation: Clues from Sediment Deposits at the Mound

Base. Deep Sea Research Part I, 56, 2263-2280. 10.1016/j.dsr.2009.08.003

Huvenne, V. A., Tyler, P. A., Masson, D. G., Fisher, E. H., Hauton, C., Huhnerbach, V., Le Bas, T. P. & Wolff, G. A. 2011. A Picture on the Wall: Innovative Mapping Reveals Cold-Water Coral Refuge in Submarine Canyon. PLoS ONE, 6, e28755. 10.1371/journal.pone.0028755

J. Clark, Mccabe, A., Bowen, D. Q. & Clark, P. U. 2012. Response of the Irish Ice Sheet to Abrupt Climate Change During the Last Deglaciation. Quaternary Science Reviews, 35, 100-115. http://dx.doi.org/10.1016/j.quascirev.2012.01.001

Jones, C., Lawton, J. & Shachak, M. 1994. Organisms as Ecosystem Engineers. Oikos, 69, 130-147.

Jonkers, L., Barker, S., Hall, I. & Prins, M. 2015. Correcting for the Influence of Ice Rafted Detritus on Grain Size Based Paleocurrent Speed Estimates. Paleoceanography, 30, 1347-1357.

Jorissen, F. J., Fontanier, C. & Thomas, E. 2007. Paleoceanographical Proxies Based on Deep-Sea Benthic Foraminiferal Assemblage Characteristics. In: HILLAIRE–MARCEL, C., DE VERNAL, A. (ed.) Proxies in Late Cenozoic Paleoceanography. Elsevier.

Kaminski, M. A., Aksu, A. E., Box, M. R., Hiscott, R. N., Filipescu, S. & Al-Salameen, M. 2002. Late Glacial to Holocene Benthic Foraminifera in the Marmara Sea: Implications for Black Sea Mediterranean Sea Connections Following the Last Deglaciation. Marine Geology, 190, 165-202. http://dx.doi.org/10.1016/S0025-3227(02)00347-X

Kano, A., Ferdelman, T. G., Williams, T., Henriet, J.-P., Ishikawa, T., Kawagoe, N., Takashima, C., Kakizaki, Y., Abe, K., Sakai, S., Browning, E. L., Li, X., Andres, M. S., Bjerager, M., Cragg, B. A., De Mol, B., Dorschel, B., Foubert, A. T. G., Frank, T. D., Fuwa, Y., Gaillot, P., Gharib, J. J., Gregg, J. M., Huvenne, V. a. I., Léonide, P., Mangelsdorf, K., Monteys, X., Novosel, I., O'Donnell, R., Rüggeberg,

A., Samarkin, V. A., Sasaki, K., Spivack, A. J., Tanaka, A., Titschack, J., Van Rooij, D. & Wheeler, A. J. 2007. Age Constraints on the Origin and Growth History of a Deep-Water Coral Mound in the Northeast Atlantic Drilled During Integrated Ocean Drilling Program Expedition 307. Geology, 35, 1051-1054. doi: 10.1130/G23917A

Kenyon, N. H., Akhmetzhanov, A. M., Wheeler, A. J., Van Weering, T. C. E., De Haas, H. & Ivanov, M. K. 2003. Giant Carbonate Mounds in the Southern Rockall Trough. Marine Geology, 195, 3-50. 10.1016/S0025-3227(02)00680-1

Klinck, J. M. 1996. Circulation near Submarine Canyons: A Modeling Study. Journal of Geophysical Research, 101, 1211-1223. http://dx.doi.org/10.1029/95JC02901

Knutz, P. C., Austin, W. E. N. & Jones, E. J. W. 2001. Millennial-Scale Depositional Cycles Related to British Ice Sheet Variability and North Atlantic Paleocirculation since 48 Kyr B.P., Barra Fan, U.K. Margin. Paleoceanography, 16, 53-64. https://doi.org/10.1029/1999PA000483

Knutz, P. C., Jones, E. J. W., Austin, W. E. N. & Weering, T. C. E. V. 2002a. Glacimarine Slope Sedimentation, Contourite Drifts and Bottom Current Pathways on the Barra Fan, Uk North Atlantic Margin. Marine Geology, 188, 129-146. http://dx.doi.org/10.1016/S0025-3227(02)00278-5

Knutz, P. C., Jones, E. J. W., Howe, J. E., Van Weering, T. C. E. & Stow, D. a. V. 2002b. Wave-Form Sheeted Contourite Drift on the Barra Fan, NW Uk Continental Margin. Geological Society, London, Memoirs, 22, 85-97. http://dx.doi.org/10.1144/GSL.MEM.2002.022.01.08

Koho, K. A., García, R., Stigter, H. C. D., Epping, E., Koning, E., Kouwenhoven, T. J. & Zwaan, G. J. V. D. 2008. Sedimentary Labile Organic Carbon and Pore Water Redox Control on Species Distribution of Benthic Foraminifera: A Case Study from Lisbož Setúbal Canyon (Southern Portugal). Progress in Oceanography, 79, 55-82. http://dx.doi.org/10.1016/j.pocean.2008.07.004

Kuijpers, A., Knutz, P. & Moros, M. 2013. Ice-Rafted Debris (Ird). In: HARFF, J., MESCHEDE, M., PETERSEN, S. & THIEDE, J. (eds.) Encyclopedia of Marine Geosciences. Dordrecht: Springer Netherlands.

Kuijpers, A., Knutz, P. C. & Moros, M. Ice-Rafted Debris (Ird). 2014.

Kämpf, J. 2018. On the Dynamics of Canyon Flow Interactions. Journal of Marine Science and Engineering, 6, 129. http://dx.doi.org/10.3390/jmse6040129

Langner, M. & Mulitza, S. 2019. Technical Note: Paleodataview@ A software Toolbox for the Collection, Homogenization and Visualization of Marine Proxy Data. Climate of The Past, 15, 2067-2072. http://dx.doi.org/10.5194/cp-15-2067-2019

Larsson, A. I., Lundälv, T. & Oevelen, D. V. 2013. Skeletal Growth, Respiration Rate and Fatty Acid Composition in the Cold-Water Coral Lophelia Pertusa under Varying Food Conditions. Marine Ecology Progress Series, 483, 169-184. http://dx.doi.org/10.3354/meps10284

Legendre, P. & Anderson, M. J. 1999. Distance Based Redundancy Analysis: Testing Multispecies Responces in Multifactorial Ecological Experiments. Ecological Monographs, 69, 1-24. http://dx.doi.org/10.1890/0012-9615(1999)069%5B0001:DBRATM%5D2.0.CO;2

Legendre, P., De Cáceres, M. & Borcard, D. 2010. Community Surveys through Space and Time: Testing the Space-Time Interaction in the Absence of Replication. Ecology, 91, 262-72. http://dx.doi.org/10.1890/09-0199.1

Levin, L. A. & Dayton, P. K. 2009. Ecological Theory and Continental Margins: Where Shallow Meets Deep. Trends in ecology & evolution, 24, 606-17. http://dx.doi.org/10.1016/j.tree.2009.04.012

Levin, L. A., Etter, R. J., Rex, M., Gooday, A. J., Smith, C. R., Pineda, J., Stuart, C. T., Hessler, R. R. & Pawson, D. L. 2001. Environmental Influences on Regional Deep-Sea Species Diversity. Annual Review of

Ecology, Evolution, and Systematics, 32, 51-93. http://dx.doi.org/10.1146/annurev.ecolsys.32.081501.114002

Levin, L. A., Sibuet, M., Gooday, A. J., Smith, C. R. & Vanreusel, A. 2010. The Roles of Habitat Heterogeneity in Generating and Maintaining Biodiversity on Continental Margins: An Introduction. Marine Ecology, 31, 1-5. http://dx.doi.org/10.1111/j.1439-0485.2009.00358.x

Lim, A., Kane, A., Arnaubec, A. & Wheeler, A. J. 2018. Seabed Image Acquisition and Survey Design for Cold Water Coral Mound Characterisation. Marine Geology, 395, 22-32. https://doi.org/10.1016/j.margeo.2017.09.008

Lim, A., O'Reilly., Luke; Summers, G.; Harris, K.; Macedo, L.; O' Hanlon, Z.; Appah, J.; O'Mahony, E.; Strachan, R.; Walsh, P.; Wheeler, A. 2019. CE19014 Cruise Report: Monitoring Changes in Submarine Canyon Coral Habitats - Leg 2 (Mocha_Scan II). https://doi.org/10.5281/zenodo.3819565

Lim, A., O'Reilly, L., Burke, S., Wheeler, A., Appah, J., Summers, G., Harris, K., Shine, A., Boolukos, C., Mcaleer, A., Conti, L., Holland 1 Rov Technical Team & Explorer, 2018. Controls of Cold-Water Coral Habitats in Submarine Canyons, Survey (CoCoHaCa II) of the Porcupine Bank Canyon, Cruise Report. http://marinegeology.ucc.ie/wp-content/uploads/sites/87/2018/08/Cruise-Report-CoCoHaCa-II.pdf

Lim, A., Wheeler, A. J. & Conti, L. A. 2020a. Cold-Water Coral Habitat Mapping: Trends and Developments in Acquisition and Processing Methods. *Geosciences,* **11,** 9. http://dx.doi.org/10.3390/geosciences11010009

Lim, A., Wheeler, A., Price, D., O'Reilly, L., Harris, K. & Conti, L. 2020b. Influence of Benthic Currents on Cold-Water Coral Habitats: A Combined Benthic Monitoring and 3d Photogrammetric Investigation. Scientific Reports, 10, 19433. http://dx.doi.org/10.1038/s41598-020-76446-y

Lindberg, B. & Mienert, J. 2005. Postglacial Carbonate Production by Cold-Water Corals on the Norwegian Shelf and Their Role in the Global Carbonate Budget. Geology, 33, 537-540. 10.1130/G21577.1

Lindberg, B., Berndt, C. & Mienert, J. 2007. The Fugløy Reef at 70°N; Acoustic Signature, Geologic, Geomorphologic and Oceanographic Setting. International Journal of Earth Sciences, 96, 201-213. http://dx.doi.org/10.1007/s00531-005-0495-y

Linke, P. & Lutze, G. F. 1993. Microhabitat Preferences of Benthic Foraminifera—a Static Concept or a Dynamic Adaptation to Optimize Food Acquisition? Marine Micropaleontology, 20, 215-234. http://dx.doi.org/10.1016/0377-8398(93)90034-U

Lipps, J. H. & Valentine, J. W. 1970. The Role of Foraminifera in the Trophic Structure of Marine Communites. Lethaia, 3, 279-286. https://doi.org/10.1111/j.1502-3931.1970.tb01271.x

Lisiecki, L. & Stern, J. V. 2016. Regional and Global Benthic Δ18o Stacks for the Last Glacial Cycle. Paleoceanography, 31, 1368-1394. https://doi.org/10.1002/2016PA003002

Liu, X., Rendle-Buehring, R. & Henrich, R. 2016. Climate and Sea-Level Controls on Turbidity Current Activity on the Tanzanian Upper Slope During the Last Deglaciation and the Holocene. Quaternary Science Reviews, 133, 15-27. http://dx.doi.org/10.1016/j.quascirev.2015.12.002

Lloyd, J. M., Moros, M., Perner, K., Telford, R. J., Kuijpers, A., Jansen, E. & McCarthy, D. J. 2011. A 100 Yr Record of Ocean Temperature Control on the Stability of Jakobshavn Isbrae, West Greenland. Geology, 39, 867-870.

Lockhart, E., Scourse, J. D., Praeg, D., Landeghem, K. J. J. V., Mellett, C. L., Saher, M. H., Callard, L., Chiverrell, R. C., Benetti, S., Ó Cofaigh, C. & Clark, C. D. 2018. A Stratigraphic Investigation of the Celtic Sea Megaridges Based on Seismic and Core Data from the Irish-Uk Sectors. Quaternary Science Reviews, 198, 156-170.

Loubere, P. W. 1991. Deep Sea Benthic Foraminiferal Assemblage Response to a Surface Ocean Productivity Gradient: A Test. Paleoceanography, 6, 193-204. http://dx.doi.org/10.1029/90PA02612

Loubere, P. W. 1998. The Impact of Seasonality on the Benthos as Reflected in the Assemblages of Deep-Sea Foraminifera. Deep Sea Research Part I: Oceanographic Research Papers, 45, 409-432. http://dx.doi.org/10.1016/S0967-0637(97)00092-7

Lowe, D. R. 1982. Sediment Gravity Flows: II Depositional Models with Special Reference to the Deposits of High-Density Turbidity Currents. Journal of Sedimentary Research, 52, 279-297. https://doi.org/10.1306/212F7F31-2B24-11D7-8648000102C1865D

Lutze, G. F. & Coulbourn, W. T. 1984. Recent Benthic Foraminifera from the Continental Margin of Northwest Africa: Community Structure and Distribution. Marine Micropaleontology, 8, 361-401. http://dx.doi.org/10.1016/0377-8398(84)90002-1

Lutze, G. F. & Thiel, H. 1989. Epibenthic Foraminifera from Elevated Microhabitats; Cibicidoides Wuellerstorfi and Planulina Ariminensis. Journal of Foraminiferal Research, 19, 153-158. http://dx.doi.org/10.2113/gsjfr.19.2.153

López Correa, M., Montagna, P., Joseph, N., Rüggeberg, A., Fietzke, J., Flögel, S., Dorschel, B., Goldstein, S. L., Wheeler, A. J. & Freiwald, A. 2012. Preboreal Onset of Cold-Water Coral Growth Beyond the Arctic Circle Revealed by Coupled Radiocarbon and U-Series Dating and Neodymium Isotopes. Quaternary Science Reviews, 34, 24-43. doi:10.1016/j.quascirev.2011.12.005

Mackensen, A., Schmiedl, G., Harloff, J. & Giese, M. 1995. Deep-Sea Foraminifera in the South Atlantic Ocean; Ecology and Assemblage Generation. Micropaleontology, 41, 342-358. http://dx.doi.org/10.2307/1485808

Mackensen, A., Sejrup, H. P. & Jansen, E. 1985. The Distribution of Living Benthic Foraminifera on the Continental Slope and Rise Off Southwest

Norway. Marine Micropaleontology, 9, 275-306. http://dx.doi.org/10.1016/0377-8398(85)90001-5

Mahaney, W. & Kalm, V. 2000. Comparative Scanning Electron Microscopy Study of Oriented Till Blocks, Glacial Grains and Devonian Sands in Estonia and Latvia. Boreas, 29, 35-51.

Mahaney, W. Atlas of Sand Grain Surface Textures and Applications. 2002.

Maier, C., Watremez, P., Taviani, M., Weinbauer, M. G. & Gattuso, J. P. 2011. Calcification Rates and the Effect of Ocean Acidification on Mediterranean Cold-Water Corals. Proceedings of the Royal Society B: Biological Sciences, 279, 1716 - 1723. http://dx.doi.org/10.1098/rspb.2011.1763

Manighetti, B. & Mccave, I. N. 1995a. Depositional Fluxes, Palaeoproductivity, and Ice Rafting in the NE Atlantic over the Past 30 Ka. Paleoceanography, 10, 579-592.

Margreth, S. 2010. Benthic Foraminifera Associated to Cold-Water Coral Ecosystems. PhD, University of Fribourg, Switzerland.

Margreth, S., Gennari, G., Rüggeberg, A., Comas, M., Pinheiro, L. C. & Spezzaferri, S. 2011. Growth and Demise of Cold-Water Coral Ecosystems on Mud Volcanoes in the West Alboran Sea: The Messages from the Planktonic and Benthic Foraminifera. Marine Geology, 282, 26-39. http://dx.doi.org/10.1016/j.margeo.2011.02.006

Margreth, S., Rüggeberg, A. & Spezzaferri, S. 2009. Benthic Foraminifera as Bioindicator for Cold-Water Coral Reef Ecosystems Along the Irish Margin. Deep Sea Research Part I: Oceanographic Research Papers, 56, 2216-2234. http://dx.doi.org/10.1016/j.dsr.2009.07.009

Masson, D. G., Bett, B. J., Billett, D. S. M., Jacobs, C. L., Wheeler, A. J. & Wynn, R. B. 2003. The Origin of Deep-Water, Coral-Topped Mounds in the Northern Rockall Trough, Northeast Atlantic. Marine Geology, 194, 159-180.

Matero, I. S. O., Gregoire, L. J., Ivanovic, R. F., Tindall, J. C. & Haywood, A. M. 2017. The 8.2 Ka Cooling Event Caused by Laurentide Ice Saddle Collapse. Earth and Planetary Science Letters, 473, 205-214. http://dx.doi.org/10.1016/j.epsl.2017.06.011

Mazzini, A., Akhmetzhanov, A., Monteys, X. & Ivanov, M. 2011. The Porcupine Bank Canyon Coral Mounds: Oceanographic and Topographic Steering of Deep-Water Carbonate Mound Development and Associated Phosphatic Deposition. Geo-Marine Letters, 32, 205-225. http://dx.doi.org/10.1007/s00367-011-0257-8

McArdle, B. & Anderson, M. J. 2001. Fitting Multivariate Models to Community Data: A Comment on Distance Based Redundancy Analysis. Ecology, 82, 290-297. http://dx.doi.org/10.1890/0012-9658(2001)082%5B0290:FMMTCD%5D2.0.CO;2

McCabe, A. & Clark, P. 1998. Ice-Sheet Variability around the North Atlantic Ocean During the Last Deglaciation. Nature, 392, 373-377.

McCave, I. N. & Andrews, J. 2019a. Distinguishing Current Effects in Sediments Delivered to the Ocean by Ice. I. Principles, Methods and Examples. Quaternary Science Reviews, 212, 92-107.

McCave, I. N. & Andrews, J. 2019b. Distinguishing Current Effects in Sediments Delivered to the Ocean by Ice. II. Glacial to Holocene Changes in High Latitude North Atlantic Upper Ocean Flows. Quaternary Science Reviews, 223, 105902.

McCave, I. N., Manighetti, B. & Beveridge, N. a. S. 1995a. Circulation in the Glacial North Atlantic Inferred from Grain-Size Measurements. Nature, 374, 149-152.

McCave, I. N., Manighetti, B. & Robinson, S. G. 1995b. Sortable Silt and Fine Sediments Size/Composition Slicing: Parameters for Paleocurrent Speed and Palaeoceanography. Paleoceanography, 10, 593-610. http://dx.doi.org/10.1029/94PA03039

McCulloch, M. T., Trotter, J. A., Montagna, P., Falter, J. L., Dunbar, R. B., Freiwald, A., Försterra, G., Correa, M. L., Maier, C., Rüggeberg, A. & Taviani, M. 2012. Resilience of Cold-Water Scleractinian Corals to Ocean Acidification: Boron Isotopic Systematics of Ph and Saturation State up-Regulation. Geochimica et Cosmochimica Acta, 87, 21-34. http://dx.doi.org/10.1016/j.gca.2012.03.027

McCulloch, M., Taviani, M., Montagna, P., López Correa, M., Remia, A. & Mortimer, G. 2010. Proliferation and Demise of Deep-Sea Corals in the Mediterranean During the Younger Dryas. Earth and Planetary Science Letters, 298, 143-152. doi:10.1016/j.epsl.2010.07.036

Miao, Q. & Thunell, R. C. 1993. Recent Deep-Sea Benthic Foraminiferal Distributions in the South China and Sulu Seas. Marine Micropaleontology, 22, 1-32. http://dx.doi.org/10.1016/0377-8398(93)90002-F

Mienis, F., De Stigter, H. C., De Haas, H. & Van Weering, T. C. E. 2009a. Near-Bed Particle Deposition and Resuspension in a Cold-Water Coral Mound Area at the Southwest Rockall Trough Margin, NE Atlantic. Deep Sea Research Part I, 56, 1026-1038. http://dx.doi.org/10.1016/j.dsr.2009.01.006

Mienis, F., De Stigter, H. C., De Haas, H., Van Der Land, C. & Van Weering, T. C. E. 2012. Hydrodynamic Conditions in a Cold-Water Coral Mound Area on the Renard Ridge, Southern Gulf of Cadiz. Journal of Marine Systems, 96-97, 61-71. https://doi.org/10.1016/j.jmarsys.2012.02.002

Mienis, F., De Stigter, H. C., White, M., Duineveld, G., De Haas, H. & Van Weering, T. C. E. 2007. Hydrodynamic Controls on Cold-Water Coral Growth and Carbonate-Mound Development at the SW and Se Rockall Trough Margin, NE Atlantic Ocean. Deep Sea Research Part I: Oceanographic Research Papers, 54, 1655-1674. http://dx.doi.org/10.1016/j.dsr.2007.05.013

Mienis, F., Duineveld, G., Davies, A. J., Lavaleye, M. S. S., Ross, S. W., Seim, H., Bane, J. M., Haren, H. V., Bergman, M. J. N., Haas, H. D., Brooke,

S. D. & Weering, T. C. E. V. 2013. Cold-Water Coral Growth under Extreme Environmental Conditions, the Cape Lookout Area, NW Atlantic. Biogeosciences, 11, 2543-2560. http://dx.doi.org/10.5194/bg-11-2543-2014

Mienis, F., Van Der Land, C., De Stigter, H. C., Van De Vorstenbosch, M., De Haas, H., Richter, T. O. & Van Weering, T. C. E. 2009b. Sediment Accumulation on a Cold-Water Carbonate Mound at the Southwest Rockall Trough Margin. Marine Geology, 265, 40-50. http://dx.doi.org/10.1016/j.margeo.2009.06.014

Mienis, F., Van Weering, T. C. E., De Haas, H., De Stigter, H. C., Huvenne, V. a. I. & Wheeler, A. J. 2006. Carbonate Mound Development at the SW Rockall Trough Margin Based on High Resolution Tobi and Seismic Recording. Marine Geology, 233, 1-19. http://dx.doi.org/10.1016/j.margeo.2006.08.003

Mohn, C., Rengstorf, A., White, M., Duineveld, G., Mienis, F., Soetaert, K. & Grehan, A. 2014. Linking Benthic Hydrodynamics and Cold-Water Coral Occurrences: A High-Resolution Model Study at Three Cold-Water Coral Provinces in the NE Atlantic. Progress in Oceanography, 122, 92-104. https://doi.org/10.1016/j.pocean.2013.12.003

Mojtahid, M., Schweizer, M., Douarin, M., Gabriel, J., Colin, C., Tisnérat-Laborde, N. & Elliot, M. 2021. From Glacial Times to Late Holocene: Benthic Foraminiferal Assemblages from Cold Water Coral Habitats Off Northwest Scotland. Marine Geology, 440, 106581. http://dx.doi.org/10.1016/j.margeo.2021.106581

Morigi, C., Sabbatini, A., Vitale, G., Pancotti, I., Gooday, A. J., Duineveld, G., Stigter, H. C. D., Danovaro, R. & Negri, A. 2012. Foraminiferal Biodiversity Associated with Cold-Water Coral Carbonate Mounds and Open Slope of Se Rockall Bank (Irish Continental Margin NE Atlantic). Deep Sea Research Part I: Oceanographic Research Papers, 59, 54-71. http://dx.doi.org/10.1016/j.dsr.2011.10.004

Morrill, C., Anderson, D. M., Bauer, B. A., Buckner, R., Gille, E. P., Gross, W. S., Hartman, M. & Shah, A. 2013. Proxy Benchmarks for Intercomparison of 8.2 Ka Simulations. Climate of The Past, 9, 423-432. http://dx.doi.org/10.5194/cp-9-423-2013

Morris, K. J., Tyler, P. A., Masson, D. G., Huvenne, V. a. I. & Rogers, A. 2013. Distribution of Cold-Water Corals in the Whittard Canyon, NE Atlantic Ocean. Deep-sea Research Part II: Topical Studies in Oceanography, 92, 136-144. http://dx.doi.org/10.1016/j.dsr2.2013.03.036

Mortensen, P. B., Hovland, M. T., Fosså, J. H. & Furevik, D. M. 2001. Distribution, Abundance and Size of Lophelia Pertusa Coral Reefs in Mid-Norway in Relation to Seabed Characteristics. Journal of the Marine Biological Association of the UK, Volume 81, Issue 04, Aug 2001, 581-597. http://dx.doi.org/10.1017/S002531540100426X

Mortensen, P. B., Hovland, M., Brattegard, T. & Farestveit, R. 1995. Deep Water Bioherms of Coral Lophelia Pertusa (L.) at 64 Degrees on the Norwegian Shelf: Structure and Associated Megafauna. Sarsia, 80, 145-158.

Mueller, C., Larsson, A. I., Veuger, B., Middelburg, J. & Van Oevelen, D. 2014. Opportunistic Feeding on Various Organic Food Sources by the Cold-Water Coral Lophelia Pertusa. Biogeosciences, 11, 123-133. https://doi.org/10.5194/bg-11-123-2014

Mullenbach, B. L., Nittrouer, C. A., Puig, P. & Orange, D. L. 2004. Sediment Deposition in a Modern Submarine Canyon: Eel Canyon, Northern California. Marine Geology, 211, 101-119. http://dx.doi.org/10.1016/j.margeo.2004.07.003

Mullins, H. T., Newton, C. R., Heath, K. & Van Buren, H. M. 1981. Modern Deep-Water Coral Mounds North of Little Bahama Bank; Criteria for Recognition of Deep-Water Coral Bioherms in the Rock Record. Journal of Sedimentary Research, 51, 999-1013. 10.1306/212f7dfb-2b24-11d7-8648000102c1865d

Murray, J. W. 2006. Ecology and Applications of Benthic Foraminifera, Cambridge University Press.

Naylor, D. & Shannon, P. Geology of Offshore Ireland and West Britain. 1975.

Nittrouer, C. A. & Wright, L. D. 1994. Transport of Particles across Continental Shelves. Reviews of Geophysics, 32, 85-113. http://dx.doi.org/10.1029/93RG02603

Noë, S., Titschack, J., Freiwald, A. & Dullo, W.-C. 2006. From Sediment to Rock: Diagenetic Processes of Hardground Formation in Deep-Water Carbonate Mounds of the NE Atlantic. Facies, 52, 183-208. https://doi.org/10.1007/s10347-005-0037-x

Oksanen, J., Guillaume Blanchet, F.G., Friendly, M., Kindt, R., Legendre, P., Mcglinn, D., Minchin, P.R., O'hara, R.B., Simpson, G.L., Solymos, P., Stevens, H.H., Szoecs E. And Wagner, H 2020. package version 2.5-7 https://CRAN.R-project.org/package=vegan

Oliveira, A., Santos, A., Rodrigues, A. & Vitorino, J. 2007. Sedimentary Particle Distribution and Dynamics on the Nazaré Canyon System and Adjacent Shelf (Portugal). Marine Geology, 246, 105-122. http://dx.doi.org/10.1016/j.margeo.2007.04.017

Orejas, C., Gori, A. & Gili, J. M. 2009. Growth Rates of Live Lophelia Pertusa and Madrepora Oculata from the Mediterranean Sea Maintained in Aquaria. Coral Reefs, 27, 255-255. 10.1007/s00338-007-0350-7

Orejas, C., Gori, A., Rad-Menendez, C., Last, K. S., Davies, A. J., Beveridge, C. M., Sadd, D., Kiriakoulakis, K., Witte, U. & Roberts, J. M. 2016. The Effect of Flow Speed and Food Size on the Capture Efficiency and Feeding Behaviour of the Cold-Water Coral Lophelia Pertusa. Journal of Experimental Marine Biology and Ecology, 481, 34-40. 10.1016/j.jembe.2016.04.002

Orr, J. C., Fabry, V. J., Aumont, O., Bopp, L., Doney, S. C., Feely, R. A., Gnanadesikan, A., Gruber, N., Ishida, A., Joos, F., Key, R. M., Lindsay, K., Maier-Reimer, E., Matear, R. J., Monfray, P., Mouchet, A., Najjar,

R. G., Plattner, G.-K., Rodgers, K. B., Sabine, C. L., Sarmiento, J. L., Schlitzer, R., Slater, R., Totterdell, I. J., Weirig, M.-F., Yamanaka, Y. & Yool, A. 2005. Anthropogenic Ocean Acidification over the Twenty-First Century and Its Impact on Calcifying Organisms. Nature, 437, 681-686. http://dx.doi.org/10.1038/nature04095

Ottesen, D., Dowdeswell, J. A. & Rise, L. 2005. Submarine Landforms and the Reconstruction of Fast-Flowing Ice Streams within a Large Quaternary Ice Sheet: The 2500-Km-Long Norwegian-Svalbard Margin (57°–80°N). GSA Bulletin, 117, B25577. doi: 10.1130/B25577.1

Owen, N. 2010. A Multi-Proxy Palaeoceanographic Investigation of Slope Deposits on Porcupine Bank, NE Atlantic Ocean. Doctor of Philosophy (Ph.D.), Trinity College (Dublin, Ireland). Department of Geology.

Ó Cofaigh, C. & Evans, D. J. A. 2001. Deforming Bed Conditions Associated with a Major Ice Stream of the Last British Ice Sheet. Geology, 29, 795-798. https://doi.org/10.1130/0091-7613(2001)029%3C0795:DBCAWA%3E2.0.CO;2

Ó Cofaigh, C. 2007. Glacimarine Sediments and Ice-Rafted Debris. In: ELIAS, S. A. (ed.) Encyclopedia of Quaternary Science. Elsevier, Amsterdam.

Ó Cofaigh, C., Callard, S. L., Roberts, D. H., Chiverrell, R. C., Ballantyne, C. K., Evans, D. J. A., Saher, M., Van Landeghem, K. J. J., Smedley, R. K., Benetti, S., Burke, M. J., Clark, C. D., Duller, G. a. T., Fabel, D., Livingstone, S. J., McCarron, S., Medialdea, A., Moreton, S. G. & Sacchetti, F. 2021. Timing and Pace of Ice Sheet Withdrawal across the Marine Terrestrial Transition West of Ireland During the Last Glaciation. Journal of Quaternary Science. http://dx.doi.org/10.1002/jqs.3295

Ó Cofaigh, C., Dunlop, P. & Benetti, S. 2010. Marine Geophysical Evidence for Late Pleistocene Ice Sheet Extent and Recession Off Northwest Ireland. Quaternary Science Reviews, 44, 147-159. doi:10.1016/j.quascirev.2010.02.005

Ó Cofaigh, C., Dunlop, P. & Benetti, S. 2012. Marine Geophysical Evidence for Late Pleistocene Ice Sheet Extent and Recession Off Northwest Ireland. Quaternary Science Reviews, 44, 147-159. http://dx.doi.org/10.1016/j.quascirev.2010.02.005

Ó Cofaigh, C., Weilbach, K., Lloyd, J., Benetti, S., Callard, S., Purcell, C., Chiverrell, R., Dunlop, P., Saher, M. H., Livingstone, S., Landeghem, K. V., Moreton, S. G., Clark, C. & Fabel, D. 2019. Early Deglaciation of the British-Irish Ice Sheet on the Atlantic Shelf Northwest of Ireland Driven by Glacioisostatic Depression and High Relative Sea Level. Quaternary Science Reviews, 208, 76-96.

O'Reilly, B., Readman, P. W. & Shannon, P. M. 2004. Cold Water Coral Mounds: Evidence for Early Holocene Climate Change and Slope Failure. Geophysical Research Letters, 31. http://dx.doi.org/10.1029/2003GL018619

O'Reilly, B., Shannon, P. M. & Readman, P. W. 2007. Shelf to Slope Sedimentation Processes and the Impact of Plio-Pleistocene Glaciations in the Northeast Atlantic, West of Ireland. Marine Geology, 238, 21-44. http://dx.doi.org/10.1016/j.margeo.2006.12.008

O'Reilly, L., Fentimen, R., Butscheck, F., Titschack, J. Lim, A., Moore, N., O'Connor, O.J., Appah, J., Harris, K., Vennemann, T. and Wheeler, A. in press. Environmental Forcing by Submarine Canyons: Evidence Between Two Closely Situated Cold-Water Coral Mounds (West Porcupine Bank and Porcupine Bank Canyon, NE Atlantic). Marine Geology

O'Reilly, L., Lim, A., Titschack, J., Moore, N., O'Connor, O. J., Appah, J., O'Reilly, L., Lim, A., Titschack, J., Moore, N., O'Connor, O. J., Appah, J., Fentimen, R., Butschek, F., Harris, K., Vennemann, T. & Wheeler, A. 2022. Using Novel Methods to Track British and Irish Ice Sheet Dynamics since the Late Pleistocene, Along the West Porcupine Bank, NE Atlantic. Quaternary Science Reviews, 284, 107463, https://doi.org/10.1016/j.quascirev.2022.107463

Øvrebø, L. K. & Shannon, P. Temporal and Spatial Variations in Late Quaternary Slope Sedimentation Along the Undersupplied Margins of the Rockall Trough, Offshore West Ireland. 2005.

Øvrebø, L. K., Haughton, P. D. W. & Shannon, P. M. 2006. A Record of Fluctuating Bottom Currents on the Slopes West of the Porcupine Bank, Offshore Ireland; Implications for Late Quaternary Climate Forcing. Marine Geology, 225, 279-309. http://dx.doi.org/10.1016/j.margeo.2005.06.034

Palanques, A., Garcia-Ladona, E., Gomis, D., Martín, J., Marcos, M., Pascual, A., Puig, P., Gili, J. M., Emelianov, M., Monserrat, S., Guillén, J., Tintoré, J., Segura, M. a. M., Jordi, A., Ruiz, S., Basterretxea, G., Font, J., Blasco, D. & Pagés, F. 2005. General Patterns of Circulation, Sediment Fluxes and Ecology of the Palamos (La Fonera) Submarine Canyon, Northwestern Mediterranean. Progress in Oceanography, 66, 89-119. http://dx.doi.org/10.1016/j.pocean.2004.07.016

Paterson, G. & Heslop, D. 2015. New Methods for Unmixing Sediment Grain Size Data. Geochemistry Geophysics Geosystems, 16, 4494-4506.

Paull, C. K., Normark, W. R., Ussler Iii, W., Caress, D. W. & Keaten, R. 2008. Association among Active Seafloor Deformation, Mound Formation, and Gas Hydrate Growth and Accumulation within the Seafloor of the Santa Monica Basin, Offshore California. Marine Geology, 250, 258-275. http://dx.doi.org/10.1016/j.margeo.2008.01.011

Peck, V. L., Hall, I. R., Zahn, R., Grousset, F. E., Hemming, S. R. & Scourse, J. D. 2007. The Relationship of Heinrich Events and Their European Precursors over the Past 60 Ka Bp: A Multi-Proxy Ice-Rafted Debris Provenance Study in the North East Atlantic. Quaternary Science Reviews, 26, 862-875. https://doi.org/10.1016/j.quascirev.2006.12.002

Peck, V. L., Hall, I. R., Zahn, R., Grousset, F. E., Hemming, S. R. & Scourse, J. D. 2007. The Relationship of Heinrich Events and Their European Precursors over the Past 60 Ka Bp: A Multi-Proxy Ice-Rafted Debris

Provenance Study in the North East Atlantic. Quaternary Science Reviews, 26, 862-875. https://doi.org/10.1016/j.quascirev.2006.12.002

Peck, V., Hall, I., Zahn, R., Elderfield, H., Grousset, F., Hemming, S. & Scourse, J. 2006. High Resolution Evidence for Linkages between NW European Ice Sheet Instability and Atlantic Meridional Overturning Circulation. Earth and Planetary Science Letters, 243, 476-488.

Peters, J., Benetti, S., Dunlop, P. & Ó Cofaigh, C. 2015. Maximum Extent and Dynamic Behaviour of the Last British Irish Ice Sheet West of Ireland. Quaternary Science Reviews, 128, 48-68.

Peters, J., Benetti, S., Dunlop, P., Ó Cofaigh, C., Moreton, S. G., Wheeler, A. & Clark, C. 2016. Sedimentology and Chronology of the Advance and Retreat of the Last British-Irish Ice Sheet on the Continental Shelf West of Ireland. Quaternary Science Reviews, 140, 101-124.

Phleger, F. B. & Soutar, A. 1973. Production of Benthic Foraminifera in Three East Pacific Oxygen Minima. Micropaleontology, 19, 110-115. http://dx.doi.org/10.2307/1484973

Piper, D. J. W. & Normark, W. R. 2009. Processes That Initiate Turbidity Currents and Their Influence on Turbidites: A Marine Geology Perspective. Journal of Sedimentary Research, 79, 347-362. http://dx.doi.org/10.2110/jsr.2009.046

Pirlet, H., Colin, C., Thierens, M., Latruwe, K., Van Rooij, D., Foubert, A., Frank, N., Blamart, D., Huvenne, V. A. & Swennen, R. 2011. The Importance of the Terrigenous Fraction within a Cold-Water Coral Mound: A Case Study. Marine Geology, 282, 13-25. http://dx.doi.org/10.1016/j.margeo.2010.05.008

Pollard, R. T., Griffiths, M. J., Cunningham, S. A., Read, J. F., Perez, F. F. & Rioz, A. F. 1996. Vivaldi 1991 - a Study of the Formation, Circulation and Ventilation of Eastern North Atlantic Waters. Progress in Oceanography, 37, 167-192. http://dx.doi.org/10.1016/S0079-6611(96)00008-0

Pomar, L. 2001. Ecological Control of Sedimentary Accommodation: Evolution from a Carbonate Ramp to Rimmed Shelf, Upper Miocene, Balearic Islands. Palaeogeography, Palaeoclimatology, Palaeoecology, 175, 249-272. http://dx.doi.org/10.1016/S0031-0182(01)00375-3

Praeg, D., McCarron, S., Dove, D., Ó Cofaigh, C., Scott, G., Monteys, X., Facchin, L., Romeo, R. & Coxon, P. 2015. Ice Sheet Extension to the Celtic Sea Shelf Edge at the Last Glacial Maximum. Quaternary Science Reviews, 111, 107-112.

Pratson, L. F., Nittrouer, C. A., Wiberg, P. L., Steckler, M. S., Swenson, J. B., Cacchione, D. A., Karson, J. A., Murray, A. B., Wolinsky, M. A., Gerber, T. P. D., Mullenbach, B. L., Spinelli, G. A., Fulthorpe, C. S., O'grady, D. B., Parker, G., Driscoll, N., Burger, R. L., Paola, C., Orange, D. L., Field, M. E., Friedrichs, C. T. & Fedele, J. 2009. Seascape Evolution on Clastic Continental Shelves and Slopes.

Price, D. M., Robert, K., Callaway, A., Lo Lacono, C., Hall, R. A. & Huvenne, V. a. I. 2019. Using 3d Photogrammetry from Rov Video to Quantify Cold-Water Coral Reef Structural Complexity and Investigate Its Influence on Biodiversity and Community Assemblage. Coral Reefs, 38, 1007–1021. http://dx.doi.org/10.1007/s00338-019-01827-3

Prins, M. & Weltje, G. 1999. End-Member Modeling of Siliciclastic Grain-Size Distributions: "End-Member Modeling of Siliciclastic Grain-Size Distributions: The Late Quaternary Record of Eolian and Fluvial Sediment Supply to the Arabian Sea and its Paleoclimatic Significance", in Numerical Experiments in Stratigraphy: Recent Advances in Stratigraphic and Sedimentologic Computer Simulations, (Eds.) John W. Harbaugh, W. Lynn Watney, Eugene C. Rankey, Rudy Slingerland, Robert H. Goldstein, Evan K. Franseen.

Prins, M. A., Bouwer, L. M., Beets, C. J., Troelstra, S. R., Weltje, G. J., Kruk, R. W., Kuijpers, A. & Vroon, P. Z. 2002. Ocean Circulation and Iceberg Discharge in the Glacial North Atlantic: Inferences from Unmixing of Sediment Size Distributions. Geology, 30, 555-558.

Puig, P. & Gili, J.-M. 2019. 27 Submarine Canyons in the Mediterranean: A Shelter for Cold-Water Corals. In: OREJAS, C. & JIMÉNEZ, C. (eds.) Mediterranean Cold-Water Corals: Past, Present and Future: Understanding the Deep-Sea Realms of Coral. Cham: Springer International Publishing.

Puig, P., Greenan, B. J. W., Li, M. Z., Prescott, R. H. & Piper, D. J. W. 2013. Sediment Transport Processes at the Head of Halibut Canyon, Eastern Canada Margin: An Interplay between Internal Tides and Dense Shelf-Water Cascading. Marine Geology, 341, 14-28. http://dx.doi.org/10.1016/j.margeo.2013.05.004

Puig, P., Palanques, A. & Martín, J. 2014. Contemporary Sediment-Transport Processes in Submarine Canyons. Annual Review of Marine Science, 6, 53-77. http://dx.doi.org/10.1146/annurev-marine-010213-135037

Purcell, C. Late Quaternary Glaciation of the Continental Shelf Offshore of NW Ireland. 2014.

Quaresma, L., Vitorino, J., Oliveira, A. & Silva, J. E. 2007. Evidence of Sediment Resuspension by Nonlinear Internal Waves on the Western Portuguese Mid-Shelf. Marine Geology, 246, 123-143. http://dx.doi.org/10.1016/j.margeo.2007.04.019

Qvale, G. & Weering, T. C. E. V. 1985. Relationship of Surface Sediments and Benthic Foraminiferal Distribution Patterns in the Norwegian Channel (Northern North Sea). Marine Micropaleontology, 9, 469-488. http://dx.doi.org/10.1016/0377-8398(85)90014-3

Raddatz, J. & Rüggeberg, A. 2021. Constraining Past Environmental Changes of Cold Water Coral Mounds with Geochemical Proxies in Corals and Foraminifera. The Depositional Record, 7, 200 - 222. http://dx.doi.org/10.1002/dep2.98

Raddatz, J., Rüggeberg, A., Liebetrau, V., Foubert, A., Hathorne, E. C., Fietzke, J., Eisenhauer, A. & Dullo, W.-C. 2014. Environmental Boundary Conditions of Cold-Water Coral Mound Growth over the Last 3 Million Years in the Porcupine Seabight, Northeast Atlantic. Deep Sea

Research Part II: Topical Studies in Oceanography, 99, 227-236. http://dx.doi.org/10.1016/j.dsr2.2013.06.009

Ransom, B. L., Shea, K., Burkett, P. J., Bennett, R. H. & Baerwald, R. J. 1998. Comparison of Pelagic and Nepheloid Layer Marine Snow: Implications for Carbon Cycling. Marine Geology, 150, 39-50. http://dx.doi.org/10.1016/S0025-3227(98)00052-8

Ratmeyer, V., Belling, R., Bergenthal, M., Beuck, L., Brakel, C., Buhmann, S., Dodds, L. A., Dorschel, B., Engemann, G., Foubert, A. T. G., Gault, J., Grehan, A. J., Hayn, C., Jurkiw, A. L., Kahl, G., Kaiser, J., Klar, S., Lutz, M., Noë, S., Papstein, H., Rüggeberg, A., Ruhland, G., Schewe, F., Schmidt, W., Schröder, M., Seiter, C., Truscheit, T. & Wienberg, C. 2006. Cruise Report Meteor Leg M61-3 Cork, Ireland - Ponta Delgada, Azores 04.06-21.06.2004. https://media.suub.uni-bremen.de/bitstream/elib/4103/1/00010679.pdf

Rea, B., Newton, A., Lamb, R. M., Harding, R., Bigg, G. R., Rose, P., Spagnolo, M., Huuse, M., Cater, J., Archer, S., Buckley, F., Halliyeva, M., Huuse, J., Cornwell, D. G., Brocklehurst, S. & Howell, J. 2018. Extensive Marine-Terminating Ice Sheets in Europe from 2.5 Million Years Ago. Science Advances, 4.

Reed, J. K., Weaver, D. C. & Pomponi, S. A. 2006. Habitat and Fauna of Deep-Water Lophelia Pertusa Coral Reefs Off the Southeastern U.S.: Blake Plateau, Straits of Florida, and Gulf of Mexico. Bulletin of Marine Science, 78, 343-375.

Reimer, P. J., Austin, W. E. N., Bard, E., Bayliss, A., Blackwell, P. G., Bronk Ramsey, C., Butzin, M., Cheng, H., Edwards, R. L., Friedrich, M., Grootes, P. M., Guilderson, T. P., Hajdas, I., Heaton, T. J., Hogg, A. G., Hughen, K. A., Kromer, B., Manning, S. W., Muscheler, R., Palmer, J. G., Pearson, C. L., Van Der Plicht, J., Reimer, R. W., Richards, D. A., Scott, E. M., Southon, J. R., Turney, C. S. M., Wacker, L., Adolphi, F., Büntgen, U., Capano, M., Fahrni, S. M., Fogtmann-Schulz, A., Friedrich, R., Köhler, P., Kudsk, S. G. K., Miyake, F., Olsen, J., Reinig, F., Sakamoto, M., Sookdeo, A. & Talamo, S. 2020. The Intcal20

Northern Hemisphere Radiocarbon Age Calibration Curve (P 55 Cal Kbp). Radiocarbon, 62, 725 - 757. http://dx.doi.org/10.1017/RDC.2020.41

Reimer, P. J., Mccormac, F. G., Moore, J. C., Mccormick, F. & Murray, E. V. 2002. Marine Radiocarbon Reservoir Corrections for the Midto Late Holocene in the Eastern Subpolar North Atlantic. The Holocene, 12, 129 - 135.

Rice, A. L., Billett, D. S. M., Thurston, M. H. & Lampitt, R. S. 1991. The Institute of Oceanographic Sciences Biological Programme in the Porcupine Seabight: Background and General Introduction. Journal of the Marine Biological Association of the United Kingdom, 71, 281-310.

Rice, A. L., Thurston, M. H. & New, A. L. 1990. Dense Aggregations of a Hexactinellid Sponge, Pheronema Carpenteri, in the Porcupine Seabight (Northeast Atlantic Ocean), and Possible Causes. Progress in Oceanography, 24, 179-196. http://dx.doi.org/10.1016/0079-6611(90)90029-2

Roberts, D. H., Evans, D., Callard, S., Clark, C., Bateman, M., Medialdea, A., Dove, D., Cotterill, C., Saher, M. H., Ó Cofaigh, C., Chiverrell, R., Moreton, S. G., Fabel, D. & Bradwell, T. 2018. Ice Marginal Dynamics of the Last British-Irish Ice Sheet in the Southern North Sea: Ice Limits, Timing and the Influence of the Dogger Bank. Quaternary Science Reviews, 198, 181-207.

Roberts, D. H., Grimoldi, E., Callard, L., Evans, D. J. A., Clark, C. D., Stewart, H. A., Dove, D., Saher, M., Ó Cofaigh, C., Chiverrell, R. C., Bateman, M. D., Moreton, S. G., Bradwell, T., Fabel, D. & Medialdea, A. 2019. The Mixe„ Bed Glacial Landform Imprint of the North Sea Lobe in the Western North Sea. Earth Surface Processes and Landforms, 44, 1233 1258.

Roberts, D. H., Ó Cofaigh, C., Ballantyne, C. K., Burke, M. J., Chiverrell, R. C., Evans, D. J. A., Clark, C. D., Duller, G. a. T., Ely, J. C., Fabel, D., Small, D. L., Smedley, R. K. & Callard, S. L. 2020. The Deglaciation of

the Western Sector of the Irish Ice Sheet from the Inner Continental Shelf to Its Terrestrial Margin. Boreas, 49, 438-460.

Roberts, J. M. & Cairns, S. D. 2014. Cold-Water Corals in a Changing Ocean. Current Opinion in Environmental Sustainability, 7, 118-126. http://dx.doi.org/10.1016/j.cosust.2014.01.004

Roberts, J. M. 2005. Reef-Aggregating Behaviour by Symbiotic Eunicid Polychaetes from Cold-Water Corals: Do Worms Assemble Reefs? Journal of the Marine Biological Association of the United Kingdom, 85, 813-819 http://dx.doi.org/10.1017/S0025315405011756

Roberts, J. M., Long, D., Wilson, J. B., Mortensen, P. B. & Gage, J. D. 2003. The Cold-Water Coral Lophelia Pertusa (Scleractinia) and Enigmatic Seabed Mounds Along the North-East Atlantic Margin: Are They Related? Marine Pollution Bulletin, 46, 7-20. http://dx.doi.org/10.1016/S0025-326X(02)00259-X

Roberts, J. M., Long, L.-a. H. D. & Hartley, J. P. 2008. Cold-Water Coral Reef Frameworks, Megafaunal Communities and Evidence for Coral Carbonate Mounds on the Hatton Bank, North East Atlantic. Facies, 54, 297-316. http://dx.doi.org/10.1007/s10347-008-0140-x

Roberts, J. M., Wheeler, A. J. & Freiwald, A. 2006. Reefs of the Deep: The Biology and Geology of Cold-Water Coral Ecosystems. Science, 312, 543-547. http://dx.doi.org/10.1126/science.1119861

Roberts, J. M., Wheeler, A. J., Cairns, S. & Freiwald, A. 2009. Cold-Water Corals: The Biology and Geology of Deep-Sea Coral Habitats, Cambridge University Press.

Rowe, G. T., Polloni, P. T. & Haedrich, R. L. 1982. The Deep-Sea Macrobenthos on the Continental Margin of the Northwest Atlantic Ocean. Deep Sea Research Part A. Oceanographic Research Papers, 29, 257-278. http://dx.doi.org/10.1016/0198-0149(82)90113-3

Roy, S., Georgiopoulou, A., Benetti, S. & Sacchetti, F. 2020. Mass Transport Deposits in the Donegal Barra Fan and Their Association with British–

Irish Ice Sheet Dynamics. Geological Society, London, Special Publications, 500, 567-586.

Ryan, J. P., Chavez, F. P. & Bellingham, J. G. 2005. Physical-Biological Coupling in Monterey Bay, California: Topographic Influences on Phytoplankton Ecology. Marine Ecology Progress Series, 287, 23-32. http://dx.doi.org/10.3354/meps287023

Rüggeberg, A., Dorschel, B., Dullo, W.-C. & Hebbeln, D. 2005. Sedimentary Patterns in the Vicinity of a Carbonate Mound in the Hovland Mound Province, Northern Porcupine Seabight. In: FREIWALD, A. & ROBERTS, J. M. (eds.) Cold-Water Corals and Ecosystems. Berlin Heidelberg: Springer.

Rüggeberg, A., Dullo, W.-C., Dorschel, B. & Hebbeln, D. 2007. Environmental Changes and Growth History of a Cold-Water Carbonate Mound (Propeller Mound, Porcupine Seabight). International Journal of Earth Sciences, 96, 57-72. http://dx.doi.org/10.1007/s00531-005-0504-1

Sacchetti, F., Benetti, S., Georgiopoulou, A., Shannon, P. M., O'Reilly, B. M., Dunlop, P., Quinn, R. & Ó Cofaigh, C. 2012. Deep-Water Geomorphology of the Glaciated Irish Margin from High-Resolution Marine Geophysical Data. Marine Geology, 291-294, 113-131. 10.1016/j.margeo.2011.11.011

Sakai, S., Kano, A. & Abe, K. 2009. Origin, Glacial-Interglacial Responses, and Controlling Factors of a Cold-Water Coral Mound in NE Atlantic. Paleoceanography, 24. http://dx.doi.org/10.1029/2008PA001695

Saldías, G. S. & Allen, S. E. 2020. The Influence of a Submarine Canyon on the Circulation and Cross-Shore Exchanges around an Upwelling Front. Journal of Physical Oceanography, 50, 1677–1698. http://dx.doi.org/10.1175/JPO-D-19-0130.1

Sandstrom, H. & Elliott, J. A. 1984. Internal Tide and Solitons on the Scotian Shelf: A Nutrient Pump at Work. Journal of Geophysical Research, 89, 6415-6426. http://dx.doi.org/10.1029/JC089iC04p06415

Sarnthein, M., Stattegger, K., Dreger, D., Erlenkeuser, H., Grootes, P., Haupt, B., Jung, S., Kiefer, T., Kuhnt, W., Pflaumann, U., Schäfer-Neth, C., Schulz, H., Schulz, M., Seidov, D., Simstich, J., Kreveld, S. V., Vogelsang, E., Völker, A., Weinelt, M., Fundamental Modes and Abrupt Changes in North Atlantic Circulation and Climate over the last 60 ky - Concepts, Reconstruction and Numerical Modeling. In: The Northern North Atlantic, Schäfer, P., Ritzrau, W., Schlüter, M., Thiede, J (Eds.), Springer, Berlin, Heidelberg, Chapter 21, http://dx.doi.org/10.1007/978-3-642-56876-3_21

Schiebel, R. & Hemleben, C. 2007. Planktonic Foraminifers in the Modern Ocean, Springer-Verlag GmbH Berlin Heidelberg.

Schiffer, C., Doré, A. G., Foulger, G., Franke, D., Geoffroy, L., Gernigon, L., Holdsworth, B. K., Kusznir, N. J., Lundin, E. R., Mccaffrey, K. J. W., Peace, A. L., Petersen, K. D., Phillips, T. B., Stephenson, R., Stoker, M. S. & Welford, J. K. 2020. Structural Inheritance in the North Atlantic. Earth-Science Reviews, 206, 102975. http://dx.doi.org/10.1016/j.earscirev.2019.102975

Schlacher, T. A., Schlacher-Hoenlinger, M. A., Williams, A., Althaus, F., Hooper, J. N. A. & Kloser, R. J. 2007. Richness and Distribution of Sponge Megabenthos in Continental Margin Canyons Off Southeastern Australia. Marine Ecology Progress Series, 340, 73-88. http://dx.doi.org/10.3354/meps340073

Schlacher, T. A., Williams, A., Althaus, F. & Schlacher-Hoenlinger, M. A. 2010. High-Resolution Seabed Imagery as a Tool for Biodiversity Conservation Planning on Continental Margins. Marine Ecology, 31, 200-221. http://dx.doi.org/10.1111/j.1439-0485.2009.00286.x

Schmiedl, G., Bovée, F. D., Buscail, R., Charrière, B., Hemleben, C., Medernach, L. & Picon, P. 2000. Trophic Control of Benthic Foraminiferal Abundance and Microhabitat in the Bathyal Gulf of Lions, Western Mediterranean Sea. Marine Micropaleontology, 40, 167-188. http://dx.doi.org/10.1016/S0377-8398(00)00038-4

Schnitker, D. 1980. Quaternary Deep-Sea Benthic Foraminifers and Bottom Water Masses. Annual Review of Earth and Planetary Sciences, 8, 343-370. http://dx.doi.org/10.1146/annurev.ea.08.050180.002015

Schröder-Ritzrau, A., Freiwald, A. & Mangini, A. 2005. U/Th-Dating of Deep-Water Corals from the Eastern North Atlantic and the Western Mediterranean Sea. In: FREIWALD, A. & ROBERTS, J. M. (eds.) Cold-Water Corals and Ecosystems. Berlin, Heidelberg, New York: Springer.

Schröder-Ritzrau, A., Mangini, A. & Lomitschka, M. 2003. Deep-Sea Corals Evidence Periodic Reduced Ventilation in the North Atlantic During the Lgm/Holocene Transition. Earth and Planetary Science Letters, 216, 399-410. doi:10.1016/S0012-821X(03)00511-9

Schulz, M. 2002. On the 1470-Year Pacing of Dansgaard-Oeschger Warm Events. Paleoceanography, 17, 4-1-4-9.

Schönfeld, J. 1997. The Impact of the Mediterranean Outflow Water (Mow) on Benthic Foraminiferal Assemblages and Surface Sediments at the Southern Portuguese Continental Margin. Marine Micropaleontology, 29, 211-236. http://dx.doi.org/10.1016/S0377-8398(96)00050-3

Schönfeld, J. 2002a. A New Benthic Foraminiferal Proxy for near-Bottom Current Velocities in the Gulf of Cadiz, Northeastern Atlantic Ocean. Deep Sea Research Part I, 49, 1853-1875. http://dx.doi.org/10.1016/S0967-0637(02)00088-2

Schönfeld, J. 2002b. Recent Benthic Foraminiferal Assemblages in Deep High-Energy Environments from the Gulf of Cadiz (Spain). Marine Micropaleontology, 44, 141-162. http://dx.doi.org/10.1016/S0377-8398(01)00039-1

Schönfeld, J., Dullo, W. C., Pfannkuche, O., Freiwald, A., Rüggeberg, A., Schmidt, S. & Weston, J. F. 2011. Recent Benthic Foraminiferal Assemblages from Cold-Water Coral Mounds in the Porcupine Seabight. Facies, 57, 187-213. http://dx.doi.org/10.1007/s10347-010-0234-0

Scourse, J. D., Haapaniemi, A. I., Colmenero-Hidalgo, E., Peck, V. L., Hall, I. R., Austin, W. E. N., Knutz, P. C. & Zahn, R. 2009. Growth, Dynamics and Deglaciation of the Last British Irish Ice Sheet: The Deep-Sea Ice-Rafted Detritus Record. Quaternary Science Reviews, 28, 3066-3084. http://dx.doi.org/10.1016/j.quascirev.2009.08.009

Scourse, J. D., Saher, M. H., Landeghem, K. V., Lockhart, E., Purcell, C., Callard, L., Roseby, Z. A., Allinson, B., Pifdkowski, A. J., O'Cofaigh, C., Praeg, D., Ward, S., Chiverrell, R., Moreton, S., Fabel, D. & Clark, C. 2019. Advance and Retreat of the Marine-Terminating Irish Sea Ice Stream into the Celtic Sea During the Last Glacial: Timing and Maximum Extent. Marine Geology, 412, 53-68.

Scourse, J. D., Ward, S. L., Wainwright, A., Bradley, S. L. & Uehara, K. 2018. The Role of Megatides and Relative Sea Level in Controlling the Deglaciation of the British-Irish and Fennoscandian Ice Sheets. Journal of Quaternary Science, 33, 139-149.

Scourse, J., Haapaniemi, A. I., Colmenero-Hidalgo, E., Peck, V. L., Hall, I., Austin, W., Knutz, P. & Zahn, R. 2009a. Growth, Dynamics and Deglaciation of the Last British Irish Ice Sheet: The Deep-Sea Ice-Rafted Detritus Record. Quaternary Science Reviews, 28, 3066-3084.

Scourse, J., Hall, I., Mccave, I. N., Young, J. & Sugdon, C. 2000. The Origin of Heinrich Layers: Evidence from H2 for European Precursor Events. Earth and Planetary Science Letters, 182, 187-195.

Sejrup, H. P., Clark, C. D. & Hjelstuen, B. O. 2016. Rapid Ice Sheet Retreat Triggered by Ice Stream Debuttressing: Evidence from the North Sea. Geology, 44, 355-358.

Sejrup, H. P., Fjaeran, T., Hald, M., Beck, L., Hagen, J., Miljeteig, I., Morvik, I. & Norvik, O. 1981. Benthonic Foraminifera in Surface Samples from the Norwegian Continental Margin between 62 Degrees N and 65 Degrees N. Journal of Foraminiferal Research, 11, 277-295. http://dx.doi.org/10.2113/gsjfr.11.4.277

Shannon, P. M. 1991. The Development of Irish Offshore Sedimentary Basins. Journal of the Geological Society London, 148, 181-189. http://dx.doi.org/10.1144/gsjgs.148.1.0181

Shannon, P. M., McDonnell, A. & Bailey, W. R. 2007. The Evolution of the Porcupine and Rockall Basins, Offshore Ireland: The Geological Template for Carbonate Mound Development. International Journal of Earth Sciences, 96, 21-35. http://dx.doi.org/10.1007/s00531-006-0081-y

Shepard, F. P. & Dill, R. F. 1966. Submarine Canyons and Other Sea Valleys, Rand McNally Co., Chicago.

Shepard, F. P. 1963. Submarine Geology, Harper and Row, New York.

Shepard, F. P. 1972. Submarine Canyons. Scientific American, 180, 40-3. http://dx.doi.org/10.1016/0012-8252(72)90032-3

Shepard, F. P. 1981. Submarine Canyons: Multiple Causes and Long-Time Persistence. AAPG Bulletin, 65, 1062-1077. https://doi.org/10.1306/03B59459-16D1-11D7-8645000102C1865D

Shepard, F. P., Marshall, N. F. & Mcloughlin, P. A. 1974. "Internal Waves" Advancing Along Submarine Canyons. Science, 183, 195 - 198. http://dx.doi.org/10.1126/science.183.4121.195

Singh, D. P., Saraswat, R. & Nigam, R. 2021. Untangling the Effect of Organic Matter and Dissolved Oxygen on Living Benthic Foraminifera in the Southeastern Arabian Sea. Marine Pollution Bulletin, 172, 112883. http://dx.doi.org/10.1016/j.marpolbul.2021.112883

Small, D. L., Benetti, S., Dove, D., Ballantyne, C. K., Fabel, D., Clark, C. D., Gheorghiu, D., Newall, J. C. H. & Xu, S. 2017. Cosmogenic Exposure Age Constraints on Deglaciation and Flow Behaviour of a Marine-Based Ice Stream in Western Scotland, 2q 16 Ka. Quaternary Science Reviews, 167, 30-46.

Small, D. L., Smedley, R. K., Chiverrell, R. C., Scourse, J. D., Ó Cofaigh, C., Duller, G. a. T., McCarron, S., Burke, M. J., Evans, D. J. A., Fabel, D.,

Gheorghiu, D., Thomas, G. S. P., Xu, S. & Clark, C. D. 2018. Trough Geometry Was a Greater Influence Than Climate-Ocean Forcing in Regulating Retreat of the Marine-Based Irish-Sea Ice Stream. Geological Society of America Bulletin, 130, 1981-1999.

Smedley, R. K., Chiverrell, R. C., Ballantyne, C. K., Burke, M. J., Clark, C. D., Duller, G. a. T., Fabel, D., Mccarroll, D., Scourse, J. D., Small, D. L. & Thomas, G. S. P. 2017. Internal Dynamics Condition Centennial-Scale Oscillations in Marine-Based Ice Stream Retreat. Geology, 45, 787-790.

Smeulders, G., Koho, K. A., Stigter, H. C. D., Mienis, F., Haas, H. D. & Weering, T. C. E. V. 2014. Cold-Water Coral Habitats of Rockall and Porcupine Bank, NE Atlantic Ocean: Sedimentary Facies and Benthic Foraminiferal Assemblages. Deep-sea Research Part Ii-topical Studies in Oceanography, 99, 270-285. http://dx.doi.org/10.1016/j.dsr2.2013.10.001

Snelgrove, P. V. R. & Smith, C. R. 2002. A Riot of Species in an Environmental Calm: The Paradox of the Species-Rich Deep-Sea Floor. Oceanography and Marine Biology.

Sobarzo, M., Figueroa, M. J. M. & Djurfeldt, L. 2001. Upwelling of Subsurface Water into the Rim of the Biobio Submarine Canyon as a Response to Surface Winds. Continental Shelf Research, 21, 279-299. 10.1016/S0278-4343(00)00082-0

Soulsby, R. 1997. Dynamics of Marine Sands, a Manual for Practical Applications Thomas Telford. London.

Spero, H.J., Bijma, Jelle, Lea, D.W., Bernis, B.E., 1997. Effect Of Seawater Carbonate Concentration On Foraminiferal Carbon And Oxygen Isotopes. Nature, 390, 6659, 497-500

Spezzaferri, S. & Coric, S. 2001. Ecology of Karpatian (Early Miocene) Foraminifers and Calcareous Nannoplankton from Laa an Der Thaya, Lower Austria: A Statistical Approach. Geologica Carpathica, 52, 361-374.

Spezzaferri, S., Ruüggeberg, A. & Stalder, C. 2015. Atlas of Benthic Foraminifera from Cold-Water Coral Reefs. Cushman Foundation for Foraminiferal Research Special Publication.

Spezzaferri, S., Rüggeberg, A., Stalder, C. & Margreth, S. 2013. Benthic Foraminifer Assemblages from Norwegian Cold-Water Coral Reefs. Journal of Foraminiferal Research, 43, 21-39. http://dx.doi.org/10.2113/gsjfr.43.1.21

Spezzaferri, S., Rüggeberg, A., Stalder, C. 2015. Atlas of Benthic Foraminifera from Cold-Water Coral Reefs. , Cushman Foundation for Foraminiferal Research Special Publication.

SpöTl, C. & Vennemann, T. 2003. Continuous-Flow Isotope Ratio Mass Spectrometric Analysis of Carbonate Minerals. Rapid communications in mass spectrometry : RCM, 17, 1004-1006. http://dx.doi.org/10.1002/rcm.1010

Squires, D. F. 1964. Fossil Coral Thickets in Wairarapa, New Zealand. Journal Paleontology, 38, 904-915.

Stalder, C., Kateb, A. E., Vertino, A., Rüggeberg, A., Camozzi, O., Pirkenseer, C. M., Spangenberg, J. E., Hajdas, I., Rooij, D. V. & Spezzaferri, S. 2018. Large-Scale Paleoceanographic Variations in the Western Mediterranean Sea During the Last 34,000 Years: From Enhanced Cold-Water Coral Growth to Declining Mounds. Marine Micropaleontology, 143, 46-62. http://dx.doi.org/10.1016/j.marmicro.2018.07.007

Stalder, C., Spezzaferri, S., Rüggeberg, A., Pirkenseer, C. & Gennari, G. 2014. Late Weichselian Deglaciation and Early Holocene Development of a Cold-Water Coral Reef Along the Lopphavet Shelf (Northern Norway) Recorded by Benthic Foraminifera and Ostracoda. Deep Sea Research Part II: Topical Studies in Oceanography, 99, 249-269. https://doi.org/10.1016/j.dsr2.2013.07.009

Stalder, C., Vertino, A., Rosso, A., Rüggeberg, A., Pirkenseer, C., Spangenberg, J. E., Spezzaferri, S., Camozzi, O., Rappo, S. & Hajdas,

I. 2015. Microfossils, a Key to Unravel Cold-Water Carbonate Mound Evolution through Time: Evidence from the Eastern Alboran Sea. PLoS ONE, 10, e0140223. 10.1371/journal.pone.0140223

Stalling, D., Westerhoff, M. & Hege, H.-C. 2005. version 2018.36 http://amira.zib.de

Stanford, J., Rohling, E. J., Bacon, S., Roberts, A. P., Grousset, F. E. & Bolshaw, M. 2011. A New Concept for the Paleoceanographic Evolution of Heinrich Event 1 in the North Atlantic. Quaternary Science Reviews, 30, 1047-1066. http://dx.doi.org/10.1016/j.quascirev.2011.02.003

Stetson, T. R., Squires, D. F. & Pratt, R. M. 1962. Coral Banks Occurring in Deep Water on the Blake Plateau. American Museum Novitates, 2114, 1-39.

Stewart, H. A., Davies, J. S., Guinan, J. & Howell, K. L. 2014. The Dangeard and Explorer Canyons, South Western Approaches Uk: Geology, Sedimentology and Newly Discovered Cold-Water Coral Mini-Mounds. Deep Sea Research Part II: Topical Studies in Oceanography, 104, 230-244. https://doi.org/10.1016/j.dsr2.2013.08.018

Streeter, S. S. & Shackleton, N. J. 1979. Paleocirculation of the Deep North Atlantic: 150,000-Year Record of Benthic Foraminifera and Oxygen-18. Science, 203, 168 - 171. http://dx.doi.org/10.1126/science.203.4376.168

Stuiver, M. & Reimer, P. J. 1993. Extended 14c Data-Base and Revised Calib. 3.0 C-14 Age Calibration Program. Radiocarbon, 35, 215-230.

Stuut, J., Kasten, S., Lamy, F. & Hebbeln, D. 2007. Sources and Modes of Terrigenous Sediment Input to the Chilean Continental Slope. Quaternary International, 161, 67-76.

Suhr, S. B., Pond, D. W., Gooday, A. J. & Smith, C. R. 2003. Selective Feeding by Benthic Foraminifera on Phytodetritus on the Western Antarctic Peninsula Shelf: Evidence from Fatty Acid Biomarker Analysis. Marine

Ecology Progress Series, 262, 153-162. http://dx.doi.org/10.3354/meps262153

Syvitski, J., Andrews, J. & Dowdeswell, J. Sediment Deposition in an Iceberg-Dominated Glacimarine Environment, East Greenland: Basin Fill Implications. 1996.

Tamborrino, L., Wienberg, C., Titschack, J., Wintersteller, P., Mienis, F., Schröder Ritzrau, A., Freiwald, A., Orejas, C., Dullo, W. C., Haberkern, J. & Hebbeln, D. 2019. Mid-Holocene Extinction of Cold-Water Corals on the Namibian Shelf Steered by the Benguela Oxygen Minimum Zone. Geology, 47, 1185. http://dx.doi.org/10.1130/G46672.1

Tarlati, S., Benetti, S., Callard, S. L., Ó Cofaigh, C., Dunlop, P., Georgiopoulou, A., Edwards, R., Landeghem, K. V. V., Saher, M., Chiverrell, R., Fabel, D., Moreton, S., Morgan, S. & Clark, C. 2020. Final Deglaciation of the Malin Sea through Meltwater Release and Calving Events. Scottish Journal of Geology, 56, 117 - 133.

Taviani, M., Angeletti, L., Beuck, L., Campiani, E., Canese, S., Foglini, F., Freiwald, A., Montagna, P. & Trincardi, F. 2015. On and Off the Beaten Track: Megafaunal Sessile Life and Adriatic Cascading Processes. Marine Geology, 369, 273-274. http://dx.doi.org/10.1016/j.margeo.2015.09.003

Team, R. C. 2021. https://www.R-project.org/

Thiem, Ø., Ravagnan, E., Fosså, J. H. & Berntsen, J. 2006. Food Supply Mechanisms for Cold-Water Corals Along a Continental Shelf Edge. Journal of Marine Systems, 60, 207-219. http://dx.doi.org/10.1016/j.jmarsys.2005.12.004

Thierens, M., Browning, E. L., Prilet, H., Loutre, M.-F., Dorschel, B., Huvenne, V. a. I., Titschack, J., Colin, C., Foubert, A. T. G. & Wheeler, A. J. 2013. Cold-Water Coral Carbonate Mounds as Unique Palaeo-Archives: The Plio-Pleistocene Challenger Mound Record (NE Atlantic). Quaternary Science Reviews, 73, 14-30. 10.1016/j.quascirev.2013.05.006

Thierens, M., Pirlet, H., Colin, C., Latruwe, K., Vanhaecke, F., Lee, J. R., Stuut, J.-B. W., Titschack, J., Huvenne, V. a. I., Dorschel, B., Wheeler, A. J. & Henriet, J.-P. 2012. Ice-Rafting from the British-Irish Ice Sheet since the Earliest Pleistocene (2.6 Million Years Ago): Implications for Long-Term Mid-Latitudinal Ice-Sheet Growth in the North Atlantic Region. Quaternary Science Reviews, 44, 229-240. 10.1016/j.quascirev.2010.12.020

Thierens, M., Titschack, J., Dorschel, B., Huvenne, V. a. I., Wheeler, A. J., Stuut, J.-B. W. & O'Donnell, R. 2010. The 2.6 Ma Depositional Sequence from the Challenger Cold-Water Coral Carbonate Mound (Iodp Exp. 307): Sediment Contributors and Hydrodynamic Palaeo-Environments. Marine Geology, 271, 260-277. doi:10.1016/j.margeo.2010.02.021

Thomas, E. R., Wolff, E. W., Mulvaney, R., Steffensen, J. P., Johnsen, S. S. J., Arrowsmith, C., White, J. W. C., Vaughn, B. H. & Popp, T. J. 2007. The 8.2 Ka Event from Greenland Ice Cores. Quaternary Science Reviews, 26, 70-81. https://doi.org/10.1016/j.quascirev.2006.07.017

Thornalley, D. J. R., Elderfield, H. & Mccave, I. N. 2009. Holocene Oscillations in Temperature and Salinity of the Surface Subpolar North Atlantic. Nature, 457, 711-714. http://dx.doi.org/10.1038/nature07717

Titschack, J., Baum, D., De Pol-Holz, R., López Correa, M., Forster, N., Flögel, S., Hebbeln, D. & Freiwald, A. 2015. Aggradation and Carbonate Accumulation of Holocene Norwegian Cold-Water Coral Reefs. Sedimentology, 62, 1873-1898. 10.1111/sed.12206

Titschack, J., Bromley, R. G. & Freiwald, A. 2005. Plio-Pleistocene Cliff-Bound, Wedge-Shaped, Warm-Temperate Carbonate Deposits from Rhodes (Greece): Sedimentology and Facies. Sedimentary Geology, 180, 29-56. 10.1016/j.sedgeo.2005.06.009

Titschack, J., Fink, H. G., Baum, D., Wienberg, C., Hebbeln, D. & Freiwald, A. 2016. Mediterranean Cold-Water Corals – an Important Regional

Carbonate Factory? The Depositional Record, 2, 74-96. 10.1002/dep2.14

Titschack, J., Thierens, M., Dorschel, B., Schulbert, C., Freiwald, A., Kano, A., Takashima, C., Kawagoe, N. & Li, X. 2009. Carbonate Budget of a Cold-Water Coral Mound (Challenger Mound, Iodp Exp. 307). Marine Geology, 259, 36-46. 10.1016/j.margeo.2008.12.007

Tjallingii, R., Claussen, M., Stuut, J., Fohlmeister, J., Jahn, A., Bickert, T., Lamy, F. & Röhl, U. 2008. Coherent High- and Low-Latitude Control of the Northwest African Hydrological Balance. Nature Geoscience, 1, 670-675.

Toucanne, S., Soulet, G., Freslon, N., Jacinto, R. S., Dennielou, B., Zaragosi, S., Eynaud, F., Bourillet, J. F. & Bayon, G. 2015. Millennial-Scale Fluctuations of the European Ice Sheet at the End of the Last Glacial, and Their Potential Impact on Global Climate. Quaternary Science Reviews, 123, 113-133. http://dx.doi.org/10.1016/j.quascirev.2015.06.010

Trotter, J. A., Pattiaratchi, C. B., Montagna, P., Taviani, M., Falter, J. L., Thresher, R. E., Hosie, A. M., Haig, D., Foglini, F., Hua, Q. & Mcculloch, M. T. 2019. First Rov Exploration of the Perth Canyon: Canyon Setting, Faunal Observations, and Anthropogenic Impacts. Frontiers in Marine Science, 6. http://dx.doi.org/10.3389/fmars.2019.00173

Tyler, P. A. 1995. Conditions for the Existence of Life at the Deep-Sea Floor : An Update. Oceanography and Marine Biology: An annual Review, 33, 221-244.

Van Aken, H. M. & Becker, G. 1996. Hydrography and through-Flow in the North-Eastern North Atlantic; the Nansen Project. Progress in Oceanography, 38, 297-346.

Van Aken, H. M. 2000. The Hydrography of the Mid-Latitude Northeast Atlantic Ocean Ii: The Intermediate Water Masses. Deep-Sea Research I, 47, 789-824.

Van Den Beld, I. M. J., Bourillet, J. F., Arnaud-Haond, S., De Chambure, L., Davies, J. S., Guillaumont, B., Olu, K. & Menot, L. 2017. Cold-Water Coral Habitats in Submarine Canyons of the Bay of Biscay. Frontiers in Marine Science, 4, 1-30. http://dx.doi.org/10.3389/fmars.2017.00118

Van Der Land, C., Mienis, F., Haas, H. D., Frank, N., Swennen, R. & Weering, T. C. E. V. 2010. Diagenetic Processes in Carbonate Mound Sediments at the South West Rockall Trough Margin. Sedimentology, 57, 912-931.

Van Der Zwaan, G. J. 1982. Paleoecology of Late Miocene Mediterranean Foraminifera. PhD, University Utrecht.

Van Nieuwenhove, N., Pearce, C., Knudsen, M. F., Røy, H. & Seidenkrantz, M. S. 2018. Meltwater and Seasonality Influence on Subpolar Gyre Circulation During the Holocene. Palaeogeography, Palaeoclimatology, Palaeoecology, 502, 104-118. http://dx.doi.org/10.1016/j.palaeo.2018.05.002

Van Oevelen, D., Duineveld, G., Lavaleye, M. S. S., Mienis, F., Soetaert, K. & Heip, C. 2009. The Cold-Water Coral Community as a Hot Spot for Carbon Cycling on Continental Margins: A Food-Web Analysis from Rockall Bank (Northeast Atlantic). Limnology and Oceanography, 54, 1829-1844. 10.4319/lo.2009.54.6.1829

Van Rooij, D., Blamart, D., Richter, T. O., Wheeler, A. J., Kozachenko, M. & Henriet, J.-P. 2007. Quaternary Sediment Dynamics in the Belgica Mound Province, Porcupine Seabight: Ice-Rafting Events and Contour Current Processes. International Journal of Earth Sciences, 96, 121-140.

Van Rooij, D., De Mol, B., Huvenne, V. a. I., Ivanov, M. K. & Henriet, J.-P. 2003. Seismic Evidences of Current-Controlled Sedimentation in the Belgica Mound Province, Upper Porcupine Slope, Southwest of Ireland. Marine Geology, 195, 31-53.

Van Weering, T. C. E., De Haas, H., De Stigter, H. C., Lykke-Andersen, H. & Kouvaev, I. 2003. Structure and Development of Giant Carbonate Mounds at the SW and Se Rockall Trough Margins, NE Atlantic Ocean.

Marine Geology, 198, 67-81. http://dx.doi.org/10.1016/S0025-3227(03)00095-1

Vetter, E. W. & Dayton, P. K. 1998. Macrofaunal Communities within and Adjacent to a Detritus-Rich Submarine Canyon System. Deep-sea Research Part II: Topical Studies in Oceanography, 45, 25-54. http://dx.doi.org/10.1016/S0967-0645(97)00048-9

Vetter, E. W. & Dayton, P. K. 1999. Organic Enrichment by Macrophyte Detritus, and Abundance Patterns of Megafaunal Populations in Submarine Canyons. Marine Ecology Progress Series, 186, 137-148. http://dx.doi.org/10.3354/meps186137

Vetter, E. W. 1994. Hotspots of Benthic Production. Nature, 372, 47-47. http://dx.doi.org/10.1038/372047a0

Vetter, E. W., Smith, C. R. & Léo, F. C. D. 2010. Hawaiian Hotspots: Enhanced Megafaunal Abundance and Diversity in Submarine Canyons on the Oceanic Islands of Hawaii. Marine Ecology, 31, 183-199. http://dx.doi.org/10.1111/j.1439-0485.2009.00351.x

Vic, C., Naveira Garabato, A. C., Green, J. a. M., Waterhouse, A. F., Zhao, Z. K., Melet, A., De Lavergne, C., Buijsman, M. C. & Stephenson, G. R. 2019. Deep-Ocean Mixing Driven by Small-Scale Internal Tides. Nature Communications, 10. http://dx.doi.org/10.1038/s41467-019-10149-5

Victorero, L., Blamart, D., Pons-Branchu, E., Mavrogordato, M. N. & Huvenne, V. a. I. 2016. Reconstruction of the Formation History of the Darwin Mounds, N Rockall Trough: How the Dynamics of a Sandy Contourite Affected Cold-Water Coral Growth. Marine Geology, 378, 186-195. http://dx.doi.org/10.1016/j.margeo.2015.12.001

Voelker, A. H. L., Salgueiro, E., Rodrigues, T., Jiménez-Espejo, F. J., Bahr, A., Alberto, A., Loureiro, I. M., Padilha, M., Rebotim, A. & Röhl, U. 2015. Mediterranean Outflow and Surface Water Variability Off Southern Portugal During the Early Pleistocene: A Snapshot at Marine Isotope Stages 29 to 34 (1020–1135 Ka). Global and Planetary Change, 133, 223-237. https://doi.org/10.1016/j.gloplacha.2015.08.015

Wadham, J., Hawkings, J., Tarasov, L., Gregoire, L., Spencer, R., Gutjahr, M., Ridgwell, A. & Kohfeld, K. 2019. Ice Sheets Matter for the Global Carbon Cycle. Nature Communications, 10.

Wagner, A. J., Morrill, C., Otto Bliesner, B. L., Rosenbloom, N. A. & Watkins, K. R. 2013. Model Support for Forcing of the 8.2 ka Event by Meltwater from the Hudson Bay Ice Dome. Climate Dynamics, 41, 2855-2873. http://dx.doi.org/10.1007/s00382-013-1706-z

Walsh, J. P. & Nittrouer, C. A. 2009. Understanding Fine-Grained River-Sediment Dispersal on Continental Margins. Marine Geology, 263, 34-45. http://dx.doi.org/10.1016/j.margeo.2009.03.016

Wang, H., Lo Iacono, C., Wienberg, C., Titschack, J. & Hebbeln, D. 2019. Cold-Water Coral Mounds in the Southern Alboran Sea (Western Mediterranean Sea): Internal Waves as an Important Driver for Mound Formation since the Last Deglaciation. Marine Geology, 412, 1-18. http://dx.doi.org/10.1016/j.margeo.2019.02.007

Wang, H., Titschack, J., Wienberg, C., Korpanty, C. A. & Hebbeln, D. 2021. The Importance of Ecological Accommodation Space and Sediment Supply for Cold-Water Coral Mound Formation, a Case Study from the Western Mediterranean Sea. Frontiers in Marine Science, 8. http://dx.doi.org/10.3389/fmars.2021.760909

Wefer, G., Berger, W., 1991. Isotope paleontology: growth and composition of extant calcareous species. Marine Geology, 199, 1-4, 207-248, http://dx.doi.org/10.1016/0025-3227(91)90234-U

Weltje, G. & Prins, M. 2003. Muddled or Mixed? Inferring Palaeoclimate from Size Distributions of Deep-Sea Clastics. Sedimentary Geology, 162, 39-62.

Weltje, G. 1997. End-Member Modeling of Compositional Data: Numerical-Statistical Algorithms for Solving the Explicit Mixing Problem. Mathematical Geology, 29, 503-549.

Wheeler, A. J., Beck, T., Thiede, J., Klages, M., Grehan, A., Monteys, F. X. & Polarstern Ark Xix/3a Shipboard Party 2005a. Deep-Water Coral Mounds on the Porcupine Bank, Irish Margin: Preliminary Results from Polarstern Ark-Xix/3a Rov Cruise. In: FREIWALD, A. & ROBERTS, J. M. (eds.) Cold-Water Corals and Ecosystems. Berlin: Springer-Verlag.

Wheeler, A. J., Beyer, A., Freiwald, A., De Haas, H., Huvenne, V. a. I., Kozachenko, M., Olu-Le Roy, K. & Opderbecke, J. 2007. Morphology and Environment of Cold-Water Coral Carbonate Mounds on the NW European Margin. International Journal of Earth Sciences, 96, 37-56. http://dx.doi.org/10.1007/s00531-006-0130-6

Wheeler, A. J., Beyer, A., Freiwald, A., De Haas, H., Huvenne, V. a. I., Kozachenko, M., Olu-Le Roy, K. & Opderbecke, J. 2007. Morphology and Environment of Cold-Water Coral Carbonate Mounds on the NW European Margin. International Journal of Earth Sciences, 96, 37-56. http://dx.doi.org/10.1007/s00531-006-0130-6

Wheeler, A. J., Capocci, R., Crippa, L., Connolly, N., Hogan, R., Lim, A., McCarthy, E., McGonigle, C., O' Donnell, E., O' Sullivan, K., Power, K., Ryan, G., Vertino, A., Holland 1 ROV Technical Team & Officers and Crew of the RV Celtic Explorer. 2015. Cruise Report: Quantifying Environmental Controls on Cold-Water Coral Reef Growth (Querci). https://www.ucc.ie/en/media/research/marinegeo/mgpdfs/Cruisereport_QuERCi_FINAL.pdf

Wheeler, A. J., Kozachenko, M., Beyer, A., Foubert, A. T. G., Huvenne, V. a. I., Klages, M., Masson, D. G., Olu-Le Roy, K. & Thiede, J. 2005b. Sedimentary Processes and Carbonate Mounds in the Belgica Mound Province, Porcupine Seabight, NE Atlantic. In: FREIWALD, A. & ROBERTS, J. M. (eds.) Cold-Water Corals and Ecosystems. Berlin Heidelberg: Springer-Verlag.

Wheeler, A. J., Kozachenko, M., Henry, L. A., Foubert, A., De Haas, H., Huvenne, V. a. I., Masson, D. G. & Olu, K. 2011. The Moira Mounds, Small Cold-Water Coral Banks in the Porcupine Seabight, NE Atlantic:

Part a—an Early Stage Growth Phase for Future Coral Carbonate Mounds? Marine Geology, 282, 53-64. 10.1016/j.margeo.2010.08.006

Wheeler, A. J., Lim, A., Butschek, F., O'Reilly, L., Harris, K. & O Driscoll, P. 2021. The "Little Monsta" Deep-Sea Benthic, Precision Deployable, Multi-Sensor and Sampling Lander Array. Sensors (Basel, Switzerland), 21, 3355. https://doi.org/10.3390/s21103355

Wheeler, A., Burke, S., Griffin, B., Lim, A., Ní Fhoalain, F., O'Reilly, L., Summers, G., Holland 1 ROV Technical Team & Crew of the RV Celtic Explorer, 2017. Controls of Cold-Water Coral Habitats in Submarine Canyons (CoCoHaCa). https://www.ucc.ie/en/media/research/marinegeo/mgpdfs/Cruise-Report_Final_CoCoHaCa.pdf

Wheeler, A., Connolly, N., Conti, L., Hogan, R., Lim, A., Massironi, C., Mullins, M., Murphy, P., Pinfield, R., Power, K., Toth, Z. & Holland 1 ROV Technical Team & Crew of the RV Celtic Explorer. 2016. Quantifying Environmental Controls on Cold-Water Coral Reef Growth: Part 2. https://www.ucc.ie/en/media/research/marinegeo/mgpdfs/Cruisereport_QuERCiII_Final.pdf

Wheeler, A., Lim, A., Peters, J., Sacchetti, F., Mcgrath, M., Browne, M., El Kateb, A., Ní Fhaoláin, F., Renken, S., Schiele, K., Vertino, A. & Crew of the RV Celtic Explorer 2014. West of Ireland Coring Programme (Wicpro). RV Celtic Explorer. Cork – Killybegs. 6th March to 18th March 2014. . https://www.ucc.ie/en/media/research/marinegeo/mgpdfs/WICPro-Cruise-Report-CE14014.pdf.

White, M. & Bowyer, P. 1997. The Shelf-Edge Current North-West of Ireland. Annales Geophysicae, 15, 1076-1083. http://dx.doi.org/10.1007/s00585-997-1076-0

White, M. & Dorschel, B. 2010. The Importance of the Permanent Thermocline to the Cold Water Coral Carbonate Mound Distribution in the NE

Atlantic. Earth and Planetary Science Letters, 296, 395-402. http://dx.doi.org/10.1016/j.epsl.2010.05.025

White, M. 2007. Benthic Dynamics at the Carbonate Mound Regions of the Porcupine Sea Bight Continental Margin. International Journal of Earth Sciences, 96, 1-9. http://dx.doi.org/10.1007/s00531-006-0099-1

White, M., Mohn, C., De Stigter, H. C. & Mottram, G. 2005. Deep-Water Coral Development as a Function of Hydrodynamics and Surface Productivity around the Submarine Banks of the Rockall Trough, NE Atlantic. In: FREIWALD, A. & ROBERTS, J. M. (eds.) Cold-Water Corals and Ecosystems. Berlin, Heidelberg, New York: Springer.

White, M., Roberts, J. M. & Van Weering, T. C. E. 2007. Do Bottom-Intensified Diurnal Tidal Currents Shape the Alignment of Carbonate Mounds in the NE Atlantic? Geo-Marine Letters, 27, 391-397. 10.1007/s00367-007-0060-8

Wienberg, C. & Titschack, J. 2017. Framework-Forming Scleractinian Cold-Water Corals through Space and Time: A Late Quaternary North Atlantic Perspective. In: ROSSI S., B. L., GORI A., OREJAS C. (ed.) Marine Animal Forests. Springer, Cham.

Wienberg, C., Beuck, L., Heidkamp, S., Hebbeln, D., Freiwald, A., Pfannkuche, O. & Monteys, F. X. 2008. Franken Mound: Facies and Biocoenoses on a Newly-Discovered “Carbonate Mound” on the Western Rockall Bank, NE Atlantic. Facies, 54, 1-24. 10.1007/s10347-007-0118-0

Wienberg, C., Frank, N., Mertens, K. N., Stuut, J.-B. W., Marchant, M., Fietzke, J., Mienis, F. & Hebbeln, D. 2010. Glacial Cold-Water Coral Growth in the Gulf of Cádiz: Implications of Increased Palaeo-Productivity. Earth and Planetary Science Letters, 298, 405-416. http://dx.doi.org/10.1016/j.epsl.2010.08.017

Wienberg, C., Hebbeln, D., Fink, H. G., Mienis, F., Dorschel, B., Vertino, A., López Correa, M. & Freiwald, A. 2009. Scleractinian Cold-Water Corals in the Gulf of Cádiz-First Clues About Their Spatial and Temporal

Distribution. Deep Sea Research Part I, 56, 1873-1893. doi:10.1016/j.dsr.2009.05.016

Wienberg, C., Titschack, J., Frank, N., Pol-Holz, R. D., Fietzke, J., Eisele, M., Kremer, A. & Hebbeln, D. 2020. Deglacial Upslope Shift of NE Atlantic Intermediate Waters Controlled Slope Erosion and Cold-Water Coral Mound Formation (Porcupine Seabight, Irish Margin). Quaternary Science Reviews, 237, 106310. http://dx.doi.org/10.1016/j.quascirev.2020.106310

Wienberg, C., Titschack, J., Freiwald, A., Frank, N., Lundälv, T., Taviani, M., Beuck, L., Schröder-Ritzrau, A., Krengel, T. & Hebbeln, D. 2018. The Giant Mauritanian Cold-Water Coral Mound Province: Oxygen Control on Coral Mound Formation. Quaternary Science Reviews, 185, 135-152. http://dx.doi.org/10.1016/j.quascirev.2018.02.012

Wienberg, C., Wintersteller, P., Beuck, L. & Hebbeln, D. 2013. Coral Patch Seamount (NE Atlantic) – a Sedimentological and Megafaunal Reconnaissance Based on Video and Hydroacoustic Surveys. Biogeosciences, 10, 3421-3443. 10.5194/bg-10-3421-2013

Wilson, A. M., Raine, R., Mohn, C. & White, M. 2015. Nepheloid Layer Distribution in the Whittard Canyon, NE Atlantic Margin. Marine Geology, 367, 130-142. http://dx.doi.org/10.1016/j.margeo.2015.06.002

Wilson, J. B. 1979. "Patch" Development of the Deep-Water Coral Lophelia Pertusa (L.) on the Rockall Bank. Journal of the Marine Biological Association of the United Kingdom, 59, 165-177. http://dx.doi.org/10.1017/S0025315400046257

Wilson, L. J. & Austin, W. 2002a. Millennial and Sub-Millennial-Scale Variability in Sediment Colour from the Barra Fan, NW Scotland: Implications for British Ice Sheet Dynamics. Geological Society, London, Special Publications, 203, 349 - 365.

Wilson, L. J., Austin, W. & Jansen, E. 2002. The Last British Ice Sheet: Growth, Maximum Extent and Deglaciation. Polar Research, 21, 243 - 250.

Wilson, P., Ballantyne, C. K., Benetti, S., Small, D. L., Fabel, D. & Clark, C. D. 2018. Deglaciation Chronology of the Donegal Ice Centre, North West Ireland. Journal of Quaternary Science, 34, 16-28.

Wilton, D., Bigg, G., Scourse, J., Ely, J. & Clark, C. 2021. Exploring the Extent to Which Fluctuations in Ic… Rafted Debris Reflect Mass Changes in the Source Ice Sheet: A Modeœ Observation Comparison Using the Last Britisˆ Irish Ice Sheet. Journal of Quaternary Science.

Woodruff, F. & Douglas, R. G. 1981. Response of Deep-Sea Benthic Foraminifera to Miocene Paleoclimatic Events, Dsdp Site 289. Marine Micropaleontology, 6, 617-632. http://dx.doi.org/10.1016/0377-8398(81)90024-4

Woodworth, P., Melet, A., Marcos, M., Ray, R., Wöppelmann, G., Sasaki, Y. N., Cirano, M., Hibbert, A., Huthnance, J., Monserrat, S. & Merrifield, M. 2019. Forcing Factors Affecting Sea Level Changes at the Coast. Surveys in Geophysics, 1-47.

Woronko, B. 2016. Frost Weathering Versus Glacial Grinding in the Micromorphology of Quartz Sand Grains: Processes and Geological Implications. Sedimentary Geology, 335, 103-119.

Wu, L., Wilson, D., Wang, R., Passchier, S., Krijgsman, W., Yu, X., Wen, T., Xiao, W. & Liu, Z. 2020. Late Quaternary Dynamics of the Lambert Glacier-Amery Ice Shelf System, East Antarctica. Quaternary Science Reviews, 106738.

Yoklavich, M. M., Greene, H. G., Cailliet, G. M., Sullivan, D. A. & Lea, R. N. Habitat Associations of Deep-Water Rockfishes in a Submarine Canyon: An Example of a Natural Refuge. Fishery Bulletin, 2000